The effects of muscle tissue mass on contractile performance

by

Stephanie A. Ross

B.Sc. (Hons), Simon Fraser University, 2015

Thesis Submitted in Partial Fulfillment of the
Requirements for the Degree of
Doctor of Philosophy

in the
Department of Biomedical Physiology and Kinesiology
Faculty of Science

SIMON FRASER UNIVERSITY
Summer 2021

Declaration of Committee

Name: **Stephanie A. Ross**

Degree: **Doctor of Philosophy**

Thesis title: **The effects of muscle tissue mass on contractile performance**

Committee:

Chair: Andy Hoffer
Professor, Biomedical Physiology and Kinesiology

James Wakeling
Supervisor
Professor, Biomedical Physiology and Kinesiology

Nilima Nigam
Committee Member
Professor, Mathematics

Max Donelan
Committee Member
Professor, Biomedical Physiology and Kinesiology

Dawn Mackey
Examiner
Associate Professor, Biomedical Physiology and Kinesiology

Thomas Daniel
External Examiner
Professor, Biology
University of Washington

Ethics Statement

The author, whose name appears on the title page of this work, has obtained, for the research described in this work, either:

a. human research ethics approval from the Simon Fraser University Office of Research Ethics

or

b. advance approval of the animal care protocol from the University Animal Care Committee of Simon Fraser University

or has conducted the research

c. as a co-investigator, collaborator, or research assistant in a research project approved in advance.

A copy of the approval letter has been filed with the Theses Office of the University Library at the time of submission of this thesis or project.

The original application for approval and letter of approval are filed with the relevant offices. Inquiries may be directed to those authorities.

Simon Fraser University Library
Burnaby, British Columbia, Canada

Update Spring 2016

Abstract

Skeletal muscles are the motors that drive human and animal locomotion. Yet despite their fundamental importance, our understanding of whole muscle behaviour is relatively limited due to practical and ethical considerations that hinder accurate *in vivo* measures. To estimate the behaviour of whole muscles, measures of single fibres or fibre bundles are often extrapolated to larger sizes without considering the consequences of the greater muscle mass. The goal of this thesis was to determine the effects of muscle mass on the contractile performance of whole skeletal muscles. In my first study, I developed a novel modelling framework to test different Hill-type model formulations under a range of cyclic contractile conditions. I then used this framework in my second study to examine the effects of distributed muscle mass on mass-specific mechanical work per cycle during cyclic contractions. I found that when the mass-enhanced muscle model was geometrically scaled from the size of a fibre bundle up to a whole human plantarflexor muscle, the mass-specific work per cycle decreased. In my third study, I examined the effects of muscle mass on the contractile behaviour of *in situ* rat plantaris muscle to validate the mass-enhanced Hill-type muscle model in my second study. In the fourth study of my thesis, I simulated cyclic contractions of a 3D continuum muscle model that accounts for tissue mass across a range of muscle sizes. I additionally compared the effects of greater muscle mass on tissue accelerations of the 3D muscle model to that of the *in situ* rat plantaris muscle from my third study to qualitatively validate the model simulations. I found that increasing the mass of the 3D muscle increased its volume-specific kinetic energy and was associated with lower mass-specific mechanical work per cycle. In my fifth study, I examined the effects of muscle mass on the metabolic cost and efficiency of muscle during cyclic contractions and how tendons of different stiffnesses alter these relationships. I found that larger muscles with greater mass are less efficient, primarily due to lower mass-specific mechanical work, and that the work and efficiency penalty of larger muscles can be offset to a certain extent by a tendon of optimal stiffness. Taken together, the results of these studies highlight that muscle mass is an important determinant of whole skeletal muscle behaviour.

Keywords: skeletal muscle, muscle mechanics, muscle mass, inertia, cyclic contractions

Acknowledgements

I would first like to thank my supervisor James Wakeling for your support, thoughtful mentorship, and endless wisdom. I have learned an immeasurable amount from you that I will take with me and continue to use throughout my career and life.

I am also grateful to my supervisor Nilima Nigam for inspiring me to be an unapologetically kick-ass researcher who just happens to be a woman.

Thank you to my mom, dad, and gramma Ross for your love and for teaching me to be hard working, independent, and to not take no for an answer. These have helped me immensely in completing this thesis and in navigating academia.

Thank you to my sister Nikki for almost always answering your phone, even when you don't want to. We might have been forced on each other, but I'm still grateful for your friendship.

I would also like to thank my friends and labmates old and new for the laughs, stories, and ski adventures. I couldn't have made it through without you.

Finally, to make half the people reading this cringe, I'll thank my dog Briar for being a good and wild pup who's always up for a run. While I'm at it I'll also thank my parents' dog Bailey for being in the words of her vet "a sweetheart who's loving life".

Table of Contents

List of Figures

List of Tables

Dissemination of Thesis Findings

Peer-reviewed publications

Ross SA, Nigam N, Wakeling JM. 2018. A modelling approach for exploring muscle dynamics during cyclic contractions. *PLoS Computational Biology*. 14(4): e1006123.

Ross SA, Ryan DS, Dominguez S, Nigam N, Wakeling JM. 2018. Size, history-dependent, activation and three-dimensional effects on the work and power produced during cyclic muscle contractions. *Integrative and Comparative Biology*. 58(2): 232-250.

Ross SA, Rimkus B, Konow N, Biewener AA, Wakeling JM. 2020. Added mass in rat plantaris muscle causes a reduction in mechanical work. *Journal of Experimental Biology*. 223: jeb224410.

Ross SA, Dominguez S, Nigam N, Wakeling JM. 2021. The energy of muscle contraction. III. Kinetic energy during cyclic contractions. *Frontiers in Physiology*. 12: 628819.

Ross SA, Wakeling JM. The energy of muscle contraction. IV. Greater mass of larger muscles decreases contraction efficiency. *Journal of the Royal Society Interface*. In review.

Presentations (underline indicates presenting author)

Invited Podium Presentations

Wakeling JM, **Ross SA**, Ryan DS, Dominguez S, Nigam N. 2018. Size, history-dependent and dimensionality effects on muscle contraction. Society for Integrative and Comparative Biology Annual Meeting. San Francisco, USA (International).

Podium Presentations

Ross SA, Dominguez S, Nigam N, Wakeling JM. 2021. The flow of tissue energy during whole muscle contraction in 3D. XXVIII Congress of the International Society of Biomechanics. Stockholm, Sweden (International).

Ross SA, Dominguez S, Nigam N, Wakeling JM. 2021. The effects of skeletal muscle size on the tissue energy distribution and work output of 3D muscle during cyclic

contractions. Society for Integrative and Comparative Biology Annual Meeting. Washington DC, USA (International). Division of Comparative Biomechanics Best Student Presentation Finalist.

Ross SA, Rimkus B, Konow N, Biewener AA, Wakeling JM. 2020. The effects of muscle internal mass on the contractile behaviour of in situ rat plantaris muscle. Society for Integrative and Comparative Biology Annual Meeting. Austin, USA (International).

Ross SA, Wakeling JM. 2019. The effects of muscle mass on contractile performance in humans. Congress of the European College of Sports Science. Prague, Czech Republic (International).

Ross SA, Nigam N, Wakeling JM. 2018. A modelling framework to evaluate muscle performance during cyclic contractions. Society for Integrative and Comparative Biology Annual Meeting. San Francisco, USA (International).

Ross SA, Nigam N, Wakeling JM. 2018. The effects of muscle mass and previous contraction history on muscle performance during cyclic contractions. Northwest Biomechanics Symposium. Bellingham, USA (Regional).

Poster Presentations

Ross SA, Wakeling JM. 2021. The effects of muscle tissue inertia and series elasticity on the metabolic cost and efficiency of contraction. Society for Integrative and Comparative Biology Annual Meeting. Washington DC, USA (International).

Ross SA, Porter JK, Wakeling JM. 2019. The effects of muscle mass on the efficiency of muscle contraction. XXVII Congress of the International Society of Biomechanics and 43rd Annual Meeting of the American Society of Biomechanics. Calgary, Canada (International).

Chapter 1

Muscle mechanics in the wild: Understanding *in vivo* whole muscle behaviour beyond controlled single fibre experiments

1.1 Introduction

Locomotion, or navigating through the external environment, is fundamental for the survival of humans and other animals. In non-human animals, locomotion facilitates hunting and foraging for food, escape from predators, and migration. Locomotion is no less important in humans, from walking to the fridge for a snack to running to catch the bus. The process of locomotion is complex and requires the integrated function of multiple body systems, including the nervous, musculoskeletal, cardiovascular, and respiratory systems. Rather than being a simple linear process in which the nervous system sends a single signal to activate muscles to accelerate the body skeleton, there is constant mechanical and sensory feedback that allows for adjustment and fine tuning to achieve the desired movement.

Muscles are an essential component of this process of moving the body. During locomotor tasks such as walking and running, muscles are cyclically activated by signals from the nervous system, which causes cyclic muscle force production and length change. This behaviour depends on the mechanical properties of the muscle's tissue and the internal forces acting to resist the cross-bridge forces, as well as external loads applied to the body and their transmission through the body's structures like bone and tendon. The nervous system can also modulate this behaviour based on sensory feedback on the position and speed of the body and its limbs, as well as the internal state of the body such as pain, and conditions of the external environment (Dickinson et al., 2000). Feedback from the level of the muscle-tendon unit via Golgi tendon organs and muscle spindles provide information about a muscle's force acting through its tendon (Houk & Henneman, 1967) as well as its change in length

(Matthews, 1933), respectively. Despite the critical contributions of skeletal muscle to locomotion, the complex mechanisms that underlie its behaviour *in vivo* are not fully understood.

From a mechanical standpoint, one of the primary functions of skeletal muscle during locomotion is to do mechanical work by generating force while cyclically changing length. To fully understand this function, it is necessary to determine how muscles in living animals produce force and change length and what mechanisms are responsible for this behaviour. Much of the early understanding of how muscles produce force emerged from controlled experiments on isolated fibres or small muscles from animals such as frogs and rats. While these studies provided valuable insight into the mechanical properties of muscle, they were not able to fully capture the complex behaviour of whole muscle *in vivo* during locomotion. Over the past 50 years, experimental techniques have been developed to quantify patterns of muscle forces and lengths that occur in living animals during locomotion. These experimental advances have been paralleled by the development of computational models of muscle to predict muscle forces where direct measures are not possible and to probe the mechanisms that underlie muscle behaviour *in vivo*. However, while these models provide accurate predictions of muscle forces *in situ* during slow, maximal contractions of muscles in small animals (Wakeling et al., 2021), they are much less accurate in predicting *in vivo* muscle forces, particularly in larger muscles, and at faster contraction speeds or lower activations (S. S. Lee et al., 2013; Dick et al., 2017; Wakeling et al., 2021). These conditions in which muscle models provide the worst predictions correspond to the conditions where the effects of muscle tissue mass would have the greatest impact. Given that muscle mass is not accounted for in most muscle models, it may be one of the missing elements that could account for the gap in understanding that is reflected in the poor accuracy of muscle model predictions during *in vivo* locomotion.

In this chapter, I will review what is known about the mechanical behaviour of whole muscle *in vivo*, including how our understanding emerged by extrapolating measures from controlled experiments on *in vitro* and *in situ* single fibres, fibre bundles, and small muscles, and expanded through *in vivo* measures and *in silico* simulations of whole muscle behaviour during locomotion. Finally, I will discuss limits to our understanding of muscle mechanical behaviour, including the consequences of muscle mass, and provide an overview of my subsequent thesis chapters.

1.2 Extrapolating whole muscle function from controlled measures of single fibres, fibre bundles, and small muscles

Much of what we know about whole muscle behaviour, in particular how it generates force and changes length to do mechanical work, comes from early experimental studies on single fibres, fibre bundles or small muscle during controlled contractions outside (*in vitro*) or partially outside (*in situ*) of the body. Some of the earliest studies on skeletal muscle mechanics, which were conducted in the 1800s (Banus & Zetlin, 1938) and later replicated in the early 1900s (e.g. Evans & Hill, 1914), examined the effects of a muscle's length on the force it could generate. These studies, which were conducted on *in situ* or *in vivo* small muscles (e.g. Evans & Hill, 1914) or *in vitro* single fibres (e.g. Ramsey & Street, 1940), showed that muscle and fibre forces are greatest at intermediate lengths and lowest at short and long lengths. During this time, similar controlled experiments were conducted on frog muscle to evaluate its force-velocity properties. A. V. Hill conducted experiments on frog sartorius muscle during isotonic shortening contractions and found that muscle shortening velocity was higher at reduced loads (Hill, 1938). These early findings of muscle behaviour have since been extended to describe the force-length and force-velocity properties of fibres, fibre bundles, and muscles from other small animals such as mice (e.g. Close, 1965; Brooks & Faulkner, 1988), rats (e.g. Ranatunga, 1984), and rabbits (e.g. Asmussen et al., 1994; Winters et al., 2011).

While these early studies provided valuable insight into how muscle generates force during controlled contractions, they were unable to fully capture the complex behaviour of muscle *in vivo* during locomotion. During locomotion, muscles typically undergo cycles of activation, force, and length change which result in external mechanical work being done by the muscle. In the late 1950s, studies conducted on asynchronous insect flight muscle, in which muscle excitation is not synchronized in time with the cycles of length change, characterized muscle forces during high frequency bursts of excitation coupled with cyclic length changes by expressing muscle force as a function of muscle length in a manner now known as a "work-loop" (Boettinger, 1957; Machin & Pringle, 1960). This experimental paradigm provided a means to understand muscle behaviour during cyclic contractions, as well as to visualize muscle mechanical work per cycle as indicated by the area inside of the work-loop. These

early work-loop studies on asynchronous muscle were later extended in the 1980s to synchronous insect flight muscle (Josephson, 1985) and crustacean muscle (Josephson & Stokes, 1989) where the timing of the excitation or action potentials is related to the phase of the contraction cycle. *In situ* and *in vitro* work-loop studies on synchronous muscle using constrained length changes have elucidated a range of features of muscle mechanical behaviour, such as that there is an optimal cycle frequency for maximizing average muscle power per cycle (product of work per cycle and cycle frequency) (Altringham & Johnston, 1990a; Swoap et al., 1993, 1997) which depends on the muscle fibre-type properties (Swoap et al., 1997).

Despite the wealth of knowledge provided by these *in situ* work-loop studies, the behaviour of whole muscle *in vivo* during locomotion cannot always be inferred or extrapolated from these *in situ* studies on single fibres, fibre bundles, or small muscles during controlled contractions. The external loads applied to muscle *in vivo* and its corresponding lengths are rarely, if ever, constant as they are during typical *in situ* or *in vitro* experiments that describe the force-velocity and force-length properties of muscle, respectively (Marsh, 1999). Even *in situ* work-loop experiments typically involve constraining the muscle length to follow a sinusoidal or similar trajectory that does not reflect the variable patterns of muscle lengths and velocities *in vivo* during locomotion. Therefore, developing experimental techniques to measure muscle forces and lengths *in vivo* during locomotion has been necessary to expand our understanding of whole muscle behaviour in living humans and other animals.

1.3 Expanding our understanding through *in vivo* measures of whole muscle behaviour

1.3.1 Studies on non-human animals

Measuring the mechanical behaviour of muscle *in vivo* during locomotion, such as its work-loop behaviour, has been possible due to advances in measurement techniques over the past 50 years. Studies on non-human animals have expanded our understanding of the fundamental mechanisms that dictate *in vivo* muscle function across the animal kingdom, and have also provided insight into human muscle behaviour as they provide direct or near direct measures of muscle force and length that are not possible in humans. Additionally, our understanding of how muscles function to move the human body has been improved by examining non-human animals with locomo-

tor function that is highly specialized to their mechanical environment. For example, *in vivo* studies on wallabies have elucidated the role of tendons in energy savings by reducing muscle work requirements during locomotion (Biewener & Baudinette, 1995; Biewener, Konieczynski, & Baudinette, 1998).

Muscle forces cannot be directly measured *in vivo* during locomotion but can be instead estimated by measuring tendon forces. By assuming tendon is in series with muscle, muscle forces can be assumed to be equal to tendon forces. Tendon force can be measured using a tendon buckle which is composed of an "E"-shaped transducer substrate with an attached semiconductor strain gauge that measures the strain induced in the substrate by the tendon force (Walmsley et al., 1978). Without this measurement technique, muscle forces would have to be resolved using measures of ground reaction forces and rigid-body dynamics calculations. However, because multiple muscles cross a single joint and contribute to the net moment about that joint, it is difficult to resolve each muscle's unique contribution (Bernstein, 1967). Tendon buckles have provided insight into the role of muscles and tendons on whole-body movement, including how the role of a given muscle varies depending on the task demands (Biewener & Roberts, 2000), how muscles work synergistically during locomotion, and how tendon elasticity contributes to whole-body energy savings (Biewener & Baudinette, 1995; Biewener, Konieczynski, & Baudinette, 1998).

Measures of muscle activation can supplement the nearly direct measures of muscle force obtained with tendon buckles by providing insight into the control of muscle and coordination during locomotion. Electromyography (EMG) is a technique that is used to measure the electrical events in muscle associated with activation of muscle fibres via the nervous system. When a muscle fibre is excited, action potentials travel along the fibre's cell membrane which causes the electrical potential across the membrane to be temporarily reversed by a depolarizing current. An EMG signal represents this depolarization process of numerous fibres near the measuring electrode superimposed over time (De Luca, 2006). For *in vivo* experiments in animals, wire electrodes are inserted into the muscle to measure fibre action potentials during locomotion (Alexander, 2003). This technique has been used to examine the patterns of muscle excitation during locomotion across a range of muscles in different animals, including pigeon pectoralis during flight (Dial et al., 1988), rhesus monkey masticatory muscles during chewing (Luschei & Goodwin, 1974), cat soleus and lateral gastrocnemius during paw shakes (Smith et al., 1980), and monitor lizard (Jayne et

al., 1990), rat (Cohen & Gans, 1975), and goat (McGuigan et al., 2009) limb muscle during treadmill gait.

Understanding the behaviour of muscle *in vivo*, including its work-loop behaviour, requires not only information about the force of the muscle, but also about the length of muscle and its fibres. Sonomicrometry is a technique that was originally developed to measure the dimensions of the heart in dogs (Rushmer et al., 1956) and has since been used to measure the tissue kinematics of skeletal muscle over time *in vivo*. In this technique, two piezoelectric crystals are inserted into the muscle at different locations. One crystal resonates and generates a sound wave into the surrounding muscle tissue when stimulated with short electrical pulses. This sound wave then travels through the tissue and intercepts with and mechanically stimulates the second crystal which causes a brief difference in electrical potential across the second crystal. The distance between the two crystals is calculated as the product between the transit time of the sound wave from the first to the second crystal and the velocity of sound in muscle tissue (Griffiths, 1987).

The action of a muscle depends on the three-dimensional (3D) behaviour of its tissue (Azizi et al., 2008; Wakeling et al., 2020). While sonomicrometry allows for the measurement and estimation of muscle strains and strain rates, fewer studies have used this technique for analyzing the 3D behaviour of skeletal muscle, including fibre pennation angle and simultaneous changes in muscle thickness and width, due to issues of interference and obstruction of signals between crystal pairs. Fluoromicrometry has been introduced as an alternative approach to measure the 3D shape and deformation of muscle *in vivo* during locomotion (Camp et al., 2016). In this technique, inert radiopaque spherical tantalum beads are inserted into the muscle tissue or attached to the external surface of the muscle with glue. The 3D position of these beads is then tracked over time using biplanar x-ray videography via two orthogonally-oriented C-arm fluoroscopes. Unlike sonomicrometry, which quantifies the position of one crystal relative to another, fluoromicrometry provides the absolute position of the beads in the global coordinate system, so it can also be used for characterizing simultaneous changes in muscle thickness and width relative to length during contraction (Konow et al., 2020).

1.3.2 Studies on humans

Animal studies allow for direct or near direct measures of muscle function that would not be possible on humans, and due to the conservation of muscle properties across vertebrates, provide a wealth of insight into the behaviour of human muscle. However, studies on human muscle *in vivo* can be beneficial in that human subjects can perform tasks that are difficult or not possible to achieve in animals, such as cycling and bipedal gait. Human studies also provide additional insight into features of muscle that are specific to humans, such as altered function in disease states like cerebral palsy. Because direct measures of human muscle forces, and therefore of mechanical work, are not possible to obtain, proxy measures such as EMG signals and muscle shape change via ultrasound have been used in an attempt to deduce the mechanical action of muscles in humans. Additionally these measures have been used as inputs for muscle models to predict human muscle forces *in vivo* during locomotion.

While EMG has been used widely in animal studies to measure the electrical events associated with muscle activation, it has been used even more extensively in human studies. Although early studies often used wire or needle EMG, which allow for more direct measures but can cause discomfort for subjects due to their invasive nature, surface EMG in which electrodes are placed over the skin is now also commonly used. In contrast to wire or needle EMG, surface EMG electrodes can capture a larger recording volume of tissue that contains more motor units, so the resultant signals may be more reflective of the overall activation state of the muscle compared to wire or needle EMG signals (De Luca et al., 2006). High-density surface EMG, in which numerous electrodes are arranged in a densely-spaced one- or two-dimensional array, provides additional information about the spatial distribution of excitation within a muscle (Blok et al., 2002). While surface EMG is more widely accessible, is less invasive, and can capture a wider region of the muscle's approximate activation state, surface EMG signals can increase the likelihood of cross-talk where the signal from the muscle of interest includes signals from neighbouring muscles. Additionally, the quality of surface EMG signals depends on sufficient contact with the skin, the quality and integrity of the skin, and the extent of subcutaneous fat (De Luca, 1997). Despite these limitations, human studies using electromyography have provided insight into how muscle excitation and motor unit recruitment patterns vary with mechanical demand during tasks such as cycling (Blake & Wakeling, 2014, 2015), and with different

disease states such as amyotrophic lateral sclerosis (Bashford et al., 2020) and stroke (Kallenberg & Hermens, 2009; Rasool et al., 2017).

B-mode ultrasound is an imaging technique that has been used in human studies to examine the deformation of muscle and its fibres during both static and dynamic contractions (Van Hooren et al., 2020). To collect an ultrasound image of muscle, an ultrasound probe containing piezoelectric crystals is placed over the skin superficial to the muscle of interest. These crystals resonate when stimulated with applied alternating current which generates sound waves that travel through the tissue. The waves are then impeded by the tissue depending on the tissue properties, which causes a portion of the waves to reflect back and stimulate the probe crystals (Aldrich, 2007). This process produces a 2D image of the tissue, including skin, connective tissue, and muscle, that is deep to the ultrasound probe. Real-time ultrasound imaging to measure muscle function in humans has aided our understanding of muscle shape change and fascicle rotations during dynamic tasks such as walking, running, and jumping (Cronin & Lichtwark, 2013).

Magnetic resonance imaging (MRI) is another imaging technique that has been extensively used to measure muscle structure, including muscle length, during static or near-static conditions, and more recently, to examine changes in muscle shape during dynamic tasks. In this imaging technique, a magnetic field is applied to the tissue which causes the tissue's hydrogen protons in water to align with the magnetic field. Radio waves are then added to the magnetic field that cause the hydrogen protons to resonate and emit radio waves back to the measuring scanner. The intensity of the signal emitted back to the scanner depends on the water content of the tissue, and so different tissue structures with different water contents appear brighter or darker on the final scan image (Berger, 2002). This technique has been used to quantify the 3D structure and properties of human muscle, including its volume (e.g. LeBlanc et al., 2000) and fat content (e.g. Kovanlikaya et al., 2005). Diffusion tensor imaging is a MRI technique that uses the anisotropic diffusion of water in muscle fibres, with greater diffusion along the fibre compared to across it (Le Bihan & Iima, 2015), to track the approximate orientation of muscle fibres during contraction (Damon et al., 2017). MRI typically has poor time resolution and so has primarily been used to examine muscle behaviour during static or near-static conditions. Dynamic MRI techniques have been used to estimate muscle deformations and strain-rates during dynamic contractions; however, depending on the specific method used (see Borotikar et al., 2017 for review), there can be challenges in accurately estimating muscle strain-

rates due to the requirement of multiple identical cycles of motion (Asakawa et al., 2003) and difficulty in measuring internal and external tendon behaviour (Blemker et al., 2007).

1.4 Expanding our understanding through *in silico* measures of whole muscle behaviour

While measures of *in vivo* muscle function have provided insight into how whole muscle behaves to do mechanical work during locomotion and other movement, complimentary *in silico* measures using muscle model simulations have greatly expanded our understanding. Although estimates of *in vivo* muscle forces during locomotion can be obtained using tendon buckles in animals, this is not possible in humans due to ethical considerations. Furthermore, tendon buckle measures can only be used to estimate forces of relatively few muscles that have long, thin tendons (Biewener et al., 1988). Indeed, it is next to impossible to measure muscle function in the majority of muscles across a wide range of species and behaviours: instead *in silico* models provide us with a means to predict muscle function when it cannot be easily measured. Muscle models can be used to predict muscle forces in these contexts in which direct measures are not possible and can additionally be used to answer "what if" questions that cannot be explored with experiments on real muscle. For example, 3D continuum muscle models have been used to examine the effects of different distributions of intramuscular fat (Rahemi et al., 2015) and activation (Rahemi et al., 2014) while controlling for other factors that may influence muscle behaviour but would not be possible to control for when measuring across subjects in experiments on real muscle.

One-dimensional (1D) Hill-type muscle models are the most commonly utilized type of muscle model in biomechanics and are used to represent the muscle actuators in musculoskeletal models, such as OpenSim (Delp et al., 2007). These models are typically composed of a contractile element, a parallel elastic element, and a series elastic element (Zajac, 1989), which represent the cross-bridges, passive sarcomere components, and passive aponeurosis and tendon contributions, respectively. Hill-type models are ideal for use in applied and clinical settings, such as predicting the outcome of surgical or rehabilitative interventions, due to their minimal requirements for muscle-specific parameters and low computational cost. However, the accuracy of

these 1D models is typically limited to the experimental contractile conditions from which the model properties were derived, namely steady contractions with maximal activation, and perform worse during more realistic submaximal and unsteady contractions (Sandercock & Heckman, 1997; Perreault et al., 2003; Wakeling et al., 2012; Millard et al., 2013; S. S. Lee et al., 2013; Dick et al., 2017). Errors in Hill-type model predictions of *in vivo* muscle forces obtained using tendon buckle transducers have been shown to increase with faster gait speeds in rats (Wakeling et al., 2021) and goats (S. S. Lee et al., 2013). Similarly, Dick and colleagues (2017) tested Hill-type model predictions of human gastrocnemius forces during cycling against estimates of *in vivo* forces obtained using ultrasound and electromyography measures and found that model errors increased with higher cadences (from 11.1% maximum isometric force at cadences of 60-80 rpm to 17.6% at 100-140 rpm), which likely translated to higher peak muscle velocities and accelerations.

A variety of different formulations have been proposed to improve 1D Hill-type model predictions and to probe the mechanisms that underlie *in vivo* muscle function. For example, a Hill-type model with two contractile elements with different fibre properties that can be independently activated has been proposed (Wakeling et al., 2012) and used (Wakeling et al., 2012; S. S. Lee et al., 2013; Dick et al., 2017; Lai et al., 2018, 2021) to mimic patterns of motor unit recruitment that vary depending on the mechanical demands of the task (Smith et al., 1980; Nardone et al., 1989; Wakeling, 2004; Wakeling et al., 2006). This two-contractile-element model has not only provided more accurate predictions of *in vivo* muscle forces during locomotion (S. S. Lee et al., 2013; Dick et al., 2017), particularly during faster and submaximal contractions, but has also highlighted that recruitment is an important determinant of muscle function *in vivo*. History-dependent effects, specifically force enhancement following active lengthening and force depression following active shortening, have also been added to the formulation of traditional Hill-type models (Meijer et al., 1998; Ettema & Meijer, 2000; McGowan et al., 2010, 2013). Accounting for these history-dependent effects in 1D models has been shown to decrease muscle model errors when predicting *in situ* muscle forces during constant length and velocity contractions and musculoskeletal model errors for predicting ground reaction forces and joint angles, but not hip height, during countermovement jumping (McGowan et al., 2013). Despite accounting for these additional factors, 1D Hill-type models are still not able to fully capture the complex behaviour of muscle *in vivo* during locomotion and also cannot

be used to explore the consequences of muscle tissue properties and deformations in 3D.

2D and 3D geometric muscle models have been developed and used to explore the role of muscle architecture and shape change on contractile performance. While Hill-type models often account for changes in fibre pennation angle and subsequent changes in component force vectors, they assume that muscle thickness remains constant so that a unique pennation angle and fascicle length can be determined for each muscle length (Woittiez & Huijing, 1983; Zajac, 1989; Millard et al., 2013). However, studies examining the shape change of muscle *in vivo* have shown that muscle does in fact change thickness across a range of contractile conditions (Maganaris et al., 1998; Azizi et al., 2008; Wakeling et al., 2011; Randhawa et al., 2013; Raiteri et al., 2016; Dick et al., 2017). 2D and 3D geometric models of muscle have been proposed to account for changes in muscle thickness that occur during contraction (Woittiez & Huijing, 1983; Randhawa & Wakeling, 2015). As opposed to 1D models that assume constant thickness, 2D geometric models typically assume a constant area of the parallelogram made by the model's length and thickness, 3D geometric models typically assume constant volume of the parallelpiped made by the model's length, thickness, and width (Randhawa & Wakeling, 2015). While 2D and 3D geometric models may not provide substantial improvements in *in vivo* muscle force predictions over 1D models (Randhawa & Wakeling, 2015; Dick & Wakeling, 2018), these geometric models can be used to explore the mechanisms that underlie muscle shape change during contraction to a greater extent than 1D Hill-type models.

While existing 3D geometric muscle models provide additional detail of muscle shape change over 1D models, they do not consider the complex and nonlinear tissue deformations that occur during whole muscle contraction. 3D continuum muscle models account for this additional complexity and have been used to examine how factors such as muscle fat accumulation (Rahemi et al., 2015) and regional activation (Rahemi et al., 2014) alter whole muscle behaviour *in vivo*. Furthermore, using these models to predict *in vivo* muscle forces in place of current 1D Hill-type muscle models in the OpenSim pipeline has been suggested as a future direction for improving whole-body musculoskeletal models (Blemker et al., 2007). However, while these models account for additional complexity of 3D muscle tissue behaviour, they require additional parameters and descriptions of tissue properties that are difficult to measure experimentally. Additionally, while the 3D deformations and shape changes of these models have been compared to *in situ* (Oomens et al., 2003) and *in vivo* muscle data

(Blemker et al., 2005; Wakeling et al., 2020), the validity of these models in predicting *in vivo* muscle forces during locomotion has not been sufficiently investigated. Despite these limitations, simulations of muscle behaviour using 3D continuum models have been invaluable for expanding our understanding of the tissue-level mechanisms that underlie whole muscle behaviour.

1.5 Limits to our understanding of whole muscle behaviour and the consequences of muscle mass

Despite the proliferation of techniques to measure and simulate *in vivo* muscle function during locomotion, we still do not fully understand the mechanisms that underlie this function. This lack of understanding is reflected in studies validating muscle models for predicting *in vivo* muscle forces, as the formulation of these models reflects assumptions about what factors are most important for muscle function. Studies evaluating the accuracy of 1D Hill-type models have found that they are only able to replicate about 50% of *in vivo* human gastrocnemii forces on average across contractile conditions, are particularly poor at predicting faster and submaximal contractions, and are only marginally improved when task-dependent motor unit recruitment strategies are accounted for in the model formulation (Dick et al., 2017). While the limited accuracy of 1D models may be due to not accounting for behaviour in other dimensions, 2D and 3D geometric (not continuum) models only provide minor improvements in the accuracy of predicted fascicle lengths and pennation angles during contraction (Dick & Wakeling, 2018). Given uncertainty surrounding input constitutive properties of 3D continuum models, such as the material properties of aponeurosis, it is not yet clear if their more detailed description of 3D muscle behaviour would improve *in vivo* muscle force predictions. Thus, there may be other mechanisms that underlie *in vivo* muscle behaviour that are not accounted for in current 1D Hill-type models beyond the effects of dimensionality that contribute to the limited accuracy of 1D models in predicting *in vivo* forces.

Studies comparing Hill-type predictions to measured *in vivo* muscle forces may provide clues as to possible mechanisms underlying muscle behaviour that may be missing from our current understanding. These studies, which have validated 1D Hill-type models against *in vivo* muscle forces in rats (Wakeling et al., 2021) and goats (S. S. Lee

et al., 2013) during treadmill gait and humans during cycling (Dick et al., 2017), have found that prediction errors increase with increasing body size, and therefore increasing muscle size, as well as increasing gait speed, and therefore increasing muscle contraction speed. These studies also found that faster contractions speed and lower muscle force, and therefore likely lower activation, resulted in larger prediction errors (S. S. Lee et al., 2013; Dick et al., 2017; Wakeling et al., 2021). While these trends may be due to differences in measurement error across animal sizes or some other factor, such as differences in medial gastrocnemius architecture across species, they may also be a consequence of muscle mass.

Typical Hill-type muscle models, as well as nearly all other mechanical models of muscle, do not account for the effects of muscle mass. 1D Hill-type models are formulated to follow dynamic similarity, such that their non-dimensional behaviour is the same regardless of muscle size. To accomplish this, the forces, lengths, and velocities of the intrinsic force-velocity and force-length curves are normalized by the muscle maximum isometric force, optimal length, and maximum shortening velocity, respectively. Once these curves, which are typically derived using experimental data from fibres or small muscles during controlled and maximal contractions, are normalized, they can be scaled up in size to estimate the forces of larger muscles with higher maximum isometric forces and optimal lengths (Zajac, 1989). Thus, a typical Hill-type muscle model assumes that a 15-kilogram elephant muscle behaves in the exact same way as a 1-milligram single fibre. While assuming that larger muscles behave the same as single fibres or small muscles during controlled, maximal contractions is convenient and often necessary due to the difficulty in measuring the behaviour of larger whole muscles, it may fail to account for the effects of muscle mass on contractile behaviour.

As muscles increase in size, their potential to generate force increases in proportion to their cross-sectional area, and their mass increases in proportion to their volume. This results in greater internal loads for larger muscles relative to the force that they can produce, and this difference becomes greater when muscle force potential decreases during submaximal contractions. These internal loads are inertial in nature, and so their magnitude depends not only the mass of the tissue but also the acceleration of that mass. Therefore, inertial resistance due to tissue mass likely has the largest effect during submaximal contractions where contractile force is low, and during unsteady or higher frequency or strain (length change) cyclic contractions where maximum accelerations of the tissue are greatest. However, because the intrinsic force-velocity

properties of muscle are taken primarily from measures on maximally-active single fibres or small muscles during constant-load shortening contractions when the fibre or whole muscle acceleration is minimal, the effects of these internal loads are not accounted for in the Hill-type model formulation. This logic is consistent with the finding that Hill-type force prediction errors are higher for faster contraction speeds and lower levels of activation. Thus, ignoring the effects of muscle mass may contribute to the discrepancy between model predictions and experimental measures.

The effect of inertial resistance due to muscle mass has rarely been studied and has primarily been provided only as a tentative explanation for experimental observations that cannot otherwise be explained. In the late 1980s, Josephson and Edman (1988) compared the maximum shortening speed of fibre bundles to that of single fibres taken from those bundles and found that faster fibres contracted slower when they were within a fibre bundle than when they were in isolation. These results led the authors to conclude that the contraction speed of faster fibres in whole muscle may be slowed by the load provided by adjacent fibres. Prior to this, whole muscle was assumed to be able to contract as fast as the fastest fibre contained within the muscle (Hill, 1970). More recently, Holt and colleagues (2014) showed that whole rat plantaris muscle contracts slower when only a portion of the fibres in the muscle are active compared to when the muscle is fully active, even if the active portion is composed entirely of fast fibres. The authors suggested that this effect was due to the inactive muscle tissue providing resistance to slow the contraction speed of the active fibres. We were able to support this conclusion by incorporating tissue mass into a Hill-type muscle model (Günther et al., 2012) and showing that increasing muscle mass reduces maximum contraction speeds during constant-load shortening contractions (Ross & Wakeling, 2016). However, despite this evidence that internal loads due to tissue mass alters muscle contractile behaviour, this effect has yet to be explored across a wider range of contractile conditions that reflect the behaviour of muscle during locomotion.

1.6 Outline and specific aims of this thesis

The overarching goal of this thesis was to determine the effects of muscle mass on the contractile performance of whole skeletal muscles. To accomplish this, I used a combination of simulations of 1D Hill-type and 3D continuum models and experiments on *in situ* muscle. The specific aims of this thesis were:

1. To develop a modelling framework to test different muscle model formulations under a range of cyclic contractile conditions
2. To evaluate the effects of muscle mass on muscle behaviour across a range of cyclic contractile conditions
3. To examine the effects of muscle mass on the behaviour of *in situ* muscle during cyclic contractions
4. To determine the effects of muscle mass on 3D muscle behaviour during cyclic contractions
5. To determine the effects of muscle mass on the metabolic cost and efficiency of muscle during cyclic contractions

In **Chapter 2**, I developed a novel modelling framework that consists of a Hill-type muscle actuator in series with a damped harmonic oscillator to represent the physical load placed on the muscle during locomotion. The system is driven by time-varying activation of the muscle actuator to simulate the contraction cycles seen *in vivo*. As part of this work, I developed and implemented novel Bézier curves to represent the force-velocity and force-length properties of muscle. I also geometrically scaled the system while preserving dynamic and kinematic similarity to explore the effects of muscle mass across muscle sizes while controlling for the dynamics of the harmonic oscillator. This work is published in Ross et al. (2018a) in *PLoS Computational Biology*. I contributed to the design of this study, designed and coded the computational model, ran the model simulations, and analyzed and interpreted the simulation results.

In **Chapter 3**, I used the modelling framework composed of a damped harmonic oscillator in series with a Hill-type muscle model (Chapter 2) that accounts for the effects of muscle tissue mass (Ross & Wakeling, 2016) to explore the effects of muscle mass on mass-specific work and average power per contraction cycle, and how these are affected by different fibre-type properties, excitations, and frequencies. I additionally compared the effects of muscle mass to the effects of force enhancement following active muscle lengthening and force depression following active shortening. This study is a portion of the work published in Ross et al. (2018b) in *Integrative and Comparative Biology*. I designed this study, designed and built the Hill-type models, ran the model simulations, and analyzed and interpreted the simulation results.

In **Chapter 4**, I examined the effects of added mass on the performance of *in situ* rat muscle during cyclic contractions and found that greater added mass resulted in lower mechanical work per cycle. While the results of Chapter 3 and those of previous studies (Günther et al., 2012; Meier & Blickhan, 2000; Böl & Reese, 2008; Ross & Wakeling, 2016) were important first steps to establishing muscle mass as an important determinant of muscle contractile behaviour, the effects of muscle mass had not yet been confirmed by studies on living muscle. I also found that greater muscle strain resulted in lower work per cycle relative to unloaded trials at the same strain to control for length change and velocity effects on the work output, possibly due to greater accelerations of the muscle mass at higher strains. I additionally compared the results of the *in situ* experiments to that of simulations of the muscle model with mass from my previous studies (Ross & Wakeling, 2016; Chapter 3) and found similar patterns of decreased mechanical work with greater added mass. This study was the first, to my knowledge, to show that muscle mass alters the mechanical behaviour of muscle in living animals. This work is published in Ross et al. (2020) in the *Journal of Experimental Biology*. I designed the study, designed and built the experimental set-up, conducted the animal preparation and surgery, conducted the *in situ* experiments, designed and built the computational model, ran the model simulations, and analyzed and interpreted the experimental and simulation results.

In **Chapter 5**, I developed and used a 3D continuum model of muscle that accounts for tissue mass to explore the effects of muscle size and mass on the mass-specific mechanical work per cycle, and how these changes in work with greater mass are associated with changes in tissue energy distribution and muscle shape change. I also qualitatively validated the model by comparing its behaviour to that of *in situ* muscle during analogous experimental trials (Chapter 4). I found that greater muscle mass resulted in relatively more mechanical energy in the form of kinetic energy during the simulated contraction cycles, and this was associated with lower mass-specific mechanical work output for larger muscles with greater mass. Larger muscles also stored more energy in the aponeurosis during contraction. In terms of muscle architecture, I found that reductions in mass-specific work with greater muscle size were lower for muscles with higher initial pennation angle. Finally, in Chapter 5 I found that the *in situ* and simulated muscle had comparable patterns of tissue accelerations across conditions which suggested that the muscle model was behaving similarly to real muscle. This work is published in Ross et al. (2021) in *Frontiers in Physiology*. I developed the 3D continuum model of muscle that accounts for tissue mass in col-

laboration with fellow PhD student, S. Dominguez. I contributed to all facets of the dynamic model development, including the estimation and sensitivity analysis of key parameters, which in turn were central to the choice of the phenomenological constitutive laws we used. I additionally designed the study, ran the model simulations, and analyzed and interpreted the experimental and simulation results.

In **Chapter 6**, I examined the effects of muscle mass on the metabolic cost and efficiency of muscle during cyclic contractions using simulations of a mass-enhanced Hill-type muscle model (Ross & Wakeling, 2016) in which bursts of excitation were timed to sinusoidal muscle length changes. I additionally explored how the behaviour of a tendon alters the relationship between muscle mass and muscle and muscle-tendon unit mass-specific mechanical work, metabolic cost, and efficiency per cycle by adding a tendon of varying stiffness in series with the muscle model. I found that larger muscles with greater mass were less efficient and that accounting for a tendon decreased the mass-specific work and efficiency penalty of greater mass in larger muscles. Overall, the results of this thesis highlight that muscle mass is an important determinant of whole muscle and muscle-tendon unit behaviour. This work is under review in Ross and Wakeling (2021, in review) in the *Journal of The Royal Society Interface*. I designed the study, developed the computational model, implemented the metabolic cost models, ran the model simulations, and analyzed and interpreted the simulation results.

Chapter 2

A modelling approach for exploring muscle dynamics during cyclic contractions

2.1 Abstract

Hill-type muscle models are widely used within the field of biomechanics to predict and understand muscle behaviour, and are often essential where muscle forces cannot be directly measured. However, these models have limited accuracy, particularly during cyclic contractions at the submaximal levels of activation that typically occur during locomotion. To address this issue, recent studies have incorporated effects into Hill-type models that are oftentimes neglected, such as size-, history-, and activation-dependent effects. However, the contribution of these effects on muscle performance has yet to be evaluated under common contractile conditions that reflect the range of activations, strains, and strain rates that occur *in vivo*. The purpose of this study was to develop a modelling framework to evaluate modifications to Hill-type muscle models when they contract in cyclic loops that are typical of locomotor muscle function. Here we present a modelling framework composed of a damped harmonic oscillator in series with a Hill-type muscle actuator that consists of a contractile element and parallel elastic element. The intrinsic force-length and force-velocity properties are described using Bézier curves where we present a system to relate physiological parameters to the control points for these curves. The muscle-oscillator system can be geometrically scaled while preserving dynamic and kinematic similarity to investigate the muscle size effects while controlling for the dynamics of the harmonic oscillator. The model is driven by time-varying muscle activations that cause the muscle to cyclically contract and drive the dynamics of the harmonic oscillator. Thus, this framework provides a platform to test current and future Hill-type model formulations and explore factors affecting muscle performance in muscles of different sizes under a range of cyclic contractile conditions.

2.2 Introduction

One of the primary functions of skeletal muscle is to perform work by cyclically contracting to move an external load during locomotion. For the last half-century, experimental work-loop studies have provided insight into how muscle force and length, and thus work, depend on interactions between neural excitation and the external load placed on the muscle during cyclic contractions. These interaction effects are supported by early in vitro studies examining the behaviour of invertebrate flight muscles coupled to external loads with different elastic, viscous and inertial properties (Machin & Pringle, 1959, 1960). More recently, *in vivo* studies on birds such as turkeys (Roberts et al., 1997) and guinea fowl (Daley & Biewener, 2003), and larger vertebrates such as wallabies (Biewener, Konieczynski, & Baudinette, 1998) and goats (McGuigan et al., 2009), have shown that altering the characteristics of the external environment can substantially change the work a muscle can do per contraction cycle. For example, (Roberts et al., 1997) found that muscle fascicles within the lateral gastrocnemius muscle in turkeys behave like a motor during uphill running by generating large forces for the duration of the shortening phase of the cycle, and act like a strut during level running by minimizing their shortening while the force is high. Thus, the behaviour of muscle depends on the demands of the task in addition to the properties of the muscle.

While work-loop studies have provided insight into how changes in neural excitation and external conditions alter the behaviour of muscle during cyclic contractions, the contribution of the mechanical properties of the muscle itself remain largely unknown. Much of what we know about the mechanisms that underlie muscle contractile behaviour is from measures on small muscles or single fibres during maximal contractions under constant load. Furthermore, the Hill-type muscle models that are used to predict and understand muscle behaviour rely on the assumption that these mechanisms seen in small muscles or fibres under controlled conditions are the same as that in large whole muscles during submaximal cyclic contractions under varying load. However, these models have limited accuracy, particularly during cyclic contractions at the submaximal levels of activation that typically occur during locomotion and other daily activities (Sandercock & Heckman, 1997; Perreault et al., 2003; Millard et al., 2013; S. S. Lee et al., 2013; Dick et al., 2017). Most recently, Dick and colleagues (2017) tested Hill-type model predictions of human gastrocnemius forces during cycling against measured ultrasound and electromyography data and found that while

model errors were low for slow contractions at high activations, errors became substantially larger with increasing contraction speed and decreasing activation. Thus, Hill-type models are currently unable to consistently replicate the salient features of muscle contractile performance in humans and animals.

To improve the ability of Hill-type models to mimic whole muscle behaviour *in vivo*, recent studies have incorporated effects into these models that are typically neglected. Wakeling and colleagues (2012) developed a Hill-type model that allowed for independent recruitment of fast and slow contractile elements. When compared to models with single contractile elements or models with fast and slow elements that followed an orderly recruitment pattern, the differential recruitment model was most accurate in predicting *in situ* (Wakeling et al., 2012) and *in vivo* (S. S. Lee et al., 2013) goat muscle forces. In addition to fibre recruitment, a muscle's force depends on its previous length and rate of length change (Abbott & Aubert, 1952; Maréchal & Plaghki, 1979; Herzog & Leonard, 1997, 2000; De Ruiter et al., 2000). When incorporated into the Hill-type muscle actuators of multibody musculoskeletal models, these history-dependent effects have been shown to substantially alter muscle power predictions in simulations of cycling (McGowan et al., 2010), and muscle force magnitude and timing predictions in simulations of countermovement jumping (McGowan et al., 2013). Other such overlooked effects include inertia due to muscle tissue mass and tendon or serial elastic element (SEE) dynamics. Ross and Wakeling (2016) found that adding mass to a Hill-type model leads to slower maximum contraction speeds, and this effect is more pronounced for larger muscles and lower levels of activation, and Curtin and others (1998) found that including a compliant SEE in the model formulation improves muscle force predictions during sinusoidal contractions. Further modelling studies have shown that serial compliance amplifies the maximum power a muscle can deliver to an inertial load (Galantis & Woledge, 2003), and varying the magnitude of this compliance substantially alters estimates of muscle efficiency during locomotor tasks such as walking and running (Lichtwark & Wilson, 2007). Together these findings show promise for improving our understanding of muscle function and our ability to use Hill-type models to predict *in vivo* muscle forces.

Despite the potential for improving Hill-type models by incorporating these different effects, their influence on muscle performance has yet to be evaluated under common contractile conditions that reflect the range of activations, strains, and strain rates that occur in real muscle. Herein we present a novel forward dynamics framework that consists of a Hill-type muscle actuator in series with a damped harmonic oscillator

to represent the physical load placed on the muscle during locomotion. The system is driven by time-varying activation of the muscle actuator to simulate the contraction cycles seen *in vivo*.

2.3 Methods and models

The model system is composed of a Hill-type muscle model in series with a damped harmonic oscillator (Figure 2.1). The Hill-type model contains a contractile element and a parallel elastic element, and does not account for the effects of a tendon. The muscle is assumed to only contain parallel fibres that generate force along the longitudinal x-axis of the system. The length of the muscle l_{m} is equal to the sum of the fixed total length of the system l_{tot} and the position x of the oscillator mass m:

$$l_{\mathrm{m}} = l_{\mathrm{tot}} - x. \tag{2.1}$$

The motion of the system is constrained to be one-dimensional along the longitudinal axis of the muscle. The dynamics of the system can be described by:

$$\sum F = F_{\mathrm{m}} - F_{\mathrm{s}} - F_{\mathrm{d}} \tag{2.2}$$

where $\sum F$ is the sum of the forces acting on the mass, F_{m} is the muscle force, F_{s} is the spring force, and F_{d} is the damping force. F_{s} is linearly dependent on the displacement Δx of the mass, m:

$$F_{\mathrm{s}} = k\Delta x \tag{2.3}$$

where k is the stiffness coefficient and Δx is equal to the difference between x and the resting length of the oscillator x_0. The force of the viscous damper is given by:

$$F_{\mathrm{d}} = b\frac{d\Delta x}{dt} \tag{2.4}$$

where b is the damping coefficient. F_{m} is given by:

$$F_{\mathrm{m}} = aF_{\mathrm{A}}F_{\mathrm{V}} + F_{\mathrm{p}} \tag{2.5}$$

where F_{A} and F_{P} are the active and passive forces as a function of the dimensionless muscle length $\hat{l}_{\mathrm{m}}$, respectively, and F_{V} is the active force as a function of the dimensionless muscle velocity $\hat{v}_{\mathrm{m}}$. $\hat{l}_{\mathrm{m}}$ is calculated as l_{m} normalized by the muscle optimal length l_0:

$$\hat{l}_{\mathrm{m}} = \frac{l_{\mathrm{m}}}{l_0} \tag{2.6}$$

and $\hat{v}_{\mathrm{m}}$ is calculated as the first time derivative of $\hat{l}_{\mathrm{m}}$ normalized by the maximum unloaded shortening strain rate, $\dot{\varepsilon}_0$:

$$\hat{v}_{\mathrm{m}} = \frac{\frac{d}{dt}\frac{l_{\mathrm{m}}}{l_0}}{\dot{\varepsilon}_0} \tag{2.7}$$

By convention, l_{m} is defined as the muscle length corresponding to the maximum isometric force and $\dot{\varepsilon}_0$ is the maximum shortening strain rate and is equal to the maximum of the first derivative of $\hat{v}_{\mathrm{m}}$ with respect to time. Combining and rearranging Equations (2.2-2.5) gives:

$$m\frac{d^2\Delta x}{dt^2} + b\frac{d\Delta x}{dt} + k\Delta x = aF_{\mathrm{A}}F_{\mathrm{V}} + F_{\mathrm{P}} \tag{2.8}$$

The model is driven with time-varying excitation u that determines the activation a by solving the following first-order bilinear differential equation (Zajac, 1989):

$$\frac{da}{dt} + a\left[\frac{1}{\tau_{\mathrm{act}}}\Big(\beta + u(1-\beta)\Big)\right] = \frac{1}{\tau_{\mathrm{act}}}u \tag{2.9}$$

where τ_{act} is the activation time constant to account for the delay between onset of excitation and maximum twitch force, β is the ratio between τ_{act} and the deactivation time delay, and u is muscle excitation. u is represented by a repeating square wave function with a characteristic frequency, f, and duty cycle, D.

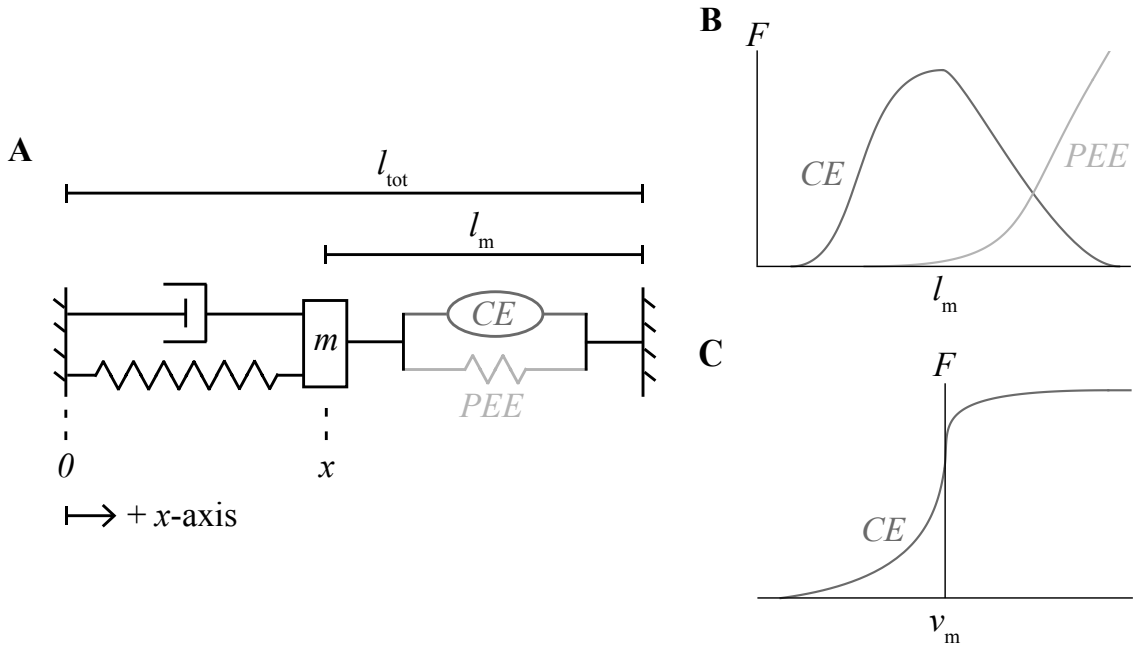

Figure 2.1: Visualization of modelling framework. Second-order dynamic system composed of a Hill-type muscle model in series with a damped harmonic oscillator (A). The force of the muscle is given by the sum of the active force due to the contractile element (CE) as a function of its length (B) and velocity (C), and the passive force due to the parallel elastic element (PEE) as a function of its length (B).

2.3.1 Root model properties

The root muscle properties were chosen to represent a bundle of parallel muscle fibres that generate force strictly along the length of the model. The maximum isometric force, F_0, of the root model is calculated as the product of the maximum isometric stress, σ_0, and the muscle cross-sectional area, A:

$$F_0 = \sigma_0 A \tag{2.10}$$

The model is assumed to be cylindrical in shape so A is given by:

$$A = \frac{\pi}{4}\left(\frac{l_0}{R}\right)^2 \tag{2.11}$$

where R is the aspect ratio between l_0 and the diameter of the muscle model. The mass of the muscle m_m is the product of the muscle density ρ and the volume, and the volume is the product of l_0 and A. Therefore:

$$m_\mathrm{m} = \rho l_0 A \tag{2.12}$$

While the properties of the muscle can be taken from empirical data, determining the properties of the harmonic oscillator is less straightforward because the external loads applied to muscle *in vivo* cannot be resolved into their individual components such as limb inertia, passive elasticity, and gravitational forces. Therefore, the properties of the harmonic oscillator are chosen so that the kinematics and dynamics of the muscle model replicate the behaviour of muscle *in vivo*.

Given that one of the primary functions of muscle is to generate power, we chose the base properties of the harmonic oscillator that maximize the average mass-specific mechanical power output of the muscle per cycle P^* (Weis-Fogh & Alexander, 1977). Power is the rate of doing work, and the net work of the muscle is given by the integral of the muscle force over the length change, so P^* can be calculated as the product of the net mechanical muscle work output per cycle and the frequency f, divided by the muscle mass m_m:

$$P^* = \frac{\int F_\mathrm{m}(dl_\mathrm{m})f}{m_\mathrm{m}} \tag{2.13}$$

Consult Josephson (1999) for further explanation of P^*. Because the muscle and harmonic oscillator are mechanically coupled in our model, both F_m and the change in l_m per cycle, and therefore P^*, depend on the chosen values of oscillator mass m, damping coefficient b, and spring stiffness coefficient k. Although these parameters can be solved for directly using optimization, we have chosen instead to link them to the properties of the muscle to reduce the number of unknown parameters and provide values with greater physiological meaning. Because the muscle and harmonic oscillator are connected in series, the change in l_m per cycle will be maximal when the amplitude of the oscillator displacement is maximal. For a simple harmonic oscillator without damping, this maximal amplitude occurs when the natural frequency ω_n is equal to the driving frequency ω_d, where ω_n is given by:

$$\omega_{\mathrm{n}} = \sqrt{\frac{k}{m}} \tag{2.14}$$

However, for a driven oscillator with damping, the maximal amplitude occurs when ω_{n} is a fraction c_1 of ω_{d} (Kleppner & Kolenkow, 2013):

$$\omega_{\mathrm{n}} = c_1 \omega_{\mathrm{d}} \tag{2.15}$$

Converting ω_{d} from an angular to a temporal frequency f_{d} gives:

$$\omega_{\mathrm{n}} = 2\pi c_1 f_{\mathrm{d}} \tag{2.16}$$

Combining Equation (2.14) and Equation (2.16) gives an expression for k in terms of c_1, m, and f_{d}:

$$k = m(2\pi c_1 f_{\mathrm{d}})^2 \tag{2.17}$$

To relate b to c_1, m, and f_{d} we can constrain b to be at a critical level (for a critically damped system) such that:

$$b = 4mk \tag{2.18}$$

Substituting Equation (2.17) into Equation (2.18) gives:

$$b = 4\pi m c_1 f_{\mathrm{d}} \tag{2.19}$$

To relate the inertial load due to mass m to the maximum isometric force F_0, we can set m to be equal to a fraction c_2 of F_0:

$$m = c_2 F_0 \tag{2.20}$$

Substituting Equation (2.20) into Equations (2.17) and (2.19) gives:

$$k = c_2 F_0 (2\pi c_1 f_\mathrm{d})^2 \tag{2.21}$$

and

$$b = 4\pi c_2 F_0 c_1 f_\mathrm{d} \tag{2.22}$$

In addition to the spring stiffness k, the force applied to the muscle due to the spring also depends on the resting length x_0 of the harmonic oscillator (Equation 2.3). If at rest l_m is equal to l_0, and the total length of the system l_tot is the sum of the lengths of the oscillator and the muscle (Equation 2.1), then the oscillator length when the muscle is at l_0 is equal to l_tot minus l_0. If we set x_0 to be a fraction c_3 of the oscillator length when l_m is l_0, then:

$$x_0 = c_3 (l_\mathrm{tot} - l_0) \tag{2.23}$$

High P^* would occur for contractions that have a high activation throughout shortening, but minimal activation during lengthening of the muscle. Thus, the value of P^* also depends on the duty cycle D that represents the fraction of each excitation cycle where the muscle is excited (Swoap et al., 1997), as well as the activation dynamics that govern how rapidly the activation state can be turned on and off for the shortening phase. The unknown parameters c_1, c_2, c_3, f_d, and D were optimized for by maximizing the model output P^* using nonlinear global optimization for a fast muscle with $\dot{\varepsilon}_0$ of 10 s^{-1} and u_max of 1. Values of the model and equation parameters can be found in Table 2.1.

Table 2.1: Model and equation parameters.

Parameter	Definition	Value	Source
l_0	Muscle optimal length	0.02 m	Estimated from literature (Alexander et al., 1981)
σ_0	Muscle maximum isometric stress	225000 Pa	Estimated from literature (Medler, 2002)
ρ	Muscle density	1060 kg m^{-3}	Literature (Mendez & Keys, 1960)
R	Muscle aspect ratio (l_0:diameter)	100	
A	Muscle cross-sectional area	Varied	Calculated (Equation 2.11)
F_0	Muscle maximum isometric force	Varied	Calculated (Equation 2.10)
m_m	Muscle mass	Varied	Calculated (Equation 2.12)
τ_act	Time constant for activation	0.045 s for $\dot{\varepsilon}_0$ of 5 s^{-1}; 0.025 s for $\dot{\varepsilon}_0$ of 10 s^{-1}	Literature (Dick et al., 2017)
β	Ratio of τ_act to deactivation time constant	0.6	Literature (Dick et al., 2017)
D	Excitation duty cycle	See Table 2.3	Optimized
f_d	Driving frequency	See Table 2.3	Optimized
c_1	Ratio between ω_n and ω_d	See Table 2.3	Optimized
c_2	Ratio between m and F_0	See Table 2.3	Optimized
c_3	Ratio between x_0 and l_0	See Table 2.3	Optimized
m	Oscillator mass	Varied	Calculated (Equation 2.20)
k	Oscillator stiffness coefficient	Varied	Calculated (Equation 2.21)
b	Oscillator damping coefficient	Varied	Calculated (Equation 2.22)
x_0	Resting length of oscillator	Varied	Calculated (Equation 2.23)
l_tot	Total length of model	2 l_0	

2.3.2 Model non-dimensionalization and scaling

The standard Hill-type formulation assumes that whole muscles behave as single fibres, with the muscle forces scaling with cross-sectional area and muscle lengths scaling with optimal length. However, it has been shown that the presence of mass in muscle causes a scale-dependent distortion that limits this assumption (Ross & Wakeling, 2016). To explore the contribution of these scale-dependent distortions in muscles of different sizes, the model framework must be able to scale geometrically while preserving kinematic and dynamic similarity. In other words, a larger muscle would have greater forces, lengths and power outputs, but the non-dimensional forms of these parameters should remain the same. To achieve this, the spring-mass-damper properties of the damped harmonic oscillator must be adjusted to preserve kinematic and dynamic similarity of the whole system. For kinematic and dynamic similarity to occur, all dimensionless parameter groups, shown in curly brackets, are held constant for simulations with different geometric scales. To identify these dimensionless parameter groups, the dimensional system variables must be non-dimensionalized using methods presented in (Fowler, 1997).

Equation (2.9) contains three dimensional variables to be normalized: a, u, and t. Because u is defined as a square wave that varies in amplitude between 0 and 1, u and a in Equation (2.9) can be denoted as $\hat{u}$ and $\hat{a}$, respectively. The remaining time variable t can be normalized by a muscle time scale, t_{m}:

$$\hat{t}_{\mathrm{m}} = \frac{t}{t_{\mathrm{m}}} \tag{2.24}$$

This gives the following equation:

$$\frac{d\hat{a}}{d\hat{t}} + \left\{\frac{t_{\mathrm{m}}\beta}{\tau_{\mathrm{act}}}\right\}\hat{a}(1-\hat{u}) = \left\{\frac{t_{\mathrm{m}}}{\tau_{\mathrm{act}}}\right\}\hat{u}(1-\hat{a}) \tag{2.25}$$

Since the excitation input is prescribed as a normalized value, $\hat{u}$ can be scaled using:

$$\hat{u} = \frac{u}{u_{\max}} \tag{2.26}$$

where $u_{\max}$ is the maximum possible muscle excitation for a given simulation. Equation 2.8 contains five dimensional variables: F_{A}, F_{P}, F_{V}, Δx, and t. The forces F_{A}, F_{P} and F_{V} are normalized by the maximum isometric force, F_0:

$$\hat{F}_{\mathrm{A}} = \frac{F_{\mathrm{A}}}{F_0} \tag{2.27}$$

$$\hat{F}_{\mathrm{P}} = \frac{F_{\mathrm{P}}}{F_0} \tag{2.28}$$

$$\hat{F}_{\mathrm{V}} = \frac{F_{\mathrm{V}}}{F_0} \tag{2.29}$$

The displacement of the harmonic oscillator, Δx, is normalized with its resting length, x_0:

$$\Delta \hat{x} = \frac{\Delta x}{x_0} \tag{2.30}$$

and t is normalized with an oscillator time scale, t_{h}:

$$\hat{t} = \frac{t}{t_{\mathrm{h}}} \tag{2.31}$$

Both t_{h} and t_{m} are set to a value of 1 as there is no experimental evidence to suggest that muscle behaviour scales in the time dimension. Combining Equation (2.9) and Equations (2.26-2.31) gives the equation of motion:

$$\left\{\frac{m x_0}{F_0 {t_{\mathrm{h}}}^2}\right\}\left[\frac{d^2\Delta\hat{x}}{d\hat{t}^2} + \left\{\frac{b t_{\mathrm{h}}}{m}\right\}\frac{d\Delta\hat{x}}{d\hat{t}} + \left\{\frac{k {t_{\mathrm{h}}}^2}{m}\right\}\Delta\hat{x}\right] = F_0 u_{\max}\left[\hat{a}\hat{F}_{\mathrm{A}}\hat{F}_{\mathrm{V}} + \hat{F}_{\mathrm{P}}\right] \tag{2.32}$$

To ensure dynamic similarity between the root and scaled model, the dimensionless groups (curly brackets) from Equation (2.32) must remain constant:

$$\frac{m_r x_{0,r}}{F_{0,r} {t_{\mathrm{h},r}}^2} = \frac{m_s x_{0,s}}{F_{0,s} {t_{\mathrm{h},s}}^2} \tag{2.33}$$

$$\frac{b_r t_{\mathrm{h},r}}{m_r} = \frac{b_s t_{\mathrm{h},s}}{m_s} \tag{2.34}$$

$$\frac{k_r {t_{\mathrm{h},r}}^2}{m_r} = \frac{k_s {t_{\mathrm{h},s}}^2}{m_s} \tag{2.35}$$

where the subscripts r and s indicate the root and scaled models, respectively. We can define the following scaling factors for each parameter, p, as the ratio λ between the parameter value of the scale model and root model:

$$\lambda_p = \frac{p_s}{p_r} \tag{2.36}$$

Rearranging Equations (2.33-2.35) and substituting in the scaling factors gives the following scaling laws:

$$\lambda_m \lambda_{x_0} = \lambda_{t_\mathrm{h}} \lambda_{F_0} \tag{2.37}$$

$$\lambda_b \lambda_{t_\mathrm{h}} = \lambda_m \tag{2.38}$$

$$\lambda_k {\lambda_{t_\mathrm{h}}}^2 = \lambda_m \tag{2.39}$$

To ensure geometric similarity between models, the muscle length scale factor is set equal to the harmonic oscillator length scale:

$$\lambda_{x_0} = \lambda_{l_0} \tag{2.40}$$

To ensure kinematic similarity, the velocity of the muscle must scale with the velocity of the harmonic oscillator. The muscle velocity scale factor is proportional to the muscle length scale factor λ_{l_0} divided by the muscle time scale factor λ_{t_m}, and the oscillator velocity scale factor is equal to the oscillator length scale factor λ_{x_0} divided by the oscillator time scale factor λ_{t_h}. This leads to:

$$\frac{\lambda_{x_0}}{\lambda_{t_\mathrm{h}}} = \frac{\lambda_{l_0}}{\lambda_{t_\mathrm{m}}} \tag{2.41}$$

Combining and rearranging Equations (2.40-2.41) gives:

$$\lambda_{t_\mathrm{h}} = \lambda_{t_\mathrm{m}} \tag{2.42}$$

To solve for the remaining scale factors in terms of λ_{l_0}, additional assumptions must be introduced. Experimental evidence suggests that the maximum isometric stress of skeletal muscle is roughly constant across a range of animals, and does not appear to scale with muscle or animal size (Medler, 2002). Therefore, we can assume that the maximum isometric stress σ_0 is constant and λ_{σ_0} is equal to 1. Stress is calculated as force over cross-sectional area which gives:

$$\lambda_{\sigma_0} = \frac{\lambda_{F_0}}{{\lambda_{l_0}}^2} \tag{2.43}$$

Substituting in the value of λ_{σ_0} leads to:

$$\lambda_{F_0} = {\lambda_{l_0}}^2 \tag{2.44}$$

In addition to stress, muscle density ρ is typically assumed to remain constant across muscles of different sizes (Weis-Fogh & Alexander, 1977), and therefore the muscle density scale factor λ_ρ is equal to 1. Density is calculated as mass divided by volume, and since the model is geometrically scaled, the change in volume is proportional to the change in length cubed:

$$\lambda_\rho = \frac{\lambda_{m_\mathrm{m}}}{{\lambda_{l_0}}^3} \tag{2.45}$$

Solving for the muscle mass scale factor λ_{m_m} gives:

$$\lambda_{m_\mathrm{m}} = {\lambda_{l_0}}^3 \tag{2.46}$$

The average mass-specific power output per cycle P^* at a given cycle frequency is also relatively constant across a range of vertebrate muscles (Weis-Fogh & Alexander, 1977). Therefore:

$$\lambda_{F_0}\lambda_{l_0} = \lambda_{t_\mathrm{m}}\lambda_{m_\mathrm{m}} \tag{2.47}$$

Combining Equation (2.44) and Equations (2.46-2.47) gives:

$$\lambda_{t_\mathrm{m}} = 1 \tag{2.48}$$

and combining Equations (2.42) and (2.48) gives:

$$\lambda_{t_\mathrm{h}} = 1 \tag{2.49}$$

Substituting Equations (2.40), (2.44) and (2.49) into Equation (2.37) results in an expression for λ_m in terms of λ_{l_0}:

$$\lambda_m = \lambda_{l_0} \tag{2.50}$$

Similarly, an expression for λ_b in terms of λ_{l_0} can be found by substituting Equations (2.49-2.50) into Equation (2.38):

$$\lambda_b = \lambda_{l_0} \tag{2.51}$$

Combining Equations (2.39) and Equations (2.49-2.50) gives:

$$\lambda_k = \lambda_{l_0} \tag{2.52}$$

A summary of the scaling factors values can be found in Table 2.2.

Table 2.2: Model scaling factors.

Scaling factor	Value	Source
λ_{l_0}	1 or 10	Varied
λ_{σ_0}	1	Literature (Medler, 2002)
λ_{ρ}	1	Literature (Weis-Fogh & Alexander, 1977)
λ_{P^*}	1	Literature (Weis-Fogh & Alexander, 1977)
λ_{x_0}	λ_{l_0}	Calculated (Equation 2.40)
λ_{F_0}	$\lambda_{l_0}^2$	Calculated (Equation 2.44)
λ_{m_m}	$\lambda_{l_0}^3$	Calculated (Equation 2.46)
λ_{t_m}	1	Calculated (Equation 2.48)
λ_{t_h}	1	Calculated (Equation 2.49)
λ_{m}	λ_{l_0}	Calculated (Equation 2.50)
λ_{b}	λ_{l_0}	Calculated (Equation 2.51)
λ_{k}	λ_{l_0}	Calculated (Equation 2.52)

2.3.3 Force-velocity and force-length curves

A variety of different functions have been used to represent the intrinsic force-velocity and force-length relationships, including piecewise (Mashima et al., 1972; Otten, 1987; Scott & Winter, 1991; Ettema & Meijer, 2000), polynomial (Scott & Winter, 1991; Ettema & Meijer, 2000; Bahler, 1968; Woittiez et al., 1984), hyperbolic (Hatze, 1977; Brown et al., 1996), trigonometric (He et al., 1991; Moody et al., 2009), logarithmic (Brown et al., 1996), and exponential (Otten, 1987; Hatze, 1977; Nussbaum & Chaffin, 1998) functions. There is typically a trade-off between accuracy and cost when choosing curves to model these intrinsic properties. For example, piecewise functions typically provide the best physiological representation but they can create computational issues due to singularities in the first derivative of the function within the operating range of muscle lengths and velocities. In contrast, polynomials are smooth continuous functions that are easy to implement; however, they are typically poor at representing the behaviour of muscle outside of the usual operating range. This particularly becomes an issue for forward dynamics simulations where the lengths and velocities can be unconstrained.

Bézier splines have been presented as an alternative formulation that provides both improved accuracy and computational efficiency over traditional representations of force-velocity and force-length curves (Millard et al., 2013). These functions are para-

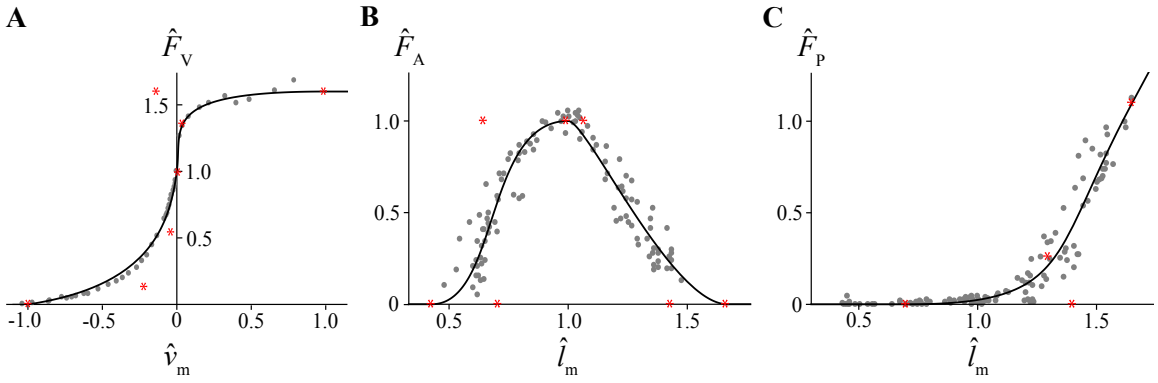

Figure 2.2: Force-velocity and force-length curves. Normalized force-velocity (A), active force-length (B) and passive force-length (C) curves (black lines). The force-velocity curve and the active and passive force-length curves are fitted to experimental data from Roots et al. (2007) and Winters et al. (2011), respectively (grey points). The Bézier control points for each curve are shown as red asterisks.

metric curves based on a set of polynomials that smoothly interpolate user-defined control points. For further details on the characteristics and formulation of Bézier curves, consult Prautzsch et al. (2002) and Mortenson (2006). For this study, we used composite cubic Bézier curves to represent the force-velocity and active force-length relationships, and a single cubic Bézier curve to represent the passive force-length relationship (Figure 2.2). We chose to use composite cubic curves rather than quintic curves as in Millard and colleagues (2013) as they allow more local control when relating the control points for the Bézier curve description to the physiological constraints within empirical muscle data.

The normalized force-velocity curve (Figure 2.2A) is composed of two cubic Bézier curves joined at a normalized muscle velocity $\hat{v}_m$ of 0 and normalized muscle force $\hat{F}_m$ equal to the maximum isometric force F_0. The concentric portion of the curve intersects with the -$\hat{v}_m$ axis at the maximum shortening strain rate $\dot{\boldsymbol{\varepsilon}}_0$, corresponding to $\hat{v}_m$ of -1, and is symmetric about the line $\hat{F}_m = -\hat{v}_m$ consistent with Hill's hyperbolic force-velocity curve (Hill, 1938). The eccentric portion of the curve passes through and plateaus at a $\hat{F}_m$ value equal to the maximum eccentric force F_{max}. The normalized force-velocity curve is linearly extrapolated for the extreme $\hat{v}_m$ values less than -1 and greater than 1, where $\hat{F}_m$ is set to be equal to 0 and F_{max}, respectively. To achieve continuity of the curve's first derivative, the slope of the eccentric and concentric portions of the curve are constrained to be equal where they meet at isometric $\hat{v}_m$. Additionally, the slope of the curve at a $\hat{v}_m$ value of 1 and $\hat{F}_m$ of F_{max} is constrained

to be equal to zero. Given these experimentally-derived physiological constraints, it is not possible to maintain C1-continuity of the concentric portion of the curve at $\dot{\boldsymbol{\varepsilon}}_0$; however, the presented curve is C1-continuous throughout the physiological range of $\hat{v}_{\mathrm{m}}$.

The normalized active force-length curve (Figure 2.2B) is composed of two cubic Bézier curves representing the ascending and descending limbs joined at optimal length and maximum isometric force which corresponds to a normalized muscle length $\hat{l}_{\mathrm{m}}$ and $\hat{F}_{\mathrm{m}}$ of 1. The slopes of both the ascending and descending limbs at l_{m} are constrained to be equal to 0, so the first derivative of the curve is continuous at this point. Similarly, the slope of the curve is set to 0 at the start of the ascending limb and at the end of the descending limb so that the curve is C1-continuous and the end points beyond where the value of $\hat{F}_{\mathrm{m}}$ is set to zero.

In contrast to the force-velocity and active force-length curves, the normalized passive force-length curve (Figure 2.2C) is a single cubic Bézier curve. $\hat{F}_{\mathrm{m}}$ is set to 0 for $\hat{l}_{\mathrm{m}}$ less than or equal to $\hat{l}_{\mathrm{m}}$ of 0.7. The curve is also linearly extrapolated for lengths longer than $\hat{l}_{\mathrm{m}}$ of 1.65, with the slope of the extrapolated region being equal to the slope of the line between the last and second to last control points. Matching the slopes on either side of the first and last control points guarantees continuity of the passive force-length curve and its first derivative.

The unconstrained degrees of freedom of the force-velocity and force-length relationships were determined by fitting the curves to experimental data from Roots et al. (2007) and Winters et al. (2011), respectively, by minimizing the coefficient of determination r^2 using numerical nonlinear global optimization.

2.3.4 Numerical simulations

To provide a computational proof of our methods, we tested the model at different excitation frequencies f, maximum activations $u_{\max}$, maximum shortening strain rates $\dot{\boldsymbol{\varepsilon}}_0$, and muscle length scale factors λ_{l_0}. The value of $u_{\max}$ was either 0.1 or 1 to simulate a muscle contracting at 10 and 100% of maximal excitation, respectively. The contractile element of the model behaved as either an entirely fast muscle with a $\dot{\boldsymbol{\varepsilon}}_0$ of 10 s^{-1} or an entirely slow muscle with a $\dot{\boldsymbol{\varepsilon}}_0$ of 5 s^{-1}. λ_{l_0} was either 1 or 10, where the models with λ_{l_0} of 1 had the geometric dimensions of the root model. Finally, f was set to a value of either 0.5, 1 or 2 Hz.

A single set of forward dynamic simulations were run for each possible combination of f, $u_{\max}$, $\dot{\varepsilon}_0$ and λ_{l_0}. The output muscle force F_{m}, velocity v_{m}, and length l_{m} were measured from the steady-state solution of the system. Due to the presence of damping, the steady-state solution does not depend on initial conditions, unlike the transient solution. The instantaneous muscle power was calculated as the product of F_{m} and v_{m}, and the average mass-specific power per cycle P^* was calculated as in Equation (2.38). All simulations were performed in Wolfram Mathematica Version 11.1.1.

2.4 Results and discussion

In this study, we presented a novel forward dynamics framework that consists of a damped harmonic oscillator in series with a Hill-type muscle actuator driven by time-varying activation. We also provided a description of how to build and implement Bézier splines to represent the intrinsic force-length and force-velocity properties of muscle. The r^2 for each fitted curve was greater than 0.87, comparable to the r^2 values for curves from previous studies (Otten, 1987; Bahler, 1968; Woittiez et al., 1984; Hatze, 1977; Brown et al., 1996; He et al., 1991; Moody et al., 2009) fitted to the same experimental data (Roots et al., 2007; Winters et al., 2011). However, the Bézier splines improve upon these more commonly used curves by allowing greater control in replicating the physiological features found in experimental muscle data.

We additionally provided methods to geometrically scale the system while preserving kinematic and dynamic similarity. Increasing λ_{l_0} from 1 to 10 altered the dimensional dynamics and kinematics of the model, with muscle lengths l_{m} and velocities v_{m} scaling with λ_{l_0}, muscle forces F_{m} scaling with ${\lambda_{l_0}}^2$, and the muscle powers scaling with ${\lambda_{l_0}}^3$ (Figure 2.3). However, the dimensionless output variables for different values of λ_{l_0} were identical for simulations with the same f, $u_{\max}$ and $\dot{\varepsilon}_0$ values, including P^* (Table 2.3). Geometrically scaling the system allows this framework to be used in future to investigate the effects of muscle size while controlling for the dynamic behaviour of the damped harmonic oscillator. Correctly modeling muscle size is important when scaling muscle data from single fibres to predict the function of whole muscles in animals and humans, and is even more important for predicting the function of large extinct species such as dinosaurs.

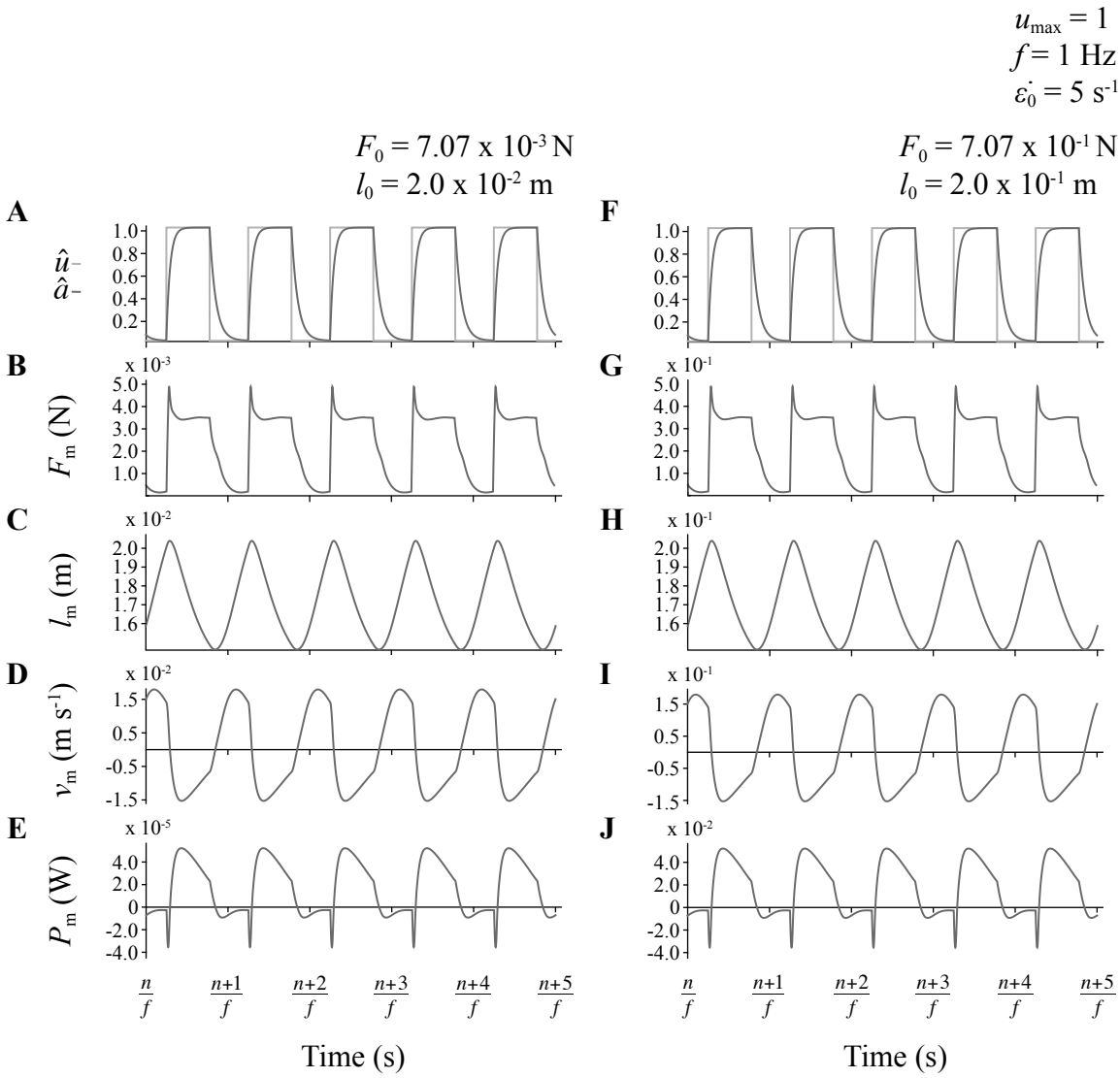

Figure 2.3: Sample raw output traces. Muscle excitation and activation (A,F), force (B,G), length (C,H), velocity (D,I) and power (E,J) traces for two representative simulations with $u_{\max}$ of 1, f of 1 Hz, $\dot{\varepsilon}_0$ of 5 s^{-1}, and λ_{l_0} of 1 (A-E) and 10 (F-J). n denotes the cycle number.

All simulations resulted in muscle length, velocity, force, and power outputs that qualitatively resemble the behaviour of *in vivo* muscle during cyclic contractions where the muscle is generating mechanical power (Figures 2.3-2.4). Faster muscles with $\dot{\varepsilon}_0$ of 10 s^{-1} generated greater average mass-specific power per cycle P^* than slower muscles with $\dot{\varepsilon}_0$ of 5 s^{-1} at a given cycle frequency f. A higher $\dot{\varepsilon}_0$ allows muscle to generate more force at a given contraction velocity which translates to greater power. Additionally, faster muscles generate greater P^* because they have faster rates of activation and deactivation than slower muscles. Theoretically, a muscle would generate the greatest

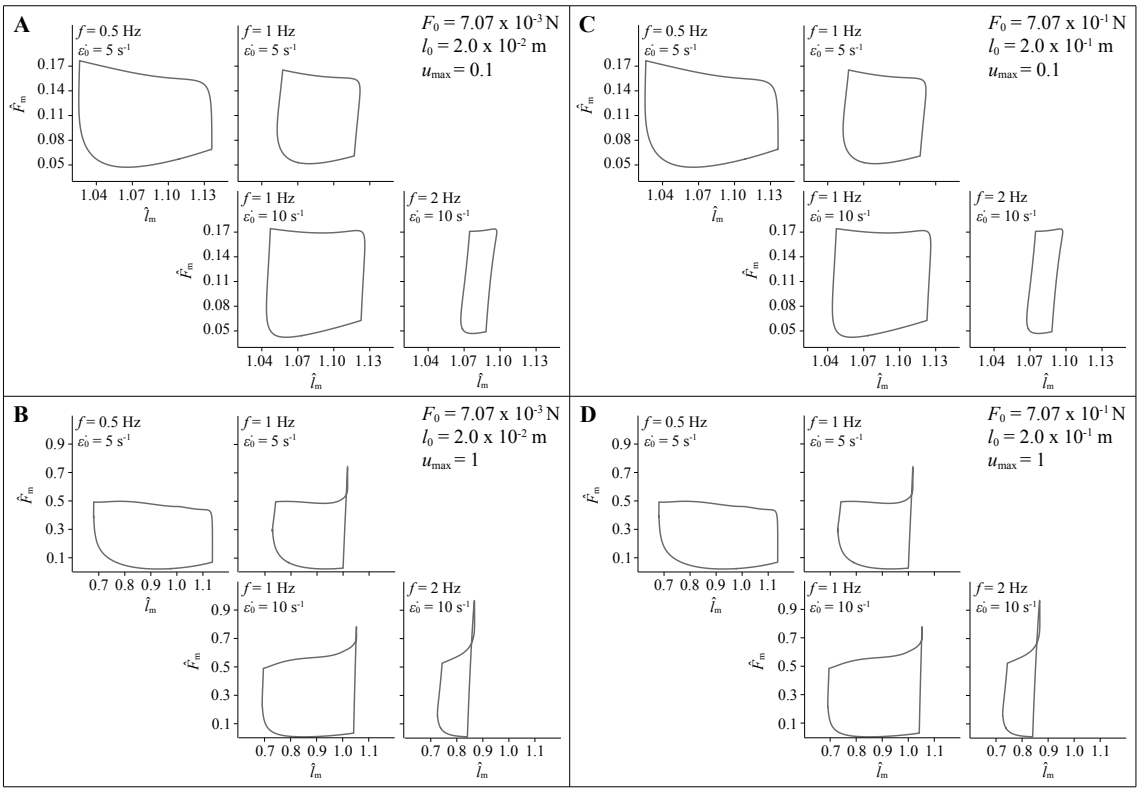

Figure 2.4: Output simulation work-loops. Muscle work-loops showing normalized muscle force $\hat{F}_{\mathrm{m}}$ versus normalized muscle length $\hat{l}_{\mathrm{m}}$ for each simulation. Simulations with $u_{\max}$ of 0.1 are shown in panels A and C, and simulations with $u_{\max}$ of 1 are shown in B and D. The non-dimensional muscle forces and lengths are identical for simulations with λ_{l_0} of 1 (A,B) and 10 (C,D).

P^* if it could activate and deactivate instantaneously at the beginning and end of the shortening phase of the contraction cycle. However, *in vivo* activation and deactivation is not instantaneous, and therefore muscle is activated before reaching peak length and deactivated while shortening to maximize mechanical work and P^* (Shadwick & Lauder, 2006), consistent with the behaviour of our model (Figure 2.3). These delays to peak activation and relaxation contribute to reduced P^* for simulations with higher values of *f*, particularly for slower muscles with greater τ_{act} where there is insufficient time in the shortening phase for the muscle to reach full activation, and insufficient time to fully deactivate during lengthening.

Some unexpected effects also occurred as a result of assumptions made in developing the system. The maximum excitation $u_{\max}$ scales the forces in the muscle and therefore the power, so higher $u_{\max}$ resulted in higher P^* values. However, this effect was greater than that predicted from sinusoidal contraction cycles about optimal length (Askew

et al., 1997) due to a shift in the operating range of muscle lengths at different values of $u_{\max}$. The muscle model contracted primarily on the ascending limb and plateau of the active force-length relationship when $u_{\max}$ was 1, and on the descending limb when $u_{\max}$ was 0.1. This effect is likely a consequence of the forward dynamics nature of the simulations where the muscle lengths respond to the dynamics of the contraction. Lower mean $\hat{F}_{\mathrm{m}}$ at lower $u_{\max}$ results in the muscle being in a less contracted state, and thus operating at longer muscle lengths. This differs from *in situ* studies (Askew et al., 1997; James et al., 1996; Askew & Marsh, 1997; Caiozzo & Baldwin, 1997; Swoap et al., 1997; Askew & Marsh, 1998; Syme & Tonks, 2004) where muscle is typically tested with contraction cycles centred about l_0.

Hill-type muscle models are widely used within the field of biomechanics to predict muscle function in living animals where measurement is oftentimes not feasible. To evaluate the effects of different model formulations, Hill-type models are typically assessed within inverse dynamics frameworks using steady, non-cyclic kinematics. However, such simulations are limited in their ability to assess how changing different muscle properties impacts the behaviour of muscle, including work and power output during cyclic contractions. The framework in this study will provide a testing platform whereby current and future formulations of Hill-type muscle models can be tested under common contractile regimes that emulate the contractions cycles typical in locomotion. This framework is also consistent across scales, and so can be used to reconcile information from single fibre to whole muscle experiments. Future work could utilize this methodology to evaluate the relative influence of effects such as history-dependent, internal mass, activation, and tendon effects on the behaviour of muscle during cyclic contractions under a wider range of cycle frequencies, excitations, and loading conditions.

2.5 Supplementary material

Table 2.3: Optimized parameter values.

Parameter	**Value**
D	0.528821
f_{d}	0.859938
c_1	1.0941
c_2	0.789365
c_3	1.30615

Table 2.4: Force-velocity Bézier control points.

Point number	$\hat{v}_{\mathbf{m}}$	$\hat{F}_{\mathbf{V}}$
1	-1	0
2	-0.216918	0.132201
3	-0.0528803	0.542295
4	0	1
5	0.0395273	1.34213
6	-0.134277	1.6
7	1	1.6

Table 2.5: Active force-length Bézier control points.

Point number	$\hat{l}_{\mathbf{m}}$	$\hat{F}_{\mathbf{A}}$
1	0.4	0
2	0.7	0
3	0.629283	1
4	1	1
5	1.08426	1
6	1.45	0
7	1.7	0

Table 2.6: Passive force-length Bézier control points.

Point number	$\hat{l}_{\mathbf{m}}$	$\hat{F}_{\mathbf{P}}$
1	0.7	0
2	1.40737	0
3	1.29739	0.248418
4	1.65	1.1

Chapter 3

Size, history-dependent, and activation effects on the work and power produced during cyclic muscle contractions

3.1 Abstract

Muscles undergo cycles of length change and force development during locomotion, and these contribute to their work and power production to drive body motion. Muscle fibres are typically considered to be nonlinear actuators whose stress depends on their length, velocity, and activation state, and whose properties can be scaled up to explain the function of whole muscles. However, experimental and modelling studies have shown that a muscle's stress additionally depends on inactive and passive tissues within the muscle, the muscle's size, and its previous contraction history. These effects have not been tested under common sets of contraction conditions, especially the cyclic contractions that are typical of locomotion. Here we evaluate the relative effects of size, history-dependent, and activation effects on the work and power produced during cyclic contractions of muscle models. Simulations of muscle contraction were optimized to generate high power-outputs: this resulted in the muscle models being largely active during shortening, and inactive during lengthening. As such, the history-dependent effects were dominated by force depression during simulated active shortening rather than force enhancement during active stretch. Internal work must be done to deform the muscle tissue, and to accelerate the internal muscle mass, resulting in reduced power and work that can be done on an external load. The effect of the muscle mass affects the scaling of muscle properties, with the inertial costs of contraction being relatively greater at larger sizes and lower activation levels.

3.2 Introduction

Muscles typically undergo cycles of activation, length change, and force development during locomotion (Dickinson et al., 2000). An understanding of how muscles operate during these cyclical regimes is thus necessary to determine the muscle design criteria for achieving locomotor tasks in a manner that is metabolically efficient or mechanically advantageous in terms of work and power. Pioneering studies on insect flight muscle in the 1950s characterized muscle forces during high frequency bursts of excitation coupled with cyclic length changes by expressing muscle force as a function of muscle length in a manner now known as a "work-loop" (Boettinger, 1957; Machin & Pringle, 1960). Boettinger (1957) noted that the slope of the major axis of the loop represented the compliance of the excited muscle, the area enclosed in the loop represented the work done against damping forces in the mechanical system, and the position of the loop in the force-length area represented the magnitude of contraction velocity. These early studies on asynchronous muscle, where the excitation is not synchronized with the contraction cycles, were later extended in the 1980s to synchronous insect flight muscle (Josephson, 1985) and crustacean muscle (Josephson & Stokes, 1989), where the timing of the excitation or action potentials is related to phase of the contraction cycle. This work-loop approach has since been generalized to a range of vertebrate muscles.

Understanding the determinants of muscle performance during vertebrate locomotion requires measures of both muscle force and length changes during *in vivo* activities. Prior to the 1980s when sonomicrometry was introduced to measure *in vivo* lengths and tendon buckles to measure in-series tendon forces (Loeb et al., 1985), work-loop studies were primarily done *in situ* or *in vitro* with imposed artificial length changes and excitation patterns. These new techniques to measure *in vivo* function fueled a proliferation of studies applying the work-loop technique in fish muscle (Altringham & Johnston, 1990b) to mimic the deformations observed *in vivo* (Franklin & Johnston, 1997), and subsequently, *in vivo* work-loops have been determined for a range of species including pigeons (Biewener, Corning, & Tobalske, 1998), turkeys (Roberts et al., 1997), guinea fowl (Daley & Biewener, 2003), mallard ducks (Williamson et al., 2001), wallabies (Biewener, Konieczynski, & Baudinette, 1998), and goats (McGuigan et al., 2009). Nonetheless, we still know very little about the *in vivo* behavior of contracting muscle for a wide range of locomotor activities in the majority of muscles in the majority of species, as well as the mechanisms that underlie this behaviour.

Hill-type muscle models are widely used in comparative biomechanics to estimate *in vivo* muscle forces where direct measures are not feasible (Van Leeuwen, 1992; Wakeling & Johnston, 1999; Hodson-Tole & Wakeling, 2009; Richards & Clemente, 2013; S. S. Lee et al., 2013), and because of our limited understanding of *in vivo* whole muscle mechanics, the intrinsic properties of these models are often derived from experiments on single fibres or fibre bundles that are maximally activated and constrained to contract in a steady manner. As a consequence, the few studies that have validated Hill-type models against *in vivo* or *in situ* measures have found that these models perform best during maximal, steady-state contractions and suffer under more functionally-relevant conditions where activations and muscle lengths and velocities are not constant. Perreault and colleagues (2003) found that model errors (percent root-mean-square) can exceed 50% when large changes in muscle length are modelled *in situ*. More recently, we have achieved modelling errors of 32% for *in vivo* locomotion in goats (S. S. Lee et al., 2013), and 13.5% in humans (Dick et al., 2017); however, correlation between measured and predicted forces only reached a maximum of $r^2 \approx 0.5$. Therefore, assuming that whole muscles behave as single fibres during controlled, steady contractions fails to account for the complex mechanisms that underlie whole muscle behaviour *in vivo*.

Hill-type muscle models typically assume that muscles are composed of a single fibre-type and contain no internal mass or inertial effects, and so can be scaled to any size without any consequences on the kinematic and dynamic behaviour of the model (Chapter 2). However, studies have shown that the presence of different fibre-types is important for muscle force production (Wakeling et al., 2012; S. S. Lee et al., 2013), and that muscle mass provides inertial damping within the muscle (Günther et al., 2012; Ross & Wakeling, 2016) that is dependent on fibre-type and activation level (Holt et al., 2014). The mass within muscle tissue takes time to move when the muscle forces cause accelerations, and this has been shown to slow contraction times (Günther et al., 2012) and maximum effective contraction speeds (Ross & Wakeling, 2016) in isotonic shortening contractions. Although the implications of these inertial effects due to muscle tissue mass on muscle performance during cyclic contractions are not yet known, we would expect the inclusion of internal muscle mass to reduce the shortening velocity of the muscle, and thus the power generated.

Most Hill-type muscle models calculate muscle force as a function of purely the instantaneous activation state, muscle length and velocity, and do not consider previous contraction history. However, history-dependent effects, which are distinct from

time-dependent effects due to excitation-activation dynamics, may be important for muscle contractile behaviour. In particular, when compared to isometric forces at a given length, muscle forces may be elevated or enhanced when the muscle reaches that length with prior active lengthening (Abbott & Aubert, 1952; Cavagna & Citterio, 1974; Edman et al., 1982; Herzog & Leonard, 2002; Hisey et al., 2009), and may be reduced or depressed when the muscle reaches that length with prior active shortening (Abbott & Aubert, 1952; Maréchal & Plaghki, 1979; Meijer et al., 1998; Herzog et al., 2000). The few experimental studies examining history-dependent effects during cyclic contractions have been limited to isokinetic stretch-shortening and shortening-stretch regimes with constant, maximal activation *in situ* in cats (Herzog & Leonard, 2000; H. D. Lee et al., 2001) or *in vivo* in humans (Seiberl et al., 2015; Fortuna et al., 2017, 2018). Furthermore, while a number of muscle models have incorporated history-dependent effects (Forcinito et al., 1998; Meijer et al., 1998; Wu & Herzog, 1999; Ettema & Meijer, 2000; Ettema, 2002; Tamura et al., 2005; McGowan et al., 2010, 2013; Williams, 2010; Nishikawa et al., 2011), none have examined the contribution of these effects during cyclic contractions with unconstrained length changes and time-varying activation.

Despite the wealth of experimental and modelling evidence that these additional effects are important for *in vivo* muscle behaviour, they have only yet been evaluated in separate studies with specific contraction regimes to elucidate their specific effects, so their individual and relative contributions are still not known. Therefore, the purpose of this study was to evaluate the contributions of internal mass, fibre-type, and history-dependent effects to the work and power output of muscle during cyclic contractions. To achieve this, we used a modelling framework that drives cyclic contractions of a Hill-type muscle model in series with a damped harmonic oscillator to create muscle work-loops (Chapter 2). These additional features were implemented within the muscle model, and so could be tested under common contractile regimes with the same intrinsic muscle properties to determine their individual and relative contributions to cyclic muscle performance.

3.3 Methods

3.3.1 System and muscle properties

The modelling framework we used to test the effects of different contractile and mechanical properties on muscle behaviour was composed of a harmonic oscillator, that represented an external load placed on the muscle, in series with the muscle model (Figure 3.1A). The whole system (muscle and oscillator) was held at constant length by fixing both ends. The system dynamics were driven by a cyclical activation signal a that caused the muscle to generate active force at the start of each activation cycle when the magnitude of activation increased. The muscle force F_{m} in turn accelerated an inertial point mass m, within the harmonic oscillator, that was considered to be external to the muscle, and this acceleration was resisted by a linear spring with stiffness k and a viscous damper with damping coefficient b that both acted only along the length (x-axis) of the system. When the muscle activation decreased at the end of each activation cycle, the harmonic oscillator force dominated the muscle force and caused the muscle to increase in length. Thus, the system allowed the muscle to cyclically contract with unconstrained muscle lengths and forces to mimic the contraction cycles seen during *in vivo* locomotion.

The activation signal a that drove the active muscle forces was derived from a pulsed square wave excitation signal u with prescribed maximum amplitude $u_{\max}$, frequency f, and duty cycle D. Excitation u was converted to a via a first-order bilinear differential equation (Zajac, 1989), the characteristics of which have been described in detail elsewhere (Chapter 2). The activity of muscle *in vivo* can be increased by recruiting more muscle fibres, and also by increasing the firing rate and thus the activity of the individual fibres. However, in our simplified model, typical of the ubiquitous Hill-type muscle models, the muscle contains only one fibre that can be scaled to any size. Thus, the activity is merely a scalar value that is applied to the muscle force.

The muscle simulated in this study was selected to contain fibres that were parallel to the line-of-action of the muscle, and has no aponeurosis or internal tendon. As such, the model ignores the structural effects that come from pennation and muscle fibre gearing. Muscle fibres are slender with an aspect ratio (length:diameter) that can approach 1000, however, whole muscles are much less slender with a lower aspect ratio. In order to create a shape for the model that was a compromise between a single fibre and a whole muscle, we selected an intermediate geometry with an aspect

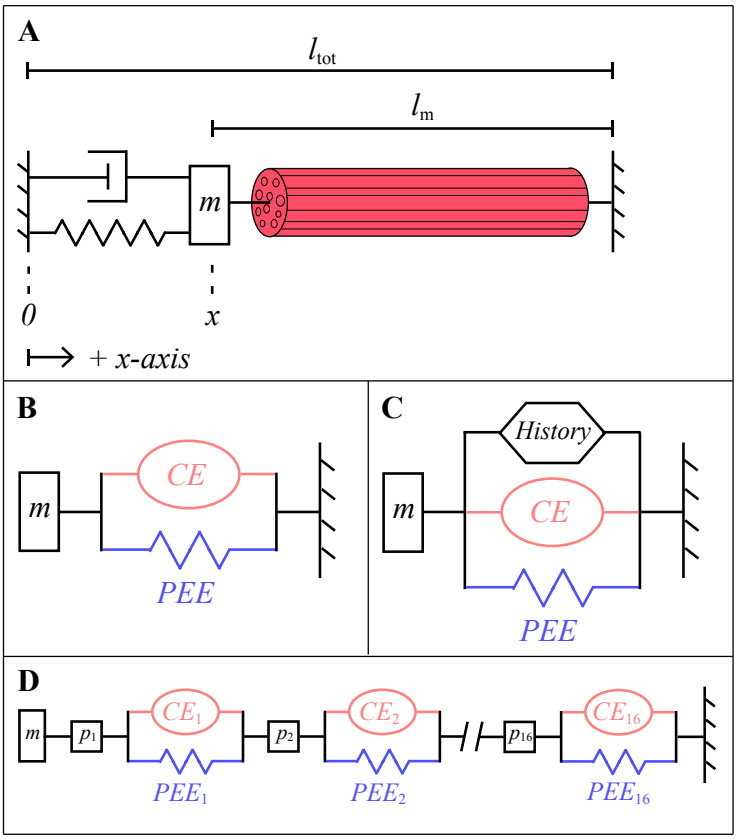

Figure 3.1: The different muscle models used for the simulated work-loops. (A) The spring, mass, and damper of the harmonic oscillator were in series connected to a muscle model (red cylinder), with the ends of the whole system being held at fixed positions. The muscle model was evaluated using a series of 1D models: (B) a Hill-type model with a contractile element (CE) and parallel elastic element (PEE); (C) a Hill-type model with an additional history-dependent element acting in parallel; (D) a mass enhanced model where the muscle mass was distributed into 16 point masses (p_1 – p_{16}), separated by Hill-type actuators.

ratio of 100. This may represent the geometry of a bundle of muscle fibres, or fascicle, but is still more slender than typical whole muscles. The optimal muscle length l_0 was set to 0.02 m and the muscle cross-sectional area A was set to 0.0314 mm^2. The maximum isometric stress σ_0 was held constant at 225 kPa.

A typical Hill-type muscle model without internal mass can be scaled to any size without any consequences on the kinematic and dynamic behaviour of the model (Chapter 2). However, the inclusion of internal muscle mass results in scale-dependent distortions where the load due to the muscle mass m_m is proportional to the muscle volume and the muscle force F_m is proportional to A (Ross & Wakeling, 2016). We tested

these mass effects by comparing muscles of different sizes with identical geometric proportions and aspect ratios. For example, a muscle with a length scale factor λ_{l_0} of 10 would have 10 times greater l_0, 100 times greater A, and 1000 times greater volume than a muscle with λ_{l_0} of 1. To control for the dynamics of the harmonic oscillator and achieve kinematic and dynamic similarity across different values of λ_{l_0}, the parameters k, b, and m for the damped harmonic oscillator were scaled according to Ross and colleagues (Chapter 2).

The average mass-specific power per cycle P^* was calculated as the product of the net mass-specific work per cycle W^* and f. The harmonic oscillator properties were chosen to allow the muscle to maximize P^*. As such, the values for k, b, and m, as well as D for the excitation signal, were determined using nonlinear global optimization with the objective of maximizing P^* for the control condition with $u_{\max}$ of 1.0, f of 1 Hz, and fast fibre-type properties. These parameters were then kept constant, except for D, which was optimized for each f and fibre-type.

3.3.2 Description of models

Root model

The root model has been previously described elsewhere (Chapter 2), and is shown in Figure 3.1B. In brief, the muscle in the root model consisted of a contractile element CE and a parallel elastic element PEE. The contractile element developed forces when activated, and the force was proportional to the activation state, the force-length and force-velocity properties within the muscle (Figure 3.2), as well as the instantaneous length and velocity of the muscle. Although the force-velocity properties of the CE result in implicit damping effects, we did not incorporate any additional damping element within the muscle. The force-length and force-velocity properties were defined by their Bézier curve descriptions (Chapter 2). The root model did not include internal mass or history-dependent effects.

Mass model

The root model does not consider the inertial properties of the muscle mass when calculating muscle forces, as is typical of most Hill-type muscle models. However, the mass within the muscle tissue takes time to move when the muscle forces cause accelerations, and this is reflected by a slowing of contraction times (Günther et al., 2012) and maximum effective contraction speeds (Ross & Wakeling, 2016). We

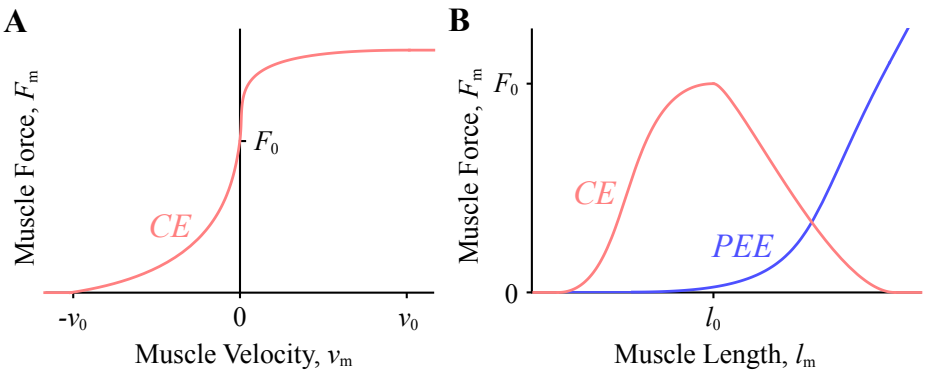

Figure 3.2: Force-velocity and force-length curves. Force-velocity (A) and force-length (B) properties for the Hill-type models of the muscle fibres. The curves were parameterized using Bézier curves (Chapter 2)

would therefore expect the inclusion of internal muscle mass to reduce the shortening velocities of the muscle model, and thus the power generated. We tested this by subdividing the muscle into a series of smaller CEs and PEEs, divided by point masses that accounted for the muscle mass, following the scheme presented by Ross and Wakeling (2016). The total muscle mass was divided into 16 contractile elements that were separated by 16 point masses (Figure 3.1D). The intrinsic properties of the CE and PEEs remained the same as for the root model. The muscle mass m_{m} was calculated as the product of the muscle volume and the density ρ, and as ρ was assumed to be constant at 1060 kg m^{-3}, m_{m} scaled in proportion to the muscle volume. As m_{m} was distributed evenly along the length of the muscle at rest, the mass of each point mass was equal to m_{m} divided by the number of point masses.

History-dependent model

To test for the effect of history-dependent phenomena on the resulting cyclic work-loops in this study, we added a history-dependent element in parallel to the CE of the root model (Figure 3.1C). The force of this history-dependent element was determined by the sum of the stretch-induced force enhancement F_{FE} and the shortening-induced force depression F_{FD}.

The method to include F_{FE} was styled from a recent theory (Rode et al., 2009; Herzog, Leonard, et al., 2012; Herzog, 2014). F_{FE} was calculated using an empirical description (in a similar manner to the force-length and force-velocity parameters of the Hill-type model), and represents the additional titin forces that are believed to

develop after active stretch. When the activation of the model increased beyond a threshold (50% maximum activation for each trial), the instantaneous muscle length at the time the threshold was reached was retained as a state constant l_e. If the instantaneous muscle length l_m was stretched beyond l_e, then F_{FE} was calculated from the normalized elastic modulus and the normalized muscle stretch:

$$F_{FE} = F_0 \left[\frac{l_m - l_e}{l_e} \right] \hat{E}^{\left(\frac{l_e}{l_0}\right)} \tag{3.1}$$

where F_0 is the maximum isometric force for the muscle, and $\hat{E}$ is the normalized elastic modulus that varies as a function of l_e normalized to l_0 in a non-linear fashion (Figure 3.3A) that was determined from experimental data for the ascending (Hisey et al., 2009) and descending (Edman et al., 1982) limbs of the force-length relationship. This empirical description of force enhancement after stretch results in predicted enhanced forces that match experimental values for steady-state contractions (Figure 3.3B). When the activation state returned below the threshold, the F_{FE} was reduced to half its value to estimate the residual force enhancement, consistent with experimental data (Hisey et al., 2009). The force enhancement F_{FE} reduced to zero, and the muscle was returned to its non-enhanced state, when l_m shortened to less than l_e. This process would then be repeated for the subsequent contraction cycles. For simulations where the excitation was increased to a submaximal level with u_{max} of 0.1 or 0.5, the maximum activation in each burst was less than 1. We assumed that only a portion of the fibres in the muscle are recruited during these submaximal simulations, and therefore, only the active portion of fibres would have enhanced titin forces and contribute to F_{FE}. Thus, F_{FE} was scaled by the maximum activation achieved in each contraction cycle.

The magnitude of force depression has been described as a linear function of the net work done during each active contraction (Herzog et al., 2000). The force depression F_{FD} was initially modelled following McGowan et al. (2010):

$$F_{FD} = -c_{FD} W_c \tag{3.2}$$

where W_c is the work done during the active contraction, and c_{FD} is the coefficient for force depression that was set to a value of 9.43 N J^{-1} (McGowan et al., 2010 from Herzog et al., 2000). However, the coefficient c_{FD} had dimensions and needed to be

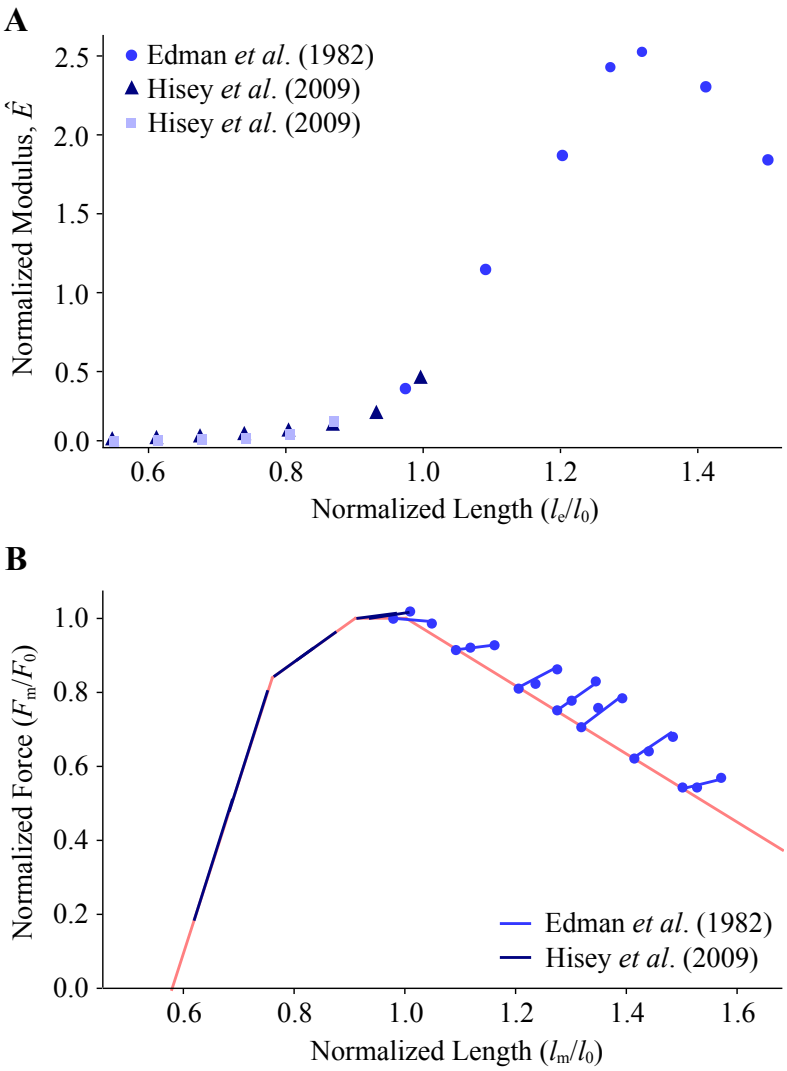

Figure 3.3: Method for calculating force enhancement that occurs during periods of active stretch. (A) The modulus of the enhanced force (relative to the length that the muscle was activated) was determined for experimental data from both the ascending (Hisey et al., 2009) and descending (Edman et al., 1982) limbs of the force-length relation. (B) The predicted enhanced forces are shown in the context of steady forces after stretch in comparison to experimental values (blue circles).

non-dimensionalized so that it could be applied across scales. Assuming that the magnitude of force depression per sarcomere is the same across all muscle sizes, the non-dimensional force depression coefficient was calculated as:

$$\hat{F}_{\mathrm{FD}} = 0.3387 \frac{\hat{F}_{\mathrm{m}}}{\hat{W}_{\mathrm{c}}} \tag{3.3}$$

where the non-dimensional work $\hat{W}_c$ and non-dimensional force $\hat{F}_m$ were given by:

$$\hat{W}_c = \frac{W_c}{W_{max}} \tag{3.4}$$

and

$$\hat{F}_m = \frac{F_m}{F_0} \tag{3.5}$$

Therefore,

$$\hat{c}_{FD} = 0.3387 \frac{F_m W_{max}}{F_0 W_c} \tag{3.6}$$

where W_{max} is the product of l_0 and F_0, calculated using data from Herzog and colleagues (2000). Thus, F_{FD} was calculated as:

$$F_{FD} = -F_0 \hat{c}_{FD} \hat{W}_c \tag{3.7}$$

If the muscle started to lengthen whilst still active, W_c would decrease and so too would F_{FD}, however, F_{FD} was set to zero if W_c became negative. In a similar manner to the force enhancement, the contribution of the force depression was assumed to only occur in active fibres. Thus, the F_{FD} was also scaled by the maximum activation achieved in each contraction cycle.

3.3.3 Simulations

We tested the root, history-dependent, and mass models under a range of maximum excitations u_{max}, frequencies f, length scale factors λ_{l_0}, and fibre-type properties to replicate the contraction regimes seen during *in vivo* locomotion. The muscle behaved as if it was composed of either entirely fast or entirely slow fibres, and this was implemented into the models by setting the maximum shortening strain-rate v_0 to either 10 s^{-1} or 5 s^{-1} and the activation rate constant τ_{act} to either 0.025 s or 0.045 s, respectively. These values are selected to represent typical properties for fast and slow fibres (Dick et al., 2017). u_{max} was set to either 0.1, 0.5, or 1.0, and f was set to either 1, 2, 4, or 8 Hz. The duty cycle D was re-optimized for the different values of

f, and decreased at with increased f. For the root model with v_0 of 10 s^{-1}, D ranged from 0.52 at f of 0.5 Hz to 0.31 at f of 8 Hz; for the slower-fibred model with v_0 of 5 s^{-1}, D ranged from 0.55 at f of 0.5 Hz to 0.29 at f of 8 Hz. The mass of the harmonic oscillator m was optimized for the control condition and scaled with λ_{l_0} across the range of muscle sizes tested (Chapter 2). We also tested a range of muscle masses from 0.67 mg at λ_{l_0} of 1, which is typical of a muscle fascicle, to 670 g at λ_{l_0} of 100, which is less than the plantar flexor muscle mass in humans (Handsfield et al., 2014), for the mass model.

When muscle is submaximally activated, not all the muscle fibres need to be recruited, and the intrinsic properties (fibre-type) of the activated fibres affect the mechanical output of the whole muscle. If the output of the whole muscle depended only on the combined output of the active fibres, for instance following Hill (1970), then recruiting slower fibres would result in lower power output than recruiting faster fibres. However, when the internal mass of the muscle is considered, the presence of inactive fibres provides inertial resistance, even when these inactive fibres are not developing active force (Holt et al., 2014; Ross & Wakeling, 2016), and this may occlude differences due purely to the fibre-type. Thus, the root model would be expected to develop different power outputs depending on its fibre-type, with these differences seen across activation levels, however, the fibre-type contribution would be smaller for the model with internal mass, particularly at larger muscle sizes. This was tested by evaluating the muscle model with slower intrinsic properties with v_0 of 5 s^{-1} and act of 0.045 s, and at the lower levels of excitation with $u_{\max}$ of 0.1 and 0.5.

3.4 Results

The muscle excitation u for each simulation was represented by a repeating square wave that took a value of either zero or $u_{\max}$. The resulting activation a increased rapidly at the beginning of each cycle of u, plateaued across mid-burst, and finally decayed at a slower rate than the rate of activation when u returned to zero. The muscle generated active forces when a was greater than zero, and this caused the muscle to shorten and accelerate the point mass m within the harmonic oscillator (Figure 3.1A). When the muscle was inactive, the restoring force due to the spring in the harmonic oscillator exceeded the muscle force, and caused m to accelerate to lengthen the muscle. The muscle length excursions were thus in-phase with the timing of u. However, there was a short time lag between when the muscle was excited and

when it started to shorten due to both the time required for the muscle force to accelerate and change the direction of the velocity of m, and the time required to reach peak a after u changes to $u_{\max}$. Similarly, the muscle started to lengthen before it was fully deactivated due to the restoring force exceeding the muscle force towards the end of the activation period.

As a consequence of the non-zero passive muscle and harmonic oscillator forces when the muscle was at l_0, the values of the initial position and velocity of m required to solve the system were not immediately evident. However, because only the transient solution of a damped system, and not the steady-state solution, depends on the choice of initial conditions, we were able to avoid finding the ideal initial conditions by examining only the steady-state solution. Thus, herein we report only steady-state results where the behaviour of the system repeats each cycle.

The greatest average mass-specific muscle power output P^* across all models and simulations was 42 W kg^{-1}, and was achieved for the control simulation in the root model where f was 1 Hz, $u_{\max}$ was 1, and the muscle had fast fibre-type properties. Rather than being of physiological importance, this was due to selecting the harmonic oscillator parameters and D to maximize P^* for only these control conditions in the root model. For these conditions, the maximum shortening velocity reached was only 11% of v_0, and the maximum stress was 66% of σ_0. However, the theoretical maximum P^* for the control simulation in the root model would have been 92 W kg^{-1}, given these force-velocity and force-length properties, σ_0, and v_0 (following Weis-Fogh & Alexander, 1977), so the control condition does not reflect the optimal conditions for maximum steady-state power production.

The main effects of f, $u_{\max}$ and fibre-type on the Hill-based root, mass, and history-dependent models are shown in Figure 3.4. The net mass-specific work per cycle W^* was lower for higher cycle frequencies, and at the highest f of 8 Hz there was insufficient time for the muscle to fully activate or deactivate. This resulted in muscle force oscillations that were too fast to drive substantial displacements of the harmonic oscillator, and thus, there was little length excursion in the muscle for the high frequencies (Figure 3.5A). The value of P^* was greatest at the intermediate f of 1 Hz where the harmonic oscillator was calibrated to allow the muscle to generate maximal power. As $u_{\max}$ decreased from 1.0 to 0.5 or 0.1, the activation and muscle force decreased. This led to the muscle operating at longer lengths with smaller excursions, as it was not able to generate large enough forces to contract to shorter lengths. Consequently,

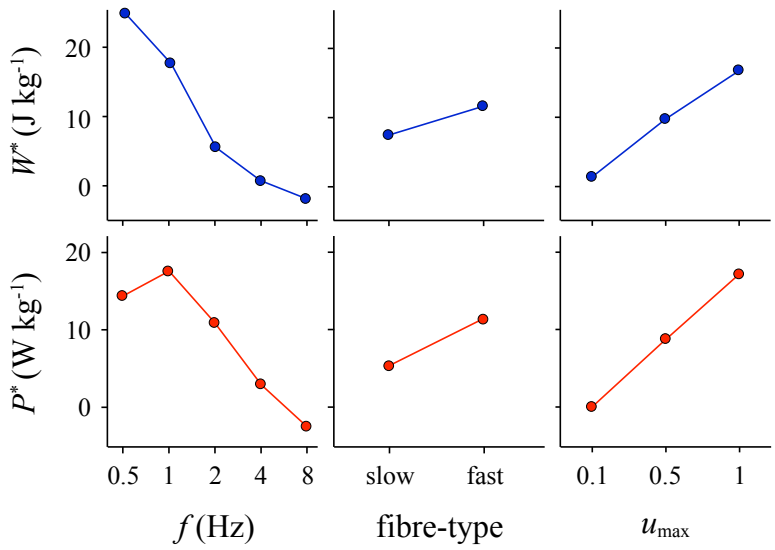

Figure 3.4: Main effects of frequency, fibre-type and excitation level on the mass-specific work W^* and power P^* from the muscle models during cyclic contractions. The main effects were calculated from a set of 166 simulations across this parameter range, and included data from the mass-enhanced, history-dependent, and root Hill-type models.

both W^* and P^* were smaller in magnitude for lower levels of $u_{\max}$ (Figures 3.4 and 3.5B). The fibre-type properties of the muscle were determined by v_0 and τ_{act}, where the fast muscles had v_0 of 10 s^{-1} and τ_{act} of 0.025 s, and the slow muscles had v_0 of 5 s^{-1} and τ_{act} of 0.045 s. Muscles composed of the slower fibre-type developed lower active force during shortening leading to smaller length excursions and lower W^* and P^* (Figures 3.4 and 3.5C).

The non-dimensional dynamics of the muscle were identical across muscle length scales λ_{l_0} for the root Hill-type model that had no mass (i.e. stress, strain, W^*, and P^*). By contrast, inclusion of internal mass within the muscle model resulted in reduced net active muscle force during contraction, as well as increased passive force during lengthening due to the inertial costs of this mass. These changes in force were subtle, but were accentuated for simulations with greater λ_{l_0}, with the larger mass-enhanced models generating lower W^* and P^*. Larger muscles and lower $u_{\max}$ resulted in smaller differences in P^* between fast and slow fibre-type conditions in the mass model compared to the massless root model.

There was minimal active stretch in the muscle after the start of each cycle of u, so the contribution of force enhancement was minimal across all conditions. How-

ever, the muscle was largely active during shortening, resulting in significant force depression effects. The lower forces in the history-dependent model due to force depression resulted in the muscle not contracting to such short lengths, so both W^* and P^* were lower for the history-dependent model compared to the root model (Figure 3.5E).

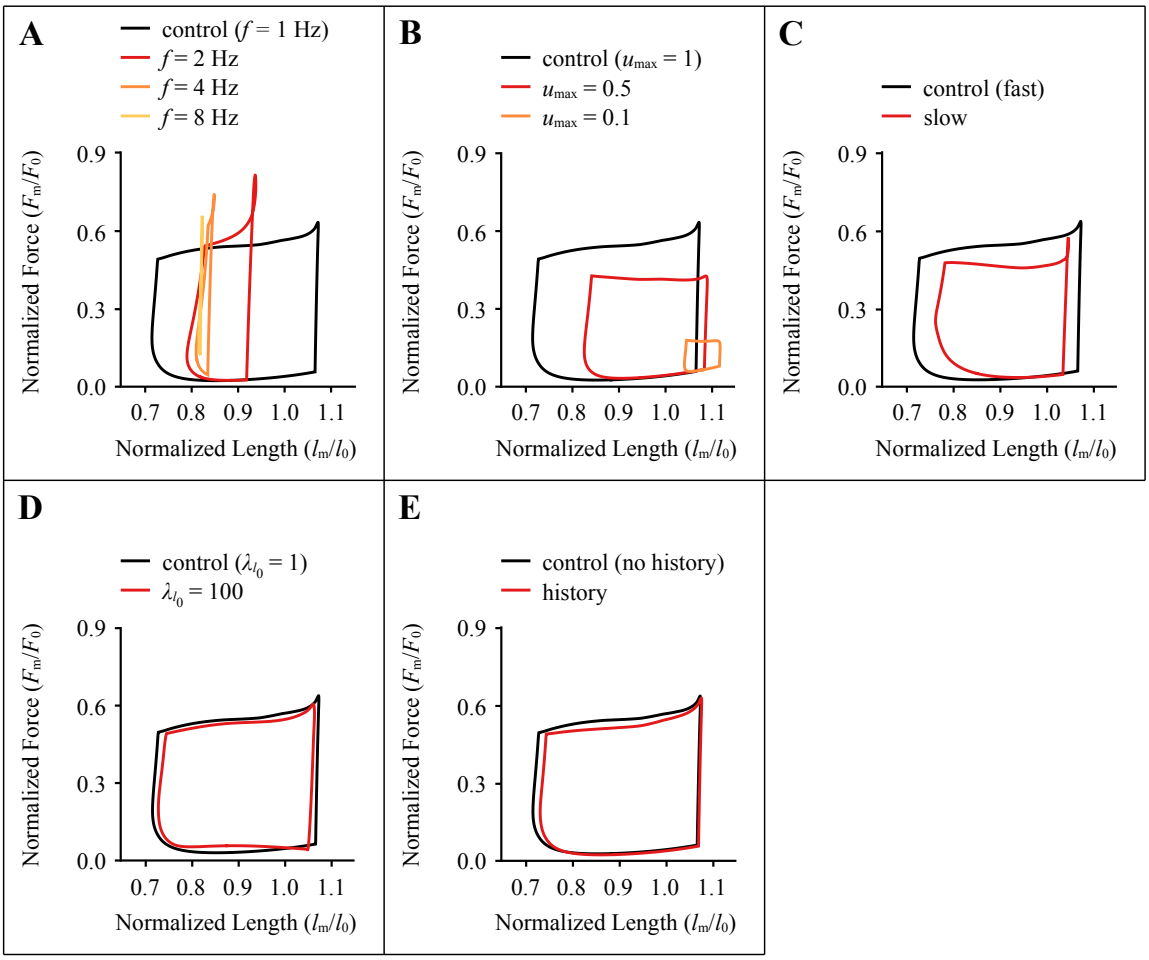

Figure 3.5: Work-loops for muscle contractions demonstrating all tested parameters. (A-E) Work-loops are compared to the control simulation at 1 Hz frequency, maximal excitation, fast-fibre type and small muscle size. Comparisons are shown that vary: (A) the frequency from 1 to 8 Hz; (B) the maximal excitation from 1.0 to 0.1; (C) the fibre-type from fast to slow; (D) the muscle size from 0.67 mg to 670 g using the mass-enhanced model; and (E) history dependent effects.

Overall, the greatest effects of the mass-enhanced and history-dependent models can be observed for the contractile conditions with f of 1 Hz and $u_{\max}$ of 1.0 (Figure 3.5D,E). The mass-enhanced model at the largest scale tested (λ_{l_0} of 100; equivalent to a 670 g muscle) generated 12% less work and power with fast fibre-type properties and

4% less with slow properties compared to the root model with the same conditions. The history-dependent model was dominated by the force depression effect for these contractions and resulted in a 7% reduction in work and power compared to the root model.

3.5 Discussion

3.5.1 Muscle mass and scaling of contractile properties

The root model was styled from a typical Hill-type muscle model, and as such, there were no mechanisms within the model to distort the intrinsic properties of the muscle as it scaled to different sizes. This implicitly means that simulations of muscles at any scale would result in the same non-dimensional muscle performance, provided the external load from the harmonic oscillator was scaled appropriately. Indeed, this is how Hill-type muscle models are typically used: they are defined using intrinsic properties measured during experiments on single fibres or small muscles, which are in turn used to predict the function of whole muscles that may be of larger size (Wakeling & Lee, 2011). The results from the root model in this study confirm that the function predicted by typical Hill-type models is conserved across scales. However, these models ignore the inertial effects of internal muscle mass on the dynamics of contraction. Previous studies have shown that internal mass acts to slow the rate of force development (Günther et al., 2012), and the maximum contraction velocity of larger muscles (Ross & Wakeling, 2016). This study confirms these findings and also demonstrates that the internal mass results in a reduction in the work and power produced by whole muscles during cyclic contractions (Figures 3.5 and 3.6).

The mass of the muscle tissue alters the properties and function of muscle depending on the scale. Muscle mass varies in proportion to its volume, whereas muscle force varies with its cross-sectional area. This means that increasing muscle size, and decreasing the area to volume ratio, would result in the internal mass increasing faster than the available forces to accelerate that mass. Thus, the mass effects will predominate at larger muscle sizes. Indeed, the mass model predicted a negligible effect of the internal mass for a scale of 1 where the muscle was 0.67 mg, whereas the mass effect was large and important for scale of 100 where the muscle was 670 g.

The effect of the internal mass of the muscle tissue was important in this study due to the dynamic nature of the contractions. It should be noted that models of isometric

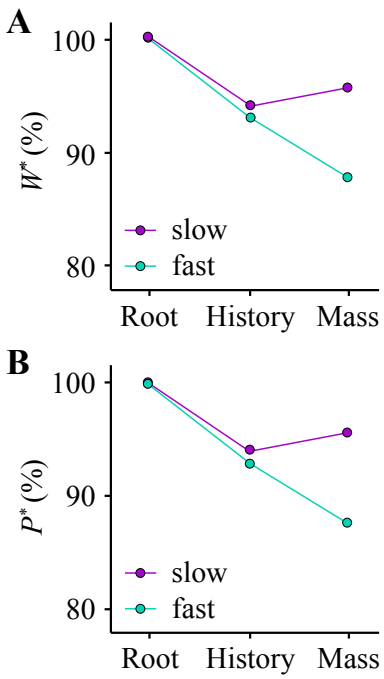

Figure 3.6: Relative changes in performance between the root model with the history-dependent and mass-enhanced models. (A) Muscle mass-specific work W^* and (B) muscle mass-specific power are shown relative to W^* and P^* for the control simulation (at 1 Hz frequency, and maximal excitation). Simulations with different fibre-types were compared to their fibre-type control.

contractions where the accelerations are negligible would show little difference if mass were included. However, internal work is required to accelerate the mass of the muscle tissue when the muscle changes length. Differences in muscle fibre-types result in different forces for given muscle lengths and velocities, and so we could expect the mass effect to depend on the intrinsic speed of the contracting fibres. Indeed, model results show that the maximum (normalized) shortening velocity of a muscle is reduced for larger sizes, and this effect is exacerbated for muscles with faster intrinsic speeds of their contractile elements (Ross & Wakeling, 2016). Here we additionally show greater reductions in the mass-specific work and power output during cyclic contractions for muscles with faster intrinsic speeds (Figure 3.6), which are caused by the dynamics of the muscle mass.

Additional mass effects are apparent in muscles that are not fully active. Inactive muscle fibres have been proposed to contribute drag to a contracting whole muscle, resulting in a mechanical cost that would diminish the mechanical output of the muscle (Josephson & Edman, 1988; Holt et al., 2014). The effects of the internal

muscle mass would predominate at lower activations in a similar manner to which they predominate at larger muscle sizes, since at low activations there would be reduced contractile force available to accelerate the internal mass of the muscle tissue. Indeed, the results of this study support this notion.

3.5.2 Muscle function and history-dependent properties

When a muscle generates high power, it must contract with high force whilst shortening, and generate negligible force when it is lengthening. This would require the muscle to be activated close to its maximum length, and to be deactivated close to its minimum length, and this pattern emerged in our contraction cycles. However, activating close to maximum length provides minimal history-dependent force enhancement during active stretch. Indeed, the magnitude of force enhancement was negligible for the stretch-shortening contraction cycles in this study (Figure 3.5E). By contrast, a substantial effect of force depression was observed. Thus, the majority of the history-dependent effects from these power-producing cyclic contractions occurred due to the force depression during shortening.

In this study, the history-dependent effects resulted in a reduction in the net work and average power output per cycle of the muscle of about 7% for the 1 Hz frequency and maximal excitation condition. Although few studies have examined history-dependent effects during cyclic contractions, similar magnitudes of force depression have been previously reported. McGowan and colleagues (2010) found a 6% reduction in isometric torque during simulated knee extension and a 28% reduction in average crank power during simulated cycling when force depression was incorporated into a lower-body musculoskeletal model. This magnitude of joint torque reduction during knee extension is comparable to a 6.5% reduction in torque reported experimentally with the same conditions (H. D. Lee et al., 1999). Despite these findings, these musculoskeletal simulations involved more than one joint and multiple muscle actuators, and the Hill-type formulation of these actuators accounted for the effects of series elasticity. Thus, the contribution of force depression to the behaviour of individual muscles in these simulations is difficult to resolve, so the results of our simulations are not directly comparable to the results of these previous studies. However, as our control simulation was designed to maximize muscle work and power output per cycle, the magnitude of force depression reported here is likely as large as would be achieved by a single muscle for contraction cycles during locomotion.

3.5.3 Intrinsic speeds and fibre-type effects

The maximum power output from a muscle depends on the intrinsic speed (maximum strain-rate) of its muscle fibres (Weis-Fogh & Alexander, 1977). Not only can faster muscle fibres contract at faster speeds than slow fibres, but they generate greater stress at any given speed. This study used forward dynamic simulations of contractile cycles, whereby the range of motion, shortening velocity, and muscle force could all vary as a function of the excitation parameters used to drive the simulations. The simulations showed that the muscle with faster intrinsic speed (v_0 of 10 versus 5 s^{-1}) generated greater forces, allowing for greater length changes and thus higher shortening velocities than the slower muscle. The resultant work-loops showed that the faster muscle generated greater work per cycle and power output for an equivalent excitation and frequency (Figure 3.5C).

Mammalian muscle is commonly comprised of a heterogeneous population of fibre-types. If a heterogeneous muscle is sub-maximally activated then the intrinsic properties of the fibres that are activated may govern the contractile properties of the whole muscle. However, experimental studies have shown that there may be less difference in the shortening velocity of whole muscle than would be predicted by fibre-type alone (Holt et al., 2014). This effect has been attributed to the 'drag' of the inactive tissue (Josephson & Edman, 1988; Holt et al., 2014), and may be caused by the inertial properties of the internal muscle mass (Ross & Wakeling, 2016), as discussed above.

The pattern of recruitment between different types of motor units is therefore important in determining the mechanical output of whole muscle. The usual recruitment pattern follows the 'size principle' whereby slower motor units are recruited first and for lower activations (Henneman et al., 1965a, 1965b). However, alternative recruitment patterns have been described that may favour recruitment of greater proportions of faster motor units at submaximal activations (see review: Hodson-Tole & Wakeling, 2009) at fast contraction speeds and high contraction frequencies (Blake & Wakeling, 2014). The simulations from this study show that, even at low excitation (10%), the type of fibres recruited alters the work and power output of the whole muscle. Additionally, our findings confirm that inertial effects from the muscle mass cause slower muscle shortening speeds and result in lower W^* and P^* than in smaller muscle or muscle without mass (Figure 3.6).

3.5.4 Assumptions, limitations, and future work

The purpose of this study was to determine the effect of contractile features that are not accounted for in most Hill-type muscle models on the force and power of muscle during cyclic contractions. As such, we chose to orient the line-of-action of the fibres in these simulations along the longitudinal x-axis of the system (Figure 3.1A). This enabled us to directly interpret the effects of the contractile properties on muscle performance because the entirety of the force vector from the fibres acted to accelerate the point mass m of the harmonic oscillator. However, not all muscles have their fibres arranged in parallel, and many have their fibres arranged at an oblique, pennate angle from the line-of-action of the muscle (Wickiewicz et al., 1983).

As muscle fibres shorten they must increase in girth to maintain their volume. Such increases in girth allow pennate fibres to shorten and increase their pennation angle so that they can maintain their packing within the muscle belly (Lieber & Ward, 2011). When the fibres rotate, their shortening velocity becomes uncoupled from that of the muscle belly in a process termed belly gearing (Wakeling et al., 2011), which lowers the fibre velocity relative to the belly velocity and alters muscle force, work, and power. Thus, architectural features of muscle, including pennation, add a layer of complexity to our understanding of muscle function *in vivo*. This understanding is further challenged when we consider that the exact nature of how muscles bulge in different directions (Maganaris et al., 1998; Azizi et al., 2008; Randhawa et al., 2013), and how variations in such bulging alters gearing (Azizi et al., 2008) is not fully known. Hence, focusing on parallel-oriented fibres allows us to probe fibre-level questions without being confounded by the additional complexity due to muscle architecture.

We also chose to exclude tendinous, or series elastic, elements from the model for similar reasons. Tendons stretch when loaded, and if a tendon is long or compliant, this stretch can uncouple the velocity of the muscle belly from that of the muscle-tendon unit in a process known as tendon gearing (Wakeling et al., 2011). To make more direct interpretations of the effect of muscle (fibre or belly) shortening on the motion of the point mass within the harmonic oscillator, we assumed that tendon stretch was negligible and that the muscle was connected to m via a rigid link. However, it should be acknowledged that where significant tendinous tissue occurs *in vivo*, the tendon can further modify the behaviour of the muscle-tendon-unit by amplifying muscle power output or attenuating muscle power input (Roberts & Azizi, 2011).

As the primary goal of this study was to examine the relative effect of different contractile phenomena on the work and power production of a muscle during cyclic contractions, the muscle model was designed to generate its maximum power for one of the intermediate contractile regimes with frequency f of 1 Hz, maximum excitation $u_{\max}$ of 1, and fast fibre-type properties. Generating maximum power is an example of the muscle acting as a motor, and indeed our test condition operated at 50% of the maximum theoretical average mass-specific power per cycle (calculated for maximal activation and constant velocity) (Weis-Fogh & Alexander, 1977). However, muscles can also act as springs, struts, or brakes during locomotion depending on the requirements of the task (Dickinson et al., 2000), and muscles may have specific adaptations to their properties depending on their primary function (Biewener, 1998; Mörl et al., 2016). The muscle model in this study was coupled to a spring-mass-damper system that acted as a damped harmonic oscillator to provide an oscillating external load to allow for cyclic contractions of the muscle. Damped harmonic oscillators, by their nature, are only able to store and return or dissipate energy, and as a result, cannot be used to make the muscle behave like a brake. Therefore, the results of this study should be considered in the context of the power producing type of contractions that they were intended to simulate.

As a consequence of only examining power-producing contraction cycles where the muscle is primarily active during shortening, force depression had a far greater effect than force enhancement in this study. However, these history-dependent effects are particularly challenging to represent mathematically due to a lack of consensus on the features of, and mechanisms behind, these effects, particularly during cyclic contractions with non-constant activations and length changes. Although force enhancement following active lengthening has been reported at sub-maximal levels of activation during voluntary (Oskouei & Herzog, 2005, 2006b, 2006a; Pinniger & Cresswell, 2007; Altenburg et al., 2008; Seiberl et al., 2012, 2013) and electrically stimulated (Abbott & Aubert, 1952; Meijer, 2002) contractions, the relationship between level of activation and magnitude of force enhancement is still poorly characterized. Furthermore, Meijer (2002) found that the magnitude of force enhancement was lower for lower levels of activation, and Oskouei and Herzog (2006a) only observed this phenomenon at sub-maximal activation in a portion of their study sample. Therefore, we chose to use 50% of maximum activation for the given simulation as a threshold value to indicate the start of force enhancement. However, as the excitation is prescribed as a square wave, the activation rises and decays rapidly so this threshold value would have

little consequence on the magnitude of force enhancement for a whole cycle. We also chose to model force enhancement using a normalized elastic modulus that varied as a function of the instantaneous length at which this activation threshold was reached (Figure 3.3A). To determine this relationship, we assumed that the enhanced muscle force as a function of muscle length (Figure 3.3B) was linear and that the modulus depended only on the length where the activation threshold was reached and not on the current muscle length. However, further experimental studies examining force enhancement and depression during sub-maximal cyclic contractions are needed to determine if these assumptions are reasonable.

In this study, we chose to model force depression as a function of muscle work, consistent with experimental evidence (De Ruiter et al., 1998; Herzog et al., 2000; Kosterina et al., 2008, 2009) and previous model formulations (McGowan et al., 2010, 2013). However, force depression has been shown to depend on contraction speed (Maréchal & Plaghki, 1979; Meijer et al., 1997), and may decay during the period of time when the muscle is shortening (Till et al., 2014). More recently, Fortuna and colleagues (2018) found the magnitude of isometric, steady-state force depression following a stretch-shortening cycle to be independent of work. Thus, there is still debate as to whether or not force depression is accurately expressed as a function of only mechanical work.

To include force depression across muscle model scales it was necessary to non-dimensionalize the force depression effect (Equation (3.7)). Assuming force depression is work-dependent, the force would scale with muscle area, but work would scale with muscle volume in a similar manner to the mass scaling arguments discussed previously. Thus, a large muscle would generate a higher ratio of work to force, and at some limit, the contractile force would be depressed more than the force the muscle could generate. Hence, we assumed that the force depression per sarcomere would be independent of muscle size so that the force depression would result in an equivalent non-dimensional effect across muscle sizes. However, future experimental studies should be conducted to test the validity of this assumption.

Hill-type muscle models typically do not use muscle-specific parameters but rather use parameter values taken from different studies on single fibres that vary widely depending on the muscle, species, temperature, preparation method (skinned versus intact), and stimulation protocol. The geometric dimensions and intrinsic properties of the muscle models in this study were chosen to reflect typical or average values

reported in the literature so that our results could be more widely applicable than if we were to select values to represent a particular muscle. While we expect that our conclusions would hold if these parameter values were changed, this has not yet been evaluated and so should be considered when interpreting the results of this study.

Using computational muscle models in this study allowed us to change features of the muscle that are difficult or impossible to manipulate experimentally. Although doing so provided a means to explore theoretical questions about muscle design and performance across muscles of different sizes under a range of conditions, it also limited our ability to directly validate our models against empirical data. Although we would expect that including more parameters in the muscle model formulation would provide more accurate predictions of *in vivo* muscle behaviour, we have not explicitly tested this assumption. However, changing different model parameters, such as the fibre-type properties, led to changes in the muscle work and power output that were in a direction consistent with experimental evidence. Furthermore, the primary goal of this study was not to improve muscle model predictions, but rather to improve our understanding of the physiological mechanisms that may underlie muscle mechanical behaviour during cyclic contractions.

3.6 Conclusions

This study examined a range of contractile properties that may contribute to the work and power output of muscle during cycling contractions. In our simulations, substantial history-dependent effects occurred for the power-producing contractions in these simulations, and were dominated by the force depression effect that occurs during active shortening. Our results show that the mechanical behaviour of whole muscle during sub-maximal contractions depends on the fibre-type of the active fibres, even when the inertial effect of inactive muscle tissue is accounted for. There is an inertial cost to moving the tissue mass that results in reduced mass-specific work and power, and this is most pronounced for large muscles and low activations. This study shows that muscle mass contributes to the dynamics of the muscle tissue and that this effect is muscle size-dependent. Thus, muscle mass should be considered for a more complete understanding of muscle function during locomotor activities, where muscle activations are often sub-maximal and time-varying, muscles undergo unsteady cycles

of length change, and whole muscles may be much larger than the single fibres from which their intrinsic properties have been determined.

Chapter 4

Added mass in rat plantaris muscle causes a reduction in mechanical work

4.1 Abstract

Most of what we know about whole muscle behaviour comes from experiments on single fibres or small muscles that are scaled up in size without considering the effects of the additional muscle mass. Previous modelling studies have shown that tissue inertia acts to slow the rate of force development and maximum velocity of muscle during shortening contractions and decreases the work and power per cycle during cyclic contractions; however, these results have not yet been confirmed by experiments on living tissue. Therefore, in this study we conducted *in situ* work-loop experiments on rat plantaris muscle to determine the effects of increasing the mass of muscle on mechanical work during cyclic contractions. We additionally simulated these experimental contractions using a mass-enhanced Hill-type model to validate our previous modelling work. We found that greater added mass resulted in lower mechanical work per cycle relative to the unloaded trials in which no mass was added to the muscle ($p = 0.041$ for both 85% and 123% increases in muscle mass). We additionally found that greater strain resulted in lower work per cycle relative to unloaded trials at the same strain to control for length change and velocity effects on the work output, possibly due to greater accelerations of the muscle mass at higher strains. These results confirm that tissue mass reduces muscle mechanical work at larger muscle sizes, and that this effect is likely amplified for lower activations.

4.2 Introduction

The behaviour of whole muscle is fundamental to human and animal movement. However, due to the difficulty in measuring whole muscle function in larger animals, most of what we know about the intrinsic properties that dictate this behaviour

comes from studies on isolated preparations of single fibres or small muscles during controlled, maximal contractions. To predict the behaviour of larger whole muscles, we scale up these intrinsic properties of single fibres or small muscles as if we were scaling the force-length properties of a massless ideal spring to larger sizes (Zajac, 1989). As a result, the forces increase in proportion to the muscle's maximum isometric force (or cross-sectional area assuming constant maximum isometric stress) and the lengths and velocities increase in proportion to the muscle's length. This method of scaling, which is used in nearly all Hill-type muscle models (Zajac, 1989; Thelen, 2003; Millard et al., 2013), assumes that the same mechanisms that dictate the behaviour of a single fibre also dictate the behaviour of whole muscle of any size. In other words, we assume that the non-dimensional behaviour of a 15-kilogram elephant muscle is the same as that of a 1-milligram single fibre. Yet, when we compare the output of these models to experimental measures of whole muscle, Hill-type models tend to perform quite poorly, particularly under conditions that differ from that of the maximal, controlled contractions used to measure the muscle's intrinsic properties (Perreault et al., 2003; Dick et al., 2017). Therefore, this method of scaling that assumes whole muscles behave the same as giant single fibres likely does not account for all of the mechanisms that underlie whole muscle behaviour.

Unlike an ideal spring, fibres and whole muscles have mass, and while the effects of this mass may be negligible for single fibres or small muscles, this may not be true for larger muscles. As muscles increase in size, their potential to generate force increases in proportion to their cross-sectional area, and their mass increases in proportion to their volume. This results in greater internal loads for larger muscles relative to the force that they can produce at any activation; however, this difference becomes greater when muscle force potential decreases during submaximal contractions, which are most relevant to *in vivo* motor behaviors (Shiavi & Griffin, 1983; Gillis & Biewener, 2001; McGuigan et al., 2009; Tikkanen et al., 2013). The effect of these internal inertial loads depends not only on the magnitude of the tissue mass but also the acceleration of that mass. Therefore, tissue inertia likely has the largest effect during submaximal contractions when muscle forces are low, and during unsteady or higher frequency or strain cyclic contractions when accelerations of the tissue are greatest. However, because the intrinsic force-velocity properties of muscle are taken primarily from measures on fully active single fibres or small muscles that have little mass, and under conditions in which the fibre or whole muscle acceleration is zero, the effects of these internal loads are likely not accounted for in the Hill-type model formulation.

Ignoring the effects of muscle mass may therefore contribute to the discrepancies observed between Hill-type model predictions and experimental measures.

The effect of muscle tissue mass has rarely been studied and has primarily been provided only as a tentative explanation for experimental observations that could not be explained otherwise. In the late 1980s, Josephson and Edman compared the maximum shortening speed of fibre bundles to that of single fibres isolated from those same bundles and found that faster fibres contracted slower when they were within a fibre bundle than when they were in isolation. This result led the authors to suggest that faster fibres within whole muscle may contract slower because of the load provided by neighbouring fibres (Josephson & Edman, 1988). Prior to this, whole muscle was assumed to be able to contract as fast as the fastest fibre within the muscle (Hill, 1970). More recently, Holt and colleagues showed that whole rat plantaris muscle contracts slower when only a portion of the fibres in the muscle are active compared to when the muscle is fully active, even if the active portion is composed entirely of fast fibres (Holt et al., 2014). The authors suggested that this effect is due to the inactive muscle tissue providing resistance to slow the contraction speed of the active fibres. Studies using a Hill-type model that accounts for tissue mass (Günther et al., 2012) have supported this conclusion and shown that lower activation results in slower maximum contraction speeds (Ross & Wakeling, 2016), as does larger muscle mass (Meier & Blickhan, 2000; Böl & Reese, 2008; Ross & Wakeling, 2016). Further, larger muscle mass has also been shown to decrease the mechanical work done and power generated during cyclic contractions (Chapter 3).

Despite these results from modelling studies, the effects of muscle mass have not yet been confirmed by experiments on living tissue. Therefore, in this study we conducted *in situ* work-loop experiments on rat plantaris muscle to determine the effects of increasing the internal mass of muscle on contractile performance, specifically mechanical work output per cycle. We also simulated the *in situ* experimental conditions using the mass-enhanced Hill-type muscle model (Günther et al., 2012; Ross & Wakeling, 2016; Chapter 3) to validate the results of the previous modelling studies.

4.2.1 *In situ* experimental set-up

We collected data on the right plantaris muscle of 7 male Sprague Dawley rats (*Rattus norvegicus*, body mass: 416.3 ± 31.9 grams (mean ± s.d.), approx. age: 3-4 months, Charles River, Wilmington, MA, USA). All experiments were conducted at Harvard

University's Concord Field Station in Bedford, MA, USA in accordance with the guidelines of the FAS Institutional Animal Care and Use Committee of Harvard University and the University Animal Care Committee of Simon Fraser University. Rats were kept under isoflurane anesthetic, administered via a mask, for the duration of the experiment (3% induction, 1.5% maintenance). To allow us to externally stimulate the plantaris muscle, we placed a bipolar nerve cuff electrode around the sciatic nerve, which we accessed through the right lateral aspect of the thigh, and then cut the nerve proximal to the cuff to remove descending control of the muscle by the central nervous system.

To completely expose and isolate the plantaris muscle, we first opened and separated the skin and fascia of the medial aspect of the hindlimb from the underlying tissue using blunt dissection. We then cut the distal tendons of the medial and lateral gastrocnemii, soleus, tibialis anterior, and digit flexors and reflected those muscles to completely expose the plantaris and prevent effects from co-contraction of the surrounding musculature. To attach the muscle of interest to the servomotor (series 305B-LR, Aurora Scientific Inc., Aurora, ON, CA), we tied Kevlar thread at the myotendinous junction and secured the knot with cyanoacrylate gel to minimize the potential effects of series elasticity and knot slippage. We then cut the distal end of the plantaris tendon near the calcaneus and tied the thread to the lever arm of the servomotor to connect the muscle to the motor. To fix the proximal end of the muscle, we secured the right hindlimb of the rat to a stereotaxic frame with a femur clamp and anchored the right foot to a metal plate attached to the frame. We maintained the temperature of the muscle at approximately 30 °C using a heat mat and lamp and kept the exposed tissue moist by regularly applying saline solution with a syringe. Following the experiments, we euthanized the deeply anesthetized rats with an overdose (150 mg kg^{-1}) of intracardially-injected pentobarbital sodium.

4.2.2 Experimental conditions

To determine the effects of tissue mass on muscle mechanical work, we conducted work-loop experiments where the muscle underwent cyclic length changes coupled with bursts of excitation timed to the phase of the contraction cycle. The area inside the work-loop created when the time-varying muscle force is plotted against muscle length gives the net mechanical work of the muscle per cycle (consult Josephson (1985) for further details). Muscles can produce a variety of different work-loop shapes

depending on the requirements of the task and conditions of the external environment (Dickinson et al., 2000). In this study, we aimed to examine the effects of mass on muscle work during cyclic contractions in which the muscle behaves as a motor, with large positive work and a boxy counter-clockwise work-loop shape, to provide a comparison to our previous simulation work (Chapter 3). The mechanical work of a muscle depends on a number of factors, including the muscle's strain trajectory relative to its force-length properties, the muscle's velocity relative to its force-velocity properties, the pattern and phase of stimulation relative to the muscle's strain trajectory, and the cycle frequency (Josephson, 1993). To maximize mechanical work per cycle, we centred the muscle strain trajectory about optimal length, which we determined from the tetanic force-length relationship for each preparation, so that the muscle would produce high force by operating primarily on the plateau of its force-length curve. Additionally, we started stimulating the muscle slightly before the start of shortening (-5%), so that the muscle force would be high for the duration of the shortening phase (Johnson & Johnston, 1991; James et al., 1996). We also stimulated the muscle with a duty cycle of 0.4 so that the muscle would not be actively producing force during the lengthening phase of the cycle (Swoap et al., 1997). This resulted in a stimulation train duration of 200 ms for the 2 Hz frequency cycles (3 V supramaximal stimulus; 0.3 ms pulse width; 150 Hz pulse frequency; S48, Grass Technologies, West Warwick, RI, USA).

The effect of muscle mass on the mechanical work output of the muscle is due to a balance between the force the muscle can produce and the internal inertial loads it must accelerate. To manipulate this balance and alter the mass effects, we altered the muscle force, the magnitude of the internal muscle mass, and the muscle accelerations. To alter the muscle force, we conducted both active and passive work-loops, in which both the active and passive forces and only the passive forces contributed to the total muscle force, respectively. We used supramaximal stimulation for the active work-loops to activate all or nearly all of the muscle volume. Reducing the total muscle force by not activating the muscle should have a similar effect to reducing the active muscle force with submaximal contractions, where the work per cycle is lower due to relatively greater inertial loads (Chapter 3). To alter the accelerations of the muscle, we modified the strain amplitude of the sinusoidal trajectory that dictated the servomotor and muscle length changes during each trial. Increasing the magnitude of the muscle strain would increase the accelerations that the tissue mass experiences, and this in turn would alter the balance of internal forces and decrease the cyclic

work output of the muscle. Although increasing the frequency of the contraction cycles would produce a similar effect to increasing the muscle strain, we chose to keep frequency constant throughout the trials to control for reductions in muscle work that occur at higher frequencies due to longer activation and deactivation times relative to the duration of the cycle shortening phase (Caiozzo & Baldwin, 1997). To alter the mass properties of the muscle, we added effective mass by inserting an insect pin (no. 3; 0.5 mm diameter; stainless steel) through the cross-section of the muscle belly, midway along its length. This pin was fixed to one end of a movement arm that passively rotated depending on the force applied by the muscle to the pin 4.1. A weight could be attached to the other end of the movement arm opposite to the pin to increase the effective mass of the muscle beyond what the movement arm alone would exert. The hollow carbon fibre movement arm rested on a cone-shaped component to reduce the area of contact with the movement arm and minimize the effects of friction (Figure 4.7). We attached this set-up to add effective mass to the muscle to a micromanipulator on a magnetic stand (Kite Manual Micromanipulator and M10 Magnetic Stand, World Precision Instruments, Sarasota, FL, USA) to allow for fine adjustment of the position of the pin.

Each muscle underwent all combinations of two force conditions (active and passive), three strain conditions (±5%, ±7.5%, and ±10% relative to optimal length, resulting in total shortening strain of 10%, 15%, and 20%), and three mass conditions (unloaded, movement arm with no weight, and movement arm + 1.1 g weight, resulting in an effective added mass of 0%, 84.9 ± 7.5%, and 122.9 ± 10.8% muscle mass) twice for a total of 36 work-loops. We did not select the mean effective mass relative to the muscle mass but rather measured this value after the experiments were completed and the muscles were excised and weighed. We additionally conducted work-loop trials using a larger weight; however, this weight was unstable on the movement arm and so these results are not reported in this paper. We blocked the work-loop trials by mass condition to reduce damage to the muscle from adjusting the pin attached to the movement arm. We then randomized these mass condition blocks to control for order effects, except for the unloaded condition which always occurred first to avoid disturbing the pin once it was placed in the muscle. Within each mass condition block, we conducted six work-loop trials (two force conditions x three strain conditions) in random order. Between each work-loop trial containing five consecutive contraction cycles, we allowed the muscle to rest for five minutes, and between each block of work-loop trials, we conducted maximal tetanic contractions at optimal length to

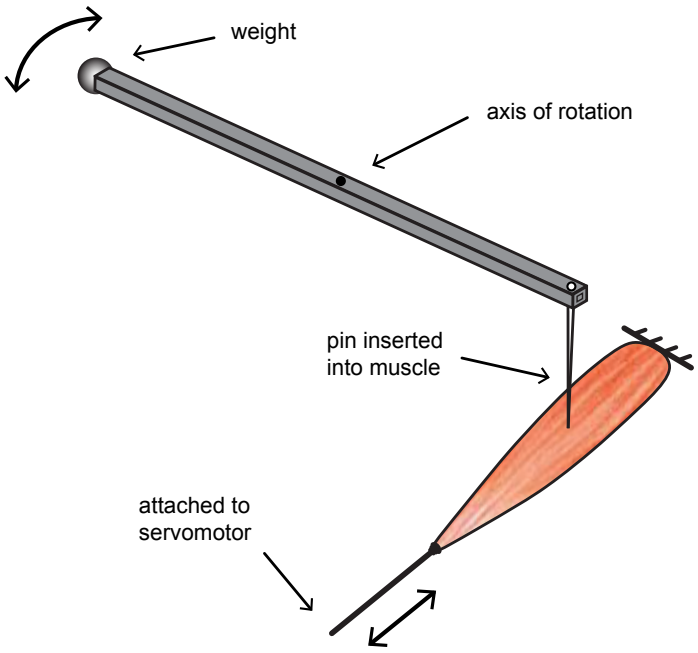

Figure 4.1: Set-up to add effective mass to the *in situ* plantaris muscles. To add mass to the muscle, we developed a system in which a 1.9 g, 14 cm long hollow carbon fibre rod rotated about a pivot. On one end of the rod we attached an insect pin which we inserted into the muscle midway along its length, and on the other end we could attach weights of different sizes to add effective mass to the muscle acting through the pin. The proximal end of the muscle was fixed by securing the hindlimb of the rat to a stereotaxic frame with a femur clamp, and the distal end was tied to the lever arm of a servomotor. Vascular supply to the muscle remained intact and we externally stimulated the sciatic nerve innervating the plantaris using a bipolar nerve cuff electrode.

monitor the extent of muscle fatigue over the duration of the experiments. After we completed all blocks of work-loop trials, we repeated the trials a second time in reverse order to further control for fatigue and order effects. We terminated the trials when we saw visual changes in work-loop shape due to fatigue, such as prolonged relaxation times (Stevens & Syme, 1989, 1993; Askew et al., 1997) and decreased ability of the muscle to maintain force during shortening (Askew et al., 1997; Wilson & James, 2004). Likely due to our relatively low cycle frequency (Stevens & Syme, 1993) and five-minute recovery periods between trials, we did not see indicators of these changes in our muscle preparations. Additionally, we inspected the muscles post mortem and found no evidence of discernable damage to the muscle tissue from the pin. For a visual of the experimental design, consult Figure 4.8 in the supplementary material.

4.2.3 Data collection and analysis

We measured output torque and position of the servomotor and the stimulus pulse delivered to the sciatic nerve in volts, and simultaneously generated the stimulus pulse at a sampling frequency of 4000 Hz using a custom-build virtual instrument and data acquisition board (IGOR Pro version 7.0.8.1, Wavemetrics, Lake Oswego, OR, USA; USB-6259, National Instruments, Austin, TX, USA). We filtered the output data using a 4th order Butterworth low-pass filter with a 55 Hz cut-off frequency and converted the output voltages to force (N) and length (m) using linear calibration curves. To determine the mechanical work per cycle of the muscle for each trial, we integrated the instantaneous mechanical power (product of muscle force and velocity) over the time duration of each cycle and then took the mean of the last three cycles. Then, to further control for the decrease in maximum muscle force over the duration of the experiments due to fatigue in addition to randomizing and repeating trials, we normalized the mean mechanical work for each active work-loop trial by the approximate maximum tetanic muscle force at the time of the trial using a linear interpolation of the maximum tetanic force from the control contractions that occurred between each block of work-loops (Figure 4.8) as a function of the trial number. While we did not observe any obvious changes in work-loop shape during the experiments, we did see a mean reduction in maximum isometric force of 22% across all rats. A typical plot of the maximum isometric force from the control tetanic contractions over the duration of the trials can be seen in Figure 4.9. We used a similar scheme to normalize the mechanical work from the passive work-loop trials but used the approximate passive force at optimal length at the time of the trial rather than the maximum tetanic force. Normalizing the mechanical work per trial by muscle force resulted in normalized work with dimensions of length, so we also normalized the work by the given muscle's optimal length to result in dimensionless work. Finally, we took the mean work from the two repeated trials so that there was only one independent sample for each rat for each condition in the analysis. We conducted all post-processing in Mathematica (version 12, Wolfram Research, Champaign, IL, USA).

4.2.4 Statistical analysis

To examine the effects of added mass and strain amplitude on the mean mechanical work per cycle, we conducted repeated measures analysis separately for active and passive trials using a linear mixed model fit using maximum likelihoods with the

function *lmer* in the package *lme4* (Bates et al., 2014) in R (version 3.6.1; R Core Team, 2019). In the model, we included dimensionless mechanical work as a continuous response variable, strain and mass as categorical fixed effects, and subject as a categorical random effect. We did not include an interaction effect between strain and mass as it did not improve the model fit on initial tests. To examine the pairwise differences in mean mechanical work across all strain and mass conditions, we used the Holm-Bonferroni method (Holm, 1979) within the package *multcomp* (Hothorn et al., 2008) to control for the increase in family-wise error rate with multiple comparisons. We repeated this same analysis but with the dimensionless work normalized to the unloaded condition at the same strain as the continuous response variable to examine how strain alters the effects of added mass. In this analysis, we excluded the unloaded 0% added mass condition as there was no variance in the normalized work for these trials. All experimental results are reported as mean ± standard error of the mean.

4.2.5 Muscle model and simulations

To validate the Hill-type model accounting for tissue mass used in Ross and Wakeling (2016) and Ross et al. (2018b; Chapter 3), and to confirm that our method of adding mass to the muscle is theoretically analogous to adding mass to the muscle model, we ran simulations with the mass-enhanced model to replicate the conditions of the *in situ* experiments in this study.

The mass-enhanced model used to predict the *in situ* muscle behaviour in this study has been described in detail elsewhere (Günther et al., 2012; Ross & Wakeling, 2016; Chapter 3). In brief, the model contains 16 point masses distributed evenly along the length of the muscle at rest to represent the mass of the muscle 4.2. The mass of each point mass is equal to the total mass of the muscle divided by the number of point masses. Between the point masses are Hill-type muscle segments that produce force as a function of their activation, length, and velocity. To model the intrinsic force-velocity and force-length properties of muscle segments, we used Bézier curves (Chapter 2) fit to experimental data from Roots et al. (2007) and Winters et al. (2011), respectively. Because the forces, lengths, and velocities in these curves are dimensionless, and we used maximum isometric force F_0, maximum intrinsic shortening velocity v_0, and optimal length L_0 values that were specific to rat plantaris muscle, we effectively only fit the dimensionless shape of the force-velocity and force-length curves. The model

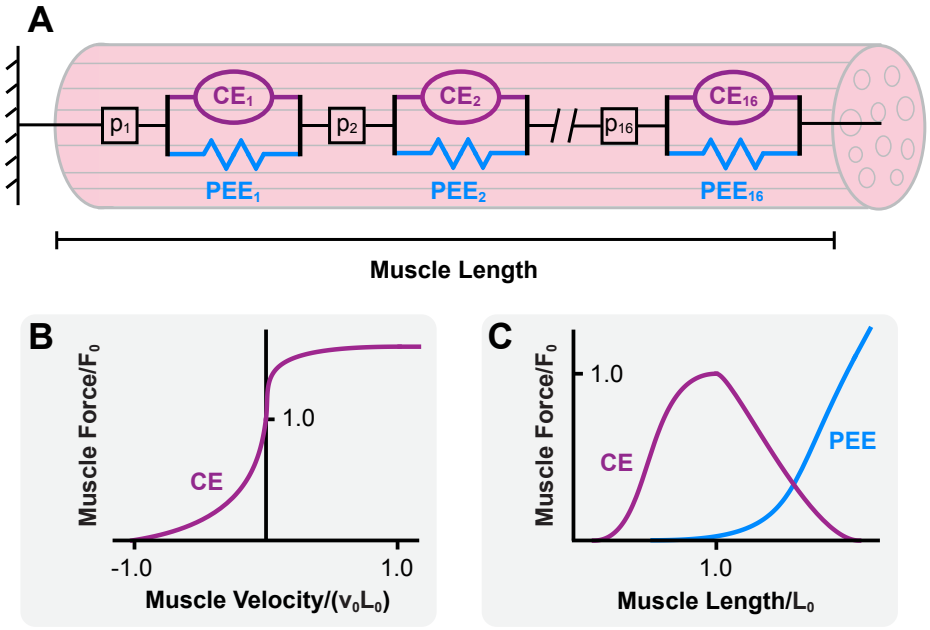

Figure 4.2: Muscle model used to simulate experimental contraction cycles. (A) The mass of the muscle was distributed along the length of the model in a series of 16 point masses (p_1 – p_{16}). The point masses were separated by Hill-type actuators that each contained a contractile element (CE) and parallel elastic element (PEE). The force of the CE was due to its force-velocity (B) and force-length (C; purple) properties and the force of the parallel elastic element depended on only its force-length properties (C; blue). The force-velocity and force-length properties were represented by Bézier curves developed in (Chapter 2) and fit to experimental data from Roots et al. (2007) and Winters et al. (2011), respectively. To replicate the *in situ* experimental work-loops, one end of the model was fixed and the other was constrained to follow a sinusoidal trajectory.

assumes that the muscle's fibres are arranged in parallel, and since we controlled for the effects of the tendon during the *in situ* experiments by tying off the Kevlar string connecting the muscle to the servomotor directly at the myotendinous junction, we did not include a series elastic element in the model formulation. The properties of the model, such as the maximum isometric force, optimal length, and rate of activation, were taken as the mean values obtained from the *in situ* experiments (Table 4.1).

To increase the mass of the muscle model, we added mass to the point mass that was located at the average position of the pin along the length of the *in situ* muscle. To mimic the work-loop conditions of the *in situ* experiments, we constrained the end of the muscle model to follow a sinusoidal trajectory, and for conditions where the muscle was producing active force, we introduced a square wave excitation-time trace

that reproduced the sciatic nerve stimulation in the experimental protocol. We then ran this excitation function through an excitation-activation transfer function (Zajac, 1989) to add delays between onset and peak activation and peak activation and complete deactivation. As in the *in situ* muscle experiments, we shifted the start of excitation 5% (25 ms) earlier in time relative to the start of shortening to maximize work per cycle. To examine the effects of muscle mass on the mechanical work of the muscle model, we replicated the *in situ* experimental conditions and varied the muscle force (active and passive), the effective mass added to the muscle model, and the strain amplitude of the contraction cycles. Due to our aim to minimize fatigue of the muscle preparations, in the experiments we were limited in the range of added mass and strain conditions we could examine. However, in the simulations we were able to extend the range of added masses to 400% muscle mass and strains to ±20% for a total shortening strain of 40%. We additionally ran simulations where the added mass was distributed evenly across all 16 point masses in the mass-enhanced model to confirm that the effects of adding mass to one point within the muscle are similar to distributing that added mass along the muscle's length. We conducted all simulations in Mathematica (version 12).

4.3 Results

The mean mass, optimal length L_0, maximum isometric force F_0, and activation rate constant τ_{act} of the muscles examined in this study can be found in Table S1. For the active work-loop experiments, we started stimulating the sciatic nerve 25 ms before the start of the shortening period (-5% relative phase) where the muscle reached its longest length. This resulted in the muscle reaching peak force close to the start of shortening and then maintaining high forces for the duration of the shortening phase of the cycle (Figure 4.3A). As a consequence of this behaviour, the mechanical work output per cycle of the muscle was positive and fairly large, resulting in counter-clockwise work-loops that resembled that of a motor (Figure 4.3A). To replicate this work-loop behaviour in the model simulations, we activated the muscle model using a time-varying excitation signal that was shifted in time so that, as with the *in situ* muscle experiments, the muscle excitation started 5% of the cycle duration before the start of the shortening phase. This resulted in simulated work-loops that were similar in shape to the experimental work-loop traces, except that the relaxation times were longer for the model simulations compared to the rat plantaris contractions (Figure

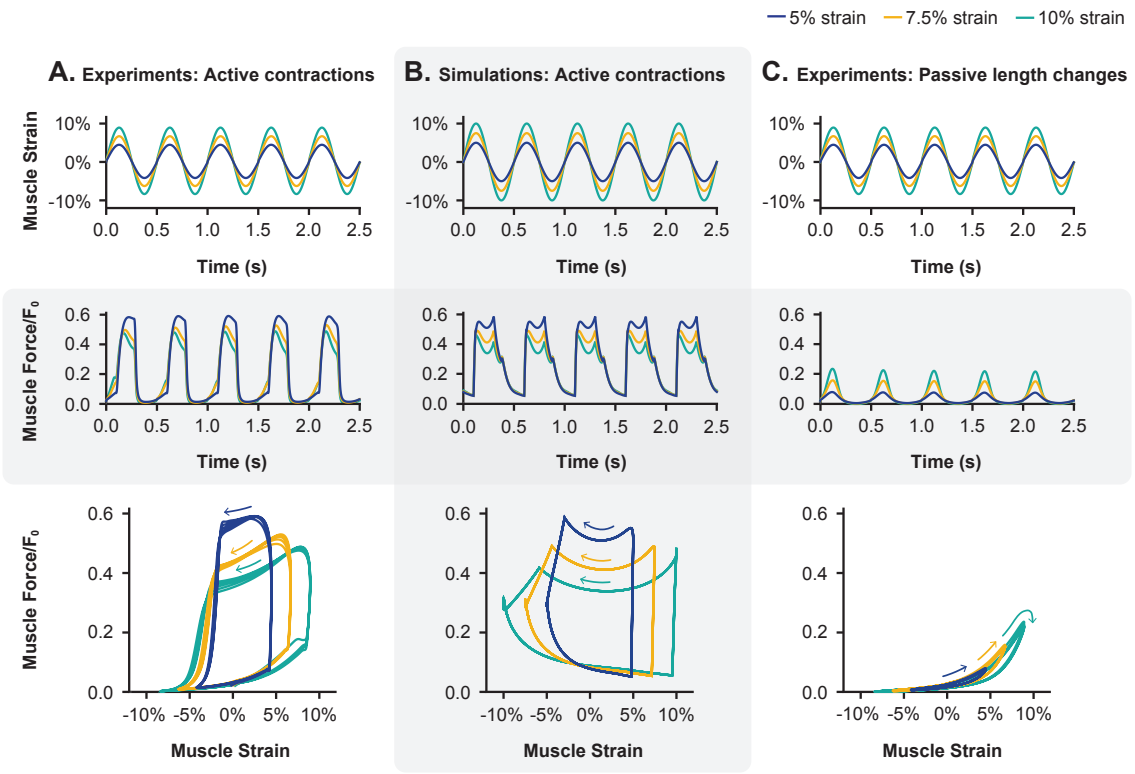

Figure 4.3: Sample raw traces for unloaded trials at different strains. Raw traces for active contractions from *in situ* experiments and simulations are shown in (A) and (B), respectively, and raw traces for passive simulations are shown in (C). The top row shows muscle strain over time, the middle row shows muscle force normalized to maximum isometric force (F_0) over time, and the bottom row shows the work-loops where normalized muscle force is plotted against muscle strain. The colour of the traces indicates the strain condition, where 5% strain is shown in dark blue, 7.5% is shown in yellow, and 10% strain is shown in teal. Muscle strain is defined as the change in muscle length from optimal length (L_0) expressed as a percentage of optimal length. The raw traces are taken from representative unloaded (0% added mass) trials in a single rat at the three different strains.

4.3B). We also conducted passive work-loop trials for the *in situ* experiments, in which the muscle length changes were identical to those for the active trials, except that the sciatic nerve was not stimulated and so active muscle force did not develop (Figure 4.3C). These passive trials resulted in negative absolute work per cycle.

We found that greater added mass resulted in lower mechanical work per cycle for the active *in situ* work-loop trials (main effect: $p = 0.021$; Figure 4.4A). There was a 4.5% ± 1.9% decrease in mean work per cycle between the unloaded (0% added mass) condition and the 85% added mass condition ($p = 0.041$). When we increased the added mass to 123% of the muscle mass, the work decreased by 4.7% ± 1.9%

relative to the unloaded condition ($p = 0.041$). We were unable to detect a difference in mechanical work per cycle between the 85% and 123% added mass conditions ($p = 0.889$). For work-loops simulated with the muscle model, we found that increasing the mass of the muscle decreased its mechanical work output per cycle, similar to the *in situ* experiments. However, the magnitudes of the differences between the mass conditions were much smaller (less than 1%) in the simulated contraction cycles compared to what we found for the *in situ* experiments, so we chose to geometrically scale the muscle by a factor of twenty-five as per (Chapter 2) to amplify these effects to within a comparable range of the experimental results. Because the geometric proportions of the model remained constant, muscle length scaled with the scaling factor, the cross-sectional area scaled with the square of the scaling factor, and the volume and tissue mass scaled with the cube of the scaling factor. As muscle maximum isometric force is proportional to the cross-sectional area, this scaling resulted in relatively larger muscle tissue mass relative to the maximum muscle forces. Conceptually, this scaling is akin to adding mass experimentally to the same size muscle. Further simulation results refer to this scaled model.

For simulations that mimicked the experimental set-up, where we added mass to the point mass closest to the average position of the pin inserted into the *in situ* muscle, we found that the mean mechanical work per cycle decreased by 1.7 and 2.4% for 85 and 123% added mass, respectively, across all three strain conditions (Figure 4.4B). For simulations where we evenly distributed the added mass across all 16 point masses in the model, we found that the mean work per cycle decreased by 0.9 and 1.2% for 85 and 123% added mass relative to the unloaded condition, respectively, across all three strain conditions (Figure 4.4C). For both these lumped and distributed added mass simulations, there was a greater reduction in mechanical work per cycle with greater cycle strain, and the magnitude of this work reduction was greater for the lumped added mass simulations that mimicked the set-up of the *in situ* experiments. For the passive *in situ* work-loops where the nerve innervating the muscle was not stimulated, we were unable to detect an effect of added mass on mean mechanical work per cycle ($p = 0.078$; Figure 4.6A).

For the active *in situ* work-loop trials, we found that greater cycle strain led to greater work; however, when the work for each condition was normalized to the unloaded (0% added mass) condition at the same strain, we found that greater cycle strain resulted in lower mean mechanical work per cycle for the added mass conditions (main effect: $p = 0.003$; Figure 4.5A). Comparing between conditions, we found that mean work

per cycle relative to the unloaded trials decreased by 4.8% ± 1.4% between the 5 and 10% strain conditions ($p = 0.002$) and 1.8% ± 1.4% between the 5 and 7.5% strain conditions; however, this difference was not significant ($p = 0.204$). Additionally, we were unable to detect a significant difference between the 7.5 and 10% strain conditions ($p = 0.071$). For the model simulations where the added mass was lumped near the centre of the muscle, we found that mean work per cycle relative to unloaded decreased by 1.1 and 3.6% for 7.5 and 10% strain, respectively, across the 85 and 123% added mass conditions (Figure 4.5B). For both the simulations where the added mass was lumped and where it was distributed along the muscle's length, we found a greater reduction in work per cycle with greater strain relative to the unloaded condition (Figure 4.5B,C). This reduction in work was greater in the lumped added mass simulations, except for the highest (20%) strain where we found the work reduction to be greater for the distributed mass simulations (Figure 4.5C). As with the mass effects, we were unable to detect an effect of strain on the muscle mechanical work per cycle relative to the unloaded trials for the passive *in situ* work-loops where the muscle was not activated ($p = 0.834$; Figure 4.6B).

4.4 Discussion

Most studies that examine the contractile properties of skeletal muscle focus on single fibres, fibre bundles, or small muscles for which the effects of muscle tissue inertia are largely negligible. As a consequence, we often assume that whole muscles behave as a scaled version of these single fibres or fibre bundles without considering the effects of the additional muscle tissue mass. However, modelling studies have shown that accounting for muscle mass can act to decrease maximum shortening velocities (Meier & Blickhan, 2000; Böl & Reese, 2008; Ross & Wakeling, 2016) and mechanical work per cycle (Chapter 3). While muscle mass can alter the behaviour of smaller or maximally active muscles, these effects are amplified by submaximal activation levels (Ross & Wakeling, 2016) and scaling muscle to larger sizes (Günther et al., 2012; Ross & Wakeling, 2016; Chapter 3). Despite these findings, as with any mathematical model, the models used in these studies are only a representation of the actual system of interest. Consequently, it is important to confirm that these mass effects occur in real muscle. Therefore, in this study we examined the effects of muscle tissue mass on the mechanical work per cycle of *in situ* rat plantaris muscle during both active and passive cycles of muscle length change (Figure 4.3). To alter the effects of tissue inertia,

we added effective mass to the muscle (Figure 4.1) and we also varied the amplitude (strain) of the contraction cycles. The effects of tissue inertia depend on the magnitude of mass as well as the acceleration of that mass. Increasing the effective mass of the muscle acting through the pin and increasing the amplitude of the sinusoidal length changes increase the inertial loads within the muscle by increasing the magnitude of the mass and its acceleration, respectively. We hypothesized that an increase in internal inertial loads would decrease net muscle force and, therefore, the work that the muscle would generate over a contraction cycle.

4.4.1 Mass effects in active contractions

We found that for active work-loop trials of the *in situ* muscle, the mean mechanical work per cycle decreased by 4.5% and 4.7% for an increase in effective mass of 85 and 123%, respectively (Figure 4.4A). Although increasing the effective mass of muscle by 85 and 123% may seem quite large, these magnitudes are fairly small relative to the effective mass of inactive tissue that acts as an inertial load on actively contracting tissue during submaximal contractions. At the around 20% activation levels that muscles typically operate at during daily locomotion, such as level walking (Shiavi & Griffin, 1983; Gillis & Biewener, 2001; McGuigan et al., 2009; Tikkanen et al., 2013), the remaining inactive 80% of the muscle tissue would exert an inertial load with 400% effective mass against which active muscle fibres must contract. Increasing the effective mass by 85 and 123% during maximal contractions, as we did in this study, in theory represents inertial loads applied to the actively contracting muscle as if approximately 54 and 45%, respectively, of the muscle tissue were active (% active mass/(% active mass + % inactive or added mass), e.g. $100/(100 + 85) \approx 54$). Therefore, the reductions in muscle work with greater added mass that we found in this study likely underestimate the reductions in work due to the inertia of inactive tissue that occur during daily activities.

In this study, we initially simulated the experimental contraction regimes using a Hill-type muscle model that accounts for tissue mass (Figure 4.2C), where the dimensions of the muscle model were identical to those taken from the mean dimensions of the experimental muscle (a scale of 1). However, while these simulations resulted in lower work per cycle for greater mass, the magnitude of these effects were much smaller than what we saw for the *in situ* experiments. Therefore, we chose to scale the muscle model to a larger size (geometrically by a factor of 25) to amplify the mass effects to

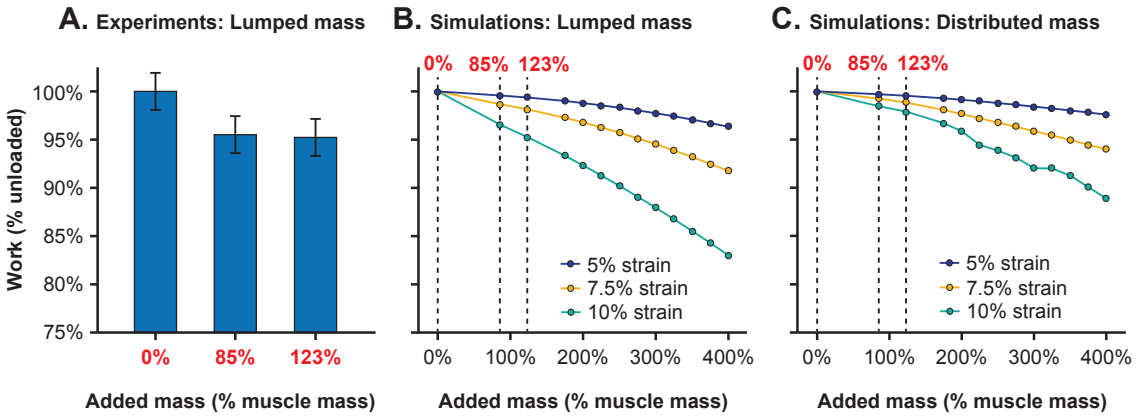

Figure 4.4: Mass effects in active contractions. (A) The effect of added mass on normalized mean mechanical work per cycle ($p = 0.021$) expressed as a percentage of the unloaded condition ($n = 7$). Using post-hoc analysis we were able to detect a difference between the 0 and 85% conditions ($p = 0.041$) and the 0 and 123% conditions ($p = 0.041$) but not between the 85 and 123% added mass conditions ($p = 0.889$). The error bars in (A) show standard error of the means from the post-hoc analysis. Normalized mean work per cycle for lumped and distributed added mass simulations are shown in (B) and (C), respectively. Each point in (B) and (C) represents the work per cycle from a single simulation, for which we used the mean properties of the experimental muscles ($n = 7$) as input parameters for the model. 5% strain is shown in dark blue, 7.5% is shown in yellow, and 10% is shown in teal. Added mass is expressed as a percentage of the mean muscle mass across all rats.

within the same order of magnitude as the experimental results. By doing so, we were able to determine if added mass resulted in the same pattern of effects on work for the *in situ* experiments as for the simulations. Additionally, the experimental conditions did not span the full range of mass effects that could be expected physiologically, and so the model provided a means to explore the more complete physiological range. For these scaled simulations with the added mass lumped as a point mass closest to the mean position of the pin inserted into the *in situ* muscle, we found that work decreased by 1.7 and 2.4% for 85 and 123% added mass, respectively, compared to the unloaded condition (Figure 4.4B).

Potential differences between the intrinsic properties of the muscle model and the *in situ* rat plantaris muscle may have led to smaller reductions in work with greater added mass for the rat plantaris scale simulations compared to the *in situ* work-loop trials. First, because we did not measure the intrinsic force-velocity or full force-length properties of the *in situ* muscles in this study to minimize fatigue, and because no complete data sets are available describing these properties of the rat plantaris over

the entire physiological range of muscle lengths (short to long) and velocities (shortening and lengthening), we fit the force-length and force-velocity curves (Chapter 2) to data from rabbit tibialis anterior muscle (Winters et al., 2011) and intact rat flexor hallucis brevis fibre bundles (Roots et al., 2007), respectively. Therefore, these fitted curves may not entirely reflect the intrinsic properties of the rat plantaris. However, because we normalized the muscle and fibre bundle forces, lengths, and velocities before we fit the intrinsic curves to the data (Figures 4.2B,C), and used F_0, L_0, and v_0 values that were specific to rat plantaris muscle in the model (Table 4.1), the fitted force-velocity and force-length curves likely did not vary substantially from that of the experimental muscles. Second, we did not incorporate history-dependent effects, such as force enhancement due to active lengthening (Abbott & Aubert, 1952; Cavagna & Citterio, 1974; Edman et al., 1982; Morgan et al., 2000; Herzog, Duvall, & Leonard, 2012) and force depression due to active shortening (Abbott & Aubert, 1952; Maréchal & Plaghki, 1979; Meijer et al., 1998; Herzog et al., 2000; Morgan et al., 2000) in our model formulation. Because these history-dependent effects are thought to be due to mechanisms at the crossbridge level (Herzog, Duvall, & Leonard, 2012) and are not directly affected by the dynamics of muscle mass, their exclusion from the model formulation likely did not alter the main conclusions of the modelling results. Third, we determined only the activation rate constant in the Zajac (1989) excitation-activation transfer function from the experimental data. To determine the deactivation rate constant, we used a ratio β between the activation and deactivation rate constants of 0.6 (Dick et al., 2017), which resulted in prolonged relaxation times for the muscle model (Figure 4.3B) relative to the rat plantaris muscles (Figure 4.3A). However, while increasing β decreased the model relaxation times and resulted in work-loops that were closer in shape to the *in situ* muscle work-loops, changing β did not alter the added mass effects. Therefore, these features of the mass-enhanced muscle model likely did not contribute to the smaller reductions in work with greater added mass for the rat plantaris scale simulations compared to the *in situ* work-loop trials.

One-dimensional (1D) Hill-type muscle models fail to account for the three-dimensional (3D) shape and architecture of muscle, and this may have contributed to the discrepancy between the simulated and measured mass effects. When a muscle contracts and shortens it must bulge in width and thickness in order to maintain nearly constant volume (Baskin & Paolini, 1967). In pennate muscle, where the muscle fibres are oriented at an angle relative to the muscle line-of-action, the fibres can also rotate to

greater angles as the muscle contracts (Gans & Bock, 1965; Fukunaga et al., 1997; Maganaris et al., 1998; Azizi et al., 2008; Randhawa et al., 2013). Because muscle fibres can rotate, they can shorten at different speeds relative to the muscle belly in a process known as architectural gearing (Azizi et al., 2008). The rat plantaris, examined here, is considered unipennate with a fibre pennation angle of 15-16 degrees (Roy et al., 1982; Eng et al., 2008) relative to the muscle line-of-action at rest. Therefore, muscle shape change (e.g. bulging in thickness and width) and architectural gearing likely influenced the cyclic work-loop contractions studied in our experiments. However, the mass-enhanced Hill-type model we used to simulate these contraction regimes is 1D and so only accounts for the muscle dynamics and kinematics along the muscle's length and does not account for the effects of tissue mass in other directions. Studies using 3D finite element models of muscle have shown that accounting for the effects of tissue mass in 3D can reduce maximum shortening velocity (Meier & Blickhan, 2000; Böl & Reese, 2008) and mechanical work per cycle (Chapter 3), similar to our previous 1D simulation results (Ross & Wakeling, 2016; Chapter 3). While no direct comparisons have yet been made between the magnitudes of the mass effects in 1D versus 3D, accounting for the effects of tissue mass in all directions, even in parallel-fibred muscles, would likely further reduce muscle work output per cycle, as greater internal work would be done to accelerate the tissue mass in transverse directions as the muscle shortens. The effects of tissue mass could be altered further in pennate muscle where the fibres can rotate relative to the line-of-action as well as change length. In our experiments, inserting the pin through the muscle along the plane perpendicular to the aponeuroses could have, to some extent, restricted changes in muscle shape and fibre rotations and altered the mechanical work output that we measured during the *in situ* experiments. Given these considerations, further work is needed to understand the 3D effects of tissue mass on whole muscle behaviour.

To confirm that adding mass to one point within the muscle results in similar effects to having that same added mass distributed along the muscle's length, we conducted additional simulations with the mass-enhanced Hill-type model but distributed the added mass evenly across all 16 point masses in the model. These simulations resulted in smaller mass effects compared to when the added mass was lumped into a single point mass midway along the muscle's length (Figure 4.4B,C). While the mass of real muscle is continuous throughout its volume, we had to discretize the mass in our model using a series of point masses to approximate the dynamics of the system. While increasing the number of point masses gives a closer approximation to

the behaviour of the continuous mass, the computational time substantially increases and, beyond 16 point masses, the increased accuracy from more point masses becomes insignificant (Günther et al., 2012). For our *in situ* rat plantaris experiments, we added effective mass to only a single location midway along the muscle's length to avoid altering the integrity of the muscle tissue. Therefore, the lumped added mass simulations and *in situ* experiments provide a coarse approximation of the change in inertial effects due to increasing muscle mass or decreasing activation during submaximal contractions. While the distributed added mass simulations better approximate the effects of continuous mass distributed throughout the volume of a muscle, few if any real muscles have their volume or mass distributed evenly along their length. Studies quantifying muscle architecture of human leg muscles using magnetic resonance imaging have shown that muscle cross-sectional area is largest towards the midpoint along the muscle's length and then tapers off towards the proximal and distal ends, but the location of this largest cross-sectional area differs between muscles (Fukunaga et al., 1992; Morse et al., 2007; Erskine et al., 2009; Cotofana et al., 2010; Maden-Wilkinson et al., 2013) and can change with active contraction (Hodgson et al., 2006). The inertia of inactive tissue during submaximal contractions are also likely not distributed evenly along the muscle's length due to regional variations in muscle activation (English, 1984; Pratt & Loeb, 1991; Boggs & Dial, 1993; Schieber, 1993; Soman et al., 2005; Wakeling, 2008; Kinugasa et al., 2011; Hodson-Tole et al., 2013). Thus, the complexity of the inertial properties of *in vivo* muscle are likely not entirely captured by either the lumped or distributed added mass simulations.

4.4.2 Strain effects in active contractions

The mechanical work performed by a muscle over a contraction cycle depends on the pattern of muscle force in relation to the length change. If force is produced during shortening, increasing the cycle strain amplitude may be expected to increase work per cycle. However, because greater strain amplitude at constant cycle frequency increases the average shortening velocity of the muscle, greater strain could alternatively decrease work by decreasing muscle force due to force-velocity effects (Hill, 1938). Therefore, maximal work per cycle typically occurs at intermediate cycle strains (Josephson, 1985; Josephson & Darrell, 1989; Askew & Marsh, 1997). We found here that greater cycle strain led to greater mean absolute work per cycle, indicating that the rat plantaris was operating at small enough strains where reductions in force due to faster shortening speeds did not outweigh increases in work due to

greater length change. In this study we were interested in using strain to manipulate the effects of inertia on muscle work by altering the accelerations of the muscle tissue and added effective mass. We expected that increasing the strain amplitude imposed by the servomotor would increase the accelerations of the muscle tissue mass and decrease mechanical work output per cycle. Indeed, we found that this was the case for the active contraction cycles when work was normalized to the unloaded (0% added mass) condition at the same strain to control for length change and velocity effects on the work output (Figure 4.5).

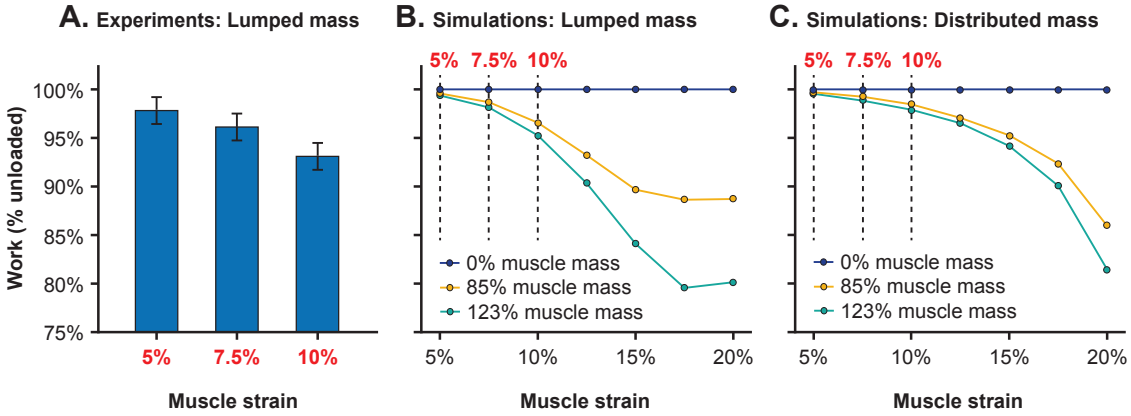

Figure 4.5: Strain effects in active contractions. (A) The effect of muscle strain on normalized mean mechanical work per cycle relative to the unloaded condition at the same strain ($p = 0.003$; $n = 7$). Using post-hoc analysis we were able to detect a difference between the 5 and 10% strain conditions ($p = 0.002$), but not between the 5 and 7.5% conditions ($p = 0.204$) or between the 7.5 and 10% conditions ($p = 0.071$). The error bars in (A) show standard error of the means from the post-hoc analysis. Normalized mean work per cycle for lumped and distributed added mass simulations are shown in (B) and (C), respectively. Each point in (B) and (C) represents the normalized work per cycle from a single simulation where we used the mean properties of the experimental muscles ($n = 7$) as input parameters for the model. 0% added mass is shown in dark blue, 85% is shown in yellow, and 123% is shown in teal. Muscle strain is defined as the change in muscle length from optimal length (L_0) expressed as a percentage of optimal length.

Studies comparing Hill-type model predictions to *in situ* and *in vivo* muscle force measures show that these massless one-dimensional models perform best during slow, maximal contractions and are least accurate when predicting faster, submaximal contractile conditions. Perreault and colleagues (2003) compared Hill-type forces to *in situ* cat soleus forces during contractions that mimicked *in vivo* length trajectories and found that errors exceeded 50% when the muscle strains were large and motor unit firing rates were low. Millard and coworkers (2013) showed that Hill-type model errors increased when predicting *in situ* cat soleus muscle forces during submaximal

contractions (Perreault et al., 2003) compared to maximal contractions (Krylow & Sandercock, 1997). Similar results have been reported for larger animals: Wakeling and others (2012) found that the correlations between predicted and measured forces of *in situ* goat medial gastrocnemius were lower for lower stimulus frequency, and Dick and colleagues (2017) showed that Hill-type prediction errors of human medial and lateral gastrocnemius forces during cycling were lowest for low speed, high force contractions and increased with higher cadences. The results of the present study, along with our previous simulation work (Ross & Wakeling, 2016; Chapter 3), indicate that the effects of muscle mass are greatest during the higher strain and submaximal contractions where traditional massless Hill-type models perform the worst. Therefore, accounting for tissue mass may be a promising avenue to improve the predictive power of these widely used muscle models.

In this study we only examined sinusoidal length changes with supramaximal nerve stimulus to activate all or nearly all of the muscle fibres. We also used a stimulus duty cycle of 0.4 so that the muscle would generate active force for the majority of the cycle shortening phase to maximize work output. However, muscle behaviour during *in vivo* contraction cycles can vary widely depending on the muscle and the task. Therefore, further work is needed to investigate how tissue inertia alters the behaviour of muscle across a wider range of activation and muscle length change patterns.

4.4.3 Passive muscle length changes

We were unable to detect an effect of either mass or strain during the passive work-loop trials (Fig. 6). Given that the magnitudes of work we measured during the cycles of passive length change were small relative to the magnitudes of work during the active contractions, it is likely that the effects of mass and strain under passive conditions were too small to detect given the variability among subjects and experimental noise in the data. When we simulated the passive work-loop conditions with the mass-enhanced muscle model, the point masses within the model oscillated at much higher frequencies than the cycle frequency, indicating that the system was unstable. This was not an issue for simulations involving active contractions because the concentric portion of the force-velocity relationship provides damping to stabilize the system and prevent the high frequency oscillations of the point masses. In contrast, because the passive force of the muscle segments between the point masses depended only on

length, there were no velocity-dependent damping effects to stabilize the model point masses during the passive work-loop simulations.

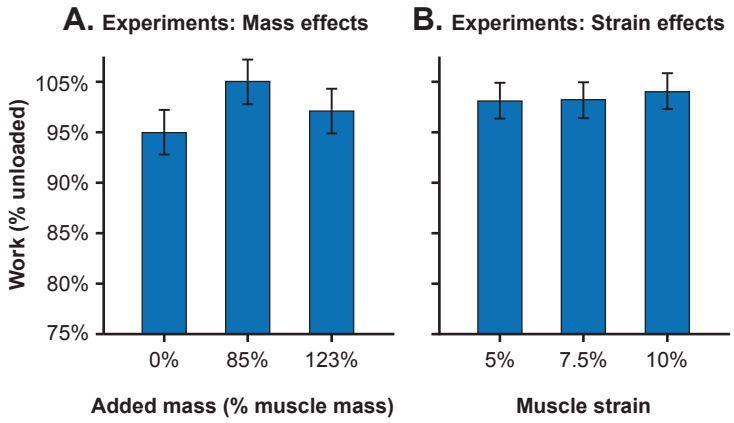

Figure 4.6: Mass and strain effects on passive *in situ* muscle. Mean normalized work per cycle relative to unloaded across added mass and strain conditions is shown in (A) and (B), respectively. We were not able to detect a significant effect of either mass ($p = 0.078$) or strain ($p = 0.834$) on the mean work per cycle normalized to the unloaded condition at the same strain for the passive work-loop trials ($n = 7$). The absolute work per cycle was negative for all passive trials, so mean work relative to unloaded greater than 100% indicates that the absolute work was negative and larger in magnitude than that for the unloaded condition. Error bars show standard error of the mean from the post-hoc analysis.

Viscous (velocity-dependent) damping has been described or discussed in studies of skeletal muscle (Gasser & Hill, 1924; Levin & Wyman, 1927; Heerkens et al., 1987; Syme, 1990; Best et al., 1994), as well as a range of other biological tissues, including cardiac muscle (Templeton & Nardizzi, 1974; Templeton et al., 1974), aponeuroses and tendons (Lieber et al., 2000; Maganaris & Narici, 2005), and fat (Chan & Titze, 1998; Schoemaker et al., 2006). Without the effects of viscosity, muscle would behave as a non-linear spring during passive length changes and return as much energy during shortening as it stores during lengthening. However, all of the passive work-loops in this study resulted in negative work per cycle (Figure 4.3C), indicating that energy was likely dissipated due to viscous damping. Except for a few studies that have incorporated viscous damping in parallel to the contractile element of muscle models to mimic the effects of viscosity within muscle tissue (Hatze, 1977; Günther et al., 2007), or to improve the numerical stability of the modelling computations and satisfy the balance of in-series forces between muscle and tendon (Millard et al., 2013), the effects of viscosity are typically neglected in the formulation of Hill-type muscle models. While viscous damping alone may have a negligible effect on muscle output

forces, lengths, and velocities, it could play an important role in dissipating energy and stabilizing the mass of *in vivo* muscle tissue.

4.4.4 Conclusions

The purpose of this study was to determine the effects of altering the mass of *in situ* muscle on mechanical work during cyclic contractions. We found a statistically significant main effect of added mass on mechanical work per cycle. The condition with the greatest added mass resulted in the lowest work relative to the unloaded condition. We additionally detected a significant main effect of cycle strain, with the greatest strain condition resulting in the lowest work relative to the unloaded condition. We were able to replicate similar results to those of the *in situ* experiments in simulations of the mass-enhanced Hill-type model, but the magnitude of these effects was smaller. Because of the difficulty of measuring whole muscle function in living animals, we often rely on Hill-type muscle models to predict and understand whole muscle behaviour. However, these models, that rarely account for the effects of muscle mass, have limited accuracy when predicting faster, higher strain and submaximal contractions where the effects of muscle mass are likely greatest. Therefore, accounting for muscle mass may be a promising avenue to improve the predictive power of Hill-type muscle models and improve our understanding of whole muscle function in living animals.

4.5 Supplementary material

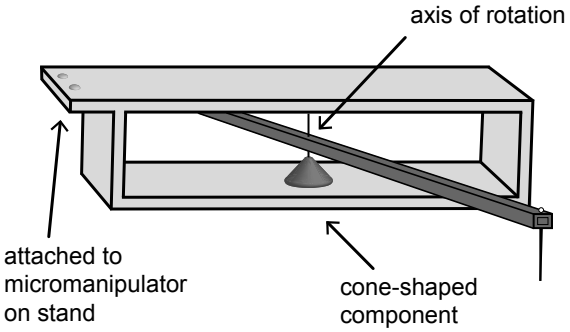

Figure 4.7: Design details of the set-up to add effective mass to the rat plantaris muscles. The carbon fibre rod rested on a cone-shaped component to reduce the area of contact between the component and the rod and minimize the effects of friction. We inserted a pin through the rod and cone to support and allow for passive rotation of the movement arm. We secured this set-up to a micromanipulator on a stand so that we could make fine adjustments to the position of the pin when inserting the pin into the rat plantaris muscles.

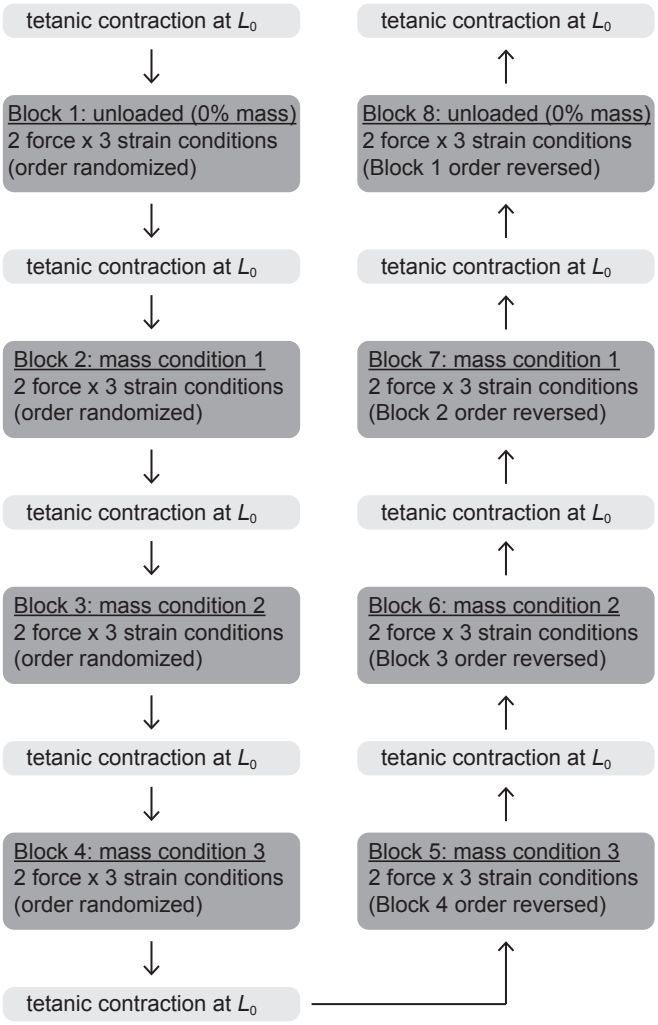

Figure 4.8: Flow diagram of the experimental trials. Each muscle underwent all combinations of the two force, three strain, and three mass conditions twice for a total of 36 work-loops. We blocked the work-loop trials by mass condition to reduce damage to the muscle from adjusting the pin attached to the movement arm. We randomized the order of the conditions within each trial and the order of the blocks within each experiment, except for the unloaded condition which always occurred first to avoid disturbing the pin once it was placed in the muscle (Block 1). We repeated Blocks 1-4 in reverse order to further control for order and fatigue effects (Blocks 5-8), and also conducted maximal tetanic contractions at optimal length L_0 to monitor the extent of muscle force drop over the duration of the experiments.

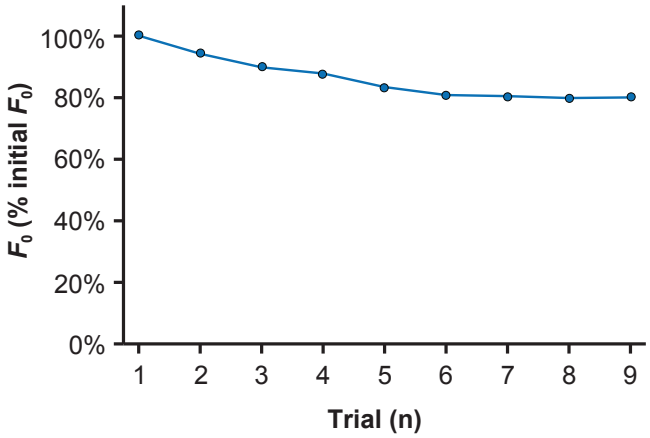

Figure 4.9: Reduction in maximum isometric muscle force F_0 over the duration of a representative experiment. We determined F_0 for each maximum tetanic contraction at optimal length that we conducted between each block of work-loops. F_0 is plotted against trial number and is expressed as a percentage of the initial L_0 at Trial 1.

Table 4.1: Muscle model parameter definitions, values, and sources.

Parameter	**Value**	**Source**
Muscle mass	5.71 x 10^{-4} kg (±5.49 x 10^{-5} kg)	Mean (s.d.) of experimental data
Optimal length, L_0	4.03 x 10^{-2} m (±2.10 x 10^{-3} m)	Mean (s.d.) of experimental data
Maximum isometric force, F_0	4.89 N (±1.70 N)	Mean (s.d.) of mean of first and last tetanic control contractions at L_0 for each rat
Activation rate constant, τ_{act}	3.30 x 10^{-2} s (±5.74 x 10^{-3} s)	Mean (s.d.) of values determined by fitting excitation-activation transfer function from Zajac (1989) to experimental twitches
Ratio between τ_{act} and deactivation rate constant, β	0.6	Dick et al. (2017)
Maximum intrinsic shortening velocity, v_0	5 s^{-1}	Approximated from Swoap et al. (1997) (4.48 s^{-1})
Location of added mass in lumped added mass simulations	9^{th} point mass from fixed end (56% of muscle length)	Closest point mass to mean of experimental data

Table 4.2: Mechanical work data for the experimental work-loop trials. The first column contains the rat identification number, the second column contains the force condition, the third column contains the added mass condition expressed as a mean percentage of the muscle mass across all rats, and the fourth column contains the strain amplitude expressed as the change in muscle length (ΔL_{m}) relative to optimal length (L_0). The final column contains the mean work values calculated over the last three cycles per trial and the two repeated trials (see Fig. S2). The mean work is dimensionless and normalized to L_0 for each rat, as well as the trial-varying maximum isometric force F_0 and passive force at L_0 for the active and passive force trials, respectively. We treated the rat identification number, force condition, added mass condition, and strain amplitude as categorical predictor variables in the statistical analysis, and we treated the mechanical work as a continuous response variable.

Rat	**Force condition**	**Mass condition (% muscle mass)**	**Strain condition $\pm\Delta L/L_0$**	**Mean work (dimensionless)**
67	active	85	0.05	0.037505077
67	active	85	0.075	0.043385166
67	active	85	0.1	0.043902879
69	active	85	0.05	0.03391169
69	active	85	0.075	0.03641887
69	active	85	0.1	0.032646523
70	active	85	0.05	0.043594129
70	active	85	0.075	0.053396042
70	active	85	0.1	0.057617127
71	active	85	0.05	0.038386622
71	active	85	0.075	0.048872741
71	active	85	0.1	0.044683968
72	active	85	0.05	0.028052619
72	active	85	0.075	0.031496283
72	active	85	0.1	0.03191401
74	active	85	0.05	0.043191216
74	active	85	0.075	0.055500994
74	active	85	0.1	0.057142656
75	active	85	0.05	0.046028037
75	active	85	0.075	0.056429282
75	active	85	0.1	0.059557703
67	active	123	0.05	0.037349666

Continued on next page

Table 4.2 – *Continued from previous page*

Rat	**Force condition**	**Mass condition (%muscle mass)**	**Strain condition $\pm\Delta L/L_0$**	**Mean work (dimensionless)**
67	active	123	0.075	0.042900917
67	active	123	0.1	0.043098728
69	active	123	0.05	0.033016527
69	active	123	0.075	0.032615227
69	active	123	0.1	0.032446271
70	active	123	0.05	0.043047635
70	active	123	0.075	0.053357753
70	active	123	0.1	0.056055207
71	active	123	0.05	0.041029364
71	active	123	0.075	0.04740685
71	active	123	0.1	0.047688016
72	active	123	0.05	0.028183772
72	active	123	0.075	0.031090163
72	active	123	0.1	0.030986062
74	active	123	0.05	0.045035563
74	active	123	0.075	0.056248564
74	active	123	0.1	0.058379592
75	active	123	0.05	0.043054498
75	active	123	0.075	0.058134446
75	active	123	0.1	0.05991716
67	active	0	0.05	0.037259843
67	active	0	0.075	0.044869281
67	active	0	0.1	0.044522062
69	active	0	0.05	0.032838984
69	active	0	0.075	0.035924233
69	active	0	0.1	0.037535752
70	active	0	0.05	0.043880845
70	active	0	0.075	0.054478824
70	active	0	0.1	0.05873498
71	active	0	0.05	0.046905908
71	active	0	0.075	0.053749609
71	active	0	0.1	0.052151549

Continued on next page

Table 4.2 – *Continued from previous page*

Rat	**Force condition**	**Mass condition (%muscle mass)**	**Strain condition** $\pm\Delta L/L_0$	**Mean work (dimensionless)**
72	active	0	0.05	0.027621163
72	active	0	0.075	0.032472811
72	active	0	0.1	0.033362881
74	active	0	0.05	0.046498161
74	active	0	0.075	0.055978972
74	active	0	0.1	0.064367157
75	active	0	0.05	0.043528375
75	active	0	0.075	0.059372975
75	active	0	0.1	0.060763282
67	passive	85	0.05	-0.043908995
67	passive	85	0.075	-0.095919248
67	passive	85	0.1	-0.183118269
69	passive	85	0.05	-0.040532523
69	passive	85	0.075	-0.094623171
69	passive	85	0.1	-0.183036739
70	passive	85	0.05	-0.039337627
70	passive	85	0.075	-0.082123567
70	passive	85	0.1	-0.149483263
71	passive	85	0.05	-0.046351291
71	passive	85	0.075	-0.099298614
71	passive	85	0.1	-0.179323325
72	passive	85	0.05	-0.042069309
72	passive	85	0.075	-0.081870644
72	passive	85	0.1	-0.151085754
74	passive	85	0.05	-0.044199135
74	passive	85	0.075	-0.086593185
74	passive	85	0.1	-0.153660888
75	passive	85	0.05	-0.039849505
75	passive	85	0.075	-0.083653601
75	passive	85	0.1	-0.153175166
67	passive	123	0.05	-0.042820057
67	passive	123	0.075	-0.096369171

Continued on next page

Table 4.2 – *Continued from previous page*

Rat	**Force condition**	**Mass condition (%muscle mass)**	**Strain condition** $\pm\Delta L/L_0$	**Mean work (dimensionless)**
67	passive	123	0.1	-0.180893826
69	passive	123	0.05	-0.032003026
69	passive	123	0.075	-0.085034322
69	passive	123	0.1	-0.15552494
70	passive	123	0.05	-0.038397464
70	passive	123	0.075	-0.08617331
70	passive	123	0.1	-0.145781365
71	passive	123	0.05	-0.044877615
71	passive	123	0.075	-0.099051412
71	passive	123	0.1	-0.177402441
72	passive	123	0.05	-0.044152974
72	passive	123	0.075	-0.087238378
72	passive	123	0.1	-0.15800527
74	passive	123	0.05	-0.036478634
74	passive	123	0.075	-0.084017161
74	passive	123	0.1	-0.140531378
75	passive	123	0.05	-0.039661492
75	passive	123	0.075	-0.085573766
75	passive	123	0.1	-0.156193005
67	passive	0	0.05	-0.038582447
67	passive	0	0.075	-0.08684778
67	passive	0	0.1	-0.165074792
69	passive	0	0.05	-0.037927554
69	passive	0	0.075	-0.090784819
69	passive	0	0.1	-0.169845226
70	passive	0	0.05	-0.036518289
70	passive	0	0.075	-0.079259127
70	passive	0	0.1	-0.142179488
71	passive	0	0.05	-0.044736211
71	passive	0	0.075	-0.096906173
71	passive	0	0.1	-0.170977102
72	passive	0	0.05	-0.03820753

Continued on next page

Table 4.2 – *Continued from previous page*

Rat	**Force condition**	**Mass condition (%muscle mass)**	**Strain condition** $\pm\Delta L/L_0$	**Mean work (dimensionless)**
72	passive	0	0.075	-0.078835332
72	passive	0	0.1	-0.137998688
74	passive	0	0.05	-0.0435985
74	passive	0	0.075	-0.085020501
74	passive	0	0.1	-0.15061893
75	passive	0	0.05	-0.039715632
75	passive	0	0.075	-0.087700603
75	passive	0	0.1	-0.153446542

Chapter 5

The energy of muscle contraction: Kinetic energy during dynamic contractions

5.1 Abstract

During muscle contraction, chemical energy is converted to mechanical energy when ATP is hydrolysed during cross-bridge cycling. This mechanical energy is then distributed and stored in the tissue as the muscle deforms or is used to perform external work. We previously showed how energy is distributed through contracting muscle during fixed-end contractions; however, it is not clear how the distribution of tissue energy is altered by the kinetic energy of muscle mass during dynamic contractions. In this study we conducted simulations of a 3D continuum muscle model that accounts for tissue mass, as well as force-velocity effects, in which the muscle underwent sinusoidal work-loop contractions coupled with bursts of excitation. We found that increasing muscle size, and therefore mass, increased the kinetic energy per unit volume of the muscle. In addition to greater relative kinetic energy per cycle, relatively more energy was also stored in the aponeurosis, and less was stored in the base material, which represented the intra and extracellular tissue components apart from the myofibrils. These energy changes in larger muscles due to greater mass were associated lower mass-specific mechanical work output per cycle, and this reduction in mass-specific work was greatest for smaller initial pennation angles. When we compared the effects of mass on the model tissue behaviour to that of *in situ* muscle with added mass during comparable work-loop trials, we found that greater mass led to lower maximum and higher minimum acceleration in the longitudinal (x) direction near the middle of the muscle compared to at the non-fixed end, which indicates that greater mass contributes to tissue non-uniformity in whole muscle. These comparable results for the simulated and *in situ* muscle also show that this modelling framework behaves in ways that are consistent with experimental muscle. Overall, the results of

this study highlight that muscle mass is an important determinant of whole muscle behaviour.

5.2 Introduction

Skeletal muscles are the motors that drive human and animal locomotion. Yet despite their fundamental importance, our understanding of whole muscle behaviour is relatively limited due to practical and ethical considerations that hinder accurate *in vivo* measures. To estimate the behaviour of whole muscle, measures of single fibres, fibre bundles, or small whole muscles during controlled, maximal contractions are often extrapolated to larger sizes by scaling the forces with cross-sectional area and the lengths and velocities with optimal length (Zajac, 1989). Because the effects of mass in maximally-active single fibres or fibre bundles are likely negligibly small, the effects of muscle mass are not accounted for in this common method of scaling. As a consequence, muscle mass is not accounted for in estimates of larger whole muscle behaviour where the effects of mass are likely not negligible.

Muscle mass is also important for understanding whole muscle behaviour in small animals, particularly when the muscle is contracting submaximally. Josephson and Edman (1988) examined the maximum shortening speed of different fibre-types and found that fast fibres contract slower when within a fibre bundle than when in isolation. The authors suggested that the load of surrounding bundle fibres acts to slow the maximum contraction speed of the fast fibres. More recently, Holt and colleagues (2014) found that whole rat plantaris muscle reaches slower maximum contraction speeds when submaximally compared to maximally active, regardless of the fibre-type composition of the active tissue. The authors suggested that inactive tissue during submaximal contractions may act to slow the maximum speed of active fibres. This conclusion was supported by a simulation study that used a mass-enhanced Hill-type muscle model to replicate the contractile conditions in Holt et al. (2014) and showed that the mass of inactive fibres slows the maximum contraction speeds of whole muscle (Ross & Wakeling, 2016).

Due to challenges in experimentally manipulating muscle mass and controlling for differences in geometry and architecture across animals of different sizes, most of our understanding of the effects of muscle mass is from simulations using one-dimensional (1D) Hill-type models that account for distributed tissue mass. These studies have

shown that the greater mass of larger muscles decreases the rate of muscle force development (Günther et al., 2012) and maximum contraction velocity (Ross & Wakeling, 2016) compared to smaller muscles. More recently, we showed that greater muscle mass decreases the mass-specific mechanical work and average power per cycle during cyclic contractions (Chapter 3), a finding we later supported with *in situ* experiments on rat plantaris muscle (Chapter 4). However, when we compared the experimental results to simulations of the mass-enhanced 1D Hill-type model, we found that the reductions in mass-specific work were greater for the experimental compared to the simulated muscle. It may be that the three-dimensional (3D) structure of the *in situ* muscle contributed to this discrepancy between the experimental and simulated mass effects.

Although whole muscles are often modelled as 1D, 3D tissue structure has important implications for muscle mechanical behaviour. When muscles contract and shorten in length, they bulge in width or depth to maintain a nearly constant volume (Zuurbier & Huijing, 1993; Böl et al., 2013; Randhawa & Wakeling, 2015), which causes energy to be stored in the tissue as it deforms (Wakeling et al., 2020). Because muscle tissue displaces in transverse directions during contraction, muscle tissue mass can be accelerated transversely, unlike in 1D mass-enhanced Hill-type models where displacements, velocities, and accelerations can only occur in the longitudinal direction. While studies using 3D continuum muscle models have shown that muscle mass decreases the rate of force development (Böl & Reese, 2008), maximum shortening speed (Meier & Blickhan, 2000; Böl & Reese, 2008), and mass-specific mechanical work per cycle (Chapter 3), it is not clear if these changes in output muscle behaviour are related to changes in tissue energy storage and distribution as a consequence of muscle mass.

In the first two papers in this series (Wakeling et al., 2020; Ryan et al., 2020), we showed that the internal energy distribution through muscle tissue is related to the 3D behaviour of whole muscle, but to date the role of internal kinetic energy has not been considered. Muscle has internal kinetic energy during dynamic contractions, due to the presence and velocity of distributed tissue mass. In this study we explore how muscle mass and its kinetic energy influence how energy is distributed through whole pennate muscle tissue, and how this energy distribution is related to 3D tissue deformations, as well as the mechanical work done during cyclic contractions. To accomplish this, we simulated cyclic contractions of a 3D continuum muscle model with bursts of activation timed to sinusoidal length changes to mimic the experimental

work-loop paradigm (Josephson, 1985). We examined the distribution of tissue energy and external mechanical work per cycle across a range of strain amplitudes, maximum excitations, and initial fibre pennation angles. To qualitatively validate the effects of muscle mass and strain amplitude on contractile behaviour, we additionally compared the tissue accelerations in the model to data collected on *in situ* rat plantaris muscle during comparable work-loop trials.

5.3 Methods

5.3.1 3D muscle model

To explore the role of muscle mass on the distribution of tissue energy and external work done by muscle during contraction, we used a 3D continuum model of whole muscle that accounts for distributed tissue mass. We modelled the muscle as a fibre-reinforced composite biomaterial, in which the model fibres represented the contractile elements, or myofilaments of the muscle fibres. These fibres were embedded in a base or background material that represented the additional tissue within and surrounding the muscle fibres, including the extracellular matrix, connective tissue, fat, and blood. The muscle model fibres only generated force along their length and the base material acted in all directions, which resulted in an overall anisotropic response of the muscle tissue.

We modelled the muscle fibre stress using a similar formulation as a 1D Hill-type model, in which the fibre stress depended on the active stress-stretch, active stress-strain rate, and passive stress-stretch relationships. We modelled the muscle base material as a non-linear and isotropic elastic material such that the base material stress depended only on the passive stress-stretch properties (Yeoh, 1993). As for the magnetic resonance imaging-derived geometries in Wakeling and colleagues (2020), we accounted for the effects of aponeuroses on whole muscle behaviour. We modelled the aponeurosis tissue as a fibre-reinforced composite biomaterial in which the embedded fibres represented collagen fibers and only generated passive stress, unlike the activatable muscle fibers. The aponeurosis base material acted as an isotropic non-linear elastic material that was stiffer than the muscle base material. For a more detailed description of the tissue material properties used in our model, consult Wakeling et al. (2020).

Our previous 3D muscle model (Wakeling et al., 2020) was quasistatic and did not account for the effects of muscle mass, or the effects of local strain rate on muscle fibre force. In addition to considering the stress-strain rate effects to the muscle fibre response (Chapter 3) we also consider the kinetic and internal energies, and account for the external work done on the system. Note that both the kinetic and internal energies depend on the velocity, unlike our previous model in Wakeling et al. (2020) and Ryan et al. (2020) which assumed quasistatic deformations. The equations for the momentum and mass balance are described in the Appendix and detailed in Ogden (1984). The Hill-type stress-stretch and stress-strain rate relations cannot be obtained through standard variations of the energy; instead, these relations are used to define the constitutive laws. We use the energy as a post-processed quantity, consistent with our approach in Wakeling et al. (2020) and Ryan et al. (2020).

We approximated the solutions of the momentum and mass balance equations (see section 5.6 Appendix) using a semi-implicit time-stepping method in which we post-processed the velocity based on the implicit computation of the displacement, pressure, and dilation via the finite element method, similar to our previous approach (Wakeling et al., 2020).

5.3.2 Muscle model geometries

We constructed the root muscle geometry to represent the approximate size and proportions of a human medial gastrocnemius muscle (Randhawa et al., 2013). The muscle fibres were oriented in the xz plane with an initial pennation angle α_0 of 20° relative to the bottom (-z) aponeurosis (Figure 5.1). This resulted in a pennation angle β_0 of 15.3° relative to the -x axis or the longitudinal direction. In this paper we varied the angle of the geometry with α_0 of the fibres, unlike in Wakeling and colleagues (2020) and Ryan and others (2020) in which we varied β_0 of the fibres within blocks of muscle tissue. To vary α_0 from the root geometry, we varied the initial fibre length and kept the initial aponeurosis length, aponeurosis thickness, muscle length in the x direction, and muscle width in the y direction constant. We examined geometries with α_0s of 15, 20, 25 and 30°, which resulted in β_0s of 11.5, 15.3, 19.0, and 22.7°. See Table 5.1 for definitions of all variables used in the main text and Table 5.2 for details of the initial dimensions of the muscle geometries.

To explore the effects of muscle mass across a range of muscle sizes, we geometrically scaled the human medial gastrocnemius-sized geometries to 2.5 and 3.5 times the

Table 5.1: Symbols and definitions of variables in the main text.

Symbol	Definition
$\mathbf{u}$	displacement vector
ψ	strain energy-density
$\overline{\psi}$	mean strain energy-density
$\overline{\psi}_{\text{apo}}$	mean aponeurosis strain energy-density
$\overline{\psi}_{\text{muscle,base}}$	mean muscle base material strain energy-density
$\overline{\psi}_{\text{muscle,act}}$	mean muscle active strain energy-density
$\overline{\psi}_{\text{muscle,pas}}$	mean muscle passive strain energy-density
$\overline{\psi}_{\text{muscle,vol}}$	mean muscle volumetric strain energy-density
$\overline{\psi}_{\text{kin}}$	mean kinetic energy-density
$\hat{e}_{\text{max}}$	normalized maximum excitation
α_0	pennation angle relative to bottom aponeurosis in the initial configuration
β_0	pennation angle relative to x-axis in the initial configuration
$\overline{\beta}$	mean pennation angle relative to x-axis in the current configuration
$\overline{\lambda}_{\text{tot}}$	total mean fibre stretch
l	muscle length
ε_{max}	maximum strain amplitude of sinusoidal muscle length changes
F_{x}	force in x-direction on $+x$ face of bottom (-z) aponeurosis
W^*	mass-specific mechanical work per cycle
a_{mid}	relative acceleration in the x-direction over time of a quadrature point near the middle of the model or of the pin inserted near the middle of the *in situ* muscle
a_{end}	relative acceleration in the x-direction over time at the end of the model or the *in situ* muscle
$a_{\text{max,end}}$	maximum a_{end} for a given simulation or experimental trial
$a_{\text{max,mid}}$	maximum a_{mid} for a given simulation or experimental trial
$a_{\text{min,end}}$	minimum a_{end} for a given simulation or experimental trial
$a_{\text{min,mid}}$	minimum a_{mid} for a given simulation or experimental trial

size (length scale factor or "scale") to approximate the behaviour of muscles in larger animals (Alexander et al., 1981). This resulted in initial muscle lengths, widths, and thicknesses that varied with the scale, areas that varied with the scale-squared, and volumes that varied with the scale-cubed. Because the initial density was constant at 1060 kg m^{-3} (Mendez & Keys, 1960), muscle mass (including that of the aponeurosis) also varied with the scale-cubed, as with the volume. This method of scaling

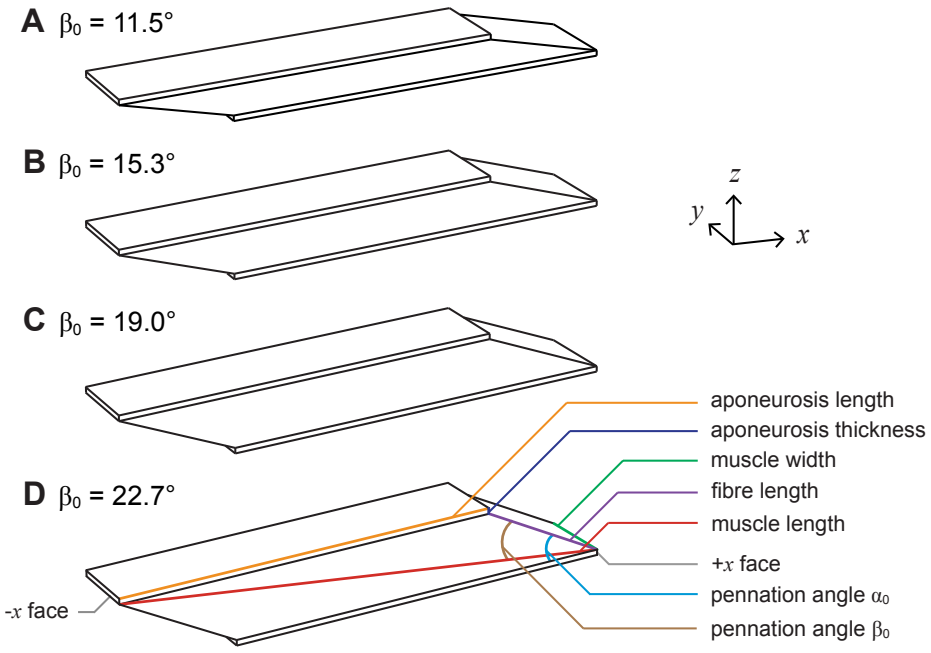

Figure 5.1: Muscle geometries. We simulated muscle with initial pennation angles relative to the bottom aponeurosis α_0 of 15° (A), 20° (B), 25° (C), and 30° (D), which resulted in initial angles relative to the -x axis β_0 of 11.5°, 15.3°, 19.0°, and 22.7°. To vary α_0, we altered the initial fibre length and kept the aponeurosis length, aponeurosis thickness, muscle width, and muscle length constant.

is described in more detail in Ross and colleagues (Chapter 2), although the scale 1 geometry in this study is the approximate size of a human medial gastrocnemius, whereas in our previous studies it was the size of a fibre bundle (Chapter 2; Chapter 3).

5.3.3 Simulations and post-processing

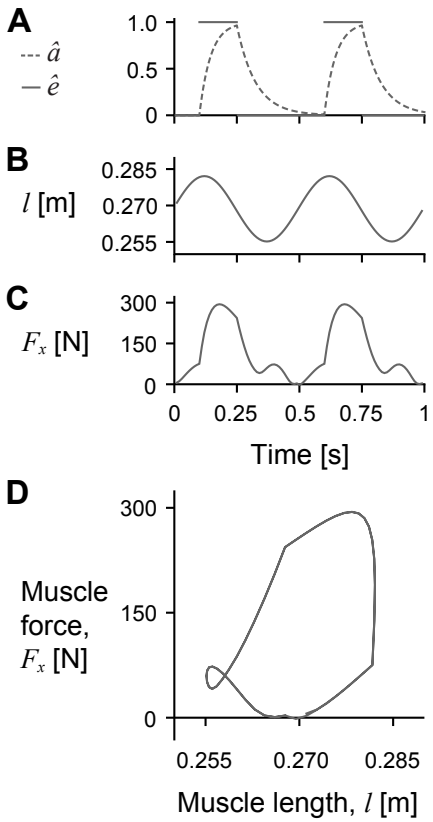

Figure 5.2: Sample raw simulation traces. Raw traces of normalised excitation $\hat{e}$ (solid lines) and activation $\hat{a}$ (dashed line) over time (A), muscle length l over time (B), muscle force F_{x} over time (C), and F_{x} over l in which the area inside the loop represents the mechanical work per cycle (D) for a representative simulation with a cycle strain amplitude of 5%, maximum normalised excitation of 1, initial pennation β_0 of 15.3°, and scale of 1.

We simulated cyclic work-loop regimes of the muscle model in which the total muscle length followed a sinusoidal trajectory timed with bursts of excitation (Josephson, 1985). To achieve the sinusoidal length changes, we fixed the -x face of the top ($+z$) aponeurosis in all directions and applied a non-zero Dirichlet boundary condition to the $+x$ face of the bottom (-z) aponeurosis to constrain it to follow a sinusoidal trajectory in the x direction and remain fixed in the z and y directions. All other surfaces of the model remained unconstrained throughout the simulations. To mimic the nerve stimulation in *in situ* work-loop experiments, we cyclically excited the muscle using a square wave excitation trace where the excitation was either 0 or the maximum excitation $\hat{e}_{\mathrm{max}}$ (Figure 5.2). Note that we chose to use $\hat{e}_{\mathrm{max}}$ to represent the maximum excitation instead of u_{max} from our previous work (Chapter 2; Chapter 3) to

avoid confusion with the displacement $\mathbf{u}$. We then converted the excitation to activation using the excitation-activation transfer function from Zajac (1989). As with typical work-loop experiments, we excited the muscle with only one burst of excitation per length cycle such that both the sinusoidal length changes and excitations had a frequency of 2 Hz. To match the experimental data collected on *in situ* muscle (described later), each excitation burst started 5% in time before the start of shortening and continued for 30% of the length cycle duration (duty cycle of 0.3). These contractile conditions resulted in the muscle generating active force primarily while shortening. For β_0 of 11.5, 19.0, and 22.7°, we set $\hat{e}_{\max}$ to 1 and the maximum strain amplitude $\boldsymbol{\varepsilon}_{\max}$ to 5% of resting optimal length for a total shortening strain of 10%. For β_0 of 15.3°, we also examined submaximal activation with $\hat{e}_{\max}$ of 0.4 in addition to maximal activation with $\hat{e}_{\max}$ of 1. We also examined $\boldsymbol{\varepsilon}_{\max}$ of 2.5% and 7.5% in addition to 5% for β_0 of 15.3°to explore how $\boldsymbol{\varepsilon}_{\max}$ alters the effects of muscle mass during cyclic contractions.

To quantify the energy distribution through the muscle tissue, we used the strain energy-density ψ which is the strain energy per unit volume of tissue in J m^{-3}. ψ is given at each quadrature point in the model, so to determine the total mean ψ for the whole muscle $\overline{\psi}$, we used the sum of the ψs at each point weighted by the volume fraction of the given point relative to the whole muscle (aponeurosis and muscle) volume. The total strain energy-density of the muscle was comprised of the aponeurosis $\overline{\psi}_{\text{apo}}$, muscle base material $\overline{\psi}_{\text{muscle,base}}$, active muscle fibre $\overline{\psi}_{\text{muscle,act}}$, passive muscle fibre $\overline{\psi}_{\text{muscle,pas}}$, volumetric $\overline{\psi}_{\text{muscle,vol}}$, and kinetic $\overline{\psi}_{\text{kin}}$ strain energy-densities. We defined $\overline{\psi}_{\text{apo}}$ as the sum of the aponeurosis fibre (passive only), volumetric, and base material strain energy-densities and $\overline{\psi}_{\text{kin}}$ as the sum of the aponeurosis and muscle kinetic strain energy-densities.

We calculated the muscle mechanical work per cycle in J as the integral of the x-component of the force perpendicular to the $+x$ face of the bottom aponeurosis F_{x} over the muscle length l for one cycle. We defined l as the distance in the x-direction between the -x face of the top aponeurosis and the $+x$ face of the bottom aponeurosis (Figure 5.1). Because larger muscles with larger cross-sectional areas and longer lengths will have greater work per cycle, we normalised the mechanical work per cycle in J by the mass of the given geometry to give the mass-specific mechanical work per cycle W^* in J kg^{-1}. We calculated the mass of each geometry as the product of the initial total volume in m^3 (muscle and aponeurosis) and the initial density of 1060 kg m^{-3}.

To determine how the muscle fibre stretches and pennation angles changed with scale and β_0, we examined the total mean fibre stretch $\overline{\lambda}_{tot}$ and mean current fibre angle relative to the -x axis $\overline{\beta}$ throughout each simulation. We calculated $\overline{\lambda}_{tot}$ as the sum of the fibre stretches at each quadrature point weighted by the volume fraction of the given point relative to the total muscle volume, and $\overline{\beta}$ as the mean fibre angle relative to the -x axis.

To explore changes in the uniformity of tissue behaviour with greater muscle scale and ε_{max}, we examined tissue accelerations in the x direction near the middle of the muscle compared to at the non-fixed end. To determine the tissue accelerations near the middle of the muscle, we identified the quadrature point closest to the middle of the geometry in the x, y, and z directions in the initial configuration and then tracked the position of that point in the x-direction throughout each simulation. We then fitted a Fourier series function with three harmonics to the position-time data, which we normalised to the distance from the fixed end to the centre quadrature point at rest (approximately $0.5 \times l$), and took the second time derivative of the fitted function to estimate the acceleration amid in s^{-2}. We repeated this same process to determine the tissue accelerations at the moving end of the muscle aend (+x face of -z aponeurosis), except we normalised the position data to the muscle length at rest. For a massless spring undergoing cyclic length changes, the acceleration in the x-direction in m s^{-2} would be smallest near the fixed end of the spring and largest near the moving end. If the acceleration was then normalised to the distance at rest between the fixed end and the location where the acceleration was measured, the acceleration in the x-direction in s^{-2} would be the same near the fixed end and middle as at the end of the spring. Thus, for cyclic muscle contractions a difference between a_{mid} and a_{end} indicates that the muscle tissue behaviour is not uniform along its length. Because we compared the simulation acceleration results to that of the *in situ* experiments, we only quantified a_{mid} and a_{end} for simulations with β_0 of 15.3°, as rat plantaris muscle has a pennation angle of approximately 15-16°at rest (Roy et al., 1982; Eng et al., 2008). We also only examined simulations with $\hat{e}_{max}$ of 1, as the *in situ* muscles were maximally excited during the work-loop trials.

5.3.4 Experimental data collection

We compared the model tissue accelerations during the simulations to previously unpublished data collected on *in situ* muscle as part of a larger study (Chapter 4). All

experiments were conducted in accordance with the guidelines of the Faculty of Arts and Sciences Institutional Animal Care and Use Committee of Harvard University and the University Animal Care Committee of Simon Fraser University. We examined the effect of adding mass to the right plantaris muscle of 7 Sprague Dawley rats (Rattus norvegicus; body mass: 416.3 ± 31.9 grams (mean ± SD); Charles River, Wilmington, MA, USA). For details of the experimental preparation and surgery, consult Ross and colleagues (Chapter 4). In brief, the animals were kept deeply anaesthetised for the duration of the experiments. We isolated and separated the plantaris muscle from underlying tissue and then cut the distal plantaris tendon and tied the distal end of the muscle to a movement arm on a servomotor (series 305B-LR; Aurora Scientific Inc.; Aurora, ON, CA). The proximal end of the muscle remained attached to the femur through the proximal tendon, and we fixed the femur using a stereotaxic frame and femur clamp. To externally stimulate the muscle, we placed a bipolar cuff electrode around the sciatic nerve and then severed the nerve proximal to the cuff to remove descending nervous control.

To alter the mass properties of the *in situ* muscle, we inserted a pin into the muscle midway along its length. This pin was attached to a movement arm, and at the other end of the arm, we attached different size weights to add effective mass to the muscle acting through the pin. We used a photodiode LED pair to track the position of the movement arm and therefore the position of the pin inserted into the muscle. We added two different effective masses to the plantaris muscles: movement arm with no weight and movement arm + 1.1 g weight, resulting in mean ± SD effective masses of 84.9 ± 7.5%, and 122.9 ± 10.8% muscle mass, respectively. As for the model simulations, we conducted work-loop trials in which we constrained the muscle length to follow a 2 Hz sinusoidal trajectory, and we supramaximally stimulated the muscle via the sciatic nerve to fully activate the muscle tissue. In addition to altering the effective mass added to the muscle, we also varied the $\varepsilon_{\max}$ of the sinusoidal muscle length trajectories (5%, 7.5% and 10% of optimal length).

5.3.5 Experimental data analysis

We filtered the output photodiode data using a 4th order Butterworth low-pass filter with a 55 Hz cut-off frequency and converted the output voltages to positions using a calibration curve. As with the simulation data, we fit Fourier series with three harmonics to discrete samples of the pin position and the end of the muscle for each

trial and took the second derivative of this function with respect to time to estimate the accelerations at the pin near the centre and at the end of the muscle. The pin and end accelerations were normalised using the distance between the proximal end of the muscle that was attached to the femur and the pin at rest and the muscle length at rest, respectively. The mean ± SD distance between the distal end of the muscle and the pin at rest was 16.4 ± 2.7 mm, and between the proximal and distal ends of the muscle (muscle length) at rest was 40.3 ± 2.1 mm. We denoted the pin acceleration as a_{mid} and the acceleration at the moving end as a_{end} to provide a comparison with the simulation results.

To examine the effects of added mass and ε_{max} on internal tissue accelerations during these *in situ* work-loop trials, we conducted repeated measures analysis using a linear mixed model that we fit using maximum likelihoods with the function *lmer* in the package *lme4* (Bates et al., 2014) in R (version 3.6.1; R Core Team, 2019). We included the difference between the maximum acceleration at the end $a_{max,end}$ and maximum acceleration near the middle $a_{max,mid}$ of the muscle as continuous response variables, max and added mass conditions as categorical fixed effects, and subject number as a categorical random effect in the model. To determine the pairwise differences in $a_{max,end}$ and $a_{max,mid}$ across all ε_{max} and added mass conditions, we used the Holm-Bonferroni method (Holm, 1979) within the package *multcomp* (Hothorn et al., 2008) to control for the increase in family-wise error rate with multiple comparisons. We repeated this analysis a second time to examine the effects of added mass and ε_{max} on the difference between the minimum acceleration at the end $a_{max,end}$ and near the middle $a_{max,mid}$ of the muscle.

5.4 Results

We excited the muscle model slightly before it reached its longest length and until the middle of the shortening phase (Figure 5.2A), which caused the muscle to reach peak activation near the middle of the cycle. The activation decayed through the second half of the shortening phase and reached zero near the end of the cycle. Because the muscle was primarily active during shortening, the net mass-specific work per cycle W^* was positive for all simulations (Figure 5.2D), although there was a short period of negative work when the muscle was producing active force during lengthening for some conditions (Figure 5.2C).

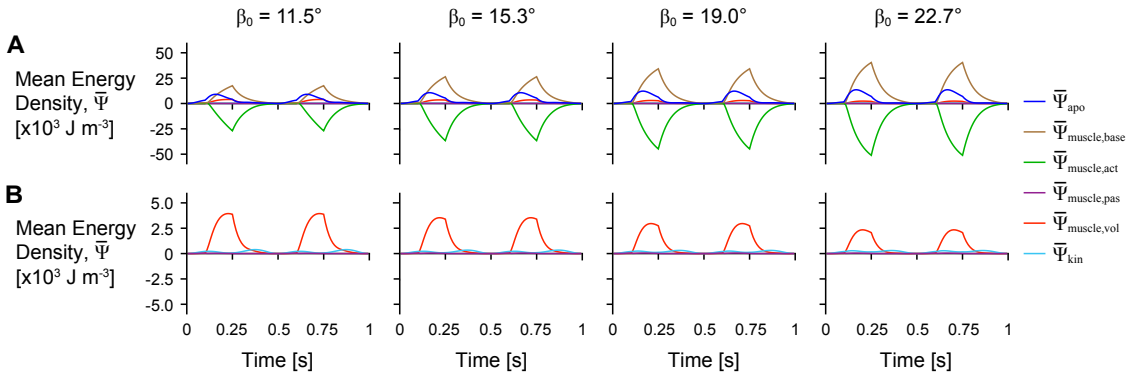

Figure 5.3: Tissue energy over time across initial pennation angles. Simulation traces of mean energy-density $\overline{\psi}$ over time for geometries with different initial pennation angles relative to the x-axis β_0 at scale 1 and with a maximum strain of 5% and normalised excitation of 1. (A) shows all of the energy components and (B) shows only the passive, kinetic and volumetric components from (A) with the y-axis rescaled to visualise changes in these smaller components.

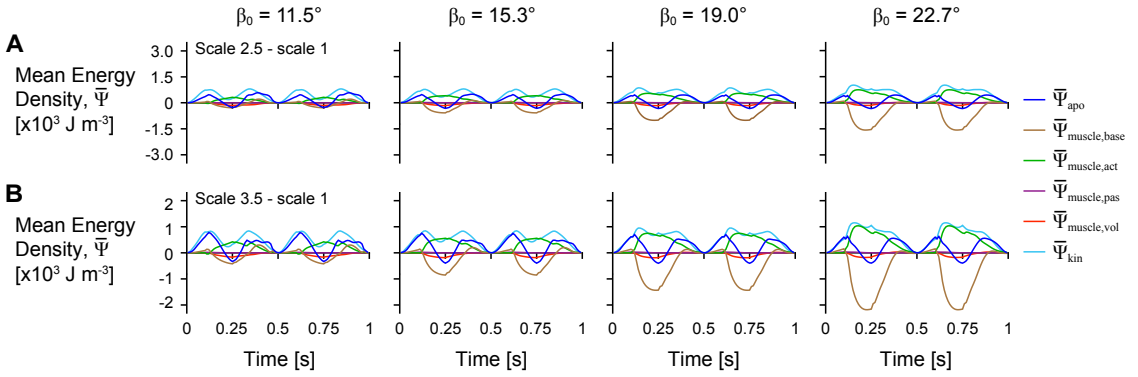

Figure 5.4: Difference in tissue energy over time between scales and across initial pennation angles. Difference in mean energy-density $\overline{\psi}$ across tissue components between scale 2.5 and scale 1 (A) and scale 3.5 and scale 1 (B) simulations. Greater scale muscles are larger in size and have greater mass. All traces are for simulations with a strain of 5%, normalised excitation of 1, and initial pennation angles β_0 ranging from 11.5 to 22.7°.

The distribution of the strain energy-density ψ, across the different components varied over time during each cycle (Figure 5.3). The energy-density due to the active fibres $\overline{\psi}_{\text{muscle,act}}$ decreased (became more negative) when the activation was greater than 0, and the other energy components increased in opposition to these decreases in $\overline{\psi}_{\text{muscle,act}}$, particularly $\overline{\psi}_{\text{muscle,base}}$ and $\overline{\psi}_{\text{apo}}$. $\overline{\psi}_{\text{apo}}$ increased with longer muscle lengths as the aponeurosis was stretched. Greater initial pennation angle β_0 resulted in slightly greater increases in $\overline{\psi}_{\text{apo}}$, greater increases in $\overline{\psi}_{\text{muscle,base}}$, and greater decreases in $\overline{\psi}_{\text{muscle,act}}$, but resulted in smaller increases in $\overline{\psi}_{\text{muscle,vol}}$ and $\overline{\psi}_{\text{kin}}$. Com-

paring the distribution of strain energy-density across scales, $\overline{\Psi}_{\text{muscle,base}}$ was lower and $\overline{\Psi}_{\text{muscle,act}}$ was higher during the shortening period with greater scale and therefore greater muscle size and mass (Figure 5.4). Greater scale resulted in higher $\overline{\Psi}_{\text{kin}}$ throughout the cycle and higher $\overline{\Psi}_{\text{apo}}$ when the muscle was at its longest and shortest lengths.

Larger scale, and therefore greater muscle mass, resulted in lower W^* (Figure 5.5). Specifically, we found a mean reduction in W^* of 8.8% for scale 2.5 relative to scale 1, and 17.1% for scale 3.5 relative to scale 1, across β_0s for simulations with $\hat{e}_{\max}$ of 1 and $\varepsilon_{\max}$ of 5%. Lower $\hat{e}_{\max}$ for the β_0 of 15.3° simulations resulted in lower absolute W^* and relative W^* with greater scale compared to higher $\hat{e}_{\max}$, indicating that muscle mass had a greater effect when $\hat{e}_{\max}$ was lower. Higher β_0 resulted in greater W^* at the same scale (Figure 5.5A) and smaller reductions in W^* with greater scale (Figure 5.5B). For simulations with $\hat{e}_{\max}$ of 1, β_0 of 22.7° resulted in a 2.7% and 7.2% smaller reduction in W^* compared to β_0 of 11.5° at scale 2.5 and scale 3.5 relative to scale 1, respectively. Greater β_0 also led to greater mean fibre stretches $\overline{\lambda}_{\text{tot}}$ and greater changes in $\overline{\beta}$ (Figure 5.6). Larger scale resulted in smaller changes in $\overline{\beta}$ over the cycle but nearly the same $\overline{\lambda}_{\text{tot}}$. Higher β_0 led to smaller differences in$\overline{\beta}$ with greater scale. Greater cycle strain amplitude $\varepsilon_{\max}$ resulted in greater absolute W^* for simulations with β_0 of 15.3° and $\hat{e}_{\max}$ of 1 at scale 1 (Figure 5.7A). At scale 2.5 and 3.5, $\varepsilon_{\max}$ of 2.5% resulted in the lowest W^* and $\varepsilon_{\max}$ of 5% resulted in the highest W^*. In terms of the effect of $\varepsilon_{\max}$ across scales, greater $\varepsilon_{\max}$ led to lower relative W^* with greater scale (Figure 5.7B).

To examine the effects of mass on the uniformity of tissue behaviour across the muscle, we compared the tissue accelerations at a single point near the middle of the muscle a_{mid} compared to at the moving ($+x$) end a_{end} for simulations with $\hat{e}_{\max}$ of 1 and β_0 of 15.3° to compare with the experiments on maximally active *in situ* muscle. We normalised a_{mid} to the x distance between the fixed end and the middle point at rest and a_{end} to the muscle length at rest to give accelerations in s^{-2}. Note that because the position of the end of both the simulated and *in situ* muscle was constrained to follow a sinusoidal trajectory, a_{end} did not vary across simulations and trials with the same $\varepsilon_{\max}$. For both the simulations and *in situ* experiments, amid decreased initially when the whole muscle length increased (Figure 5.8). The minimum acceleration of the point near the middle of the muscle $a_{\text{min,mid}}$ occurred earlier than the minimum acceleration at the end $a_{\text{min,end}}$ across all strain and scale and added mass conditions and was lower with greater $\varepsilon_{\max}$. The time when a_{mid} was zero and the muscle short-

ening velocity would be maximal occurred earlier than for a_{end} and was earlier with lower $\boldsymbol{\varepsilon}_{max}$, greater scale for the simulations, and greater added mass for the *in situ* experiments.

For the model simulations, the reduction in $a_{max,mid}$ relative to $a_{max,end}$ was greater for larger scales (Figure 5.9A). We also found similar results for the *in situ* contraction cycles where greater added mass resulted in greater reductions in $a_{max,mid}$ relative to $a_{max,end}$ ($p = 0.0056$). Specifically, the reduction in $a_{max,mid}$ compared to $a_{max,end}$ was 0.063 s^{-2} (3.1%) greater for the 123% added mass condition compared to the 85% added mass condition (SE = 0.023 s^{-2}). Similar to the difference in a_{max}, we also found greater increases (closer to zero) in $a_{min,mid}$ relative to $a_{min,end}$ for simulations in which the muscle was larger (Figure 5.9B) and for *in situ* experiments in which greater effective mass was added to the muscle ($p = 0.0076$). Specifically, the increase in $a_{min,mid}$ compared to $a_{min,end}$ was 0.073 s^{-2} (3.9%) greater for the 123% compared to the 85% added mass condition (SE = 0.028 s^{-2}). While the effect of greater mass was similar for the simulations as for the *in situ* experiments, because we used different paradigms to manipulate the mass in that we geometrically scaled the simulated muscle to larger sizes and added effective mass acting through a pin inserted into the *in situ* muscle, the simulation and *in situ* mass effect results are not directly comparable.

We found that greater $\boldsymbol{\varepsilon}_{max}$ of the imposed motion at the end of the muscle led to greater decreases in $a_{max,mid}$ relative to $a_{max,end}$ for both the model simulations and *in situ* experiments (Figure 5.10A; $p < 0.001$). For the *in situ* muscle trials, there was a 0.91 s^{-2} (75.5%) greater reduction in $a_{max,mid}$ relative to $a_{max,end}$ for $\boldsymbol{\varepsilon}_{max}$ of 7.5% compared to 5% (SE = 0.027 s^{-2}, $p < 0.001$), and a 0.65 s^{-2} (30.9%) greater reduction for $\boldsymbol{\varepsilon}_{max}$ of 10% compared to 7.5% (SE = 0.028 s^{-2}, $p < 0.001$). Finally, we found a 1.56 s^{-2} (129.7%) greater reduction $a_{max,mid}$ relative to $a_{max,end}$ for $\boldsymbol{\varepsilon}_{max}$ of 10% compared to 5% (SE = 0.028 s^{-2}, $p < 0.001$). We found that greater $\boldsymbol{\varepsilon}_{max}$ led to greater increases (closer to zero) in $a_{max,mid}$ relative to $a_{max,end}$ for both the simulations and *in situ* experiments (Figure 5.10; $p < 0.001$). For the *in situ* experiments, we found a 0.79 s^{-2} (68.5%) greater increase in the difference in a_{min} for 7.5% $\boldsymbol{\varepsilon}_{max}$ compared to 5% (SE = 0.033 s^{-2}, $p < 0.001$), a 0.73 s^{-2} (37.3%) greater increase for 10% $\boldsymbol{\varepsilon}_{max}$ compared to 7.5% (SE = 0.034 s^{-2}, $p < 0.001$), and a 1.51 s^{-2} (131.1%) greater increase for 10% $\boldsymbol{\varepsilon}_{max}$ compared to 5% (SE = 0.034 s^{-2}, $p < 0.001$). While we examined different ranges of $\boldsymbol{\varepsilon}_{max}$ for the experimental trials and simulations, the differences in $a_{max,mid}$

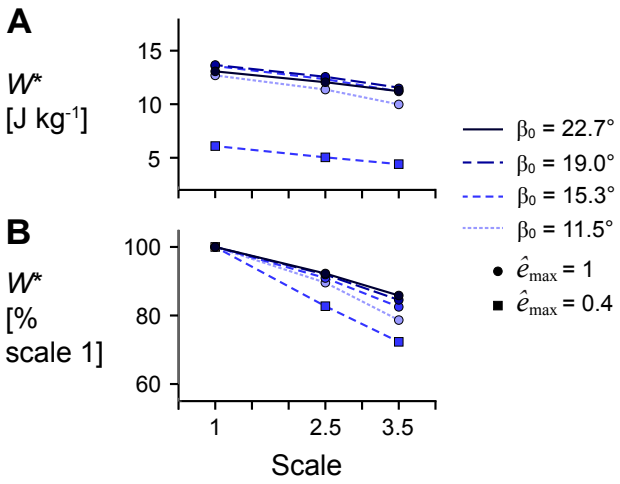

Figure 5.5: Effect of initial pennation angle on the relationship between scale and mass-specific mechanical work. (A) Absolute mass-specific mechanical work per cycle W^* across geometry length scales (muscle sizes) for different initial pennation angles β_0 ranging from 11.5 to 22.7° relative to the x-axis for maximum strain of 5% and maximum relative excitation $\hat{e}_{\max}$ of 1 (circles) and 0.4 (squares). W^* across scales as a percentage of scale 1 W^* at the same β_0 and $\hat{e}_{\max}$ are shown in (B). All cycles had a frequency of 2 Hz. Note that the lines connecting discrete points are intended to aid in visualization rather than to imply a linear relationship.

compared to $a_{\max,\text{end}}$ relative to 5% $\varepsilon_{\max}$ were of similar magnitude for the *in situ* experiments and simulations.

5.5 Discussion

5.5.1 Tissue energy distribution in whole muscle during cyclic contractions

Muscles in living animals are activated by motor neurons that carry impulses from the central nervous system. These impulses cause myosin and actin filaments to bind and form cross-bridges to generate active force, a process that is fueled by chemical energy from the hydrolysis of adenosine triphosphate (ATP). The active force acts to deform the muscle tissue, and so the energy of the sliding filaments is then stored as potential energy in the deformed tissues or spent doing external mechanical work. In the 3D muscle model, we simulated the increase in muscle energy via nervous system stimulation by prescribing a time-varying activation that increased the active energy.

The active energy available to deform the tissue also depended on the local fibre stretches and velocities and was distributed and stored in the deformed tissue.

In the first paper in this series (Wakeling et al., 2020), we examined how energy is distributed across muscle tissue during fixed-end contractions where no external work was done when the muscle was fixed at its resting length. To do this, we used a quasistatic model formulation in which tissue kinetic energy was not accounted for, nor were the effects of velocity on the active energy. Despite this, there were a number of similarities in the energy distribution across tissue components between the fixed-end quasistatic contractions in our previous study and the cyclic dynamic contractions reported here. As we activated the muscle, the active energy of the fibres became more negative as the fibres contracted (Figure 5.3A). This active energy was stored as potential energy in the deformed tissue, particularly the muscle base material that represents additional tissue within and surrounding the fibres, including the extracellular matrix. The volumetric energy, or the energy due to the muscle volume change, also increased as the active force became more negative as in Wakeling and colleagues (2020), but to a far lesser extent than the muscle base material energy.

In this study we additionally accounted for the kinetic energy of tissue mass and found that the kinetic energy-density (total energy across the tissue relative to the sum of the total muscle and aponeuroses volumes in J m^{-3}) was greatest when the muscle was near its shortest and longest lengths (Figure 5.3B). Although the overall muscle velocity in the x direction was lowest at these times, the kinetic energy depends on the local tissue velocities that have components in all three directions, and so motion of the tissue in transverse directions (y and z) may account for the high kinetic energy when the muscle x velocity was low (Figure 5.11). The local velocity also varies across the tissue: the tissue lags behind the motion of the non-fixed end due to its own inertia. The kinetic energy-density throughout a contraction cycle was greater for larger muscles with greater mass (Figure 5.4). In the quasistatic model that does not account for the effects of muscle mass and kinetic energy, the non-dimensional behaviour of the model, including the energy-density distribution, would be identical for models of different sizes. Accounting for kinetic energy creates a scale-dependent distortion such that models of different sizes but the same geometric proportions will have different distributions of energy-density. We found that the active energy-density was higher (less negative), the muscle base material energy-density was lower, and the aponeurosis energy-density was higher for larger compared to smaller muscles (Figure 5.4). Thus, larger muscles may make use of base material, or the extracellular

matrix, less and aponeurosis more for energy storage and return during contraction than smaller muscles.

Both the quasistatic (Wakeling et al., 2020; Ryan et al., 2020) and dynamic model formulations do not account for energy dissipation in the form of heat. Muscles in living animals constantly dissipate heat, and the amount of thermal energy loss depends on a range of contractile factors, such as the activation, contraction speed and fibre-type properties of the muscle (Woledge et al., 1985). In our simulations, more energy may have been stored in the tissue or been available to do external work than if heat dissipation were accounted for in the model energy balance equation. However, it is unlikely that accounting for heat dissipation would have substantially altered our reported effects of muscle mass. Future work could aim to account for energy loss through heat dissipation in the formulation of 3D muscle models.

5.5.2 Implications of muscle mass for whole muscle function

Comparative studies have long sought to examine the maximum mechanical work or average mechanical power during cyclic contractions across animals of different sizes (Weis-Fogh & Alexander, 1977; Pennycuick & Rezende, 1984). The net mechanical work per cycle depends on the force a muscle generates over its change in length. Because muscle force scales with cross-sectional area, and muscle length change scales with optimal length, larger muscles will have higher absolute mechanical work per cycle than smaller muscles due to their larger cross-sectional areas and longer optimal lengths. However, since muscle force scales with cross-sectional area that has dimensions of length-squared, and the length change scales with optimal length which has dimensions of length, the work scales with the volume which has dimensions of length-cubed. Muscle tissue density is often considered to be constant across muscles, so the work per cycle also scales with muscle mass. Thus, based on these assumptions, two muscles with the same geometric proportions of different sizes or length scales would, in theory, generate the same mass-specific mechanical work per cycle. However, as muscle force and work are difficult to measure, particularly in larger animals, this theory has not been directly tested.

These earlier comparative studies, as with most studies in biomechanics, ignored the effects of muscle mass on contractile behaviour. While a muscle's force increases in proportion to its area, or the length-squared, the muscle's mass and acceleration in-

crease in proportion to the volume, or length-cubed, and length, respectively. Thus, the loads due to muscle mass increase faster than the muscle force available to accelerate the tissue loads as muscles increase in size. As a consequence, the larger of the two muscles with the same geometric proportions but different sizes or length scales will have lower mass-specific mechanical work per cycle due to its greater muscle mass (Chapter 3; Chapter 4). Submaximal fibre activation can amplify the effects of muscle mass, as evidenced by studies that have shown lower maximum shortening speeds during submaximal compared to maximal contractions of rat-sized muscle (Holt et al., 2014; Ross & Wakeling, 2016). In this study, we found that the reduction in mass-specific work due to muscle mass with greater muscle size is amplified with submaximal activation (Figure 5.5B), which is consistent with the results of previous 1D model simulations (Chapter 3). Therefore, muscle mass is an important determinant of whole muscle behaviour, particularly for larger muscles and during submaximal contractions.

Larger muscles may mitigate the effects of their greater mass by having different geometric proportions and architecture than smaller muscles. In this study, we found that greater initial pennation angle resulted in smaller reductions in mass-specific work per cycle with greater muscle size (Figure 5.5B). While data on scaling of muscle pennation angle with body sizes are limited, positive allometry for pennation angle has been shown for monitor lizard muscles across a range of body sizes (8 gram short-tailed monitors to 40 kilogram Komodo dragons), in that larger animals have higher muscle pennation angles than smaller animals (Dick & Clemente, 2016). While we varied fibre length with the initial pennation angle of the muscle model, we geometrically scaled the model to larger sizes such that the initial fibre lengths were the same relative length across models of different sizes. However, muscles in larger animals tend to have relatively shorter fibres compared to muscles in smaller animals (Alexander et al., 1981; Pollock & Shadwick, 1994a; Eng et al., 2008). While we found greater maximum fibre strains with greater initial pennation angles, this did not vary with scale, unlike pennation angle over time (Figure 5.6), so scaling fibre length with muscle size likely would not have altered our results. Thus, scaling of fibre length with body mass in living animals may be due to space constraints within a limb compartment rather than as a means to minimise the contractile consequences of muscle mass.

We found that the mean fibre pennation angle increased when both the muscle and fibres were shortening (Figure 5.6), which is consistent with previous *in vivo* ultrasound measures of human muscles during cyclic contractions (Kurokawa et al., 2001;

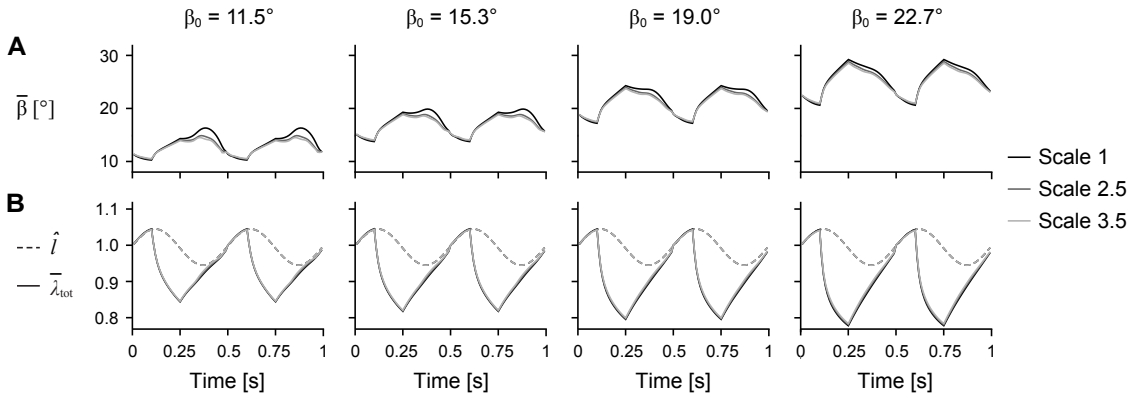

Figure 5.6: Mean fibre angle and stretch over time. Mean fibre pennation angle relative to the -x axis $\overline{\beta}$ (A) and normalised muscle length $\hat{l}$ and total mean fibre stretch $\overline{\lambda}_{\text{tot}}$ (B) over time across initial pennation angles relative to the x-axis β_0 for different scales.

Lichtwark et al., 2007; Wakeling et al., 2011; Dick & Wakeling, 2017; Randhawa & Wakeling, 2018). Rotating to higher angles during shortening allows the fibres to shorten slower than the muscle belly, and as a consequence, generate greater forces. However, this increase in force with higher fibre rotation is balanced by a force reduction due to the fibres no longer being oriented along the longitudinal axis of the muscle. We found smaller fibre rotations over a contraction cycle for larger muscles; however, this difference in fibre rotation with greater muscle size was smaller with higher initial pennation angle (Figure 5.6). Higher fibre angles during shortening may allow larger muscles to overcome the effects of their mass and achieve higher mass-specific work per cycle, although whether this relationship is causal cannot be determined from our simulations.

We may have seen different fibre strains and rotations had we constrained movement of the model aponeuroses. The bulging of muscle and movement of aponeuroses in transverse directions *in vivo* is limited by resistive forces applied by neighbouring muscles, connective tissue, and skin, which can alter muscle fibre strains and rotations (Wakeling et al., 2013; Ryan et al., 2019). In our simulations, we did not apply transverse compressive tractions to the muscle to mimic the effects of loads from surrounding tissue, as these loads acting on muscle during dynamic contractions are poorly understood. As a result, our muscle model and aponeuroses were free to bulge and rotate in ways that may not entirely reflect the behaviour of muscle *in vivo*. While the lack of transverse loads in our simulations may have altered the fibre strains and rotations, it is unlikely that they would have substantially influenced our reported

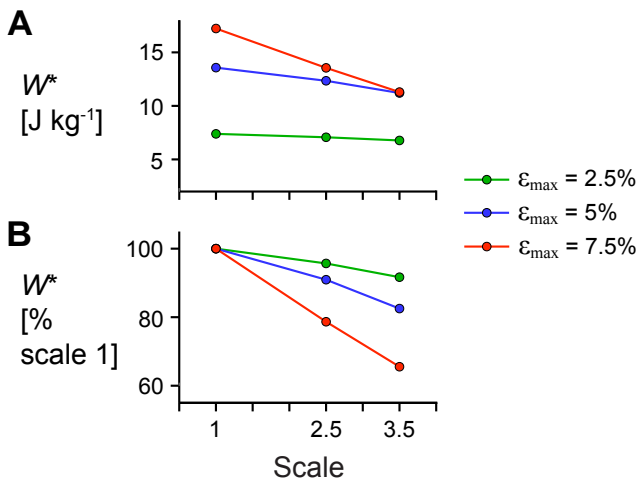

Figure 5.7: Effect of cycle strain amplitude on the relationship between scale and mass-specific mechanical work. (A) Absolute mass-specific mechanical work per cycle W^* across scales (muscle sizes) for different maximum strain amplitudes ε_{max} and (B) W^* as a percentage W^* for scale 1 simulations at the same ε_{max}. All W^* results are for simulations with a maximum relative excitation of 1, initial pennation angle β_0 of 15.3°, and 2 Hz cycle frequency. Note that the lines connecting discrete points are intended to aid in visualization rather than to imply a linear relationship.

effects of muscle mass, given that we previously found a similar pattern of mass effects across scales for a mass-enhanced 1D model.

Studies have shown that the properties of aponeurosis can alter fibre strains and rotations (Rahemi et al., 2015; Eng & Roberts, 2018), and so the properties of our aponeuroses may have also influenced the fibre strains across the different initial pennation angles in our simulations. To model the aponeuroses, we used two sheets of tissue that were uniform in thickness and composed of a base material with embedded collagen-like fibres. These fibres were unidirectional and oriented along the length of each aponeurosis at rest so that the overall behaviour of the tissue was anisotropic, consistent with previous experimental studies (Azizi & Roberts, 2009; Azizi et al., 2009). We selected the thickness and material properties of the aponeuroses so that the longitudinal and transverse aponeurosis strains during maximal fixed-end contractions matched *in situ* measures of intact aponeurosis during the same contractile conditions (Azizi & Roberts, 2009). However, the utility of these *in situ* aponeurosis measures is limited, as only muscle forces acting externally and not forces applied to the aponeurosis can be measured or controlled. Thus, it is not clear to what extent our modelled aponeuroses reproduced the behaviour of *in vivo* aponeuroses, and so further

work is needed to quantify the structural and material properties of aponeurosis and determine its role in constraining fibre strains and rotations during contraction.

The properties of aponeurosis may also vary with muscle scale, and this may have influenced our reported effects of muscle mass. Aponeurosis tissue, as well as tendon, likely plays an important role in energy storage and return during locomotion (Wager & Challis, 2016; Arellano et al., 2019). In our simulations, we assumed that the aponeurosis had the same relative effect on the model across different length scales or sizes, in that the stress-strain properties were constant, and the thickness, length, and width of the aponeuroses scaled with the length scale. While there is some evidence that tendon cross-sectional area relative to that of muscle varies with animal body mass (Alexander et al., 1981; Pollock & Shadwick, 1994a), it is not yet known if the material or structural properties of aponeurosis vary with body and muscle size. It may be that the energetic role of these elastic structures varies with body size and alters the contractile effects of muscle mass.

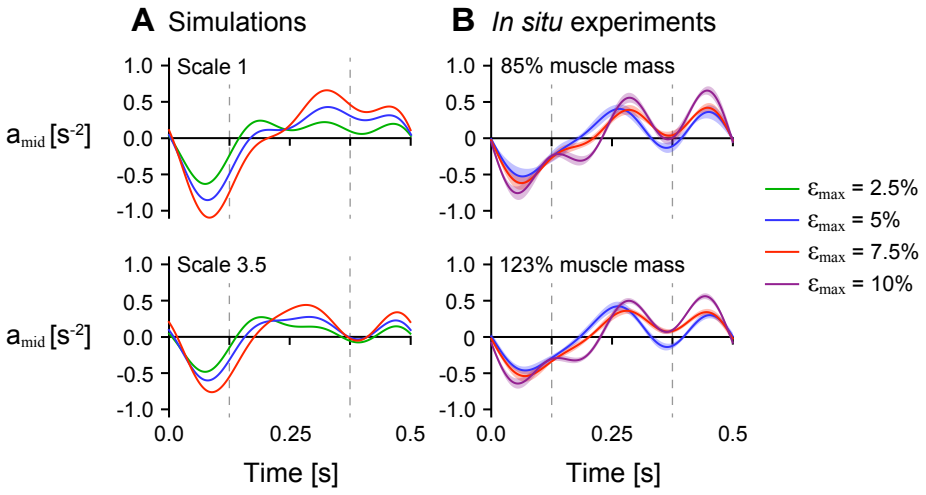

Figure 5.8: Normalised acceleration midway along the muscle's length over time across strain conditions. Normalised tissue acceleration in the x-direction of a point midway along the muscle's length amid over time for simulations with initial pennation angle β_0 of 15.3° (A) and *in situ* experiments (B). The dashed vertical bars at 0.125 s and 0.375 s indicates the times when the muscle was at its longest and shortest lengths, respectively. a_{mid} was normalised using the x distance between the centre point and the moving end of the muscle at rest for the simulations and between the inserted pin and the moving end of the *in situ* muscle at rest for the experiments. The maximum normalised excitation was 1 for the simulations and the *in situ* muscle was supramaximally stimulated to activate all the muscle fibres. The shaded intervals in (B) show the standard error of the mean at each time point.

5.5.3 Effects of tissue properties on cyclic muscle contractions

Whole muscles are typically considered to behave as single units where the strains and strain rates are uniform along the muscle's length, and this assumption is reflected in 1D Hill-type models in which a single contractile element with a single length at any given time is used to represent the active muscle force (Zajac, 1989). In reality, whole muscles are composed of thousands of sarcomeres grouped into myofibrils at the microscopic level, which constitute muscle fibres at the cellular level that are then bundled into fascicles at the tissue level. Experiments on *in situ* and *in vivo* muscle during dynamic contractions have shown that fascicles within different regions of whole muscle can have different strains and be at different positions on their force-length curves at a given time (Pappas et al., 2002; Ahn et al., 2003; Soman et al., 2005; Shin et al., 2009; Ahn et al., 2018).

In this study we found that tissue accelerations in the longitudinal direction varied along the muscle's length for both the *in situ* and simulated contractions, and this non-uniformity in accelerations was more pronounced with greater muscle size or greater added mass (Figure 5.9). While the non-uniformity in muscle behaviour at the tissue level could be due to regional variations in activation (Monti et al., 2003; Rahemi et al., 2014) and myofascial force transmission (Tijs et al., 2015), in this study we show that the presence of muscle mass may also contribute to this non-uniformity during cyclic contractions.

Muscle mass may also have implications for non-uniformity at the microscopic level. Consider a massless ideal spring with uniform structural and material properties along its length. If one end of the spring is fixed and a tensile load is applied to the other, the spring's response will be uniform in that the strain will be constant everywhere along its length. If the distributed mass of the spring is then accounted for, the spring's response to the same tensile load will be different and will depend on the size and mass of the spring. Initially, the strains will be high near the applied load and low or zero near the fixed end. Then, a wave of strains will propagate along the length of the spring, causing a time delay between when the material near the free and fixed ends experience extension. Once the system settles, the strain across the spring's length will become more uniform. This pattern of behaviour in a spring with mass, which has also been shown in simulations of a mass-enhanced 1D Hill-type model (Ross & Wakeling, 2016) and the 3D model in this study, is consistent with experimental

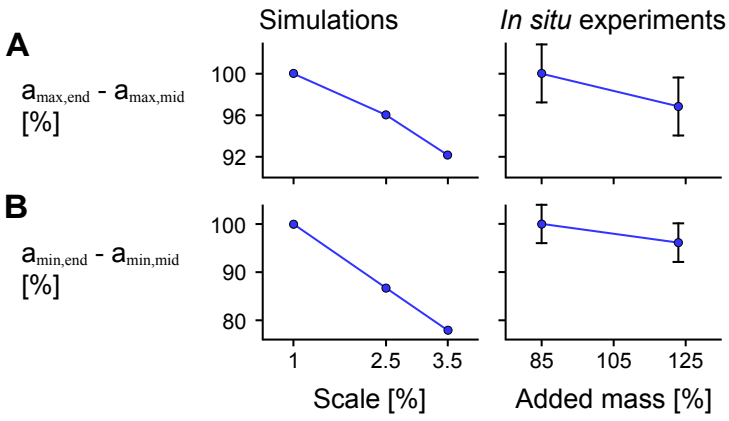

Figure 5.9: Difference in maximum and minimum acceleration near the middle compared to at the end of the muscle across scales and added masses. Mean difference in maximum normalised acceleration in the x-direction at the end $a_{max,end}$ compared to that of a point near the middle of the muscle $a_{max,mid}$ across scales (muscle sizes) for simulations relative to scale 1 (left) and *in situ* experiments relative to 85% added muscle mass relative to the muscle mass (right; $p = 0.0056$) calculated across all maximum strains (A). (B) shows the mean difference in minimum acceleration $a_{min,end}$ in the x-direction at the end compared to near the middle of the muscle $a_{min,mid}$ ($p = 0.0076$ for the *in situ* experiments). $a_{max,end}$ and $a_{min,end}$ were normalised to the muscle optimal length and $a_{max,mid}$ and $a_{min,mid}$ were normalised to the x distance between the centre point and the moving end of the muscle at rest for the simulations and between the inserted pin and the moving end of the *in situ* muscle at rest for the experiments. Although we show similar trends for greater added mass as for greater scale, we caution against directly comparing the magnitude of effects as altering the added mass and scale manipulate the tissue mass in different ways. The initial pennation angle β_0 was 15.3° and the maximum normalised excitation was 1 for the simulations and the *in situ* muscle was supramaximally stimulated to activate all the muscle fibres. The error bars for the *in situ* experiments represent the standard error of the mean. Note that the lines connecting discrete points are intended to aid in visualization rather than to imply a linear relationship.

findings of sarcomere strains across different regions of intact whole muscle. Moo and colleagues (2016) found that sarcomere strains are not uniform across different regions of intact muscle, and that the greatest sarcomere strains occur close to the myotendinous junction where external loads are applied. These strains become less uniform when muscle is activated during fixed-end contractions (Moo et al., 2017), but this non-uniformity in sarcomere strains decreases over time (Moo & Herzog, 2020). This pattern of sarcomere non-uniformity may be in part due to muscle mass and may vary depending on the size of the muscle, much like the response of the spring with mass and 1D and 3D muscle models that account for muscle mass.

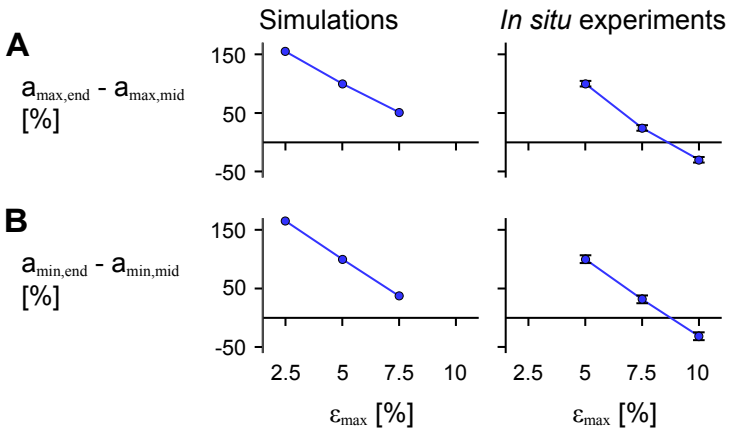

Figure 5.10: Difference in maximum and minimum acceleration near the middle compared to at the end of the muscle across maximum strains. Mean difference in maximum normalised acceleration in the x-direction at the end $a_{max,end}$ compared to that of a point near the middle of the muscle $a_{max,mid}$ across cycle strains for simulations relative to scale 1 (left) and *in situ* experiments relative to 85% added muscle mass (right; $p < 0.001$) calculated across all scales and added masses (A). (B) shows the mean difference in minimum acceleration $a_{min,end}$ in the x-direction at the end compared to near the middle of the muscle $a_{min,mid}$ ($p < 0.001$ for the *in situ* experiments). $a_{max,end}$ and $a_{min,end}$ were normalised to the muscle optimal length. $a_{max,mid}$ and $a_{min,mid}$ were normalised to the x distance between the centre point and the moving end of the muscle at rest for the simulations and between the inserted pin and the moving end of the *in situ* muscle at rest for the experiments. The initial pennation angle β_0 was 15.3° and the maximum normalised excitation was 1 for the simulations and the *in situ* muscle was supramaximally stimulated to activate all the muscle fibres. The error bars for the *in situ* experiments represent the standard error of the mean. Note that the lines connecting discrete points are intended to aid in visualization rather than to imply a linear relationship.

5.5.4 Conclusions

Over the last decade there has been growing interest in using 3D muscle models to explain the mechanisms that underly whole muscle contraction. As these models become more refined, they are increasingly able to replicate features of *in situ* and *in vivo* muscle behaviour. Rahemi and colleagues (2014) showed that muscle tissue activation results in S-shaped fibres during simulated fixed-end contractions, which is consistent with findings from *in vivo* measures of human medial gastrocnemius muscle (Namburete et al., 2011). More recently, we showed similar magnitudes and patterns of muscle bulging during submaximal contractions for the 3D model (Wakeling et al., 2020) as for *in vivo* muscle visualized using ultrasound (Randhawa et al., 2013) and magnetic resonance with diffusion tensor imaging (Wakeling et al., 2020). We also showed a similar reduction in muscle thickness and pennation angle with transverse

compression (Ryan et al., 2020) as measures of *in vivo* human calf muscle (Ryan et al., 2019). In this study, in which we used a model formulation that accounts for distributed muscle mass and fibre force-velocity effects, we were again able to show similarities in behaviour between the simulated 3D model and experimental muscle. We found that greater muscle size, and therefore mass, for the simulations and greater added mass for the *in situ* experiments, as well as higher maximum strain amplitude, led to lower maximum and higher minimum acceleration in the longitudinal direction near the middle of the muscle compared to at the non-fixed end. Greater muscle size and higher maximum strain also led to greater reductions in mass-specific work per cycle, consistent with previous results from experiments on *in situ* rat plantaris muscle (Chapter 4). This reduction in mass-specific work with larger muscle size was lower for simulated muscles with higher initial pennation angles. We also found that larger muscle size resulted in higher relative kinetic energy per cycle, relatively more energy stored in the aponeurosis, and less stored in the base material that represented the intra and extracellular tissue components apart from the myofibrils. While these results highlight that muscle mass can substantially decrease muscle performance, higher initial pennation angle and greater energy storage in elastic tissues may mitigate some of these performance losses.

5.6 Appendix: Details of model formulation

The model we used in this paper is based on the three-dimensional model introduced in Wakeling and colleagues (2020) to approximate the deformation of muscles during fixed-end contractions. We added inertial and velocity effects to this model to capture the dynamic behaviour of muscle tissue. The combined momentum and mass balance in the current configuration V of the muscle is as follows:

$$\frac{\partial(\rho\mathbf{v})}{\partial t} + \mathbf{div}(\rho\mathbf{v}\otimes\mathbf{v}) = \mathbf{div}\sigma(\mathbf{u},\mathbf{v},p,J), \quad J - I_3(\mathbf{u}) = 0, \quad p - \frac{\kappa}{2}\left(J - \frac{1}{J}\right) = 0, \quad (5.1)$$

where ρ is the density of the muscle, $\mathbf{v}$ is the tissue velocity, $\mathbf{u}$ is the tissue displacement, σ is the Cauchy tensor, J is the dilation, I_3 is the third invariant, p is the pressure, and κ is the bulk modulus. Bold symbols indicate vector variables and $\otimes$ denotes the usual outer product between two vectors. The kinetic energy K_{int} of the muscle in V is defined as:

$$K_{\text{int}}(\mathbf{v}) = \frac{1}{2}\int_V \rho \mathbf{v} \cdot \mathbf{v} dV, \tag{5.2}$$

where "$\cdot$" denotes the three-dimensional dot product. The muscle fibre stress relative to the maximum isometric stress $\hat{\sigma}_{\text{mus,fibre}}$ depends on the isovolumetric stretch λ_{iso}. Using the active stress-stretch $\hat{\sigma}_{\text{stretch}}(\lambda_{\text{iso}})$, passive stress-stretch $\hat{\sigma}_{\text{pas}}(\lambda_{\text{iso}})$ and stress-strain rate relationships $\hat{\sigma}_{\text{vel}}(\lambda_{\text{iso}})$, $\hat{\sigma}_{\text{mus,fibre}}$ is defined as:

$$\hat{\sigma}_{\text{mus,fibre}}(\mathbf{u}, \mathbf{v}) := \mathbf{a}(q_0, t)\hat{\sigma}_{\text{stretch}}(\lambda_{\text{iso}})\hat{\sigma}_{\text{vel}}(\dot{\lambda}_{\text{iso}}) + \hat{\sigma}_{\text{pas}}(\lambda_{\text{iso}}), \tag{5.3}$$

where q_0 is a point in the initial configuration of the muscle V_0. The fibre stretch λ_{iso} is the length of the current orientation vector $\mathbf{a}$ and we define the strain rate in the current direction of the fibre $\dot{\lambda}_{\text{iso}}$ as:

$$\dot{\lambda}_{\text{iso}} = \frac{\mathbf{a}^{\text{T}}\text{dev}[\boldsymbol{\varepsilon}(\mathbf{v})]\mathbf{a}}{\lambda_{\text{iso}}}, \tag{5.4}$$

where

$$\text{dev}[\boldsymbol{\varepsilon}(\mathbf{v})] = \boldsymbol{\varepsilon}(\mathbf{v}) - \frac{1}{3}\text{div}(\mathbf{v})\mathbf{I} = \frac{1}{2}(\nabla\mathbf{v} + \nabla\mathbf{v}^{\text{T}}). \tag{5.5}$$

The tensor $\boldsymbol{\varepsilon}(\mathbf{v})$ is the strain rate tensor and $\mathbf{I}$ is the identity matrix. The active stress tensor is defined as in Wakeling et al. (2020) but with the added term from $\hat{\sigma}_{\text{vel}}$ such that

$$\hat{\sigma}_{\text{act}}(\mathbf{u}, \mathbf{v}) := \hat{\sigma}_{\text{mus,fibre}}\mathbf{a} \otimes \mathbf{a} \tag{5.6}$$

The numerical implementation of the momentum and mass balance is semi-implicit in time, in which the velocity $\mathbf{v}$ is updated explicitly, whereas the displacement $\mathbf{u}$ is implemented implicitly. As such, the implementation $\hat{\sigma}_{\text{act}}$ only depends on the current state of $\mathbf{u}$ (computed via the finite element method) and $\mathbf{u}$ at the previous time step. We implemented the model in the finite element library deal.II version 8.5.1 (Arndt et al., 2017) using the tutorial step-44 (Pelteret & McBride, 2012; Pelteret, 2014).

5.7 Appendix: Details of model geometries

Table 5.2: Initial dimensions of model geometries.

scale	α_0 (°)	β_0 (°)	**muscle length (m)**	**muscle width (m)**	**fibre length (m)**	**aponeurosis length (m)**	**aponeurosis thickness (m)**
1	15	11.5	0.27	0.055	0.06366284	0.208	0.003
2.5	15	11.5	0.675	0.1375	0.15915709	0.52	0.0075
3.5	15	11.5	0.945	0.1925	0.22281993	0.728	0.0105
1	20	15.3	0.27	0.055	0.065	0.208	0.003
2.5	20	15.3	0.675	0.1375	0.1625	0.52	0.0075
3.5	20	15.3	0.945	0.1925	0.2275	0.728	0.0105
1	25	19.0	0.27	0.055	0.06677424	0.208	0.003
2.5	25	19.0	0.675	0.1375	0.1669356	0.52	0.0075
3.5	25	19.0	0.945	0.1925	0.23370983	0.728	0.0105
1	30	22.7	0.27	0.055	0.06902991	0.208	0.003
2.5	30	22.7	0.675	0.1375	0.17257477	0.52	0.0075
3.5	30	22.7	0.945	0.1925	0.24160468	0.728	0.0105

5.8 Nomenclature

Activation specifically refers to the active *state* of the contractile elements (muscle fibres) and is used to scale the active force that they can develop. In muscle physiology, **excitation** refers to the electrical potentials on the membrane of the muscle fibre that are typically recorded using EMG.

Muscle contraction is the *process* of muscle developing forces when its activation level is greater than zero. In muscle physiology, contraction does not necessarily mean shortening because tension can be developed without a change in length.

The **longitudinal direction** is the major x-axis of the muscle. This can be considered the direction that would be between the proximal and distal tendons in a fusiform muscle, and so it is in the commonly phrased 'line of action'. We do not use 'line-of-action' because forces and deformations occur in three dimensions in this study and so there is no unique line-of-action.

Transverse direction is used to describe directions in the yz plane, and thus is perpendicular to the longitudinal direction of the muscle. This is sometimes called the radial direction in other studies.

Muscle mass refers to the total mass in kilograms of the muscle belly, including the muscle fibres, aponeuroses, and connective tissue. Note that this muscle mass is distributed throughout the tissue.

Added mass refers to the effective mass that we added to the *in situ* muscle at a single location along the muscle's length. See the Sections 5.3.4 Experimental data collection and 5.3.5 Experimental data analysis for further details. **Scale** refers to the length scale factor that multiplied the lengths of the muscle geometries to geometrically scale the muscle model to larger sizes. See the Section 5.3.2 Muscle model geometries for details of this scaling. Both increasing the added mass and scale increase the total mass of the muscle, although the effective mass in the *in situ* experiments was added only to a single location whereas increasing the model scale increased the mass distributed throughout the muscle and aponeurosis tissue.

5.9 Supplementary material

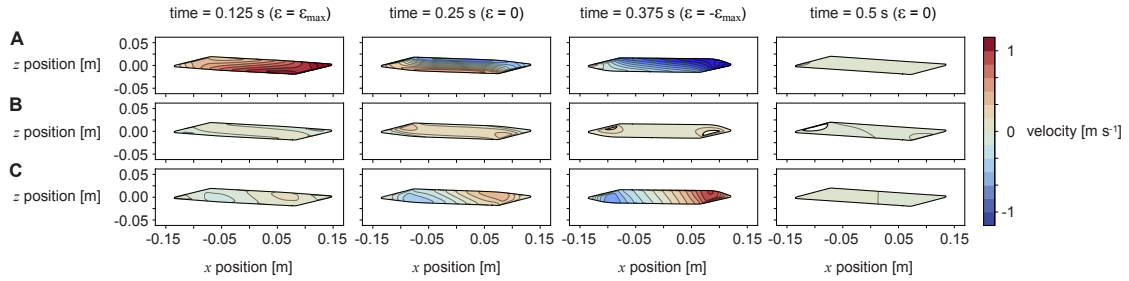

Figure 5.11: Local velocity of quadrature points over time. x (A), y (B), and z (C) components of the local velocity in the current direction (shading) of quadrature points as a function of their current z and x positions for a sample simulation with scale 1, initial pennation angle of 15.3°, maximum normalised excitation of 1, and maximum strain amplitude of 5%. We measured the local velocity in the current configuration at points that were in the xz plane at $y = 0$ in the initial configuration at times $t = 0.125$ s when the muscle was at its longest length, $t = 0.25$ s halfway through the shortening phase, $t = 0.375$ s when the muscle was at its shortest length, and $t = 0.5$ s when the muscle was at its initial length.

Chapter 6

The greater mass of larger muscles decreases contraction efficiency

6.1 Abstract

While skeletal muscle mass has been shown to decrease mass-specific mechanical work per cycle, it is not yet known how muscle mass alters contraction efficiency. In this study we examined the effect of muscle mass on mass-specific metabolic cost and efficiency during cyclic contractions in simulated muscles of different sizes. We additionally explored how tendon and its stiffness alters the effects of muscle mass on mass-specific work, mass-specific metabolic cost, and efficiency across different muscle sizes. To examine contraction efficiency, we estimated the metabolic cost of the cycles using established cost models. We found that for motor contractions in which the muscle was primarily active during shortening, greater muscle mass resulted in lower contraction efficiency, primarily due to lower mass-specific mechanical work per cycle. The addition of a tendon in series with the mass-enhanced muscle model improved the mass-specific work and efficiency per cycle with greater mass for motor contractions, particularly with a shorter excitation duty cycle, despite higher predicted metabolic cost. The results of this study indicate that muscle mass is an important determinant of whole muscle contraction efficiency.

6.2 Introduction

The majority of the energetic cost of locomotion can be attributed to skeletal muscles converting chemical energy, that arises from metabolism of the food we eat, to mechanical work to move the body. However, due to the difficulty in directly measuring these processes in whole muscle *in vivo*, most of what we know about this behaviour comes from studies on isolated single fibres or small muscles. To estimate the metabolic cost of contraction in larger whole muscles, the results of these stud-

ies on small muscles or single fibres are often extrapolated to larger sizes with the assumption that heat and metabolic cost scale with muscle volume and mass, as is typically done with mechanical work and power (Pennycuick & Rezende, 1984). Based on these assumptions, two muscles with identical geometric proportions but different mass are typically assumed to produce the same mass-specific mechanical work and metabolic cost, and therefore efficiency.

Inertial resistance due to muscle mass may limit this assumption that work and metabolic cost scale with muscle volume and mass. Experimental studies examining the intrinsic properties of different fibre-type populations within whole muscle (Holt et al., 2014) or fibre bundles (Josephson & Edman, 1988) have shown that surrounding tissue can act to slow the maximum shortening velocity of muscle fibres. Recent modelling work has shown that muscle tissue mass acts to slow the rate of force development (Günther et al., 2012) and maximum shortening speed of whole muscle (Ross & Wakeling, 2016), and this effect is greater for larger muscles (Böl & Reese, 2008; Meier & Blickhan, 2000; Ross & Wakeling, 2016) and submaximal contractions (Ross & Wakeling, 2016). Inertial resistance due to muscle mass also acts to decrease the mechanical work output of muscle during simulated (Chapter 3) and *in situ* (Chapter 4) cyclic contractions. While muscle mass has been shown to alter the mechanical work of muscle, the metabolic and efficiency consequences of accelerating this internal mass have not yet been described.

In this study we examine the effects of muscle tissue mass on the metabolic cost and efficiency of contraction. Additionally, we explore the extent to which muscle fibre-type properties and excitation, external loading conditions, and series elasticity alter the relationship between muscle mass and muscle metabolic cost and efficiency. To accomplish this, we predicted the mass-specific mechanical work, metabolic cost, and efficiency of cyclic contractions using a Hill-type muscle model that we modified to account for the dynamics of muscle size and mass.

6.3 Methods

6.3.1 Muscle model formulations

The force of the massless Hill-type model (Figure 6.1A) was composed of a contractile element (CE) and parallel elastic element (PEE). The CE force depended on the muscle's activation, length, and velocity, whereas the PEE force depended only on the

muscle's length. We modelled the active and passive force-length and force-velocity curves as Bézier curves fit to experimental data from Winters and colleagues (2011) and Roots and others (2007), respectively. Details of these curves can be found in (Chapter 2). As with most Hill-type muscle models, the massless model does not account for the effects of muscle tissue mass. We added a linear damping term in parallel to the CE to provide viscoelasticity and stabilize the distributed mass of the mass model described below. We used the minimum nondimensional damping constant required to stabilize the masses (0.08), which was similar in magnitude to the value previously used to mimic viscosity effects within muscle tissue (Günther et al., 2007).

The mass-enhanced Hill-type model (Figure 6.1B) is described in detail elsewhere (Günther et al., 2012; Ross & Wakeling, 2016; Ross et al., 2018b). Briefly, the model accounts for muscle mass in a series of 16 point masses distributed along the muscle's length, which are separated by Hill-type actuators that produce force to accelerate the point masses. We modelled the actuator segments between point masses with the same formulation as the massless Hill-type model.

We ran additional simulations with a massless tendon in series with the mass-enhanced model (Figure 6.1C). Our previous work examining mass effects on muscle performance controlled for series elasticity by excluding a series elastic element from the model formulations (Ross & Wakeling, 2016; Chapter 2), or by minimizing tendon effects during *in situ* muscle experiments by attaching the muscle to the servomotor at the myotendinous junction (Ross et al., 2020). By doing so, we were able to make more direct interpretations of the effects of muscle mass without the confounding effects of series elasticity. However, tendons stretch when loaded, and if a tendon is long or compliant, this stretch can uncouple the muscle belly velocity from that of the muscle-tendon unit (MTU); this process may reduce muscle energy requirements (Lichtwark & Barclay, 2010; Lichtwark & Wilson, 2005a) and act to amplify muscle power output (Roberts & Azizi, 2011). Thus, we also examined simulations with a tendon, as series elasticity has important implications for muscle energetics and could modulate the relationship between muscle mass and contraction work, metabolic cost, and efficiency. To model the tendon, we fit the passive force-length Bézier curve to experimental measures of the human Achilles tendon (Dick et al., 2016).

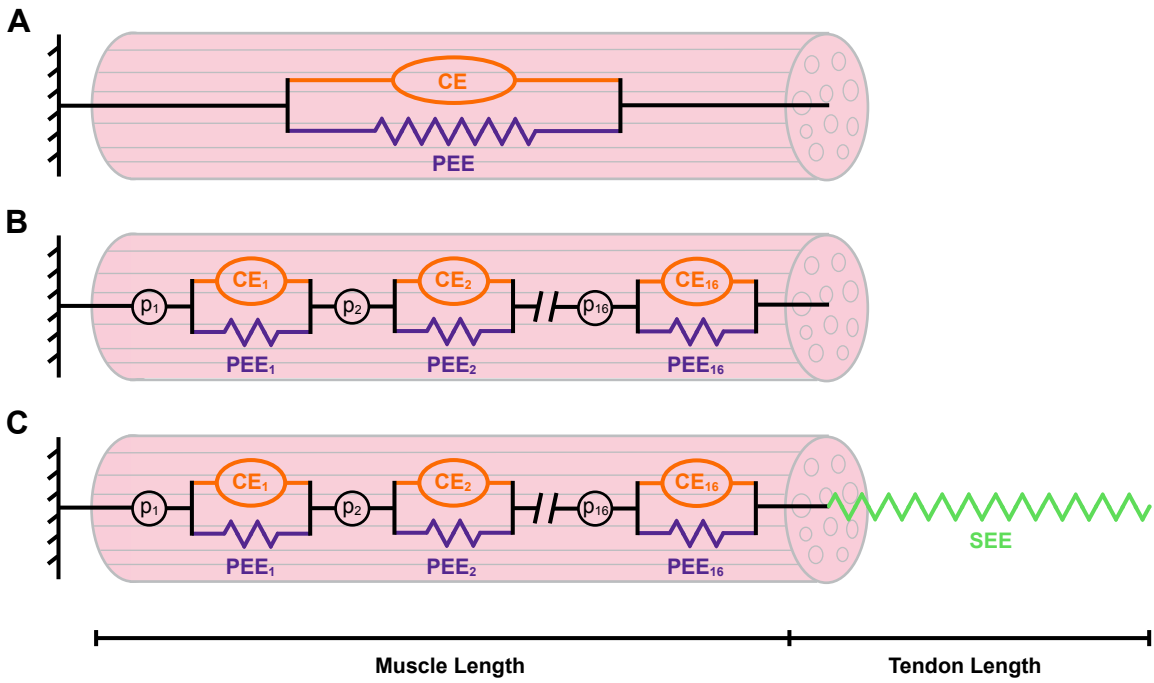

Figure 6.1: Diagram of the muscle models. We simulated contraction cycles of a typical massless Hill-type model with a contractile element (CE) and parallel elastic element (PEE) (A), a mass-enhanced Hill-type model with 16 point masses (p_1 – p_{16}) in series separated by Hill-type segments (B), and a mass-enhanced model with a series tendon or series elastic element (SEE) (C). One end of the muscle models was fixed, and the other was constrained to follow a sinusoidal trajectory. For the model with a tendon, the end of the tendon was constrained to follow a sinusoidal trajectory, rather than the end of the muscle.

6.3.2 Simulations and post-processing

In our previous work examining the effects of muscle mass on mass-specific mechanical work (Chapter 3), we used a framework that coupled the muscle model with a damped harmonic oscillator to simulate cyclic contraction regimes (Chapter 2). By doing so we were able to simulate more variable muscle lengths, velocities, and forces than if the muscle length change was constrained to follow a pre-determined sinusoidal path; this allowed us to examine cycles that more closely mimicked the range of contractions seen during locomotion. However, because damped harmonic oscillators are only able to store and return or dissipate energy, they cannot add energy to the system to allow the muscle to act as a brake (Dickinson et al., 2000). Therefore, we also simulated contraction cycles using constrained sinusoidal length changes to explore mass effects across a wider physiological range.

The damped harmonic oscillator was composed of a point mass, viscous damper, and linear spring. We optimized the oscillator properties and excitation duty cycle to maximize the mass-specific mechanical work per cycle W^* of the massless muscle model for 1 Hz frequency cycles. To drive the muscle and harmonic oscillator system, we converted a time-varying square wave excitation function to activation using an excitation-activation transfer function (Zajac, 1989). This activation scaled the active muscle force and was constant across the muscle tissue at each point in time.

For the sinusoidal contractions, we constrained the muscle length to follow a sinusoidal trajectory with a maximum strain amplitude of ± 10% of optimal muscle length and frequency of 1 Hz. We used the same activation as for the harmonic oscillator simulations in which the excitation started slightly before the start of shortening (-2.6% of cycle or 26 ms). We also shifted the excitation phase by +50% of the cycle duration so that the muscle was primarily active during lengthening and varied the maximum excitation $u_{\max}$ between 0.2 and 1.0, which scaled the excitation amplitude. In addition to using the optimal excitation duty cycle for the harmonic oscillator simulations, we also examined a shorter duty cycle of 0.3. We tested fast and slow fibre-type properties for the harmonic oscillator and sinusoidal simulations without a tendon and tested only fast properties for simulations with a tendon. The fast and slow fibres had maximum shortening strain-rates v_0 and activation rate constants of 10 s^{-1} and 25 ms and 5 s^{-1} and 45 ms, respectively. For simulations with a tendon, we constrained the total MTU (muscle-tendon unit) rather than just the muscle length. Because tendons can uncouple muscle and MTU lengths and velocities, we optimized the stimulation phase relative to the MTU length (using the secant method) so that the excitation would start at the desired time relative to the muscle length. We examined a range of tendon stiffnesses by scaling the slope of the linear region of the tendon force-length curve with the tendon stiffness factor k_{t} (Figure 6.2).

To explore the effects of muscle mass across a range of muscle sizes, we geometrically scaled the models using a length scale factor that we herein refer to as "scale". This method of scaling, described in detail in Ross and colleagues (Chapter 2), resulted in muscle optimal length l_0 and tendon slack length scaling with the scale, muscle maximum isometric force F_0 with scale^2, and muscle volume and mass mm scaling with scale^3, assuming a constant muscle density of 1060 kg m^{-3} and maximum isometric stress of 225 kN m^{-2}. The scale 1 geometry was the approximate size of a fibre bundle with muscle optimal and tendon slack (or resting) lengths of 0.02 m and an aspect ratio (length:width) of 100. As with our previous work (Chapter 3), we found minimal

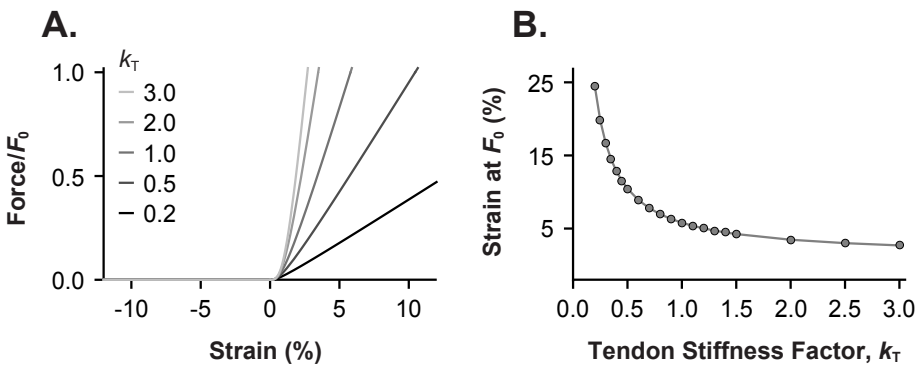

Figure 6.2: Tendon force-strain properties across stiffnesses. (A) Tendon force relative to muscle maximum isometric force F_0 versus tendon strain as a percentage of resting or slack length across selected tendon stiffness factors k_t. (B) Tendon strain at F_0 as a function of k_t.

differences between the scale 1 and 10 simulations and so we report only scale 10 and 100 results in this paper.

We estimated cycle efficiency η as W^* divided by the mass-specific metabolic cost E^*_{met}. A number of different models have been used to estimate E^*_{met} (Bhargava et al., 2004; Houdijk et al., 2006; Lichtwark & Wilson, 2005b; Minetti & Alexander, 1997; Umberger et al., 2003; Umberger, 2010), and there is currently no consensus on which model best reflects muscle metabolic cost *in vivo*. Therefore, we chose to estimate η across the results of six cost models. Four of the six models estimate the rate of E^*_{met}, $\dot{E}^*_{\text{met}}$, as the sum of the mass-specific heat rate $\dot{H}^*_{\text{total}}$ and mechanical power $\dot{W}^*$ (Bhargava et al., 2004; Houdijk et al., 2006; Lichtwark & Wilson, 2005b; Umberger et al., 2003). Because $\dot{W}^*$ is defined as negative during lengthening, if $\dot{H}^*_{\text{total}}$ is low and $\dot{W}^*$ is higher and negative, $\dot{E}^*_{\text{met}}$ and E^*_{met} can be negative, suggesting the muscle can produce metabolic energy through contraction. Therefore, we additionally calculated the metabolic rate as the sum of $\dot{H}^*_{\text{total}}$ and $|\dot{W}^*|$, which we denoted as $\dot{E}^*_{\text{met,abs}}$, to constrain the muscle to only consume and not generate metabolic energy during contraction. To calculate the efficiency η_{abs}, we divided W^* by $E^*_{\text{met,abs}}$ which we determined by integrating $\dot{E}^*_{\text{met,abs}}$ over time for one cycle. Details of these calculations and the cost model formulations can be found in the electronic supplementary material.

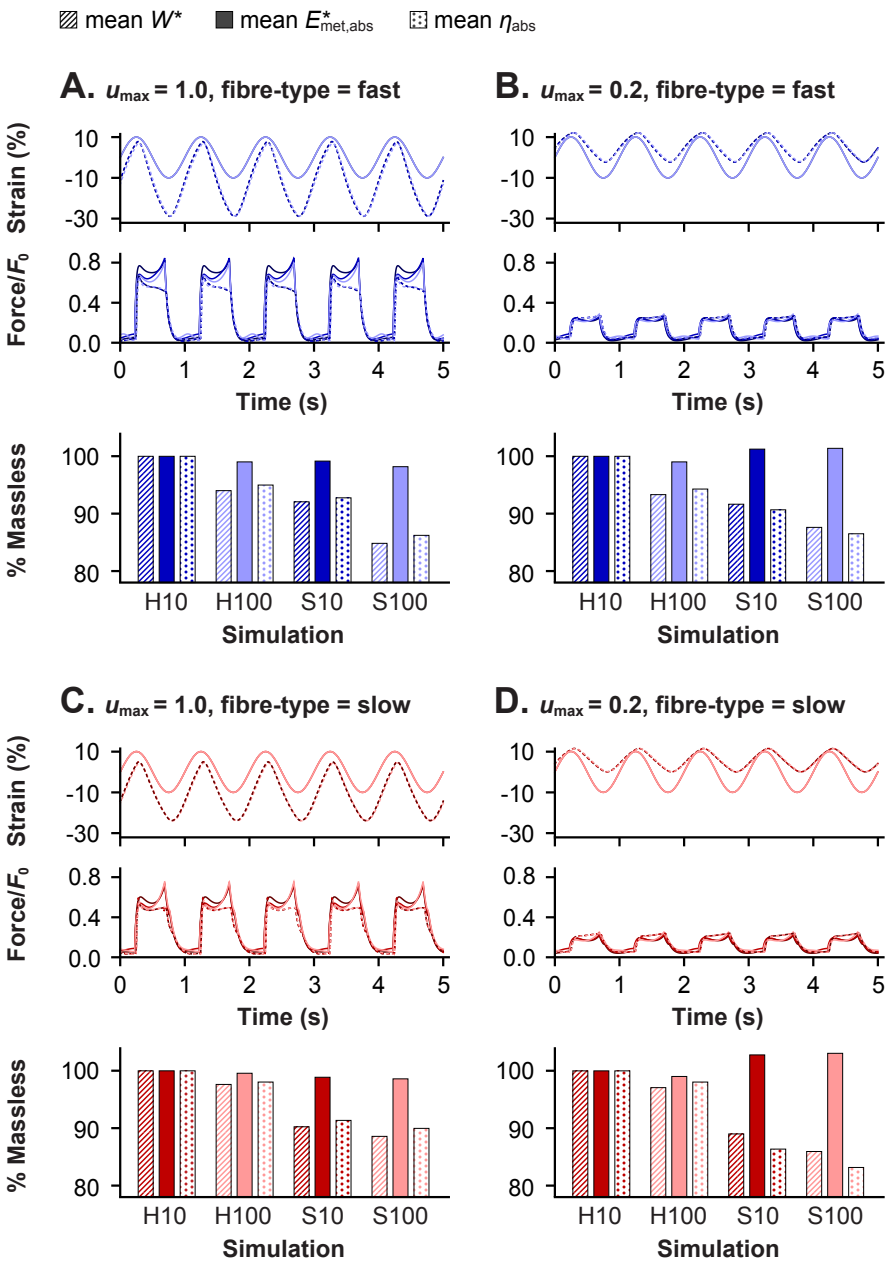

Figure 6.3: Harmonic oscillator versus sinusoidal simulations. Harmonic oscillator versus sinusoidal simulations for maximum excitation $u_{\max}$ of 1.0 and fast fibre-type properties (A), $u_{\max}$ of 0.2 and fast fibre-type properties (B), $u_{\max}$ of 1.0 and slow fibre-type properties (C), and $u_{\max}$ of 0.2 and slow fibre-type properties (D). The top plot in each panel shows muscle strain as a percentage of muscle optimal length and the middle plot shows muscle force normalized to maximum isometric force F_0 over the time of five contraction cycles for harmonic oscillator (dashed) and sinusoidal (solid) simulations. Massless model simulations are shown in the darkest, scale 10 simulations are shown in the intermediate, and scale 100 simulations are shown in the lightest colour. The bar chart in each panel shows the mass-specific mechanical work per cycle W^* (striped), mean metabolic cost $E^*_{\text{met,abs}}$ (solid) and efficiency η_{abs} (bottom; polka dots) relative to the massless condition for harmonic oscillator scale 10 (H10) and scale 100 (H10), and sinusoidal scale 10 (S10) and scale 100 (S100) simulations.

6.4 Results

6.4.1 Mass effects in motor and brake contractions

For the harmonic oscillator simulations, we excited the muscle with a frequency of 1 Hz and for approximately 46% of the total cycle (duty cycle of 0.46). The muscle developed force when it was activated; this caused the muscle to shorten and the harmonic oscillator to stretch to lengths longer than its resting length. The muscle force decreased with deactivation, and because the harmonic oscillator was at a length longer than its resting, the harmonic oscillator force dominated that of the muscle which caused the muscle to stretch. This behaviour repeated every cycle so that the muscle cyclically contracted in time with the activation. Greater $u_{\max}$ resulted in larger muscle shortening strains (Figure 6.3), as did faster fibre-type properties, as these conditions resulted in larger muscle forces to counteract the harmonic oscillator force. In contrast, when the muscle lengths were constrained to follow a sinusoidal trajectory, $u_{\max}$ and the muscle fibre-type properties did not affect the muscle strains.

Despite these differences in muscle strains, both the sinusoidal and harmonic oscillator simulations showed lower W^* with greater muscle mass (Figure 6.3,6.4A), except that there was no difference between the harmonic oscillator massless and scale 10 simulations (Figure 6.3). On average across $u_{\max}$ of 0.2 and 1.0 and both fast and slow fibre-types (total of four simulations), we found a 9.2% reduction in W^* for sinusoidal scale 10 simulations relative to massless, and a 4.5 and 13.2% reduction in W^* for harmonic oscillator and sinusoidal scale 100 simulations relative to massless, respectively. While higher $u_{\max}$ and fast fibre-type properties resulted in greater mean $E^*_{\text{met,abs}}$ across all cost models (Figure 6.4B,C), when $u_{\max}$ and fibre-type properties were controlled for, the effect of muscle mass on $E^*_{\text{met,abs}}$ was small, particularly for the harmonic oscillator contractions (Figure 6.3).

As the effect of mass on $E^*_{\text{met,abs}}$ was minimal for simulations without a tendon, the effect of mass on η_{abs} primarily followed changes in W^*. For both the harmonic oscillator and sinusoidal contractions, greater mass resulted in lower η_{abs} relative to massless across values of $u_{\max}$ and both fibre-types, except for harmonic oscillator contractions at scale 10 relative to massless in which there was no difference in W^*, $E^*_{\text{met,abs}}$, or η_{abs} (Figure 6.3,6.4A). The reduction in η_{abs} due to larger mass was greater on average for sinusoidal (9.7% for scale 10 and 13.5% for scale 100 relative to

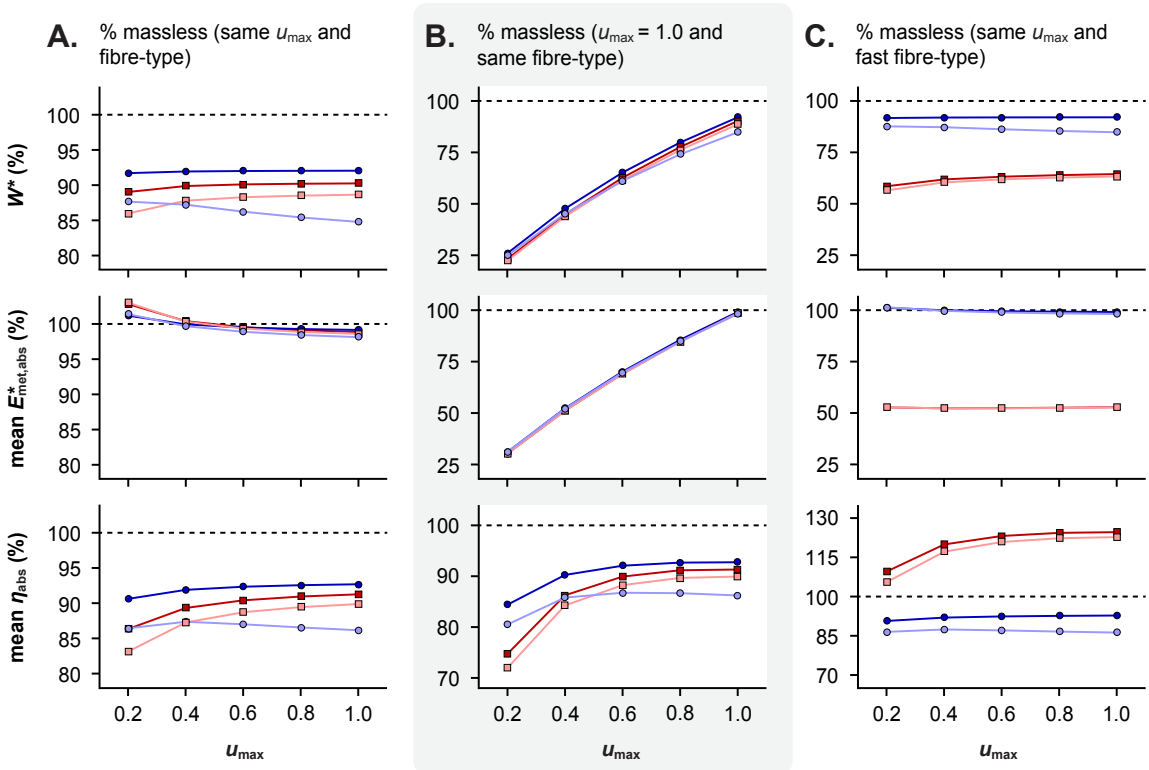

Figure 6.4: Effects of muscle mass across fibre-types and excitations for motor (phase +0%) contractions. Effects of muscle mass on mass-specific work per cycle W^*, mean metabolic cost $E^*_{\text{met,abs}}$, and efficiency η_{abs} during sinusoidal contractions as a percentage of massless at the same maximum excitation u_{max} and fibre-type (A), at u_{max} of 1.0 and the same fibre-type (B), and at the same u_{max} and fast fibre-type (C). Fast fibres are shown as blue squares, slow fibres as red circles, and scale 10 and 100 are shown in dark and light colours, respectively.

massless) compared to harmonic oscillator contractions (0.0% for scale 10 and 3.7% for scale 100 relative to massless) across u_{max} of 0.2 and 1.0 and both fibre-types (Figure 6.3). Both η_{abs} and η were lower for greater mass across all six metabolic cost models.

Because harmonic oscillators can only store and return or dissipate energy and cannot inject energy into the system, as is required for eccentric braking contractions, we only simulated braking contraction cycles with sinusoidal muscle length changes and not with the harmonic oscillator. W^* was negative for these simulations, so a reduction in W^* as a percentage of that of the massless condition indicates negative W^* that is lower in magnitude relative to massless. All scale 10 and 100 simulations showed reductions in W^* relative to massless, indicating less energy was absorbed

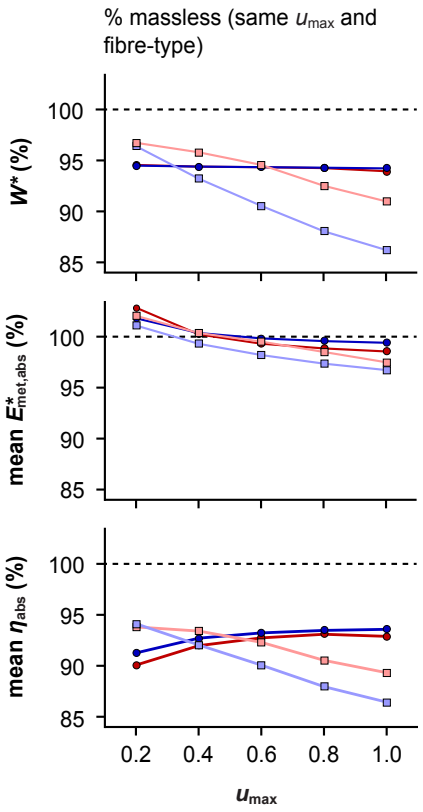

Figure 6.5: Effects of muscle mass across fibre-types and excitations for brake (phase +50%) contractions. Effects of muscle mass on mass-specific work per cycle W^*, mean metabolic cost $E^*_{\text{met,abs}}$, and mean efficiency η_{abs} during sinusoidal contractions as a percentage of massless at the same maximum excitation u_{max} and fibre-type. Fast fibres are shown as blue squares, slow fibres as red circles, and scale 10 and 100 are shown in dark and light colours, respectively.

or dissipated by the muscle (Figure 6.5). Across u_{max} of 0.2 and 1.0 and both fibre-types, we found a 5.7% and 7.4% reduction in W^* for sinusoidal scale 10 and 100 simulations relative to massless, respectively. As with motor contractions, differences in η_{abs} relative to massless primarily followed changes in W^* with both scale 10 and 100 simulations showing lower η_{abs} relative to massless. These trends in η_{abs} were consistent across all six cost models; however, η depended on the cost model used and its treatment of negative $\dot{W}^*$.

6.4.2 Effects of series elasticity and muscle mass

For the motor simulations (Figure 6.6A,B), the tendon (with k_{t} of 1) mitigated some of the reduction in W^* due to greater mass (Figure 6.7A). On average across u_{max} of

0.2 and 1.0, W^* was 1.7% higher for scale 10 and 3.4% higher for scale 100 simulations with a duty cycle of 0.46, and 10.8% higher for scale 10 and 9.4% higher for scale 100 simulations with a duty cycle of 0.3 with a tendon compared to without. Across both duty cycles, scales, and $u_{\max}$s, adding a tendon in series to the muscle increased $E^*_{\text{met,abs}}$ by 3.1% (Figure 6.7A). The added tendon had little effect on η_{abs} for simulations with a duty cycle of 0.46, whereas the tendon increased η_{abs} by 7.3% on average across both $u_{\max}$s and scales for duty cycle of 0.3. These results were the same for mean E^*_{met} and η, and LW05 was the only cost model that predicted lower $E^*_{\text{met,abs}}$ and E^*_{met} with a tendon and duty cycle of 0.46. For duty cycle of 0.3, the added tendon resulted in higher $E^*_{\text{met,abs}}$, E^*_{met}, η_{abs}, and η across all cost models.

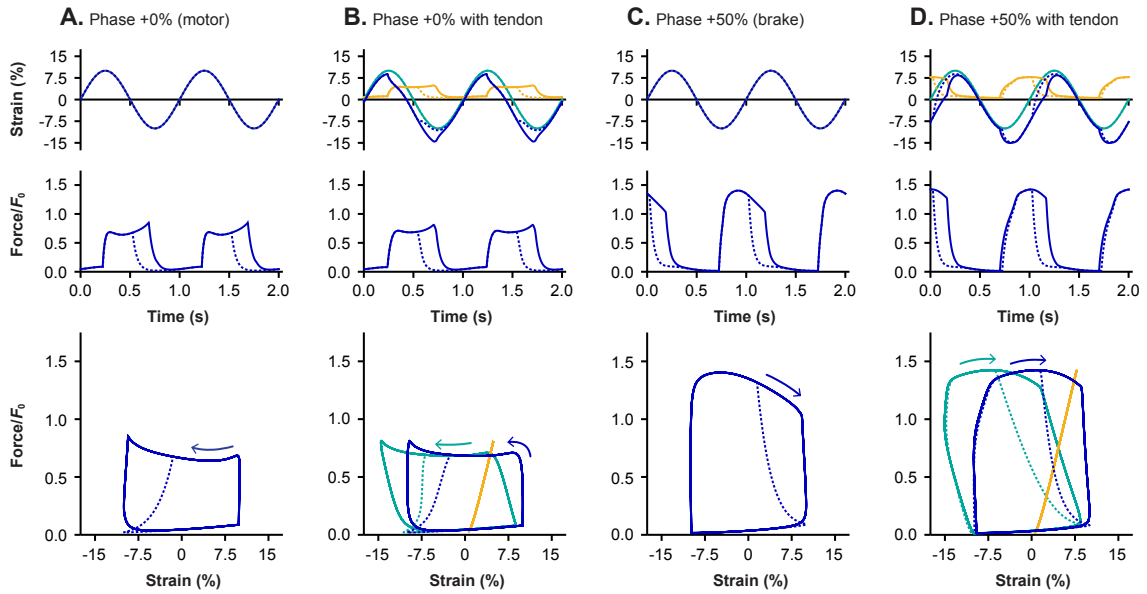

Figure 6.6: Effects of the added tendon and excitation phase on muscle strain and force. Muscle strain as a percentage of optimal length over time (top row), muscle force normalized to maximum isometric force F_0 over time (middle row), and work-loops of normalized muscle force versus strain (bottom) for the scale 10 mass model. (A) phase +0% (motor) contractions without a tendon, (B) phase +0% (motor) contractions with a tendon, (C) phase +50% (brake) contractions without a tendon, and (D) phase +50% (brake) contractions with a tendon. The muscle is shown in dark blue, the muscle-tendon unit is teal, and the tendon is orange. Solid lines show simulations with a duty cycle of approximately 0.46 and dashed lines show simulations with duty cycle of 0.3.

For the brake simulations (Figure 6.6C,D), the added tendon resulted in 1.6% higher W^* relative to mass simulations without a tendon (more negative absolute W^*) on average across both scales and $u_{\max}$s with 0.46 duty cycle. The effect of series elasticity was less clear for simulations with a duty cycle of 0.3 (Figure 6.7B). As with the

motor contractions, the addition of a tendon increased the $E^*_{\text{met,abs}}$ for both scales, duty cycles, and $u_{\max}$ values, and this was consistent across all six cost models. Brake simulations with a tendon resulted in 13.0% lower η_{abs} on average (less negative absolute η_{abs}) relative to mass simulations without a tendon for both scales, duty cycles and $u_{\max}$s. The effect of a tendon on E^*_{met} and η during braking contractions depended on the cost model used.

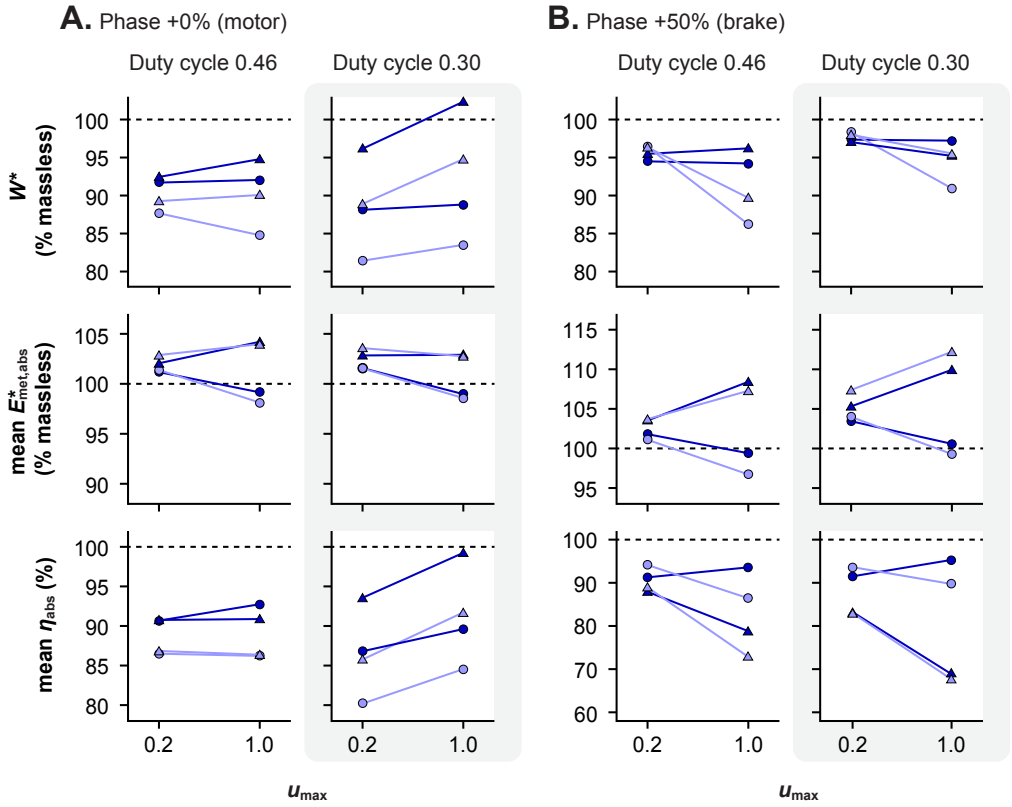

Figure 6.7: Effects of series elasticity and muscle mass. Effects of muscle mass on mass-specific work per cycle W^*, mean metabolic cost $E^*_{\text{met,abs}}$, and mean efficiency η_{abs} during sinusoidal contractions as a percentage of massless for simulations with excitation phase of +0% (A) and +50% (B), duty cycle of 0.46 and 0.3, maximum excitations $u_{\max}$ of 0.2 and 1.0, and fast fibre-type properties. Simulations with a tendon of base stiffness (k_{t} of 1) are shown as triangles and those without a tendon as circles, and scale 10 and 100 are shown as dark blue and light blue, respectively.

6.4.3 Effects of mass and series elasticity on instantaneous mechanical power

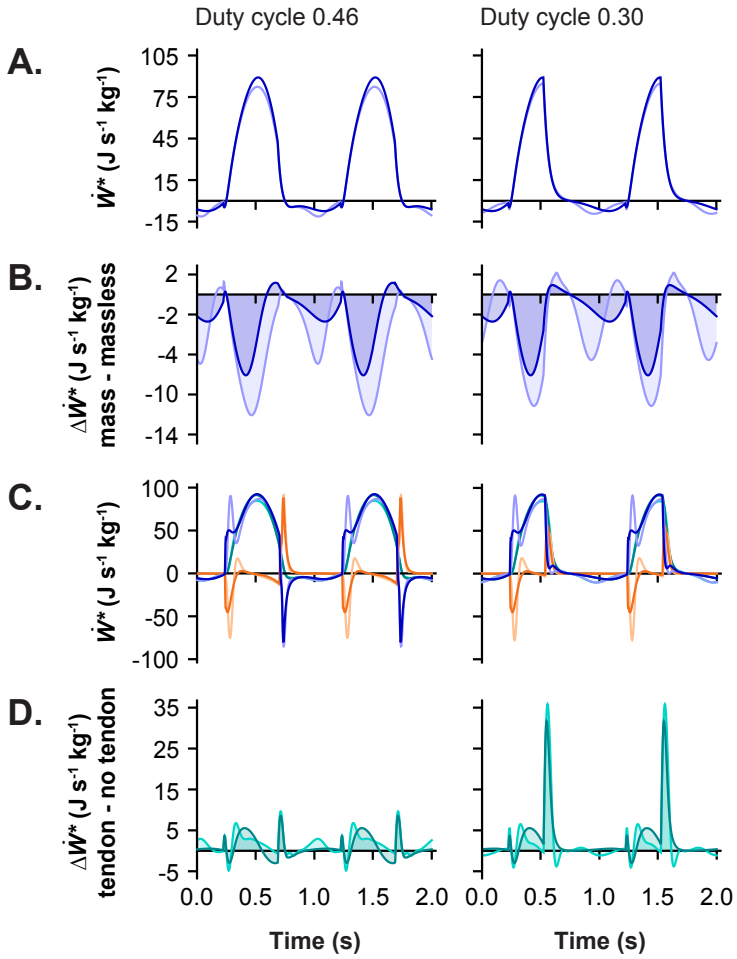

Figure 6.8: The effects of muscle mass and series elasticity on mechanical power. Mass-specific mechanical power $\dot{W}^*$ in J s^{-1} kg^{-1} for mass model simulations (A) and difference in $\dot{W}^*$ between mass model and otherwise equivalent massless model simulations $\Delta\dot{W}^*$ (B) for scale 10 (dark blue) and 100 (light blue) simulations without a tendon over time. (C) Mass-specific mechanical power $\dot{W}^*$ of the muscle (blue), tendon (orange), and muscle-tendon unit (green) for scale 10 (dark colours) and 100 (light colours) mass simulations with a tendon over time. (D) Difference in muscle-tendon unit $\dot{W}^*$ for mass model simulations with a tendon and otherwise equivalent simulations of the mass model without a tendon $\Delta\dot{W}^*$. The left panel shows simulations with an excitation duty cycle of approximately 0.46 and the right shows simulations with an excitation duty cycle of 0.3. All simulations are for fast fibre-type properties and maximum excitation of 1.0.

For motor contractions at $u_{\max}$ of 1.0 without a tendon, $\dot{W}^*$ increased when the muscle was activated and reached its peak approximately halfway through the shortening phase when the muscle shortening velocity was greatest (Figure 6.8A). $\dot{W}^*$ became

negative when the muscle started to lengthen, and the magnitude of this negative $\dot{W}^*$ was greater for 0.46 duty cycle simulations compared to 0.3, as the muscle was still active for a short period of time at the start of lengthening. Greater muscle mass decreased the maximum $\dot{W}^*$ during shortening (Fig 6.8B). Across both duty cycles, we found a 4.4 and 10.0 J s^{-1} kg^{-1} (4.7% and 10.7%) decrease in peak $\dot{W}^*$ for scale 10 and 100 relative to massless, respectively.

We activated the muscle 2.6% of the cycle duration prior to the start of muscle shortening, which allowed the tendon to stretch and store energy when the muscle shortened and the MTU length was nearly constant (Figure 6.6B,6.8C). The tendon then stayed at a longer length until the muscle was deactivated, where the tendon shortened and released stored elastic energy to increase $\dot{W}^*$ of the MTU (Figure 6.8D). Because this tendon energy release occurred after peak MTU $\dot{W}^*$, the tendon did not act to amplify $\dot{W}^*$ of the MTU beyond what the muscle alone could generate (Figure 6.8C).

6.4.4 Effects of altering tendon stiffness

For the motor contractions at $u_{\max}$ of 1.0, increasing the tendon stiffness decreased W^* for both scale 10 and 100 simulations (Figure 6.9). This decrease was much greater with a duty cycle of 0.3 compared to 0.46. The maximum W^* for simulations with a tendon occurred at a tendon stiffness that was more compliant than the base stiffness (k_{t} of 1). The maximum W^* also occurred at a lower stiffness when the muscle mass was larger, with the maximum occurring at a k_{t} of 0.6 for scale 10 and 0.3 for scale 100 with a duty cycle of 0.46, and 0.35 for scale 10 and 0.3 for scale 100 with a duty cycle of 0.3. Lower k_{t} resulted in higher E^*_{met} for both duty cycles, and this was the case across all six cost models. With a duty cycle of 0.46, the highest η_{abs} occurred at the highest tendon stiffnesses, due to large increases in $E^*_{\mathrm{met,abs}}$ at low stiffnesses (Figure 6.9A). For a duty cycle of 0.3, maximum η_{abs} occurred at k_{t} of 0.5 for scale 10 and 0.7 for scale 100 (Figure 6.9B). These results did not vary when E^*_{met} was used to estimate η.

6.5 Discussion

6.5.1 Mass effects across excitations and fibre-types for motor contractions

We found that for motor contractions where the muscle was primarily active during shortening, greater mass resulted in lower mass-specific mechanical work per cycle. This is consistent with our previous modelling studies using this mass model (Chapter 3; Chapter 4), and with our experimental results showing that increasing muscle effective mass *in situ* decreases mechanical work per cycle (Chapter 4). Because altering the mass of muscle had little effect on metabolic cost, greater mass also resulted in lower efficiency per cycle for motor contractions due to the lower mechanical work (Figure 6.3,6.4A). In our previous simulation work (Chapter 3), and for the simulations here in which the muscle contracted against a damped harmonic oscillator (Figure 6.3), we found that lower excitation resulted in larger reductions in mass-specific mechanical work with greater muscle mass for both fast and slow fibre-type properties. This is consistent with experimental (Holt et al., 2014) and simulation (Ross & Wakeling, 2016) findings in which submaximal activation of either fast or slow fibres within whole muscle resulted in slower maximum contraction speeds compared to maximal activation of the entire muscle tissue, due to the greater inertia of inactive tissue during the submaximal contractions.

For the sinusoidal contractions, we found that lower excitations only resulted in larger reductions in work with greater mass when the muscle had slow fibre-type properties, whereas muscles with fast fibre-type properties showed the greatest reductions in mass-specific work per cycle at the highest excitations (Figure 6.4A). This difference in mass effects across excitations for fast muscle between the sinusoidal and harmonic oscillator simulations may be due to differences in muscle strain during the cycle shortening phase. Because muscle length was not constrained in the harmonic oscillator simulations, higher muscle forces in simulations with higher excitations and fast fibre-type properties resulted in larger shortening strains, whereas strains in the sinusoidal simulations were unaffected by both excitation and muscle fibre-type. For sinusoidal contractions, we also found greater reductions in muscle force with greater muscle mass, primarily near the start of shortening, compared to harmonic oscillator contractions. During locomotion, muscle lengths are not directly controlled, and rather emerge due to muscle forces relative to the external loads (Dickinson et al.,

2000), similar to the harmonic oscillator simulations. However, unlike the harmonic oscillator simulations, muscle lengths can be indirectly controlled by altering the neural drive using sensory feedback. Therefore, whether the sinusoidal or harmonic oscillator simulations better reflect *in vivo* mass effects for faster muscle is not clear.

Fast fibres resulted in lower mass-specific work with greater mass compared to slow fibres across all excitations. When muscle is activated, smaller, slower motor units are typically recruited before larger, faster ones in accordance with the size principle (Henneman et al., 1965a). However, strictly following the size principle may pose a mechanical paradox under certain conditions (for review, see Hodson-Tole & Wakeling, 2009), such as contractions faster than the maximum intrinsic shortening speed of slow fibres (Rome et al., 1988). Thus, under these conditions, slow fibres cannot contribute to force production or work output but still incur a metabolic cost. To address this paradox, faster motor units may be recruited first when slower motor units would be mechanically ineffective, and this has been supported by experimental studies (Citterio et al., 1982; Wakeling et al., 2006). The extent to which this alternate recruitment strategy occurs may also depend on muscle mass in addition to contraction speed. In this study, we found that reductions in mass-specific work and efficiency were greater for fast fibres compared to slow (Figure 6.4A). While the slow fibres were still more efficient than fast fibres due to the relatively slow sinusoidal velocities (Figure 6.4C), the contraction speed at which fast fibres become more efficient may be faster for larger muscles with greater mass. Thus, there may be less mechanical benefit of recruiting faster fibres before slower fibres during faster contractions for larger muscles.

6.5.2 Effects of series elasticity and muscle mass

Compliant tendons have been shown to increase MTU work and efficiency per cycle by decreasing muscle shortening velocity and increasing muscle force during contraction cycles with prescribed excitation (Ettema, 2001; Lichtwark & Barclay, 2010), or to decrease muscle work requirements and increase efficiency by allowing the muscle to contract over a shorter length range during locomotion (Biewener, Konieczynski, & Baudinette, 1998; Biewener et al., 2004; Fukunaga et al., 2001). We found that the addition of a tendon with the approximate stiffness of a human Achilles tendon (Dick et al., 2016) increased work per cycle for motor contractions and mitigated some of the work reductions due to greater mass (Figure 6.7A), and this work in-

crease was greater with the shorter excitation duty cycle of 0.3. With a duty cycle of 0.3, the tendon increased efficiency as it allowed the muscle to contract nearly isometrically during tendon recoil (Figure 6.6B). In contrast, with a duty cycle of 0.46, the muscle underwent greater shortening than the MTU, which increased both work and metabolic cost (Figure 6.7A). This is consistent with a study by Lichtwark and Wilson (2005a) in which peak average power occurred at a duty cycle between 0.3 and 0.4 and peak efficiency occurred at a much lower duty cycle of around 0.1. Thus, while the work increases due to series elasticity with a duty cycle of 0.3 may be close to maximal, greater increases in efficiency may have been possible with a shorter duty cycle at the expense of high work output.

The effect of a tendon on MTU work also depends on the excitation phase relative to the start of MTU shortening (Ettema, 1996, 2001; Lichtwark & Barclay, 2010; Lichtwark & Wilson, 2005a; Sawicki et al., 2015). Earlier activation of the muscle while the MTU is still lengthening can allow for greater storage of elastic energy, as the tendon can store energy from external work as well as work done by the shortening fibres (Ettema, 2001). This additional elastic energy can then be returned later during the shortening phase to increase MTU work output and efficiency. In this study, we used an excitation phase of -2.6% relative to the start of muscle shortening to match the phase that emerged from the harmonic oscillator simulations. For the base tendon with a stiffness factor of 1, this resulted in a phase of -3.8% relative to the start of MTU shortening. Because we selected the harmonic oscillator properties to maximize mechanical work per cycle in the massless model without a tendon, this phase may not be optimal for maximizing work and efficiency in the mass-enhanced model with a tendon. Thus, an earlier phase may have led to greater energy storage in the tendon during MTU lengthening. We also used this same excitation phase and duty cycle across all simulations, but because greater muscle mass decreases the rate of force development (Günther et al., 2012), larger muscles may require earlier phases to maximize work per cycle so the tendon can fully stretch and store energy before the start of MTU shortening.

6.5.3 Effects of mass and series elasticity on instantaneous mechanical power

Achieving high instantaneous muscle power output is required for a variety of locomotor tasks, such as jumping and accelerating the body from rest, and is thought to be

limited by the muscle's intrinsic force-velocity properties (Biewener & Patek, 2018). In this study we found that greater muscle mass decreased muscle mass-specific peak instantaneous power (Figure 6.8A,B), indicating that a muscle's mass may be an important consideration for maximizing power in addition to its intrinsic force-velocity properties.

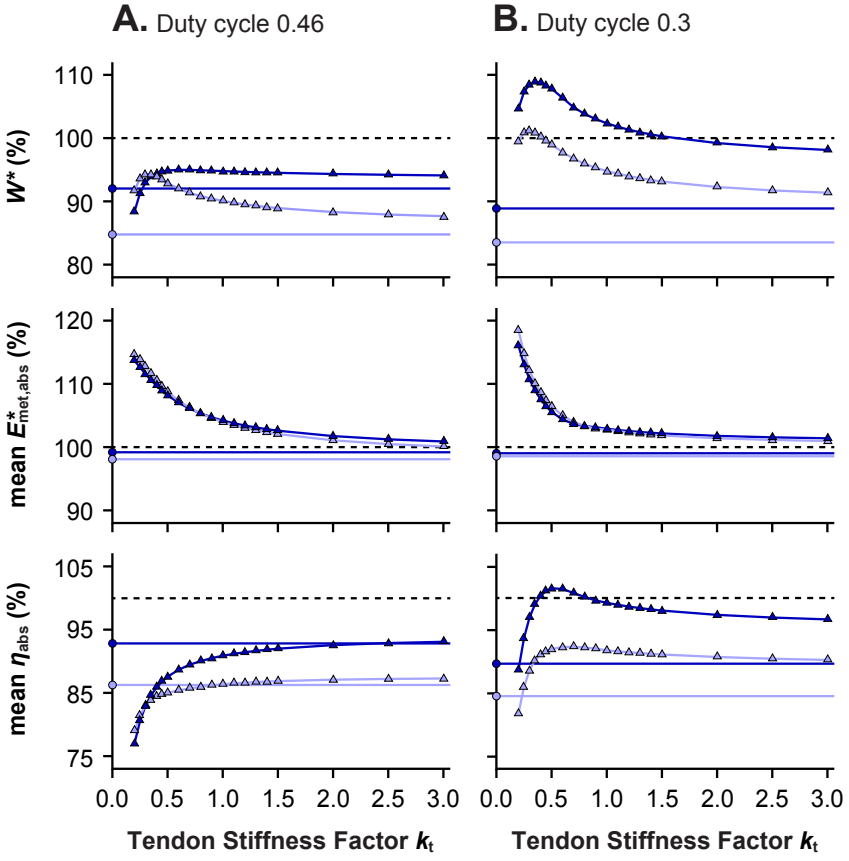

Figure 6.9: Effects of tendon stiffness across muscle masses. Mass-specific work per cycle W^*, mean metabolic cost $E^*_{\text{met,abs}}$, and mean efficiency η_{abs} during sinusoidal contractions expressed as a percentage of massless simulations without a tendon across tendon stiffness factors k_{t} for simulations with a duty cycle of 0.46 (A) and 0.3 (B). Scale 10 simulations are shown in dark blue, scale 100 are shown in light blue, and mass simulations with and without a tendon are shown as triangles and circles, respectively. All simulations are with fast fibre-type properties and maximum excitation of 1.0.

The mechanical power requirements of tasks such as jumping have been shown to exceed the maximum instantaneous power output predicted from the intrinsic force-velocity properties of muscle. MTU instantaneous power can be increased using elastic mechanisms in which energy stored in the elastic structure is rapidly released to amplify the MTU power to beyond what muscle alone can generate (Roberts & Azizi,

2011). For amplification to occur, the tendon must first stretch to store elastic energy, and then later release this energy at the time coinciding with peak muscle power (Ker et al., 1988). In this study, we found that tendon energy release occurred later than peak MTU power for both excitation duty cycles (Figure 6.8C,D). For a duty cycle of 0.46, the tendon recoiled and released its stored energy near the start of lengthening, and the elastic energy release was not effective in increasing peak instantaneous MTU power. With a duty cycle of 0.3, tendon energy release occurred during shortening, which enhanced the instantaneous MTU power output but did not amplify the maximum power. As with increasing mechanical work per cycle, power amplification to mitigate reductions in peak instantaneous power with greater mass may be achieved with a shorter duty cycle or shifting the excitation phase earlier relative to the start of MTU shortening.

6.5.4 Effects of altering tendon stiffness

Measures of tendon mechanical properties have shown that their stiffness relative to maximum muscle force varies widely across mammals (Ker et al., 1988), and tendon stiffness can change with age (Nakagawa, 1996), and training (Duclay et al., 2009). Even within the same tendon, like the extensively studied human Achilles tendon, stiffness can vary substantially, even within single studies using the same measurement technique (Burgess et al., 2009; Morrison et al., 2015). Compliant tendons can increase cyclic work and efficiency to a greater extent than stiff tendons (Ettema, 1996, 2001; Lichtwark & Barclay, 2010; Lichtwark & Wilson, 2007, 2008), but if a tendon is too compliant, the muscle must shorten too quickly to stretch the tendon and store elastic energy before the start of MTU shortening (Lichtwark et al., 2007), increasing metabolic cost (Uchida et al., 2016) and decreasing efficiency (Lichtwark et al., 2007). Our results confirm that an intermediate tendon stiffness results in the highest work and efficiency per cycle compared to overly compliant or stiff tendons (Figure 6.9). Regardless of the duty cycle or muscle mass, optimal work and efficiency occurred at more compliant stiffnesses than the base tendon with human Achilles tendon properties (stiffness factor of 1). This may be because our muscle model properties and geometry did not reflect those of a muscle that attaches to the Achilles tendon *in vivo*. Modelling the muscle as a human plantarflexor muscle may have resulted in the optimal work and efficiency occurring closer to the base tendon stiffness, as in (Lichtwark & Wilson, 2007), assuming that the material properties of tendon are optimized to maximize work and efficiency for a given muscle design.

For simulations in which we varied tendon stiffness, we kept both the excitation duty cycle and phase relative to the muscle (not MTU) length constant. As with different scales, the optimal duty cycle and phase for peak work and efficiency per cycle may vary depending on the tendon stiffness. Compliant tendons have been shown to achieve high average power output and efficiency with earlier excitation phases relative to the start of MTU shortening (Ettema, 2001; Lichtwark & Wilson, 2005a) and shorter duty cycles or longer periods of relaxation during shortening (Ettema, 2001; Lichtwark & Barclay, 2010) compared to stiffer tendons. Despite the possibly non-optimal work and efficiency across tendon stiffnesses, work reductions due to muscle mass were entirely compensated for by a tendon with optimal stiffness with a duty cycle of 0.3 (Figure 6.9B). While reductions in efficiency were only entirely compensated for with the smaller scale 10 simulations, the largest scale 100 model was able to overcome approximately half of the efficiency reduction due to its mass with an optimal stiffness tendon.

6.5.5 Implications for whole-body locomotion and comparative biomechanics

In this study, we found that larger muscles are less efficient because they generate less work due to their greater mass compared to smaller muscles or simulated massless models. In living animals, skeletal muscles do work to move the skeleton and also account for a large proportion of metabolic energy expenditure during locomotion. Thus, one could expect that whole-body efficiency during locomotion would be lower for larger animals. However, comparative studies have found that larger animals exhibit lower mass-specific metabolic cost of locomotion relative to smaller animals (Taylor et al., 1970). Because mass-specific mechanical work required to move a given distance varies little across animals of different sizes (Heglund et al., 1982), the overall efficiency of the body during locomotion increases with body size. Differences in the mechanical design of MTUs in smaller and larger animals, such as differences in speed and muscle fibre-type properties, elastic energy storage, and muscle geometry, may account for this difference in locomotor efficiency predicted by our muscle-level results compared to measured whole-body values.

1. Allometry of muscle fibre-type properties and speed of locomotion

The reduction in efficiency of larger muscles may be mitigated in larger animals by them having slower and less costly muscle fibres-types. At the fibre level, a faster

fibre will have higher work output for an otherwise equivalent contraction cycle than a slower fibre because it can generate more force at a given shortening velocity (or strain-rate) and also activate and deactivate more quickly. However, because faster fibres also incur higher metabolic cost compared to slower fibres (Barclay et al., 1993; Reggiani et al., 1997), faster fibres are less efficient at slower shortening velocities (Reggiani et al., 1997) but more efficient at faster velocities where their force and work is higher than slower fibres (He et al., 2000). If muscles with faster fibres experience a greater reduction in mass-specific mechanical work per cycle due to greater mass compared to muscles with slower fibres, as we found in this study (Figure 6.4), the contraction velocity at which faster fibres become more efficient may be higher for larger muscles. Thus, faster fibres may have less value in larger animals with muscles that operate at velocities below those corresponding with this efficiency threshold. Additionally, smaller animals have faster stride frequencies (Heglund et al., 1974) that require rapid rates of force development and relaxation. Faster fibres that activate and deactivate quickly are required to achieve this rapid force development and relaxation, which increases metabolic cost and decreases efficiency. Again, there may be less need for larger animals to operate faster, but more costly, fibres because of their slower stride frequencies.

Muscle fibres in larger animals do in fact have lower maximum intrinsic shortening velocities than equivalent fibres-types in smaller animals (Rome et al., 1990; Seow & Ford, 1991), and they also operate at lower frequencies (Heglund et al., 1974) and strain rates (Medler, 2002). These differences in muscle fibre physiology that are adapted to the slower gait parameters may mitigate the otherwise possible reductions in efficiency that would occur with recruiting the fastest fibres for the largest animals.

2. Allometry of elastic energy storage and return

Our results show that tendon with appropriate stiffness can increase MTU work and efficiency and offset some of the performance deficits due to greater muscle mass. For larger muscle, this work and efficiency benefit was greatest at a lower tendon stiffness compared to smaller muscle with lower mass. Studies have shown that the elastic modulus of tendon is relatively constant across terrestrial animals of different sizes (Bennett et al., 1986; Pollock & Shadwick, 1994b); however, tendon cross-sectional area relative to that of muscle, and therefore their approximate ability to withstand forces, decreases with body size (Alexander et al., 1981; Pollock

& Shadwick, 1994a). This means that tendons in larger animals will stretch and store more elastic energy for a given relative muscle stress, which is mechanically akin to varying tendon stiffness as we did in this study. Although there have been opposing arguments to suggest elastic energy savings are more important in smaller animals (Bullimore & Burn, 2005), greater elastic savings in larger animals could help mitigate the effects of their greater muscle mass.

3. Allometry of muscle geometry and architecture

Larger muscles may have different geometry and architecture to limit reductions in work and efficiency due to greater muscle mass. The effects of mass on contractile performance are due to a balance between the contractile element forces within muscle and the inertial loads due to the tissue mass. If muscles were parallel-fibred and scaled isometrically in size, in that the length l, width, and thickness increased proportionately, like the muscle models scaled in this study, the muscle force would scale in proportion to the muscle cross-sectional area A and the inertial load (product of mass and acceleration) would scale in proportion to $A\ l^2$, assuming constant density and maximum isometric stress. Thus, in this scenario the mass effects would scale with the muscle length squared, or in simpler terms, longer muscles would experience greater reductions in work and efficiency compared to shorter muscles. Studies comparing muscle architecture across a range of animal sizes have shown that muscles in larger animals have relatively larger cross-sectional areas and shorter fibres (Alexander et al., 1981; Pollock & Shadwick, 1994a). While this has been suggested to reduce the high stresses and increase the safety factor of muscles in larger animals, it may also have work and efficiency benefits for larger muscles.

While this is an appealing explanation, only a small proportion of muscles are considered to be entirely parallel-fibred; in reality, most muscles are pennate and non-uniform in geometry. In pennate muscle, fibres are oriented at an angle relative to the force-generating axis of the muscle. We previously found smaller reductions in mass-specific mechanical work due to greater mass in muscles with higher fibre pennation angles at rest (Chapter 5). If we assume that pennation angle has little effect on metabolic cost, which may be reasonable given how little muscle mass altered metabolic cost in this study, muscles with higher pennations may be more efficient for larger muscles in larger animals. Pennation angle has been shown to increase with body mass in Monitor lizards ranging in size from 8 grams to 40

kilograms (Dick & Clemente, 2016), and this may be a mechanism to limit the work and efficiency penalty of greater muscle mass. Aponeurosis may also play a role in limiting the effects of muscle mass in larger animals. We previously showed that larger muscles with greater mass store more energy in aponeurosis during cyclic contractions (Chapter 5). However, it is not yet clear what role this energy storage has in mitigating the effects of greater muscle mass, and if this role is altered with changes in aponeurosis properties with body size.

6.6 Supplementary material

6.6.1 Implementation of metabolic cost models

In this study, we examined the effects of muscle mass on the mass-specific mechanical work, mass-specific metabolic cost, and efficiency of contraction. We calculated the efficiency as the net mass-specific mechanical work per cycle divided by the net mass-specific metabolic cost per cycle and estimated the metabolic cost using six different cost models established in the literature: Bhargava et al., 2004 (B04), Houdijk et al., 2006 (H06), Lichtwark & Wilson, 2005b (LW05), Minetti & Alexander, 1997 (MA97), Umberger et al., 2003 (U03), and Umberger, 2010 (U10). Variables and definitions that are general across the Hill-type muscle and metabolic cost model simulations can be found in Table S1 and those that are specific to each model can be found in the table within the given model's subsection. Where possible we used variables from the original sources when implementing the metabolic cost models.

We calculated the mechanical efficiency η as:

$$\eta = \frac{W^*}{E^*_{\text{met}}} \tag{6.1}$$

where E^*_{met} is the mass-specific metabolic cost per cycle and is given by the integral of the mass-specific metabolic energy rate $\dot{E}^*_{\text{met}}$ over the time of each cycle (t_1 to t_2):

$$E^*_{\text{met}} = \int_{t_1}^{t_2} \dot{E}^*_{\text{met}} dt. \tag{6.2}$$

For B04, H06, LW05, and U03, the mass-specific metabolic energy rate $\dot{E}^*_{\text{met}}$ was given by:

$$E^*_{\text{met}} = \dot{H}^*_{\text{total}} + \dot{W}^* \tag{6.3}$$

where $\dot{H}^*_{\text{total}}$ is the mass-specific total heat rate:

$$\dot{H}^*_{\text{total}} = \frac{H^*_{\text{total}}}{m_{\text{m}}} \tag{6.4}$$

Table 6.1: Variables and parameters across all metabolic cost models.

Variable	Definition
m_m	muscle mass (kg)
u	muscle excitation (dimensionless)
$\hat{a}$	muscle activation (dimensionless)
v	muscle velocity (m s^{-1})
v_0	maximum shortening strain-rate (s^{-1})
F	muscle force (N)
$\hat{F}$	muscle force/maximum isometric force (dimensionless)
F_0	maximum isometric force (N)
$\dot{F}$	muscle force rate (N s^{-1})
F_{A}	Active muscle force as a function of length/F_0 (dimensionless)
F_{V}	Active muscle force as a function of velocity/F_0 (dimensionless)
l	muscle length (m)
$\hat{l}$	muscle length/optimal length (dimensionless)
l_0	optimal length (m)
$\dot{W}^*$	instantaneous mass-specific mechanical power (J s^{-1} kg^{-1})
W^*	mass-specific mechanical work per cycle (J kg^{-1})
$\dot{H}_{\mathrm{total}}$	total heat rate (J s^{-1})
$\dot{H}^*_{\mathrm{total}}$	mass-specific total heat rate (J s^{-1} kg^{-1})
H^*_{total}	mass-specific total heat per cycle (J kg^{-1})
$\dot{E}^*_{\mathrm{met}}$	mass-specific metabolic energy rate (J s^{-1} k^{-1})
E^*_{met}	mass-specific metabolic cost per cycle (J kg^{-1})
$\dot{E}^*_{\mathrm{met,abs}}$	mass-specific metabolic energy rate calculated using $\lvert\dot{W}^*\rvert$ (J s^{-1} kg^{-1})
$E^*_{\mathrm{met,abs}}$	mass-specific metabolic cost calculated using $\dot{E}^*_{\mathrm{met,abs}}$ (J kg^{-1})
η	mechanical efficiency (dimensionless)
η_{abs}	mechanical efficiency calculated using $E^*{}_{\mathrm{met,abs}}$ (dimensionless)

and $\dot{W}^*$ is the mass-specific mechanical power:

$$\dot{W}^* = \frac{Fv}{m_{\mathrm{m}}}. \tag{6.5}$$

MA97 and U10 directly calculate $\dot{E}^*_{\mathrm{met}}$ rather than estimate it as the sum of $\dot{H}^*_{\mathrm{total}}$. To obtain the mass-specific mechanical work per cycle W^* to calculate η, we integrated $\dot{W}^*$ over the time of each cycle (t_1 to t_2):

$$W^* = \int_{t_1}^{t_2} \dot{W}^* dt. \tag{6.6}$$

We additionally calculated the mass-specific metabolic energy rate $\dot{E}^*_{\text{met,abs}}$ for the models that estimate $\dot{E}^*_{\text{met}}$ as the sum of $\dot{H}^*_{\text{total}}$ and $\dot{W}^*$ (B04, H06, LW05, and U03) using the absolute value of the mass-specific mechanical power:

$$\dot{E}^*_{\text{met,abs}} = \dot{H}^*_{\text{total}} + |\dot{W}^*| \tag{6.7}$$

Integrating $\dot{E}^*_{\text{met,abs}}$ over the time of each cycle gave:

$$E^*_{\text{met,abs}} = \int_{t_1}^{t_2} \dot{E}^*_{\text{met,abs}} dt. \tag{6.8}$$

Finally, the mechanical efficiency η_{abs} using $E^*_{\text{met,abs}}$ was given by:

$$\eta_{\text{abs}} = \frac{W^*}{E^*_{\text{met,abs}}} \tag{6.9}$$

Bhargava et al., 2004 (B04)

$$\dot{H}_{\text{total}} = \dot{H}_{\text{activation}} + \dot{H}_{\text{maintenance}} + \dot{H}_{\text{shortening}} + \dot{H}_{\text{basal}} \tag{6.10}$$

$$\dot{H}_{\text{activation}} = \phi m_{\text{m}} (\text{f}_{\text{fast}} \dot{A}_{\text{fast}} u_{\text{fast}} + \text{f}_{\text{slow}} \dot{A}_{\text{slow}} u_{\text{slow}}) \tag{6.11}$$

$$\phi = 0.06 + e^{\frac{-t_{\text{stim}} u}{\tau_\phi}} \tag{6.12}$$

$$\dot{H}_{\text{maintenance}} = L_{\text{maintenance}} m_{\text{m}} (\text{f}_{\text{fast}} \dot{M}_{\text{fast}} u_{\text{fast}} + \text{f}_{\text{slow}} \dot{M}_{\text{slow}} u_{\text{slow}}) \tag{6.13}$$

Table 6.2: Variables and constants specific to Bhargava et al. (2004)

Variable	Definition
$\dot{H}_{\text{activation}}$	activation heat rate (J s^{-1})
$\dot{H}_{\text{maintenance}}$	maintenance heat rate (J s^{-1})
$\dot{H}_{\text{shortening}}$	shortening heat rate (J s^{-1})
$\dot{H}_{\text{basal}}$	basal heat rate (J s^{-1})
f_{fast}	mass fraction of fast fibres (dimensionless)
f_{slow}	mass fraction of slow fibres (dimensionless)
u_{fast}	excitation level of fast fibres (dimensionless)
u_{slow}	excitation level of slow fibres (dimensionless)
$\dot{A}_{\text{fast}}$	activation heat rate constant for fast fibres (J s^{-1} kg^{-1})
$\dot{A}_{\text{slow}}$	activation heat rate constant for slow fibres (J s^{-1} kg^{-1})
$\dot{M}_{\text{fast}}$	maintenance heat rate constant of fast fibres (J s^{-1} kg^{-1})
$\dot{M}_{\text{slow}}$	maintenance heat rate constant of slow fibres (J s^{-1} kg^{-1})
ϕ	decay function (dimensionless)
τ_{ϕ}	decay time constant (ms)
α	proportionality constant for $\dot{H}_{\text{shortening}}$ (N)
t_{stim}	time since u was above 10% (s)
$L_{\text{maintenance}}$	length dependence of $\dot{H}_{\text{maintenance}}$ (dimensionless)

$$L_{\text{maintenance}} = \begin{cases} 0.5 & \hat{l} < 0.5 \\ \hat{l} & 0.5 \leq \hat{l} < 1 \\ -2\hat{l} + 3 & 1 \leq \hat{l} < 1.5 \\ 0 & \hat{l} \geq 1.5 \end{cases} \tag{6.14}$$

$$\dot{H}_{\text{shortening}} = -\alpha v \tag{6.15}$$

$$\alpha = \begin{cases} 0.16(\hat{F}_{\text{A}}\hat{a}) + 0.18F & v \leq 0 \\ 0.157F & v > 0 \end{cases} \tag{6.16}$$

$$\dot{H}_{\text{basal}} = 0.0225 m_{\text{m}} \tag{6.17}$$

The muscle model was composed of either entirely fast or entirely slow fibres. When the model was fast, f_{fast} was 1, f_{slow} was 0, u_{fast} was u, u_{slow} was 0, and τ_{ϕ} was 25

ms, and when the model was slow, f_{fast} was 0, f_{slow} was 1, u_{fast} was 0, u_{slow} was u, and τ_ϕ was 45 ms. Across all simulations, $\dot{A}_{fast}$ was 133 J s^{-1} kg^{-1}, $\dot{A}_{slow}$ was 40 J s^{-1} kg^{-1}, $\dot{M}_{fast}$ was 111 J s^{-1} kg^{-1}, $\dot{M}_{slow}$ was 74 J s^{-1} kg^{-1}. While values for $\dot{A}_{fast}$, $\dot{A}_{slow}$, $\dot{M}_{fast}$, and $\dot{M}_{slow}$ for both human and frog muscle are reported in Bhargava and colleagues (2004), we used those specific to human muscle for this study.

Houdijk et al., 2006 (H06)

Table 6.3: Variables and constants specific to Houdijk et al. (2006).

Variable	Definition
$\dot{H}_{activation}$	activation heat rate (J s^{-1})
$\dot{H}_{maintenance}$	maintenance heat rate (J s^{-1})
$\dot{H}_{shortening}$	shortening heat rate (J s^{-1})
$\overline{g}$	muscle specific activation heat (J s^{-1} kg^{-1})
$\overline{h}$	maintenance heat coefficient (J s^{-1} kg^{-1})
c_1	constant for $\dot{H}_{activation}$ (dimensionless)
c_2	constant for $\dot{H}_{activation}$ (dimensionless)
c_3	constant for $\dot{H}_{activation}$ (dimensionless)
ϕ	fraction of maintenance heat to total isometric heat at l_0 (dimensionless)
$\overline{a}$	muscle specific shortening heat coefficient (N)
f_{stim}	nerve stimulation frequency (Hz)
$f_{stim,max}$	maximum nerve stimulation frequency (Hz)

$$\dot{H}_{total} = \dot{H}_{activation} + \dot{H}_{maintenance} + \dot{H}_{shortening} \tag{6.18}$$

$$\dot{H}_{activation} = m_m \overline{g} \begin{cases} 0 & \hat{a} \leq 0 \\ c_1\hat{a}^3 + c_2\hat{a}^2 + c_3\hat{a} & \hat{a} > 0 \end{cases} \tag{6.19}$$

$$\overline{g} = \phi(\overline{g} + \overline{h}) \tag{6.20}$$

$$\dot{H}_{maintenance} = m_m \hat{a}(\overline{g} + \overline{h})(\hat{F}_A - \phi) \tag{6.21}$$

$$\dot{H}_{\text{shortening}} = \begin{cases} -\overline{a}\hat{a}\hat{F}_{\text{A}}v & -v > 0 \\ 0 & -v \leq 0 \end{cases} \tag{6.22}$$

Houdijk and colleagues (2006) reported values of $\overline{g} + \overline{h}$, ϕ, and $\overline{a}$ for both mouse soleus and extensor digitorum longus muscle. Because soleus and extensor digitorum longus muscle are primarily comprised of slow and fast fibres, respectively, we used soleus values when muscle model was composed entirely of slow fibres, and extensor digitorum longus values when the model was entirely fast fibres. When the model was slow, $\overline{g} + \overline{h}$ was 24.4 J s^{-1} kg^{-1}, ϕ was 0.35, and $\overline{a}$ was 0.16 F_0, and when the model was fast, $\overline{g} + \overline{h}$ was 150 J s^{-1} kg^{-1}, ϕ was 0.45, and $\overline{a}$ was 0.28 F_0.

In this study we prescribed excitation u, which represents the electrical membrane potentials of the muscle fibres, instead of the stimulus frequency of the motor nerve f_{stim} as in Houdijk et al. (2006). To make $\dot{H}_{\text{activation}}$ a function of $\hat{a}$ instead of f_{stim} and $f_{\text{stim,max}}$, we replaced the term:

$$f_{\text{stim}}\left[\frac{1 - e^{-0.25-\frac{18.2}{f_{\text{stim}}f_{\text{stim,max}}}}}{1 - e^{-0.25-\frac{18.2}{f_{\text{stim,max}}}}}\right]$$

in equation (1) in Houdijk et al. (2006) with:

$$\dot{H}_{\text{shortening}} = \begin{cases} 0 & \hat{a} \leq 0 \\ c_1\hat{a}^3 + c_2\hat{a}^2 + c_3\hat{a} & \hat{a} > 0 \end{cases} \tag{6.23}$$

using $f_{\text{stim}} = \hat{a}^2$ and $f_{\text{stim,max}} = k_1 + k_2\hat{a}$ from Koelewijn and colleagues (2019), where k_1 was 6 for slow and 12 for fast fibres and k_2 was 8 for slow and 14 for fast fibres. We determined c_1, c_2, and c_3 by fitting the third order polynomial to match the term in equation (1) in Houdijk et al. (2006). c_1 was -1.0662, c_2 was 2.1257, and c_3 was -0.0586 for fast fibres and c_1 was -0.4920, c_2 was 1.5307, and c_3 was -0.0191 for slow fibres. We assumed that the velocity of this model was defined as positive during shortening, consistent with Koelewijn et al. (2019).

Lichtwark & Wilson, 2005b (LW05)

Table 6.4: Variables and constants specific to Lichtwark and Wilson (2005b).

Variable	Definition
$\dot{H}_{\text{stable}}$	stable heat rate (s^{-1})
$\dot{H}_{\text{labile}}$	labile heat rate (s^{-1})
$\dot{H}_{\text{shortening}}$	shortening heat rate (s^{-1})
$\dot{H}_{\text{thermoelastic}}$	thermoelastic heat rate (s^{-1})
t_{reset}	time relative to the start of activation each cycle (s)
g	stable heat rate constant (dimensionless)

$$\dot{H}_{\text{total}} = \begin{cases} l_0 F_0 [\dot{H}_{\text{stable}} + \dot{H}_{\text{labile}} + \dot{H}_{\text{shortening}} + \dot{H}_{\text{thermoelastic}}] & -v \geq 0 \\ l_0 F_0 [0.3\dot{H}_{\text{stable}} + (\dot{H}_{\text{stable}} e^{-8\hat{F}_{\text{V}}\hat{F}_{\text{A}}}) - 1 + \hat{F}\frac{-v}{l_0}] & -v < 0 \end{cases} \tag{6.24}$$

$$\dot{H}_{\text{stable}} = \hat{a}\hat{F}_{\text{A}}\frac{v_0}{g^2} \tag{6.25}$$

$$\dot{H}_{\text{labile}} = 0.8\dot{H}_{\text{stable}} e^{-0.72 t_{\text{reset}}} + 0.175\dot{H}_{\text{stable}} e^{-0.022 t_{\text{reset}}} \tag{6.26}$$

$$\dot{H}_{\text{shortening}} = \hat{a}\hat{F}_{\text{A}}\frac{-v}{g l_0} \tag{6.27}$$

$$\dot{H}_{\text{thermoelastic}} = -0.014\frac{\dot{F}}{F_0} \tag{6.28}$$

$$g = 0 \tag{6.29}$$

In Lichtwark and Wilson (2005b), the authors used a normalized force potential P which accounted for only force-velocity and activation and not force-length effects. This was because their simulations of interest only involved contractions on the plateau region of the force-length relationship where accounting for the effects of length on muscle force would have no impact. In this study, our muscle models contracted over a range of lengths, particularly in harmonic oscillator simulations in which muscle length over time was not constrained. Thus, we replaced all Ps in the

cost model equations with $\hat{F}$ which accounts for force-length effects and the fraction of bound cross-bridges at a given muscle length. Shortening velocity is defined as positive in Lichtwark and Wilson (2005b), so we multiplied the velocities by -1 as our muscle model velocity is negative during shortening.

Minetti & Alexander, 1997 (MA97)

$$\dot{E}_{\text{met}} = \hat{a} F_0 v_0 l_0 \left[\frac{0.054 + 0.506\frac{-v}{v_0 l_0} + 2.46(\frac{-v}{v_0 l_0})^2}{1 - 1.13\frac{-v}{v_0 l_0} + 12.8(\frac{-v}{v_0 l_0})^2 - 1.64(\frac{-v}{v_0 l_0})^3} \right] \tag{6.30}$$

$$\dot{E}^*_{\text{met}} = \frac{\dot{E}_{\text{met}}}{m_{\text{m}}} \tag{6.31}$$

Umberger et al., 2003 (U03)

Table 6.5: Variables and constants specific to Umberger et al. (2003).

Variable	Definition
$\dot{H}_{\text{act,maint}}$	activation and maintenance heat rate (J s^{-1} kg^{-1})
$\dot{H}_{\text{shortening}}$	shortening heat rate (J s^{-1} kg^{-1})
$\dot{H}_{\text{lengthening}}$	lengthening heat rate (J s^{-1} kg^{-1})
$\%FT$	percentage of fast fibres
$\alpha_{\text{S,ST}}$	shortening heat coefficient for slow fibres (J kg^{-1})
$\alpha_{\text{S,FT}}$	shortening heat coefficient for fast fibres (J kg^{-1})
α_{L}	lengthening heat coefficient (J kg^{-1})
A	activation dependence scaling factor (dimensionless)
A_{AM}	activation dependence scaling factor for $\dot{H}_{\text{act,maint}}$ (dimensionless)
A_{S}	activation dependence scaling factor for $\dot{H}_{\text{shortening}}$ (dimensionless)
$v_{0,\text{slow}}$	maximum shortening velocity for slow fibres (s^{-1})
$v_{0,\text{fast}}$	maximum shortening velocity for fast fibres (s^{-1})
S	aerobic dependence scaling factor for $\dot{H}^*_{\text{total}}$

$$\dot{H}_{\text{total}} = \begin{cases} (\dot{H}^*_{\text{act,maint}} A_{\text{AM}} + \dot{H}^*_{\text{shortening}} A_{\text{S}}) S & l \leq l_0 \cap v \leq 0 \\ (\dot{H}^*_{\text{act,maint}} A_{\text{AM}} + \dot{H}^*_{\text{lengthening}} A) S & l \leq l_0 \cap v > 0 \\ \left[(0.4 + 0.6\hat{F}_{\text{A}}) \dot{H}^*_{\text{act,maint}} A_{\text{AM}} + \dot{H}^*_{\text{shortening}} \hat{F}_{\text{A}} A_{\text{S}} \right] S & l > l_0 \cap v \leq 0 \\ \left[(0.4 + 0.6\hat{F}_{\text{A}}) \dot{H}^*_{\text{act,maint}} A_{\text{AM}} + \dot{H}^*_{\text{lengthening}} \hat{F}_{\text{A}} A \right] S & l > l_0 \cap v > 0 \end{cases} \tag{6.32}$$

$$\dot{H}^*_{\text{act,maint}} = 1.28\%FT + 25 \tag{6.33}$$

$$\dot{H}^*_{\text{shortening}} = \alpha_{\text{S,ST}}\frac{v}{l_0}(1 - \frac{\%FT}{100}) - \alpha_{\text{S,FT}}\frac{v}{l_0}\frac{\%FT}{100} \tag{6.34}$$

$$\dot{H}^*_{\text{lengthening}} = \alpha_{\text{L}}\frac{v}{l_0} \tag{6.35}$$

$$\dot{H}_{\text{total}} = \begin{cases} u & u > \hat{a} \\ \frac{u+\hat{a}}{2} & u \leq \hat{a} \end{cases} \tag{6.36}$$

$$A_{\text{AM}} = A^{0.6} \tag{6.37}$$

$$A_{\text{S}} = A^{2.0} \tag{6.38}$$

$$\alpha_{\text{S,ST}} = \frac{100}{v_{0,\text{slow}}} \tag{6.39}$$

$$\alpha_{\text{S,FT}} = \frac{153}{v_{0,\text{fast}}} \tag{6.40}$$

$$v_{0,\text{slow}} = 5 \tag{6.41}$$

$$v_{0,\text{fast}} = 10 \tag{6.42}$$

$$\alpha_{\text{L}} = 4\alpha_{\text{S,ST}} \tag{6.43}$$

When the model was slow, S was 1.5 and $\%FT$ was 0, and when the model was fast, S was 1.0 and $\%FT$ was 100. In Umberger et al. (2003), A is dependent on the variable *stim* which was input into the Zajac (1989) excitation-activation transfer

function to determine the time-varying activation. Because we used the square wave excitation u as the input for the Zajac function, we replaced *stim* with u in the equation for A.

Umberger, 2010 (U10)

This model is a variant of the U03 model, in which the heat rate during lengthening is only due to the total heat rate $\dot{H}^*_{\text{total}}$ and not the mechanical power $\dot{W}^*$:

$$\dot{E}^*_{\text{met}} = \begin{cases} \dot{H}^*_{\text{total}} + \dot{W}^* & v \leq 0 \\ \dot{H}^*_{\text{total}} & v > 0 \end{cases} \tag{6.44}$$

The lengthening heat rate $\dot{H}^*_{\text{lengthening}}$ in U03 is also scaled down in U10 with a lower value for the lengthening heat coefficient α_{L}:

$$\alpha_{\text{L}} = 0.3\alpha_{\text{S,ST}} \tag{6.45}$$

6.6.2 Differences in predicated cost across models

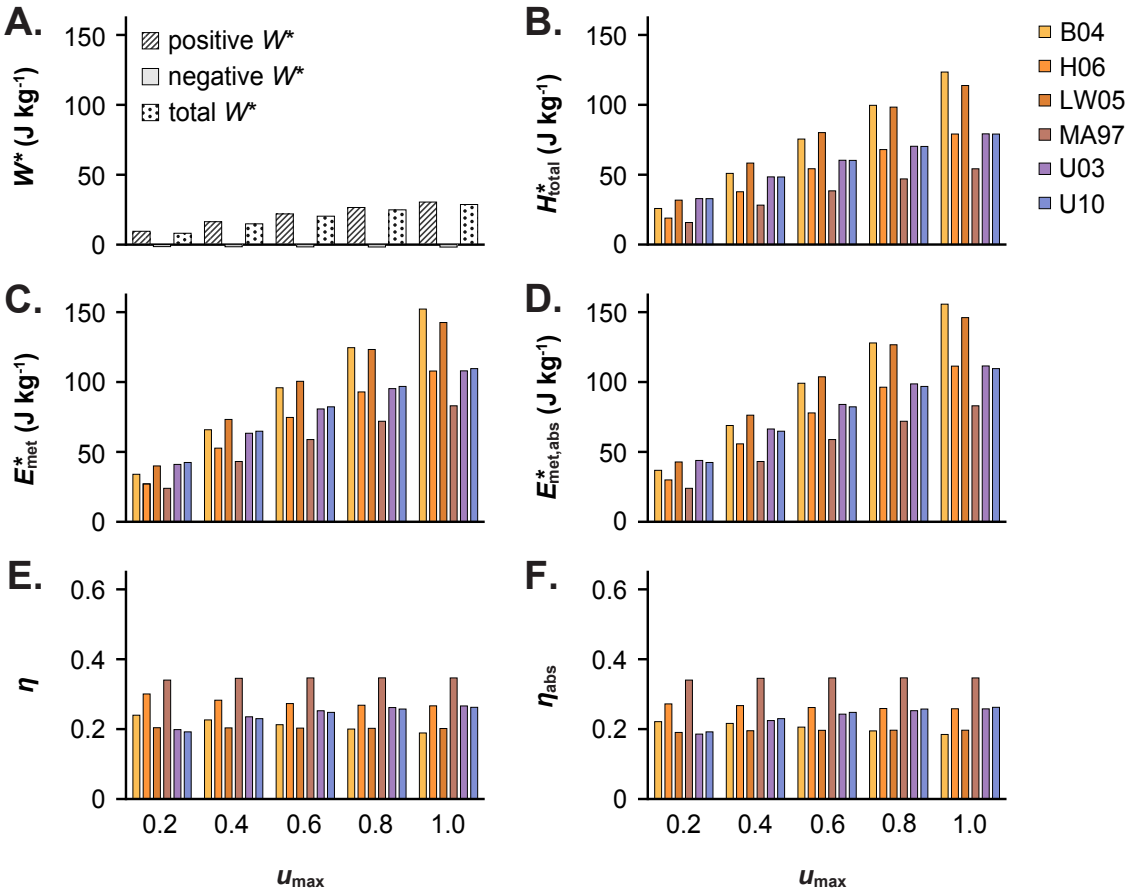

Figure 6.10: The effect of maximum excitation on metabolic cost model predictions. The effect of maximum excitation $u_{\max}$ on mass-specific work per cycle W^* (A), mass-specific heat per cycle H^*_{total} (B), mass-specific metabolic cost per cycle E^*_{met} (C), mass-specific metabolic cost per cycle calculated using the absolute value of the mechanical power $E^*_{\text{met,abs}}$ (D), efficiency per cycle η (E), and efficiency per cycle calculated using $E^*_{\text{met,abs}}$, η_{abs} (F). W^* in (A) is the net mass-specific work per cycle (dots) and was calculated as the sum of the positive W^* during shortening (diagonal stripes) and negative W^* during lengthening (grey). Note that for MA97 and U10, E^*_{met} is equivalent to $E^*_{\text{met,abs}}$ and η_{abs} is equivalent to η. The displayed data are for motor simulations (phase +0%) of the massless model without a tendon with an excitation duty cycle of 0.46, and fast fibre-type properties.

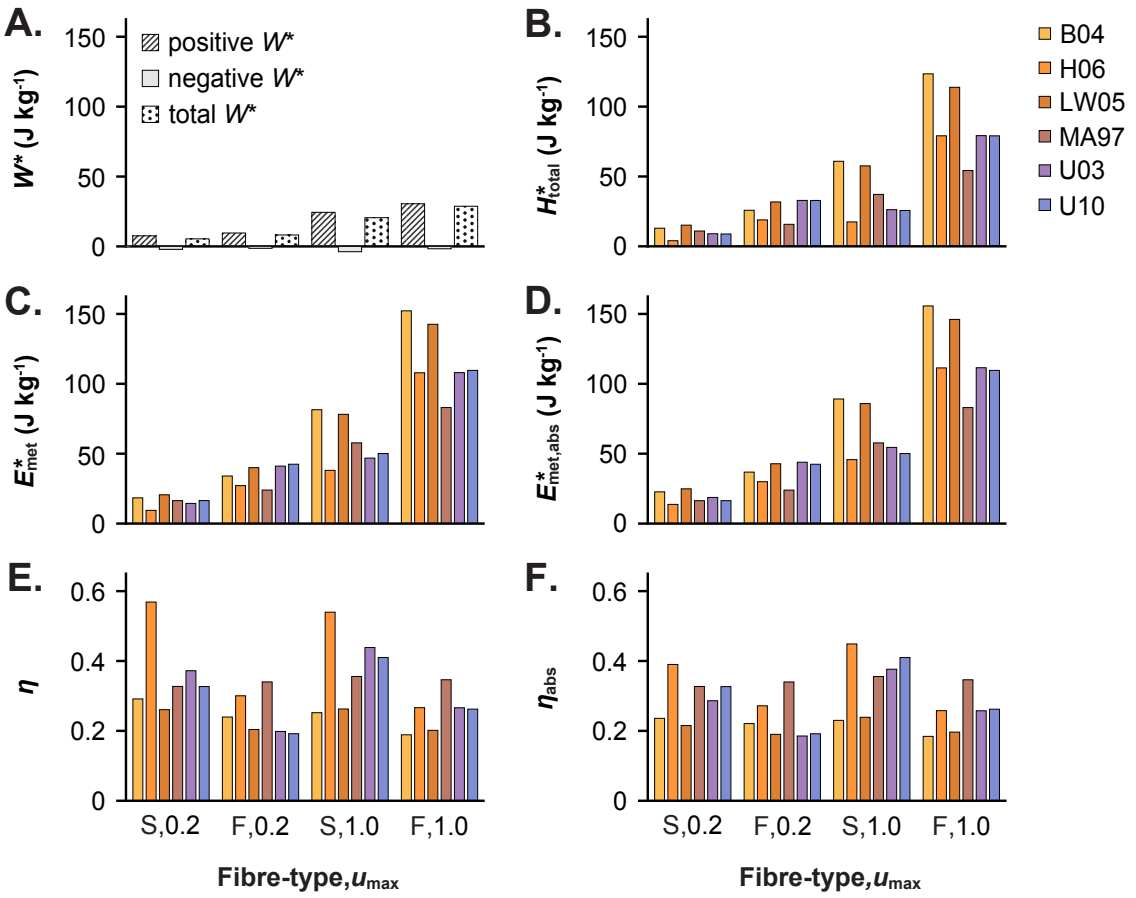

Figure 6.11: The effect of fibre-type on metabolic cost model predictions. The effect of fibre-type and maximum excitation $u_{\max}$ on mass-specific work per cycle W^* (A), mass-specific heat per cycle H^*_{total} (B), mass-specific metabolic cost per cycle E^*_{met} (C), mass-specific metabolic cost per cycle calculated using the absolute value of the mechanical power $E^*_{\text{met,abs}}$ (D), efficiency per cycle η (E), and efficiency per cycle calculated using $E^*_{\text{met,abs}}$, η_{abs} (F). W^* in (A) is the net mass-specific work per cycle (dots) and was calculated as the sum of the positive W^* during shortening (diagonal stripes) and negative W^* during lengthening (grey). Note that for MA97 and U10, E^*_{met} is equivalent to $E^*_{\text{met,abs}}$ and η_{abs} is equivalent to η. The displayed data are for motor simulations (phase +0%) of the massless model without a tendon and with an excitation duty cycle of 0.46, fast F and slow S fibre-type properties, and $u_{\max}$ of 0.2 and 1.0.

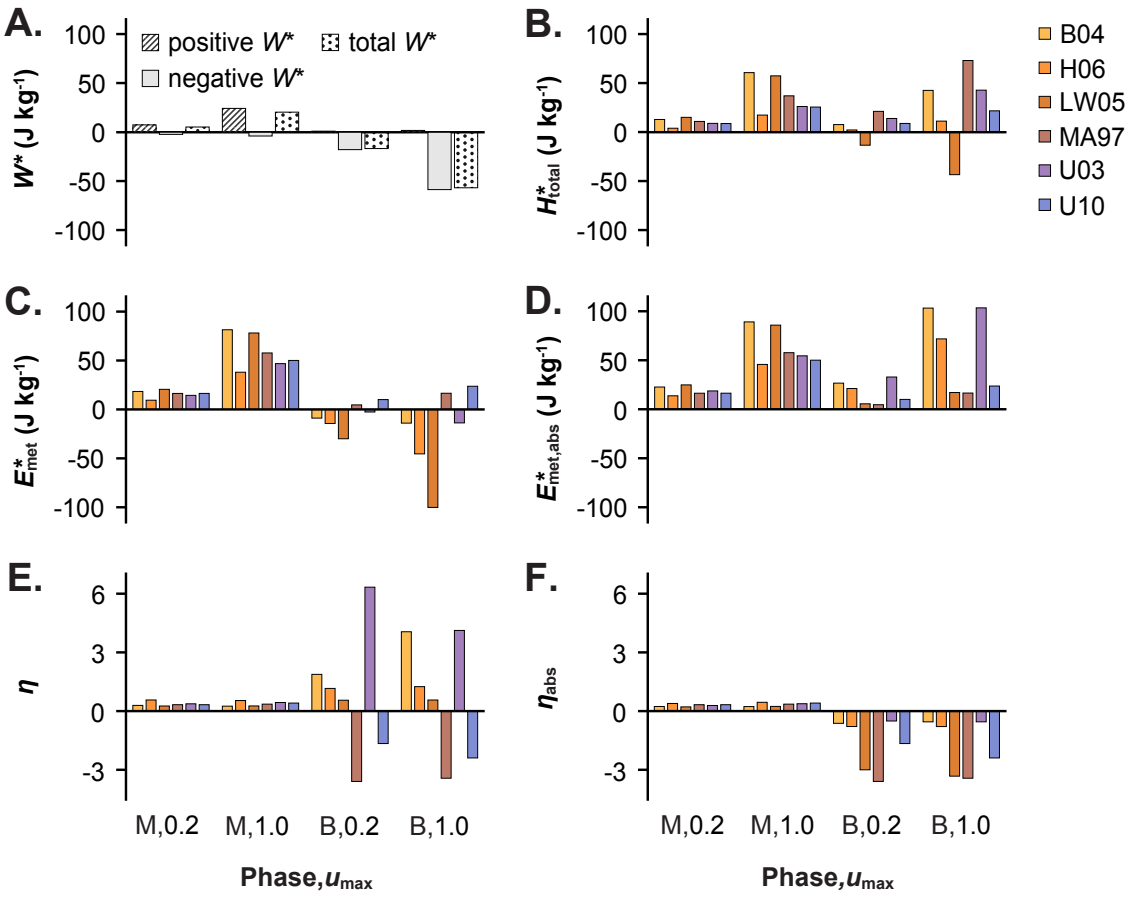

Figure 6.12: The effect of excitation phase on metabolic cost model predictions. The effect of excitation phase and maximum excitation $u_{\max}$ on mass-specific work per cycle W^* (A), mass-specific heat per cycle H^*_{total} (B), mass-specific metabolic cost per cycle E^*_{met} (C), mass-specific metabolic cost per cycle calculated using the absolute value of the mechanical power $E^*_{\text{met,abs}}$ (D), efficiency per cycle η (E), and efficiency per cycle calculated using $E^*_{\text{met,abs}}$, η_{abs} (F). W^* in (A) is the net mass-specific work per cycle (dots) and was calculated as the sum of the positive W^* during shortening (diagonal stripes) and negative W^* during lengthening (grey). Note that for MA97 and U10, E^*_{met} is equivalent to $E^*_{\text{met,abs}}$ and η_{abs} is equivalent to η. The displayed data are for motor M (phase +0%) and brake B (phase +50%) simulations of the massless model without a tendon and with an excitation duty cycle of 0.46, fast fibre-type properties, and $u_{\max}$ of 0.2 and 1.0.

Chapter 7

Consequences of muscle mass on contractile performance: Implications, applications, and future directions

7.1 Summary of thesis findings

Muscle mass is rarely considered in our current understanding of whole muscle behaviour and is thus rarely accounted for in models that predict muscle forces and behaviour *in vivo* during locomotion. The few studies that have investigated the effects of muscle mass on muscle performance have shown that greater muscle mass decreases the rate of muscle force development (Günther et al., 2012) and maximum contraction velocity (Meier & Blickhan, 2000; Böl & Reese, 2008; Ross & Wakeling, 2016), an effect which is amplified with submaximal activation (Ross & Wakeling, 2016). However, these studies all examined the effects of muscle mass during highly controlled contractions that do not reflect the range of muscle activations, strains, and strain rates that occur *in vivo* during locomotor tasks such as walking and running. The studies in this thesis provide insight into the effects of muscle mass on contractile performance during these more realistic conditions.

In my previous work (Ross & Wakeling, 2016), I used a mass-enhanced Hill-type model to explore the effects of muscle mass during isotonic shortening contractions. To use this model to examine the effects of muscle mass during more variable cyclic contractions, I developed a modelling framework in Chapter 2 that was composed of a damped harmonic oscillator in series with a Hill-type muscle model. This included implementing novel Bézier curves to represent the force-velocity and force-length properties of muscle and geometrically scaling the system while preserving dynamic and kinematic similarity to explore the effects of muscle mass across muscle sizes while controlling for the dynamics of the harmonic oscillator. In addition to facilitating testing the effects of muscle mass, this framework can also be used to test

different muscle model formulations, such as those that account for force enhancement following active stretch and task-dependent motor unit recruitment, under common contractile conditions.

In Chapter 3, I used the modelling framework composed of a damped harmonic oscillator in series with a Hill-type muscle model (Chapter 2) that accounted for the effects of muscle tissue mass (Ross & Wakeling, 2016) to explore the effects of muscle mass on mass-specific mechanical work and average power per cycle during cyclic contractions. I additionally compared the effects of muscle mass to force enhancement following active lengthening and force depression following active shortening, which are more well-established phenomena in muscle mechanics. I showed for the first time to my knowledge that accounting for muscle tissue mass decreases the mass-specific work and average power of muscle during the types of cyclic contractions that occur during human movement. I also showed that the effects of muscle mass on mass-specific work and average power were of similar magnitude as that due to the effects of force enhancement and depression, and that the effects of muscle mass on work and power were greater for muscles with faster fibre-type properties.

While the results of Chapter 3 and those of previous studies (Günther et al., 2012; Meier & Blickhan, 2000; Böl & Reese, 2008; Ross & Wakeling, 2016) were important first steps to establishing muscle mass as an important determinant of muscle contractile behaviour, the effects of muscle mass had not yet been confirmed by studies on living muscle. In Chapter 4, I examined the effects of added mass on the performance of *in situ* rat muscle during cyclic contractions and found that greater added mass resulted in lower mechanical work per cycle. I also found that greater muscle strain resulted in lower work per cycle relative to unloaded trials, possibly due to greater accelerations of the muscle mass at higher strains. I additionally compared the results of the *in situ* experiments to those of simulations of the muscle model with mass from my previous studies (Ross & Wakeling, 2016; Chapter 3) and found similar patterns of decreased mechanical work with greater added mass. This study was the first time to my knowledge that muscle mass was shown to alter the mechanical behaviour of muscle in living animals.

In Chapter 5, I used a 3D continuum model of muscle that accounts for tissue mass to explore the effects of muscle size and mass on the mass-specific mechanical work per cycle, and how these changes in work with greater mass are associated with changes in tissue energy distribution and muscle shape change. I also qualitatively

validated the model by comparing its behaviour to that of *in situ* muscle during analogous experimental trials (Chapter 4). I found that greater muscle mass resulted in relatively more mechanical energy in the form of kinetic energy during the simulated contraction cycles, and this was associated with lower mass-specific mechanical work output for larger muscles with greater mass. Larger muscles also stored more energy in the aponeurosis during contraction, which may allude to elastic tissues having greater importance for energy savings in larger animals. In terms of muscle architecture, I found that reductions in mass-specific work with greater muscle size were lower for muscles with higher initial pennation angle, indicating that there may be a mechanical benefit of larger animals having more pennate muscles. Finally, in Chapter 5 I found that the *in situ* and simulated muscle had comparable patterns of tissue accelerations across conditions, which suggested that the muscle model was behaving similarly to real muscle.

While my previous studies showed that the mass-specific mechanical work per contraction cycle is lower for larger muscles due to their greater mass (Chapters 3-5), it was still not clear how this greater mass alters the metabolic cost and efficiency of contraction. In Chapter 6, I examined the effects of muscle mass on the metabolic cost and efficiency of muscle during cyclic contractions using simulations of a mass-enhanced Hill-type muscle model (Ross & Wakeling, 2016) in which bursts of excitation were timed to sinusoidal muscle length changes. I additionally explored how the behaviour of a tendon alters the relationship between muscle mass and muscle and muscle-tendon unit mass-specific mechanical work, metabolic cost, and efficiency per cycle by adding a tendon of varying stiffness in series with the muscle model. I found that larger muscles with greater mass were less efficient and that accounting for a tendon decreased the mass-specific work and efficiency penalty of greater mass in larger muscles. Overall, the results of this thesis highlight that muscle mass is an important determinant of whole muscle and muscle-tendon unit behaviour.

7.2 Implications and potential applications

It is near impossible to measure the function, in particular the forces, of the majority of muscles across a wide range of species and behaviours. Muscle models provide a means to predict muscle forces where direct measures are not possible and can also be used to answer "what if" questions that explore mechanisms and manipulate factors that cannot be manipulated experimentally. For example, in Chapter 3 I examined the

effects of accounting for muscle mass on contractile behaviour by comparing the mass-specific work and average power per cycle of a typical massless and mass-enhanced Hill-type model. Experimentally it is not possible to remove a muscle's mass while maintaining the integrity of its tissue and so this study would not have been possible without the use of muscle modelling and simulation.

Muscle models are also important for predicting whole-body motion, as the muscle actuators in musculoskeletal models such as OpenSim (Delp et al., 2007) are composed of 1D Hill-type models. Musculoskeletal models that predict human movement have the potential to revolutionize medicine and health care by providing a tool that clinicians can use to predict the outcome and monitor the efficacy of interventions at the individual patient level. In the orthopedic and rehabilitation settings, these models could be used to predict the outcome of surgeries, design customized non-surgical treatment plans, and to monitor rehabilitation interventions (Killen et al., 2020). However, translation of these models to the clinical setting has been limited in part due to poor model accuracy in predicting human movement, and a substantial portion of the model errors can likely be attributed to how muscles are represented in whole-body models (Dick et al., 2017). Studies evaluating the accuracy of models that represent muscle actuators in whole-body musculoskeletal models have found that these models perform best during maximal and slow contractions and suffer during submaximal and faster contractions (Perreault et al., 2003; S. S. Lee et al., 2013; Dick et al., 2017; Wakeling et al., 2021). Because most muscles operate submaximally during most locomotor tasks, such as walking and running, these models likely have limited accuracy during the majority of contractions *in vivo* during locomotion.

These conditions in which traditional massless Hill-type models have the poorest accuracy, namely submaximal and faster contractions, correspond to the conditions in which muscle mass has the greatest impact. As muscles increase in size, their potential to generate force increases in proportion to their cross-sectional area, and their mass increases in proportion to their volume. This results in greater internal loads for larger muscles relative to the force that they can produce, and this difference becomes greater when muscle force potential decreases during submaximal contractions. These internal loads are inertial in nature, and so their magnitude depends not only the mass of the tissue but also the acceleration of that mass. Therefore, inertial resistance due to tissue mass likely has the largest effect during submaximal contractions, and during unsteady or higher frequency or strain (length change) cyclic contractions where accelerations of the tissue are greatest. This is consistent with my previous findings

and the results of this thesis in which the effects of muscle mass were greatest at lower excitations (Ross & Wakeling, 2016: Chapter 3; Chapter 5), which translates to lower activations and higher strains (Chapter 4; Chapter 5), and greater accelerations. The intrinsic force-velocity properties of muscle are taken primarily from measures on maximally-active single fibres or small muscles during constant-load shortening contractions when the fibre or whole muscle acceleration is zero and the effects of these internal loads in negligible. Because of this, muscle mass was traditionally not accounted for in typical Hill-type model formulations. The findings from this thesis now show that ignoring the effects of muscle mass may contribute to the discrepancy between model predictions and experimental measures.

The results of the studies in this thesis highlight that, while the effects of muscle mass are greatest during submaximal and fast contractions, muscle mass has important consequences for muscles in the size range of human muscles that are important for locomotion, such as the medial and lateral gastrocnemii, even during maximal and slower contractions. In Chapter 3 I found that increasing the size of muscle model from that of a fibre bundle up to a whole human plantarflexor resulted in an 8% reduction in mass-specific work per cycle on average across conditions and both slow and fast fibre-types and a 12% reduction across conditions for fast fibres (Figure 3.6). In Chapter 5 when I modelled the muscle using dimensions and architecture taken from the human medial gastrocnemius (Randhawa et al., 2013), I found an 8.3, 17.5, and 34.5 percent reduction in mass-specific work per cycle when the dimensions of the muscle were scaled by a factor of 3.5 for a cycle strain amplitude of 2.5, 5, and 7.5 percent, respectively. Even without increasing the size of the muscle, the presence of muscle mass altered the tissue accelerations along the muscle's length such that there was a substantial reduction in relative tissue acceleration near the middle of the muscle compared to at the end that was constrained to follow a sinusoidal trajectory (Figure 5.9). If mass had no consequences on muscle mechanical behaviour, the relative tissue accelerations would be the same all along the muscle's length. Thus, muscle mass is clearly an important determinant of whole muscle behaviour in humans under most contractile conditions.

The results of the studies in this thesis also highlight that muscle mass is important to consider for understanding, and likely for accurately predicting, the behaviour of elastic tissues such as aponeurosis and tendon. Tendons have been shown to increase muscle-tendon unit (MTU) work and efficiency per cycle by decreasing muscle shortening velocity and increasing muscle force during contraction cycles with prescribed

excitation (Ettema, 2001; Lichtwark & Barclay, 2010), or to decrease muscle work and increase efficiency by allowing the muscle to contract over a shorter length range during locomotion (Biewener, Konieczynski, & Baudinette, 1998; Biewener et al., 2004; Fukunaga et al., 2001; Lai et al., 2014). Aponeurosis has also been suggested to play a role in energy savings by storing elastic energy during gait (Wager & Challis, 2016; Arellano et al., 2019). In Chapter 5, I found that greater muscle mass resulted in a greater amount of energy stored in aponeurosis during contraction (Figure 5.4). While this does not necessarily signify that aponeurosis energy storage mitigates the consequences of greater muscle mass in larger muscles, it does suggest that muscle mass alters how aponeurosis behaves and stores energy during contraction. Similarly, in Chapter 6 I found that a tendon not only altered the effects of muscle mass, but that muscle mass altered the effects of a tendon on MTU mechanical work and efficiency during cyclic contractions (Figure 6.7). Thus, accounting for muscle mass is likely important for accurately representing the behaviour of elastic tissues during locomotion.

Muscle mass is also important to consider for representing the behaviour of muscle and MTUs in animals, including extinct species. There has long been interest in understanding the movement of dinosaurs and other extinct animals, and this interest has grown with the emergence of computational tools, such as musculoskeletal models (Hutchinson, 2012), to simulate their motion. While the largest modern terrestrial animal, the African elephant, can reach body sizes of up to 5.5 tonnes (Laws, 1966) and can have muscles with approximate masses of 15 kg (Alexander et al., 1979), the largest animals to ever roam the earth were far larger, with dinosaurs such as *Apatosaurus* and *Brachiosaurus* that are estimated to have reached between 30 and 65 tonnes (Alexander, 1985; Anderson et al., 1985; Cawley & Janacek, 2010). Even some extinct mammals far exceeded the size of modern elephants, like the *Indricotherium*, a type of hornless rhinoceros from the Mongolia area, that is estimated to have reached body masses between 20 (Economos, 1981 via Alexander, 1989) and 34 tonnes (Alexander, 1989). While no estimates have been made as to the mass of these giant animals' muscles, it is reasonable to assume that they were enormous and much larger in mass than the largest muscles explored in this thesis. Considering that muscle mass has substantial effects on contractile performance at the size of a human muscle and how many times larger the muscles of these giant extinct animals must have been in comparison, it begs the question as to what mechanisms they used, if any, to overcome the massive internal loads of their muscle mass. Extending

the analysis of the effects of muscle mass to include these larger muscles of extinct species could provide clearer insight into how modern extant species deal with the consequences of their muscle mass. In any case, given the likely size of their muscles, muscle mass should be considered when predicting the movement of these larger extinct animals.

The results of this thesis also have implications for how we mimic the function of muscles and tendons in robotic prostheses and exoskeletons. Powered prostheses, in which an actuator or motor generates forces to mimic the function of muscles in the body, have the potential to restore function in individuals with limb amputation (Grimmer & Seyfarth, 2014). Similarly, powered exoskeletons can be used to assist in gait training for patients with spinal cord injury and stroke in the rehabilitation setting (Federici et al., 2015). Studies on the mechanics of muscles and tendons have informed the design of these powered systems to create muscle-like actuators that mimic the behaviour of their biological counterparts and provide a more natural experience for users (Herr & Kornbluh, 2004). For example, series elasticity has been integrated into the design of powered robotic systems to improve force control and mimic the energetic benefits of tendons during locomotion (Paluska & Herr, 2006). Accounting for the effects of muscle mass in actuator design could further advance efforts to provide actuator forces that mimic the forces of muscle *in vivo*. While there may be alternative designs that provide simpler and equally robust actuation of powered prostheses and exoskeletons as real muscle, evolution likely converged on some advantageous design features for powering human movement that could further inform future robotic design.

While improving the design of muscle models and the actuation of robotic prostheses and exoskeletons are potential applications of the findings of this thesis, given the fundamental nature of this work, it is ultimately not clear how these findings will be used in the future. This is not to say that this work is not valuable; in fact, some of the most important studies that have shaped the current state of biomechanics, and science in general, likely did not have a clear application at the time they were undertaken. For example, at the time that A.V. Hill conducted his Nobel Prize winning work on the energetics and heat production of muscle that resulted in his experiments to quantify the force-velocity properties of muscle (Hill, 1938), Hill would not have been able to predict that his findings would be used to develop muscle and musculoskeletal models as computers did not yet exist. Hill's work, and the valuable insight it has provided, would not have been possible had he been required to forecast the future applications

and impact of his work. While applied research has clear value in that it allows the knowledge we gain from research to be used to benefit society, progress in the applied research setting cannot exist without parallel progress in fundamental research that provides the foundation of knowledge with which to apply.

7.3 Gaps in knowledge and future directions

While examining cyclic contractions as the studies in this thesis did expands our understanding of how muscle mass impacts the performance of muscle during locomotion, it does not entirely capture the full range of possible contraction conditions. Our external environment contains obstacles and changing conditions that we must navigate during locomotion and that our nervous system must adjust and account for in the signals it sends to activate muscles. These adjustments cause variations in muscle forces, lengths, and velocities within and between cycles (Biewener & Daley, 2007) that are not captured by the cyclic contraction regimes that were explored in this thesis. Similarly, we can experience both unexpected and expected perturbations during locomotion due to external forces acting on the body. For example, if a bus has to stop quickly and unexpectedly, standing passengers have to overcome the unexpected perturbation to stay upright, which requires an integrated response of the neuromuscular system that results in complex patterns of muscle behaviour (Horak et al., 1997). Because overcoming such perturbations requires quick responses and likely fast muscle contractions, and as I found in Chapters 4 and 5 that muscle mass has greater impact during faster contractions, these perturbation-induced responses are likely affected by muscle mass. However, this has not been directly examined, so it is not clear how muscle mass impacts these more variable and unsteady locomotor conditions.

In addition to more variable contractions, the studies in this thesis did not explore the full range of muscle geometries and architecture that occur in living animals and how they are impacted by the effects of muscle mass. In Chapters 4 and 5, I geometrically scaled the mass-enhanced Hill-type model to larger sizes using methods presented in Chapter 2, such that the muscle model maintained the same geometric proportions, to explore the effects of muscle mass across muscle sizes. Because the root or scale 1 geometry in Chapters 3 and 6 represented the dimensions of a fibre bundle from which the intrinsic force-velocity and force-length properties of Hill-type muscle models are typically taken, this method of scaling resulted in unrealistically

long and thin muscles when the model was scaled to larger sizes. However, given that I found substantial effects of muscle mass using geometries and architectures that more accurately reflect that of human whole muscle in Chapter 4, I expect that the conclusions of Chapters 3 and 5 would still hold if more realistic muscle geometries were used. Nonetheless, future work could aim to explore the consequences of muscle mass across a wider range of muscle geometries and architectures.

References

Abbott, B. C., & Aubert, X. M. (1952). The force exerted by active striated muscle during and after change of length. *Journal of Physiology*, *117*(1), 77-86. doi: 10.1113/jphysiol.1952.sp004733

Ahn, A. N., Konow, N., Tijs, C., & Biewener, A. A. (2018). Different segments within vertebrate muscles can operate on different regions of their force–length relationships. *Integrative and Comparative Biology*, *58*(2), 219-231. doi: 10 .1093/icb/icy040

Ahn, A. N., Monti, R. J., & Biewener, A. A. (2003). In vivo and in vitro heterogeneity of segment length changes in the semimembranosus muscle of the toad. *The Journal of Physiology*, *549*(3), 877-888. doi: 10.1113/jphysiol.2002.038018

Aldrich, J. E. (2007). Basic physics of ultrasound imaging. *Critical Care Medicine*, *35*(5), S131-S137.

Alexander, R. M. (1985). Mechanics of posture and gait of some large dinosaurs. *Zoological Journal of the Linnean Society*, *83*(1), 1-25.

Alexander, R. M. (1989). *Dynamics of dinosaurs and other extinct giants*. New York: Columbia University Press.

Alexander, R. M. (2003). *Principles of animal locomotion*. Princeton: Princeton University Press.

Alexander, R. M., Jayes, A. S., Maloiy, G. M., & Wathuta, E. M. (1981). Allometry of the leg muscles of mammals. *Journal of Zoology*, *194*(4), 539-552.

Alexander, R. M., Maloiy, G. M. O., Hunter, B., Jayes, A. S., & Nturibi, J. (1979). Mechanical stresses in fast locomotion of buffalo (*Syncews coffer*) and elephant (*Loxodonta africana*). *Journal of Zoology*, *189*(2), 135-144.

Altenburg, T. M., de Ruiter, C. J., Verdijk, P. W., van Mechelen, W., & de Haan, A. (2008). Vastus lateralis surface and single motor unit emg following submaximal shortening and lengthening contractions. *Applied Physiology, Nutrition, and Metabolism*, *33*, 1086-1095.

Altringham, J. D., & Johnston, I. A. (1990a). Modelling muscle power output in a swimming fish. *Journal of Experimental Biology*, *148*(1), 395-402.

Altringham, J. D., & Johnston, I. A. (1990b). Scaling effects on muscle function: Power output of isolated fish muscle fibres performing oscillatory work. *Journal of Experimental Biology*, *151*(1), 453-467.

Anderson, J. F., Hall-Martin, A., & Russell, D. A. (1985). Long-bone circumference and weight in mammals, birds and dinosaurs. *Journal of Zoology*, *207*(1), 53-61.

Arellano, C. J., Konow, N., Gidmark, N. J., & Roberts, T. J. (2019). Evidence of a tunable biological spring: elastic energy storage in aponeuroses varies with transverse strain in vivo. *Proceedings of the Royal Society B*, *286*(1900), 20182764. doi: 10.1098/rspb.2018.2764

Arndt, D., Bangerth, W., Davydov, D., Heister, T., Heltai, L., Kronbichler, M., ... Wells, D. (2017). The deal. ii library, version 8.5. *Journal of Numerical Mathematics*, *25*(3), 137-145. doi: 10.1515/jnma-2017-0058

Asakawa, D., Pappas, G., Blemker, S., Drace, J., & Delp, S. (2003). Cine phase-contrast magnetic resonance imaging as a tool for quantification of skeletal muscle motion. *Seminars in Musculoskeletal Radiology*, *7*(4), 287-295.

Askew, G. N., & Marsh, R. L. (1997). The effects of length trajectory on the mechanical power output of mouse skeletal muscles. *Journal of Experimental Biology*, *200*(24), 3119-3131.

Askew, G. N., & Marsh, R. L. (1998). Optimal shortening velocity (v/vmax) of skeletal muscle during cyclical contractions: length-force effects and velocity-dependent activation and deactivation. *Journal of Experimental Biology*, *201*(10), 1527-1540.

Askew, G. N., Young, I. S., & Altringham, J. D. (1997). Fatigue of mouse soleus muscle, using the work loop technique. *Journal of Experimental Biology*, *200*(22), 2907-2912.

Asmussen, G., Beckers-Bleukx, G., & Maréchal, G. (1994). The force-velocity relation of the rabbit inferior oblique muscle; influence of temperature. *Pflügers Archiv*, *426*(6), 542-547.

Azizi, E., Brainerd, E. L., & Roberts, T. J. (2008). Variable gearing in pennate muscles. *Proceedings of the National Academy of Sciences*, *105*(5), 1745-1750. doi: 10.1073/pnas.0709212105

Azizi, E., Halenda, G. M., & Roberts, T. J. (2009). Mechanical properties of the gastrocnemius aponeurosis in wild turkeys. *Integrative and Comparative Biology*, *49*(1), 51-58. doi: 10.1093/icb/icp006

Azizi, E., & Roberts, T. J. (2009). Biaxial strain and variable stiffness in aponeuroses. *The Journal of Physiology*, *587*(17), 4309-4318. doi: 10.1113/jphysiol.2009.173690

Bahler, A. S. (1968). Modeling of mammalian skeletal muscle. *IEEE Transactions in Biomedical Engineering*, *BME-15*(4), 249-257. doi: 10.1109/TBME.1968.4502575

Banus, M. G., & Zetlin, A. M. (1938). The relation of isometric tension to length in skeletal muscle. *Journal of Cellular and Comparative Physiology*, *12*(3), 403-420.

Barclay, C. J., Constable, J. K., & Gibbs, C. L. (1993). Energetics of fast- and slow-twitch muscles of the mouse. *Journal of Physiology*, *472*(1), 61-80.

Bashford, J., Mills, K., & Shaw, C. (2020). The evolving role of surface electromyography in amyotrophic lateral sclerosis: A systematic review. *Clinical Neurophysiology*, *131*(4), 942-950.

Baskin, R. J., & Paolini, P. J. (1967). Volume change and pressure development in muscle during contraction. *American Journal of Physiology-Legacy Content*, *213*(4), 1025-1030.

Bates, D., Mächler, M., Bolker, B., & Walker, S. (2014). Fitting linear mixed-effects models using lme4. *Journal of Statistical Software*, *67*(1), 1-48. doi: 10.18637/jss.v067.i01

Bennett, M. B., Ker, R. F., Imery, N. J., & Alexander, R. M. (1986). Mechanical properties of various mammalian tendons. *Journal of Zoology*, *209*(4), 537-548. doi: 10.1111/j.1469-7998.1986.tb03609.x

Berger, A. (2002). How does it work?: Magnetic resonance imaging. *British Medical Journal*, *324*(7328), 35.

Bernstein, N. (1967). *The co-ordination and regulation of movements.* Oxford: Pergamon Press.

Best, T. M., McElhaney, J., Garrett Jr, W. E., & Myers, B. S. (1994). Characterization of the passive responses of live skeletal muscle using the quasi-linear theory of viscoelasticity. *Journal of Biomechanics*, *27*(4), 413-419. doi: 10.1016/0021-9290(94)90017-5

Bhargava, L. J., Pandy, M. G., & Anderson, F. C. (2004). A phenomenological model for estimating metabolic energy consumption in muscle contraction. *Journal of Biomechanics*, *37*(1), 81-88. doi: 10.1016/S0021-9290(03)00239-2

Biewener, A. A. (1998). Muscle function in vivo: A comparison of muscles used for elastic energy savings versus muscles used to generate mechanical power. *American Zoologist*, *38*(4), 703-717.

Biewener, A. A., & Baudinette, R. (1995). In vivo muscle force and elastic energy storage during steady-speed hopping of tammar wallabies (macropus eugenii). *Journal of Experimental Biology*, *198*(9), 1829-1841.

Biewener, A. A., Blickhan, R., Perry, A. K., Heglund, N. C., & Taylor, C. R. (1988). Muscle forces during locomotion in kangaroo rats: force platform and tendon buckle measurements compared. *Journal of Experimental Biology*, *137*(1), 191-205.

Biewener, A. A., Corning, W. R., & Tobalske, B. W. (1998). In vivo pectoralis muscle force-length behavior during level flight in pigeons (columba livia). *Journal of Experimental Biology*, *201*(24), 3293-3307.

Biewener, A. A., & Daley, M. A. (2007). Unsteady locomotion: Integrating muscle function with whole body dynamics and neuromuscular control. *Journal of Experimental Biology*, *210*(17), 2949-2960.

Biewener, A. A., Konieczynski, D. D., & Baudinette, R. V. (1998). In vivo muscle force-length behavior during steady-speed hopping in tammar wallabies. *Journal of Experimental Biology*, *201*(11), 1681-1694.

Biewener, A. A., McGowan, C., Card, G. M., & Baudinette, R. V. (2004). Dynamics of leg muscle function in tammar wallabies (m. eugenii) during level versus incline hopping. *Journal of Experimental Biology*, *207*(2), 211-223. doi: 10.1242/jeb.00764

Biewener, A. A., & Patek, S. N. (2018). *Animal locomotion* (2nd ed.). Oxford: Oxford Press.

Biewener, A. A., & Roberts, T. J. (2000). Muscle and tendon contributions to force, work, and elastic energy savings: A comparative perspective. *Exercise and Sport Sciences Reviews*, *28*(3), 99-107.

Blake, O. M., & Wakeling, J. M. (2014). Early deactivation of slower muscle fibres at high movement frequencies. *Journal of Experimental Biology*, *217*(19), 3528-3534.

Blake, O. M., & Wakeling, J. M. (2015). Muscle coordination limits efficiency and power output of human limb movement under a wide range of mechanical demands. *Journal of Neurophysiology*, *114*(6), 3283-3295.

Blemker, S. S., Asakawa, D. S., Gold, G. E., & Delp, S. L. (2007). Image-based musculoskeletal modeling: applications, advances, and future opportunities. *Journal of Magnetic Resonance Imaging*, *25*(2), 441-451.

Blemker, S. S., Pinsky, P. M., & Delp, S. L. (2005). A 3d model of muscle reveals the causes of nonuniform strains in the biceps brachii. *Journal of Biomechanics*, *38*(4), 657-665.

Blok, J. H., Van Dijk, J. P., Drost, G., Zwarts, M. J., & Stegeman, D. F. (2002). A high-density multichannel surface electromyography system for the characterization of single motor units. *Review of Scientific Instruments*, *73*(4), 1887-1897.

Boettinger, E. G. (1957). The machinery of insect flight. In B. T. Scheer (Ed.), *Recent advances in invertebrate physiology* (p. 117-142). Eugene: University of Oregon Publications.

Boggs, D. F., & Dial, K. P. (1993). Neuromuscular organization and regional emg activity of the pectoralis in the pigeon. *Journal of Morphology*, *218*(1), 43-57. doi: 10.1002/jmor.1052180104

Böl, M., Leichsenring, K., Weichert, C., Sturmat, M., Schenk, P., Blickhan, R., & Siebert, T. (2013). Three-dimensional surface geometries of the rabbit soleus muscle during contraction: Input for biomechanical modelling and its validation. *Biomechanics and Modeling in Mechanobiology*, *12*(6), 1205-1220. doi: 10.1007/s10237-013-0476-1

Böl, M., & Reese, S. (2008). Micromechanical modelling of skeletal muscles based on the finite element method. *Computer methods in biomechanics and biomedical engineering*, *11*(5), 489-504. doi: 10.1080/10255840701771750

Borotikar, B., Lempereur, M., Lelievre, M., Burdin, V., Ben Salem, D., & Brochard, S. (2017). Dynamic mri to quantify musculoskeletal motion: A systematic review of concurrent validity and reliability, and perspectives for evaluation of musculoskeletal disorders. *PLoS One*, *12*(12), e0189587.

Brooks, S. V., & Faulkner, J. A. (1988). Contractile properties of skeletal muscles from young, adult and aged mice. *The Journal of Physiology*, *404*(1), 71-82.

Brown, I. E., Scott, S. H., & Loeb, G. E. (1996). Mechanics of feline soleus: Ii design and validation of a mathematical model. *Journal of Muscle Research and Cell Motility*, *17*(2), 221-233. doi: 10.1007/BF00124244

Bullimore, S. R., & Burn, J. F. (2005). Scaling of elastic energy storage in mammalian limb tendons: Do small mammals really lose out? *Biology Letters*, *1*, 57-59. doi: 10.1098/rsbl.2004.0243

Burgess, K. E., Pearson, S. J., Breen, L., & Onambélé, G. N. L. (2009). Tendon structural and mechanical properties do not differ between genders in a healthy community-dwelling elderly population. *Journal of Orthopaedic Research*, *27*(6), 820-825. doi: 10.1002/jor.20811

Caiozzo, V. J., & Baldwin, K. M. (1997). Determinants of work produced by skeletal muscle: potential limitations of activation and relaxation. *American Journal of Physiology-Cell Physiology*, *273*(3), C1049-C1056. doi: 10.1152/ajpcell.1997.273.3.C1049

Camp, A. L., Astley, H. C., Horner, A. M., Roberts, T. J., & Brainerd, E. L. (2016). Fluoromicrometry: A method for measuring muscle length dynamics with biplanar videofluoroscopy. *Journal of Experimental Zoology Part A: Ecological Genetics and Physiology*, *325*(7), 399-408.

Cavagna, G. A., & Citterio, G. (1974). Effect of stretching on the elastic characteristics and the contractile component of frog striated muscle. *Journal of Physiology*, *239*(1), 1-14. doi: 10.1113/jphysiol.1974.sp010552

Cawley, G. C., & Janacek, G. J. (2010). On allometric equations for predicting body mass of dinosaurs. *Journal of Zoology*, *280*(4), 355-361.

Chan, R. W., & Titze, I. R. (1998). Viscosities of implantable biomaterials in vocal fold augmentation surgery. *Laryngoscope*, *108*(5), 725-731. doi: 10.1097/00005537-199805000-00019

Citterio, G., Agostoni, E., Piccoli, S., & Sironi, S. (1982). Selective activation of parasternal muscle fibers according to breathing rate. *Respiration Physiology*, *48*(2), 281-295. doi: 10.1016/0034-5687(82)90086-X

Close, R. (1965). Force: velocity properties of mouse muscles. *Nature*, *206*(4985), 718-719.

Cohen, A. H., & Gans, C. (1975). Muscle activity in rat locomotion: movement analysis and electromyography of the flexors and extensors of the elbow. *Journal of Morphology*, *146*(2), 177-196.

Cotofana, S., Hudelmaier, M., Wirth, W., Himmer, M., Ring-Dimitriou, S., Sänger, A. M., & Eckstein, F. (2010). Correlation between single-slice muscle anatomical cross-sectional area and muscle volume in thigh extensors, flexors and adductors of perimenopausal women. *European Journal of Applied Physiology*, *110*(1), 91-97. doi: 10.1007/s00421-010-1477-8

Cronin, N. J., & Lichtwark, G. (2013). The use of ultrasound to study muscle–tendon function in human posture and locomotion. *Gait & Posture*, *37*(3), 305-312.

Curtin, N. A., Gardner-Medwin, A. R., & Woledge, R. C. (1998). Predictions of the time course of force and power output by dogfish white muscle fibres during brief tetani. *Journal of Experimental Biology*, *201*(1), 103-114.

Daley, M. A., & Biewener, A. A. (2003). Muscle force-length dynamics during level versus incline locomotion: A comparison of in vivo performance of two guinea fowl ankle extensors. *Journal of Experimental Biology*, *206*(17), 2941-2958. doi: 10.1242/jeb.00503

Damon, B. M., Froeling, M., Buck, A. K., Oudeman, J., Ding, Z., Nederveen, A. J., ... Strijkers, G. J. (2017). Skeletal muscle diffusion tensor-mri fiber track-

ing: rationale, data acquisition and analysis methods, applications and future directions. *NMR in Biomedicine*, *30*(3), e3563.

Delp, S. L., Anderson, F. C., Arnold, A. S., Loan, P., Habib, A., John, C. T., ... Thelen, D. G. (2007). Opensim: Open-source software to create and analyze dynamic simulations of movement. *IEEE Transactions on Biomedical Engineering*, *54*(11), 1940-1950.

De Luca, C. J. (1997). The use of surface electromyography in biomechanics. *Journal of Applied Biomechanics*, *13*(2), 135-163.

De Luca, C. J. (2006). Electromyography. In J. G. Webster (Ed.), *Encyclopedia of medical devices and instrumentation* (p. 98-109). New York: John Wiley & Sons.

De Luca, C. J., Adam, A., Wotiz, R., Gilmore, L. D., & Nawab, S. H. (2006). Decomposition of surface emg signals. *Journal of Neurophysiology*, *96*(3), 1646-1657.

De Ruiter, C. J., De Haan, A. D., Jones, D. A., & Sargeant, A. J. (1998). Shortening-induced force depression in human adductor pollicis muscle. *The Journal of Physiology*, *507*(Pt 2), 583-591.

De Ruiter, C. J., Didden, W. J., Jones, D. A., & De Haan, A. D. (2000). The force-velocity relationship of human adductor pollicis muscle during stretch and the effects of fatigue. *Journal of Physiology*, *526*(3), 671-81. doi: 10.1111/j.1469-7793.2000.00671.x

Dial, K. P., Kaplan, S. R., Goslow, G. E., & Jenkins, F. A. (1988). A functional analysis of the primary upstroke and downstroke muscles in the domestic pigeon (columba livia) during flight. *Journal of Experimental Biology*, *134*(1), 1-16.

Dick, T. J., Arnold, A. S., & Wakeling, J. M. (2016). Quantifying achilles tendon force in vivo from ultrasound images. *Journal of Biomechanics*, *49*(14), 3200-3207. doi: 10.1016/j.jbiomech.2016.07.036

Dick, T. J., Biewener, A. A., & Wakeling, J. M. (2017). Comparison of human gastrocnemius forces predicted by hill-type muscle models and estimated from ultrasound images. *Journal of Experimental Biology*, *220*(9), 1643-1653. doi: 10.1242/jeb.154807

Dick, T. J., & Clemente, C. J. (2016). How to build your dragon: scaling of muscle architecture from the world's smallest to the world's largest monitor lizard. *Frontiers in Zoology*, *13*(1), 8. doi: 10.1186/s12983-016-0141-5

Dick, T. J., & Wakeling, J. M. (2017). Shifting gears: Dynamic muscle shape changes and force-velocity behavior in the medial gastrocnemius. *Journal of Applied Physiology*, *123*(6), 1433-1442. doi: 10.1152/japplphysiol.01050.2016

Dick, T. J., & Wakeling, J. M. (2018). Geometric models to explore mechanisms of dynamic shape change in skeletal muscle. *Royal Society Open Science*, *5*(5), 172371.

Dickinson, M. H., Farley, C. T., Full, R. J., Koehl, M. A. R., Kram, R., & Lehman, S. (2000). How animals move: An integrative view. *Science*, *288*(5463), 100-106. doi: 10.1126/science.288.5463.100

Duclay, J., Martin, A., Duclay, A., Cometti, G., & Pousson, M. (2009). Behavior of fascicles and the myotendinous junction of human medial gastrocnemius fol-

lowing eccentric strength training. *Muscle and Nerve*, *39*(6), 819–827. doi: 10.1002/mus.21297

Economos, A. C. (1981). The largest land mammal. *Journal of Theoretical Biology*, *89*(2), 211-214.

Edman, K. A., Elzinga, G., & Noble, M. I. (1982). Residual force enhancement after stretch of contracting frog single muscle fibers. *The Journal of General Physiology*, *80*(5), 769-784. doi: 10.1085/jgp.80.5.769

Eng, C. M., & Roberts, T. J. (2018). Aponeurosis influences the relationship between muscle gearing and force. *Journal of Applied Physiology*, *125*(2), 513-519. doi: 10.1152/japplphysiol.00151.2018

Eng, C. M., Smallwood, L. H., Rainiero, M. P., Lahey, M., Ward, S. R., & Lieber, R. L. (2008). Scaling of muscle architecture and fiber types in the rat hindlimb. *Journal of Experimental Biology*, *211*(14), 2336-2345. doi: 10.1242/jeb.017640

English, A. W. (1984). An electromyographic analysis of compartments in cat lateral gastrocnemius muscle during unrestrained locomotion. *Journal of Neurophysiology*, *52*(1), 114-125. doi: 10.1152/jn.1984.52.1.114

Erskine, R. M., Jones, D. A., Maganaris, C. N., & Degens, H. (2009). In vivo specific tension of the human quadriceps femoris muscle. *European Journal of Applied Physiology*, *106*(6), 827. doi: 10.1007/s00421-009-1085-7

Ettema, G. J. (1996). Mechanical efficiency and efficiency of storage and release of series elastic energy in skeletal muscle during stretch-shorten cycles. *Journal of Experimental Biology*, *199*(9), 1983–1997.

Ettema, G. J. (2001). Muscle efficiency: The controversial role of elasticity and mechanical energy conversion in stretch-shortening cycles. *European Journal of Applied Physiology*, *85*(5), 457-465. doi: 10.1007/s004210100464

Ettema, G. J. (2002). Effects of contraction history on control and stability in explosive actions. *Journal of Electromyography and Kinesiology*, *12*(6), 455-461.

Ettema, G. J., & Meijer, K. (2000). Muscle contraction history: Modified hill versus an exponential decay model. *Biological Cybernetics*, *83*(6), 491-500. doi: 10.1007/s004220000190

Evans, C. L., & Hill, A. V. (1914). The relation of length to tension development and heat production on contraction in muscle. *The Journal of Physiology*, *49*(1-2), 10-16.

Federici, S., Meloni, F., Bracalenti, M., & De Filippis, M. L. (2015). The effectiveness of powered, active lower limb exoskeletons in neurorehabilitation: A systematic review. *NeuroRehabilitation*, *37*(3), 321-340.

Forcinito, M., Epstein, M., & Herzog, W. (1998). Can a rheological muscle model predict force depression/enhancement? *Journal of Biomechanics*, *31*(12), 1093-1099.

Fortuna, R., Groeber, M., Seiberl, W., Power, G. A., & Herzog, W. (2017). Shortening-induced force depression is modulated in a time-and speed-dependent manner following a stretch-shortening cycle. *Physiological Reports*, *5*(12), e13279. doi: 10.14814/phy2.13279

Fortuna, R., Kirchhuebel, H., Seiberl, W., Power, G. A., & Herzog, W. (2018). Force depression following a stretch-shortening cycle is independent of stretch peak force and work performed during shortening. *Scientific Reports*, *8*(1), 1-8. doi: 10.1038/s41598-018-19657-8

Fowler, A. C. (1997). *Mathematical models in the applied sciences*. Cambridge, UK: Cambridge University Press.

Franklin, C. E., & Johnston, I. A. (1997). Muscle power output during escape responses in an antarctic fish. *Journal of Experimental Biology*, *200*(4), 703-712.

Fukunaga, T., Ichinose, Y., Ito, M., Kawakami, Y., & Fukashiro, S. (1997). Determination of fascicle length and pennation in a contracting human muscle in vivo. *Journal of Applied Physiology*, *82*(1), 354-358. doi: 10.1152/jappl.1997.82.1.354

Fukunaga, T., Kubo, K., Kawakami, Y., Fukashiro, S., Kanehisa, H., & Maganaris, C. N. (2001). In vivo behaviour of human muscle tendon during walking. *Proceedings of the Royal Society B: Biological Sciences*, *268*(1464), 229-223. doi: 10.1098/rspb.2000.1361

Fukunaga, T., Roy, R. R., Shellock, F. G., Hodgson, J. A., Day, M. K., Lee, P. L., ... Edgerton, V. R. (1992). Physiological cross-sectional area of human leg muscles based on magnetic resonance imaging. *Journal of Orthopaedic Research*, *10*(6), 926-934. doi: 10.1002/jor.1100100623

Galantis, A., & Woledge, R. C. (2003). The theoretical limits to the power output of a muscle–tendon complex with inertial and gravitational loads. *Proceedings of the Royal Society B: Biological Sciences*, *270*(1523), 1493-1498. doi: 10.1098/rspb.2003.2403

Gans, C., & Bock, W. J. (1965). The functional significance of muscle architecture – a theoretical analysis. *Advances in Anatomy, Embryology, and Cell Biology*, *38*, 115-142.

Gasser, H. S., & Hill, A. V. (1924). The dynamics of muscular contraction. *Proceedings of the Royal Society of London Series B: Biological Sciences*, *96*(678), 398-437. doi: 10.1098/rspb.1924.0035

Gillis, G. B., & Biewener, A. A. (2001). Hindlimb muscle function in relation to speed and gait: in vivo patterns of strain and activation in a hip and knee extensor of the rat (rattus norvegicus). *Journal of Experimental Biology*, *204*(15), 2717-2731.

Griffiths, R. I. (1987). Ultrasound transit time gives direct measurement of muscle fibre length in vivo. *Journal of Neuroscience Methods*, *21*(2-4), 159-165.

Grimmer, M., & Seyfarth, A. (2014). Mimicking human-like leg function in prosthetic limbs. In P. Artemiadis (Ed.), *Neuro-robotics* (p. 105-155). Dordrecht: Springer.

Günther, M., Röhrle, O., Haeufle, D. F., & Schmitt, S. (2012). Spreading out muscle mass within a hill-type model: A computer simulation study. *Computational and Mathematical Methods in Medicine*, *2012*, 848630. doi: 10.1155/2012/848630

Günther, M., Schmitt, S., & Wank, V. (2007). High-frequency oscillations as a consequence of neglected serial damping in hill-type muscle models. *Biological Cybernetics*, *97*(1), 63-79. doi: 10.1007/s00422-007-0160-6

Handsfield, G. G., Meyer, C. H., Hart, J. M., Abel, M. F., & Blemker, S. S. (2014). Relationships of 35 lower limb muscles to height and body mass quantified using mri. *Journal of Biomechanics*, *47*(3), 631-638.

Hatze, H. (1977). A myocybernetic control model of skeletal muscle. *Biological Cybernetics*, *25*(2), 103-119. doi: 10.1007/BF00337268

He, J., Levine, W. S., & Loeb, G. E. (1991). Feedback gains for correcting small perturbations to standing posture. *IEEE Transactions on Automatic Control*, *36*(3), 322-332. doi: 10.1109/9.73565

Heerkens, Y. F., Woittiez, R. D., Kiela, J., Huijing, P. A., Huson, A., van Ingen Schenau, G. J., & Rozendal, R. H. (1987). Mechanical properties of passive rat muscle during sinusoidal stretching. *Pflügers Archiv*, *409*(4), 438-447.

Heglund, N. C., Fedak, M. A., Taylor, C. R., & Cavagna, G. A. (1982). Energetics and mechanics of terrestrial locomotion. iv. total mechanical energy changes as a function of speed and body size in birds and mammals. *Journal of Experimental Biology*, *97*(1), 57-66.

Heglund, N. C., Taylor, C. R., & Mcmahon, T. A. (1974). Scaling stride frequency and gait to animal size: Mice to horses. *Science*, *186*(4169), 1112-1113. doi: 10.1126/science.186.4169.1112

Henneman, E., Somjen, G., & Carpenter, D. O. (1965a). Excitability and inhibitability of motoneurons of different sizes. *Journal of Neurophysiology*, *28*(3), 599-620.

Henneman, E., Somjen, G., & Carpenter, D. O. (1965b). Functional significance of cell size in spinal motoneurons. *Journal of Neurophysiology*, *28*(3), 560-580.

Herr, H. M., & Kornbluh, R. D. (2004). New horizons for orthotic and prosthetic technology: Artificial muscle for ambulation. *Proc. SPIE 5385, Smart Structures and Materials 2004: Electroactive Polymer Actuators and Devices (EAPAD)*, *5385*, 1-9.

Herzog, W. (2014). The role of titin in eccentric muscle contraction. *Journal of Experimental Biology*, *217*(16), 2825-2833.

Herzog, W., Duvall, M., & Leonard, T. R. (2012). Molecular mechanisms of muscle force regulation: A role for titin? *Exercise and Sport Sciences Reviews*, *40*(1), 50-57.

Herzog, W., Leonard, T., Joumaa, V., DuVall, M., & Panchangam, A. (2012). The three filament model of skeletal muscle stability and force production. *Molecular & Cellular Biomechanics*, *9*(3), 175-191.

Herzog, W., & Leonard, T. R. (1997). Depression of cat soleus forces following isokinetic shortening. *Journal of Biomechanics*, *30*(9), 865-872. doi: 10.1016/S0021-9290(97)00046-8

Herzog, W., & Leonard, T. R. (2000). The history dependence of force production in mammalian skeletal muscle following stretch-shortening and shortening-stretch cycles. *Journal of Biomechanics*, *33*(5), 531-542. doi: 10.1016/S0021-9290(99)00221-3

Herzog, W., & Leonard, T. R. (2002). Force enhancement following stretching of skeletal muscle a new mechanism. *Journal of Experimental Biology*, *205*(9), 1275-1283.

Herzog, W., Leonard, T. R., & Wu, J. Z. (2000). The relationship between force depression following shortening and mechanical work in skeletal muscle. *Journal of Biomechanics*, *33*(6), 659-668. doi: 10.1016/S0021-9290(00)00008-7

Hill, A. V. (1938). The heat of shortening and the dynamic constants of muscle. *Proceedings of the Royal Society B: Biological Sciences*, *126*(843), 136-195. doi: 10.1098/rspb.1938.0050

Hill, A. V. (1970). *First and last experiments in muscle mechanics*. Cambridge, UK: Cambridge University Press.

Hisey, B., Leonard, T. R., & Herzog, W. (2009). Does residual force enhancement increase with increasing stretch magnitudes? *Journal of Biomechanics*, *42*(10), 1488-1492.

Hodgson, J. A., Finni, T., Lai, A. M., Edgerton, V. R., & Sinha, S. (2006). Influence of structure on the tissue dynamics of the human soleus muscle observed in mri studies during isometric contractions. *Journal of Morphology*, *267*(5), 584-601. doi: 10.1002/jmor.10421

Hodson-Tole, E. F., Loram, I. D., & Vieira, T. M. (2013). Myoelectric activity along human gastrocnemius medialis: Different spatial distributions of postural and electrically elicited surface potentials. *Journal of Electromyography and Kinesiology*, *23*(1), 43-50. doi: 10.1016/j.jelekin.2012.08.003

Hodson-Tole, E. F., & Wakeling, J. M. (2009). Motor unit recruitment for dynamic tasks: current understanding and future directions. *Journal of Comparative Physiology B*, *179*(1), 57-66.

Holm, S. (1979). A simple sequentially rejective multiple test procedure. *Scandinavian Journal of Statistics*, *6*(2), 65-70.

Holt, N. C., Wakeling, J. M., & Biewener, A. A. (2014). The effect of fast and slow motor unit activation on whole-muscle mechanical performance: The size principle may not pose a mechanical paradox. *Proceedings of the Royal Society B: Biological Sciences*, *281*(1783), 20140002. doi: 10.1098/rspb.2014.0002

Horak, F. B., Henry, S. M., & Shumway-Cook, A. (1997). Postural perturbations: New insights for treatment of balance disorders. *Physical Therapy*, *77*(5), 517-533.

Hothorn, T., Bretz, F., & Westfall, P. (2008). Simultaneous inference in general parametric models. *Biometrical Journal: Journal of Mathematical Methods in Biosciences*, *50*(2), 346-363. doi: 10.1002/bimj.200810425

Houdijk, H., Bobbert, M. F., & De Haan, A. (2006). Evaluation of a hill based muscle model for the energy cost and efficiency of muscular contraction. *Journal of Biomechanics*, *39*(3), 536-543. doi: 10.1016/j.jbiomech.2004.11.033

Houk, J., & Henneman, E. (1967). Responses of golgi tendon organs to active contractions of the soleus muscle of the cat. *Journal of Neurophysiology*, *30*(3), 466-481.

Hutchinson, J. R. (2012). On the inference of function from structure using biomechanical modelling and simulation of extinct organisms. *Biology Letters*, *8*(1), 115-118.

James, R. S., Young, I. S., Cox, V. M., Goldspink, D. F., & Altringham, J. D. (1996). Isometric and isotonic muscle properties as determinants of work loop power output. *Pflügers Archiv - European Journal of Physiology*, *432*(5), 767-774.

Jayne, B. C., Bennett, A. F., & Lauder, G. V. (1990). Muscle recruitment during terrestrial locomotion: How speed and temperature affect fibre type use in a lizard. *Journal of Experimental Biology*, *152*(1), 101-128.

Johnson, T. P., & Johnston, I. A. (1991). Power output of fish muscle fibres performing oscillatory work: Effects of acute and seasonal temperature change. *Journal of Experimental Biology*, *157*(1), 409-423.

Josephson, R. K. (1985). Mechanical power output from striated muscle during cyclic contraction. *Journal of Experimental Biology*, *114*(1), 493-512.

Josephson, R. K. (1993). Contraction dynamics and power output of skeletal muscle. *Annual Review of Physiology*, *55*(1), 527-546.

Josephson, R. K. (1999). Dissecting muscle power output. *Journal of Experimental Biology*, *202*(23), 3369-3375.

Josephson, R. K., & Darrell, S. R. (1989). Strain, muscle length and work output in a crab muscle. *Journal of Experimental Biology*, *145*(1), 45-61.

Josephson, R. K., & Edman, K. A. P. (1988). The consequences of fibre heterogeneity on the force-velocity relation of skeletal muscle. *Acta Physiologica Scandinavica*, *132*(3), 341-352. doi: 10.1111/j.1748-1716.1988.tb08338.x

Josephson, R. K., & Stokes, D. R. (1989). Strain, muscle length and work output in a crab muscle. *Journal of Experimental Biology*, *145*(1), 45-61.

Kallenberg, L. A., & Hermens, H. J. (2009). Motor unit properties of biceps brachii in chronic stroke patients assessed with high-density surface emg. *Journal of the American Association of Electrodiagnostic Medicine*, *39*(2), 177-185.

Ker, R. F., Alexander, R. M., & Bennett, M. B. (1988). Why are mammalian tendons so thick? *Journal of Zoology*, *216*(2), 309-324. doi: 10.1111/j.1469-7998.1988.tb02432.x

Killen, B. A., Falisse, A., De Groote, F., & Jonkers, I. (2020). In silico-enhanced treatment and rehabilitation planning for patients with musculoskeletal disorders: Can musculoskeletal modelling and dynamic simulations really impact current clinical practice? *Applied Sciences*, *10*(20), 7255.

Kinugasa, R., Kawakami, Y., Sinha, S., & Fukunaga, T. (2011). Unique spatial distribution of in vivo human muscle activation. *Experimental Physiology*, *96*(9), 938-948. doi: 10.1113/expphysiol.2011.057562

Kleppner, D., & Kolenkow, R. (2013). *An introduction to mechanics* (2nd ed.). Cambridge, UK: Cambridge University Press.

Koelewijn, A. D., Heinrich, D., & Van Den Bogert, A. J. (2019). Metabolic cost calculations of gait using musculoskeletal energy models, a comparison study. *PloS One*, *14*(9), e0222037. doi: 10.1371/journal.pone.0222037

Konow, N., Collias, A., & Biewener, A. A. (2020). Skeletal muscle shape change in relation to varying force requirements across locomotor conditions. *Frontiers in Physiology*, *11*, 143.

Kosterina, N., Westerblad, H., & Eriksson, A. (2009). Mechanical work as predictor of force enhancement and force depression. *Journal of Biomechanics*, *42*(11), 1628-1634.

Kosterina, N., Westerblad, H., Lännergren, J., & Eriksson, A. (2008). Muscular force production after concentric contraction. *Journal of Biomechanics*, *41*(11), 2422-2429.

Kovanlikaya, A., Mittelman, S. D., Ward, A., Geffner, M. E., Dorey, F., & Gilsanz, V. (2005). Obesity and fat quantification in lean tissues using three-point dixon mr imaging. *Pediatric Radiology*, *35*(6), 601-607.

Kurokawa, S., Fukunaga, T., & Fukashiro, S. (2001). Behavior of fascicles and tendinous structures of human gastrocnemius during vertical jumping. *Journal of Applied Physiology*, *90*(4), 1349-1358. doi: 10.1152/jappl.2001.90.4.1349

Lai, A. K., Arnold, A. S., Biewener, A. A., Dick, T. J., & Wakeling, J. M. (2018). Does a two-element muscle model offer advantages when estimating ankle plantar flexor forces during human cycling? *Journal of Biomechanics*, *68*, 6-13.

Lai, A. K., Dick, T. J., Biewener, A. A., & Wakeling, J. M. (2021). Task-dependent recruitment across ankle extensor muscles and between mechanical demands is driven by the metabolic cost of muscle contraction. *Journal of the Royal Society Interface*, *18*(174), 20200765.

Lai, A. K., Schache, A. G., Lin, Y. C., & Pandy, M. G. (2014). Tendon elastic strain energy in the human ankle plantar-flexors and its role with increased running speed. *Journal of Experimental Biology*, *217*(17), 3159-3168.

Laws, R. M. (1966). Age criteria for the african elephant: *Loxodonta a. africana*. *African Journal of Ecology*, *4*(1), 1-37.

Le Bihan, D., & Iima, M. (2015). Diffusion magnetic resonance imaging: What water tells us about biological tissues. *PLoS Biology*, *13*(7), e1002203.

LeBlanc, A., Lin, C., Shackelford, L., Sinitsyn, V., Evans, H., Belichenko, O., ... Hedrick, T. (2000). Muscle volume, mri relaxation times (t2), and body composition after spaceflight. *Journal of Applied Physiology*, *89*(6), 2158-2164.

Lee, H. D., Herzog, W., & Leonard, T. (2001). Effects of cyclic changes in muscle length on force production in in-situ cat soleus. *Journal of Biomechanics*, *34*(8), 979-987.

Lee, H. D., Suter, E., & Herzog, W. (1999). Force depression in human quadriceps femoris following voluntary shortening contractions. *Journal of Applied Physiology*, *87*(5), 1651-1655.

Lee, S. S., Arnold, A. S., de Boef Miara, M., Biewener, A. A., & Wakeling, J. M. (2013). Accuracy of gastrocnemius muscles forces in walking and running goats predicted by one-element and two-element hill-type models. *Journal of Biomechanics*, *46*(13), 2288-2295. doi: 10.1016/j.jbiomech.2013.06.001

Levin, A., & Wyman, J. (1927). The viscous elastic properties of muscle. *Proceedings of the Royal Society of London Series B: Biological Sciences*, *101*(709), 218-243. doi: 10.1098/rspb.1927.0014

Lichtwark, G. A., & Barclay, C. J. (2010). The influence of tendon compliance on muscle power output and efficiency during cyclic contractions. *Journal of Experimental Biology*, *213*(5), 707–714. doi: 10.1242/jeb.038026

Lichtwark, G. A., Bougoulias, K., & Wilson, A. M. (2007). Muscle fascicle and series elastic element length changes along the length of the human gastrocnemius during walking and running. *Journal of Biomechanics*, *40*(1), 157-164. doi: 10.1016/j.jbiomech.2005.10.035

Lichtwark, G. A., & Wilson, A. M. (2005a). Effects of series elasticity and activation conditions on muscle power output and efficiency. *Journal of Experimental Biology*, *208*(15), 2845–2853. doi: 10.1242/jeb.01710

Lichtwark, G. A., & Wilson, A. M. (2005b). A modified hill muscle model that predicts muscle power output and efficiency during sinusoidal length changes. *Journal of Experimental Biology*, *208*(15), 2831–2843. doi: 10.1242/jeb.01709

Lichtwark, G. A., & Wilson, A. M. (2007). Is achilles tendon compliance optimised for maximum muscle efficiency during locomotion? *Journal of Biomechanics*, *40*(8), 1768-1775. doi: 10.1016/j.jbiomech.2006.07.025

Lichtwark, G. A., & Wilson, A. M. (2008). Optimal muscle fascicle length and tendon stiffness for maximising gastrocnemius efficiency during human walking and running. *Journal of Theoretical Biology*, *252*(4), 662–673. doi: 10.1016/j.jtbi.2008.01.018

Lieber, R. L., Leonard, M. E., & Brown-Maupin, C. G. (2000). Effects of muscle contraction on the load-strain properties of frog aponeurosis and tendon. *Cells Tissues Organs*, *166*(1), 48-54. doi: 10.1159/000016708

Lieber, R. L., & Ward, S. R. (2011). Skeletal muscle design to meet functional demands. *Philosophical Transactions of the Royal Society B: Biological Sciences*, *366*(1570), 1466-1476.

Loeb, G. E., Hoffer, J. A., & Pratt, C. A. (1985). Activity of spindle afferents from cat anterior thigh muscles. i. identification and patterns during normal locomotion. *Journal of Neurophysiology*, *54*(3), 549-564.

Luschei, E. S., & Goodwin, G. M. (1974). Patterns of mandibular movement and jaw muscle activity during mastication in the monkey. *Journal of Neurophysiology*, *37*(5), 954-966.

Machin, K. E., & Pringle, J. W. (1959). The physiology of insect fibrillar muscle. ii. mechanical properties of a beetle flight muscle. *Proceedings of the Royal Society B: Biological Sciences*, *151*(943), 204-225. doi: 10.1098/rspb.1959.0060

Machin, K. E., & Pringle, J. W. (1960). The physiology of insect fibrillar muscle. iii. the effect of sinusoidal changes of length on a beetle flight muscle. *Proceedings of the Royal Society B: Biological Sciences*, *152*(948), 311-330. doi: 10.1098/rspb.1960.0041

Maden-Wilkinson, T., Degens, H., Jones, D. A., & McPhee, J. S. (2013). Comparison of mri and dxa to measure muscle size and age-related atrophy in thigh muscles. *Journal of Musculoskeletal & Neuronal Interactions*, *13*(3), 320-328.

Maganaris, C. N., Baltzopoulos, V., & Sargeant, A. J. (1998). In vivo measurements of the triceps surae complex architecture in man: implications for muscle function. *The Journal of Physiology*, *512*(2), 603-614. doi: 10.1111/j.1469-7793.1998.603be.x

Maganaris, C. N., & Narici, M. V. (2005). Mechanical properties of tendons. In N. Maffulli, P. Renstrom, & W. B. Leadbetter (Eds.), *Tendon injuries-basic science and clinical medicine* (p. 14-21). London, UK: Springer.

Maréchal, G., & Plaghki, L. (1979). The deficit of the isometric tetanic tension redeveloped after a release of frog muscle at a constant velocity. *The Journal of General Physiology*, *73*(4), 453-467. doi: 10.1085/jgp.73.4.453

Marsh, R. L. (1999). How muscles deal with real-world loads: The influence of length trajectory on muscle performance. *Journal of Experimental Biology*, *202*(23), 3377-3385.

Mashima, H., Akazawa, K., Kushima, H., & Fujii, K. (1972). The force-load-velocity relation and the viscous-like force in the frog skeletal muscle. *Japanese Journal of Physiology*, *22*(1), 103-120. doi: 10.2170/jjphysiol.22.103

Matthews, B. H. (1933). Nerve endings in mammalian muscle. *The Journal of Physiology*, *78*(1), 1-53.

McGowan, C. P., Neptune, R. R., & Herzog, W. (2010). A phenomenological model and validation of shortening-induced force depression during muscle contractions. *Journal of Biomechanics*, *43*(3), 449-454. doi: 10.1016/j.jbiomech.2009.09.047

McGowan, C. P., Neptune, R. R., & Herzog, W. (2013). A phenomenological muscle model to assess history dependent effects in human movement. *Journal of Biomechanics*, *46*(1), 151-157. doi: 10.1016/j.jbiomech.2012.10.034

McGuigan, M. P., Yoo, E., Lee, D. V., & Biewener, A. A. (2009). Dynamics of goat distal hind limb muscle–tendon function in response to locomotor grade. *Journal of Experimental Biology*, *212*(13), 2092-2104. doi: 10.1242/jeb.028076

Medler, S. (2002). Comparative trends in shortening velocity and force production in skeletal muscles. *American Journal of Physiology - Regulatory, Integrative and Comparative Physiology*, *283*(2), R368-R378.

Meier, P., & Blickhan, R. (2000). FEM-simulation of skeletal muscle: The influence of inertia during activation and deactivation. In W. Herzog (Ed.), *Skeletal muscle mechanics: From mechanisms to function* (p. 207-233). Chichester, UK: John Wiley & Sons.

Meijer, K. (2002). History dependence of force production in submaximal stimulated rat medial gastrocnemius muscle. *Journal of Electromyography and Kinesiology*, *12*(6), 463-470.

Meijer, K., Grootenboer, H. J., Koopman, B. F., & Huijing, P. A. (1997). Fully isometric length-force curves of rat muscle differ from those during and after concentric contractions. *Journal of Applied Biomechanics*, *13*(2), 164-181.

Meijer, K., Grootenboer, H. J., Koopman, H. F., van Der Linden, B. J. J. J., & Huijing, P. A. (1998). A hill type model of rat medial gastrocnemius muscle that accounts for shortening history effects. *Journal of Biomechanics*, *31*(6), 555-563. doi: 10.1016/S0021-9290(98)00048-7

Mendez, J., & Keys, A. (1960). Density and composition of mammalian muscle. *Metabolism*, *9*, 184-188.

Millard, M., Uchida, T., Seth, A., & Delp, S. L. (2013). Flexing computational muscle: Modeling and simulation of musculotendon dynamics. *Journal of Biomechanical Engineering*, *135*(2), 021005. doi: 10.1115/1.4023390

Minetti, A. E., & Alexander, R. M. (1997). A theory of metabolic costs for bipedal gaits. *Journal of Theoretical Biology*, *186*(4), 467–476. doi: 10.1006/jtbi.1997.0407

Monti, R. J., Roy, R. R., Zhong, H., & Edgerton, V. R. (2003). Mechanical properties of rat soleus aponeurosis and tendon during variable recruitment in situ. *Journal of Experimental Biology*, *206*(19), 3437-3445. doi: 10.1242/jeb.00550

Moo, E. K., Fortuna, R., Sibole, S. C., Abusara, Z., & Herzog, W. (2016). In vivo sarcomere lengths and sarcomere elongations are not uniform across an intact muscle. *Frontiers in Physiology*, *7*, 187. doi: 10.3389/fphys.2016.00187

Moo, E. K., & Herzog, W. (2020). Sarcomere lengths become more uniform over time in intact muscle-tendon unit during isometric contractions. *Frontiers in Physiology*, *11*, 448. doi: 10.3389/fphys.2020.00448

Moo, E. K., Leonard, T. R., & Herzog, W. (2017). In vivo sarcomere lengths become more non-uniform upon activation in intact whole muscle. *Frontiers in Physiology*, *8*, 1015. doi: 10.3389/fphys.2017.01015

Moody, C. B., Barhorst, A. A., & Schovanec, L. (2009). A neuro-muscular elasto-dynamic model of the human arm part 2: Musculotendon dynamics and related stress effects. *Journal of Bionic Engineering*, *6*(2), 108-119. doi: 10.1016/S1672-6529(08)60108-0

Morgan, D. L., Whitehead, N. P., Wise, A. K., Gregory, J. E., & Proske, U. (2000). Tension changes in the cat soleus muscle following slow stretch or shortening of the contracting muscle. *Journal of Physiology*, *522*(3), 503-513. doi: 10.1111/j.1469-7793.2000.t01-2-00503.x

Mörl, F., Siebert, T., & Häufle, D. (2016). Contraction dynamics and function of the muscle-tendon complex depend on the muscle fibre-tendon length ratio: A simulation study. *Biomechanics and Modeling in Mechanobiology*, *15*(1), 245-258.

Morrison, S. M., Dick, T. J. M., & Wakeling, J. M. (2015). Structural and mechanical properties of the human achilles tendon: Sex and strength effects. *Journal of Biomechanics*, *48*(12), 3530–3533. doi: 10.1016/j.jbiomech.2015.06.009

Morse, C. I., Degens, H., & Jones, D. A. (2007). The validity of estimating quadriceps volume from single mri cross-sections in young men. *European Journal of Applied Physiology*, *100*(3), 267-274. doi: 10.1007/s00421-007-0429-4

Mortenson, M. E. (2006). *Geometric modeling* (3rd ed.). New York, USA: Industrial Press.

Nakagawa, Y. (1996). Age-related changes in biomechanical properties of the achilles tendon in rabbits. *European Journal of Applied Physiology and Occupational Physiology*, *73*(1-2), 7-10. doi: 10.1007/BF00262803

Namburete, A. I., Rana, M., & Wakeling, J. M. (2011). Computational methods for quantifying in vivo muscle fascicle curvature from ultrasound images. *Journal of Biomechanics*, *44*(14), 2538-2543. doi: 10.1016/j.jbiomech.2011.07.017

Nardone, A., Romano, C., & Schieppati, M. (1989). Selective recruitment of high-threshold human motor units during voluntary isotonic lengthening of active muscles. *The Journal of Physiology*, *409*(1), 451-471.

Nishikawa, K. C., Monroy, J. A., Uyeno, T. E., Yeo, S. H., Pai, D. K., & Linstedt, S. L. (2011). Is titin a 'winding filament'? a new twist on muscle contraction. *Proceedings of the Royal Society B: Biological Sciences*, *279*(1730), 981-990.

Nussbaum, M. A., & Chaffin, D. B. (1998). Lumbar muscle force estimation using a subject-invariant 5-parameter emg-based model. *Journal of Biomechanics*, *31*(7), 667-672. doi: 10.1016/S0021-9290(98)00055-4

Ogden, R. W. (1984). *Nonlinear elastic deformations*. New York: John Wiley & Sons.

Oomens, C. W. J., Maenhout, M., Van Oijen, C. H., Drost, M. R., & Baaijens, F. P. (2003). Oomensetal2003. *Philosophical Transactions of the Royal Society of London. Series B: Biological Sciences*, *358*(1437), 1453-1460.

Oskouei, A. E., & Herzog, W. (2005). Observations on force enhancement in sub-maximal voluntary contractions of human adductor pollicis muscle. *Journal of Applied Physiology*, *98*(6), 2087-2095.

Oskouei, A. E., & Herzog, W. (2006a). The dependence of force enhancement on activation in human adductor pollicis. *European Journal of Applied Physiology*, *98*(1), 22-29.

Oskouei, A. E., & Herzog, W. (2006b). Force enhancement at different levels of voluntary contraction in human adductor pollicis. *European Journal of Applied Physiology*, *97*(3), 280-287.

Otten, E. (1987). A myocybernetic model of the jaw system of the rat. *Journal of Neuroscience Methods*, *21*(2), 287-302. doi: 10.1016/0165-0270(87)90123-3

Paluska, D., & Herr, H. (2006). The effect of series elasticity on actuator power and work output: Implications for robotic and prosthetic joint design. *Robotics and Autonomous Systems*, *54*(8), 667-673.

Pappas, G. P., Asakawa, D. S., Delp, S. L., Zajac, F. E., & Drace, J. E. (2002). Nonuniform shortening in the biceps brachii during elbow flexion. *Journal of Applied Physiology*, *92*(6), 2381-2389. doi: 10.1152/japplphysiol.00843.2001

Pelteret, J. P. (2014). *A computational neuromuscular model of the human upper airway with application to the study of obstructive sleep apnoea* (Unpublished doctoral dissertation). University of Cape Town.

Pelteret, J. P., & McBride, A. (2012). *The deal.ii tutorial step-44: Three-field formulation for non-linear solid mechanics.* `https://dealii.org/developer/doxygen/deal.II/step_44.html`. (doi: 10.5281/zenodo.439772)

Pennycuick, C. J., & Rezende, M. A. (1984). The specific power output of aerobic muscle, related to the power density of mitochondria. *Journal of Experimental Biology*, *108*(1), 377-392.

Perreault, E. J., Heckman, C. J., & Sandercock, T. G. (2003). Hill muscle model errors during movement are greatest within the physiologically relevant range of motor unit firing rates. *Journal of Biomechanics*, *36*(2), 211-218. doi: 10.1016/S0021-9290(02)00332-9

Pinniger, G. J., & Cresswell, A. G. (2007). Residual force enhancement after lengthening is present during submaximal plantar flexion and dorsiflexion actions in humans. *Journal of Applied Physiology*, *102*(1), 18-25.

Pollock, C. M., & Shadwick, R. E. (1994a). Allometry of muscle, tendon, and elastic energy storage capacity in mammals. *American Journal of Physiology-Regulatory, Integrative and Comparative Physiology*, *266*(3), R1022-R1031. doi: 10.1152/ajpregu.1994.266.3.R1022

Pollock, C. M., & Shadwick, R. E. (1994b). Relationship between body mass and biomechanical properties of limb tendons in adult mammals. *American Journal of Physiology - Regulatory Integrative and Comparative Physiology*, *266*(3), R1016-R1021. doi: 10.1152/ajpregu.1994.266.3.r1016

Pratt, C. A., & Loeb, G. E. (1991). Functionally complex muscles of the cat hindlimb. i. patterns of activation across sartorius. *Experimental Brain Research*, *85*(2), 243-256. doi: 10.1007/bf00229404

Prautzsch, H., Boehm, W., & Paluszny, M. (2002). *Bézier and b-spline techniques*. Berlin, Germany: Springer.

Rahemi, H., Nigam, N., & Wakeling, J. M. (2014). Regionalizing muscle activity causes changes to the magnitude and direction of the force from whole muscles. *Frontiers in Physiology*, *5*, 298.

Rahemi, H., Nigam, N., & Wakeling, J. M. (2015). The effect of intramuscular fat on skeletal muscle mechanics: Implications for the elderly and obese. *Journal of the Royal Society Interface*, *12*(109), 20150365.

Raiteri, B. J., Cresswell, A. G., & Lichtwark, G. A. (2016). Three-dimensional geometrical changes of the human tibialis anterior muscle and its central aponeurosis measured with three-dimensional ultrasound during isometric contractions. *PeerJ*, *4*, e2260.

Ramsey, R. W., & Street, S. F. (1940). The isometric length-tension diagram of isolated skeletal muscle fibers of the frog. *Journal of Cellular and Comparative Physiology*, *15*(1), 11-34.

Ranatunga, K. W. (1984). The force-velocity relation of rat fast-and slow-twitch muscles examined at different temperatures. *The Journal of Physiology*, *351*(1), 517-529.

Randhawa, A., Jackman, M. E., & Wakeling, J. M. (2013). Muscle gearing during isotonic and isokinetic movements in the ankle plantarflexors. *European Journal of Applied Physiology*, *113*(2), 437-447. doi: 10.1007/s00421-012-2448-z

Randhawa, A., & Wakeling, J. M. (2015). Multidimensional models for predicting muscle structure and fascicle pennation. *Journal of Theoretical Biology*, *382*, 57-63. doi: 10.1016/j.jtbi.2015.06.001

Randhawa, A., & Wakeling, J. M. (2018). Transverse anisotropy in the deformation of the muscle during dynamic contractions. *Journal of Experimental Biology*, *221*(15), jeb175794. doi: 10.1242/jeb.175794

Rasool, G., Afsharipour, B., Suresh, N. L., & Rymer, W. Z. (2017). Spatial analysis of multichannel surface emg in hemiplegic stroke. *IEEE Transactions on Neural Systems and Rehabilitation Engineering*, *25*(10), 1802-1811.

R Core Team. (2019). *R: A language and environment for statistical computing*. Vienna, Austria: R Foundation for Statistical Computing.

Reggiani, C., Potma, E. J., Bottinelli, R., Canepari, M., Pellegrino, M. A., & Stienen, G. J. M. (1997). Chemo-mechanical energy transduction in relation to myosin isoform composition in skeletal muscle fibres of the rat. *Journal of Physiology*, *502*(2), 449–460. doi: 10.1111/j.1469-7793.1997.449bk.x

He, Z. H., Bottinelli, R., Pellegrino, M. A., Ferenczi, M. A., & Reggiani, C. (2000). Atp consumption and efficiency of human single muscle fibers with different myosin isoform composition. *Biophysical Journal*, *79*(2), 945–961. doi: 10.1016/S0006-3495(00)76349-1

Richards, C. T., & Clemente, C. J. (2013). Built for rowing: Frog muscle is tuned to limb morphology to power swimming. *Journal of the Royal Society Interface*, *10*(84), 20130236.

Roberts, T. J., & Azizi, E. (2011). Flexible mechanisms: The diverse roles of biological springs in vertebrate movement. *Journal of Experimental Biology*, *214*(3), 353-361.

Roberts, T. J., Marsh, R. L., Weyand, P. G., & Taylor, C. R. (1997). Muscular force in running turkeys: The economy of minimizing work. *Science*, *275*(5303), 1113-1115. doi: 10.1126/science.275.5303.1113

Rode, C., Siebert, T., & Blickhan, R. (2009). Titin-induced force enhancement and force depression: A 'sticky-spring' mechanism in muscle contractions? *Journal of Theoretical Biology*, *259*(2), 350-360.

Rome, L. C., Funke, R. P., Alexander, R. M., Lutz, G., Aldridge, H., Scott, F., & Freadman, M. (1988). Why animals have different muscle fibre types. *Nature*, *335*(6193), 824-827. doi: 10.1038/335824a0

Rome, L. C., Sosnicki, A. A., & Goble, D. O. (1990). Maximum velocity of shortening of three fibre types from horse soleus muscle: Implications for scaling with body size. *The Journal of Physiology*, *431*(1), 173–185. doi: 10.1113/jphysiol.1990.sp018325

Roots, H., Offer, G. W., & Ranatunga, K. W. (2007). Comparison of the tension responses to ramp shortening and lengthening in intact mammalian muscle fibres: Crossbridge and non-crossbridge contributions. *Journal of Muscle Research and Cell Motility*, *28*(2-3), 123-139. doi: 10.1007/s10974-007-9110-0

Ross, S. A., Dominguez, S., Nigam, N., & Wakeling, J. M. (2021). The energy of muscle contraction. iii. kinetic energy during cyclic contractions. *Frontiers in Physiology*, *12*, 628819. doi: 10.3389/fphys.2021.628819

Ross, S. A., Nigam, N., & Wakeling, J. M. (2018a). A modelling approach for exploring muscle dynamics during cyclic contractions. *PLoS Computational Biology*, *14*(4), e1006123. doi: 10.1371/journal.pcbi.1006123

Ross, S. A., Rimkus, B., Konow, N., Biewener, A. A., & Wakeling, J. M. (2020). Added mass in rat plantaris muscle causes a reduction in mechanical work. *Journal of Experimental Biology*, *223*(19), jeb224410. doi: 10.1242/jeb.224410

Ross, S. A., Ryan, D. S., Dominguez, S., Nigam, N., & Wakeling, J. M. (2018b). Size, history-dependent, activation and three-dimensional effects on the work and power produced during cyclic muscle contractions. *Integrative and Comparative Biology*, *58*(2), 232-250. doi: 10.1093/icb/icy021

Ross, S. A., & Wakeling, J. M. (2016). Muscle shortening velocity depends on tissue inertia and level of activation during submaximal contractions. *Biology Letters*, *12*(6), 20151041. doi: 10.1098/rsbl.2015.1041

Ross, S. A., & Wakeling, J. M. (2021, in review). The energy of muscle contraction. vi. greater mass of larger muscles decreases contraction efficiency. *Journal of The Royal Society Interface*.

Roy, R. R., Meadows, I. D., Baldwin, K. M., & Edgerton, V. R. (1982). Functional significance of compensatory overloaded rat fast muscle. *Journal of Applied Physiology*, *52*(2), 473-478. doi: 10.1152/jappl.1982.52.2.473

Rushmer, R. F., Franklin, D. L., & Ellis, R. M. (1956). Left ventricular dimensions recorded by sonocardiometry. *Circulation Research*, *4*(6), 684-688.

Ryan, D. S., Domínguez, S., Ross, N., S. A. Nigam, & Wakeling, J. M. (2020). The energy of muscle contraction. ii. transverse compression and work. *Frontiers in Physiology*, *11*, 538522. doi: 10.3389/fphys.2020.538522

Ryan, D. S., Stutzig, N., Siebert, T., & Wakeling, J. M. (2019). Passive and dynamic muscle architecture during transverse loading for gastrocnemius medialis in man. *Journal of Biomechanics*, *86*, 160-166. doi: 10.1016/j.jbiomech.2019.01.054

Sandercock, T. G., & Heckman, C. J. (1997). Force from cat soleus muscle during imposed locomotor-like movements: experimental data versus hill-type model predictions. *Journal of Neurophysiology*, *77*(3), 1538-52.

Sawicki, G. S., Robertson, B. D., Azizi, E., & Roberts, T. J. (2015). Timing matters: Tuning the mechanics of a muscle-tendon unit by adjusting stimulation phase during cyclic contractions. *Journal of Experimental Biology*, *2018*(19), 3150–3159. doi: 10.1242/jeb.121673

Schieber, M. H. (1993). Electromyographic evidence of two functional subdivisions in the rhesus monkey's flexor digitorum profundus. *Experimental Brain Research*, *95*(2), 251-260.

Schoemaker, I., Hoefnagel, P. P. W., Mastenbroek, T. J., Kolff, C. F., Schutte, S., van der Helm, F. C. T., ... Simonsz, H. J. (2006). Elasticity, viscosity, and

deformation of orbital fat. *Investigative Ophthalmology and Visual Science*, *47*(11), 4819-4826. doi: 10.1167/iovs.05-1497

Scott, S. H., & Winter, D. A. (1991). A comparison of three muscle pennation assumptions and their effect on isometric and isotonic force. *Journal of Biomechanics*, *24*(2), 163-167. doi: 10.1016/0021-9290(91)90361-P

Seiberl, W., Hahn, D., Herzog, W., & Schwirtz, A. (2012). Feedback controlled force enhancement and activation reduction of voluntarily activated quadriceps femoris during sub-maximal muscle action. *Journal of Electromyography and Kinesiology*, *22*(1), 117-123.

Seiberl, W., Paternoster, F., Achatz, F., Schwirtz, A., & Hahn, D. (2013). On the relevance of residual force enhancement for everyday human movement. *Journal of Biomechanics*, *46*(12), 1996-2001.

Seiberl, W., Power, G. A., Herzog, W., & Hahn, D. (2015). The stretch-shortening cycle (ssc) revisited: Residual force enhancement contributes to increased performance during fast sscs of human m. adductor pollicis. *Physiological Reports*, *3*(5), e12401.

Seow, C. Y., & Ford, L. E. (1991). Shortening velocity and power output of skinned muscle fibers from mammals having a 25,000-fold range of body mass. *Journal of General Physiology*, *97*(3), 541-560. doi: 10.1085/jgp.97.3.541

Shadwick, R. E., & Lauder, G. V. (2006). *Fish physiology: Fish biomechanics*. Boston, USA: Academic Press.

Shiavi, R., & Griffin, P. (1983). Changes in electromyographic gait patterns of calf muscles with walking speed. *IEEE Transactions on Biomedical Engineering*, *BME-30*(1), 73-76. doi: 10.1109/TBME.1983.325171

Shin, D. D., Hodgson, J. A., Edgerton, V. R., & Sinha, S. (2009). In vivo intramuscular fascicle-aponeuroses dynamics of the human medial gastrocnemius during plantarflexion and dorsiflexion of the foot. *Journal of Applied Physiology*, *107*(4), 1276-1284. doi: 10.1152/japplphysiol.91598.2008

Smith, J. L., Betts, B., Edgerton, V. R., & Zernicke, R. F. (1980). Rapid ankle extension during paw shakes: selective recruitment of fast ankle extensors. *Journal of Neurophysiology*, *43*(3), 612-620.

Soman, A., Hedrick, T. L., & Biewener, A. A. (2005). Regional patterns of pectoralis fascicle strain in the pigeon columba livia during level flight. *Journal of Experimental Biology*, *208*(4), 771-786. doi: 10.1242/jeb.01432

Stevens, E. D., & Syme, D. A. (1989). The relative changes in isometric force and work during fatigue and recovery in isolated toad sartorius muscle. *Canadian Journal of Physiology and Pharmacology*, *67*(12), 1544-1548. doi: 10.1139/y89-249

Stevens, E. D., & Syme, D. A. (1993). Effect of stimulus duty cycle and cycle frequency on power output during fatigue in rat diaphragm muscle doing oscillatory work. *Canadian Journal of Physiology and Pharmacology*, *71*(12), 910-916. doi: 10.1139/Y09-002

Swoap, S. J., Caiozzo, V. J., & Baldwin, K. M. (1997). Optimal shortening velocities for in situ power production of rat soleus and plantaris muscles.

American Journal of Physiology-Cell Physiology, *273*(3), C1057-C1063. doi: 10.1152/ajpcell.1997.273.3.C1057

Swoap, S. J., Johnson, T. P., Josephson, R. K., & Bennett, A. F. (1993). Temperature, muscle power output and limitations on burst locomotor performance of the lizard dipsosaurus dorsalis. *Journal of Experimental Biology*, *174*(1), 185-197.

Syme, D. A. (1990). Passive viscoelastic work of isolated rat, rattus norvegicus, diaphragm muscle. *Journal of Physiology*, *424*(1), 310-315. doi: 10.1113/jphysiol.1990.sp018068

Syme, D. A., & Tonks, D. M. (2004). Fatigue and recovery of dynamic and steady-state performance in frog skeletal muscle. *American Journal of Physiology - Regulatory, Integrative and Comparative Physiology*, *286*(5), R916-R926. doi: 10.1152/ajpregu.00347.2003

Tamura, Y., Saito, M., & Nagato, R. (2005). A new motor model representing the stretch-induced force enhancement and shortening-induced force depression in skeletal muscle. *Journal of Biomechanics*, *38*(4), 877-884.

Taylor, C. R., Schmidt-Nielsen, K., & Raab, J. L. (1970). Scaling of energetic cost of running to body size in mammals. *The American Journal of Physiology*, *219*(4), 1104–1107. doi: 10.1152/ajplegacy.1970.219.4.1104

Templeton, G. H., & Nardizzi, L. R. (1974). Elastic and viscous stiffness of the canine left ventricle. *Journal of Applied Physiology*, *36*(1), 123-127. doi: 10.1152/jappl.1974.36.1.123

Templeton, G. H., Wildenthal, K., Willerson, J. T., & Reardon, W. C. (1974). Influence of temperature on the mechanical properties of cardiac muscle. *Circulation Research*, *34*(5), 624-634. doi: 10.1161/01.RES.34.5.624

Thelen, D. G. (2003). Adjustment of muscle mechanics model parameters to simulate dynamic contractions in older adults. *Journal of Biomechanical Engineering*, *125*(1), 70-77. doi: 10.1115/1.1531112

Tijs, C., van Dieën, J., & Maas, H. (2015). Effects of epimuscular myofascial force transmission on sarcomere length of passive muscles in the rat hindlimb. *Physiological Reports*, *3*(11), e12608. doi: 10.14814/phy2.12608

Tikkanen, O., Haakana, P., Pesola, A. J., Häkkinen, K., Rantalainen, T., Havu, M., ... Finni, T. (2013). Muscle activity and inactivity periods during normal daily life. *PLoS One*, *8*(1), e52228. doi: 10.1371/journal.pone.0052228

Till, O., Siebert, T., & Blickhan, R. (2014). Force depression decays during shortening in the medial gastrocnemius of the rat. *Journal of Biomechanics*, *47*(5), 1099-1103.

Uchida, T. K., Hicks, J. L., Dembia, C. L., & Delp, S. L. (2016). Stretching your energetic budget: How tendon compliance affects the metabolic cost of running. *PLoS ONE*, *11*(3), e0150378. doi: 10.1371/journal.pone.0150378

Umberger, B. R. (2010). Stance and swing phase costs in human walking. *Journal of the Royal Society Interface*, *7*(50), 1329–1340. doi: 10.1098/rsif.2010.0084

Umberger, B. R., Gerritsen, K. G. M., & Martin, P. E. (2003). A model of human muscle energy expenditure. *Computer Methods in Biomechanics and Biomedical Engineering*, *6*(2), 99-111. doi: 10.1080/1025584031000091678

Van Hooren, B., Teratsias, P., & Hodson-Tole, E. F. (2020). Ultrasound imaging to assess skeletal muscle architecture during movements: A systematic review of methods, reliability, and challenges. *Journal of Applied Physiology*, *128*(4), 978-999.

Van Leeuwen, J. L. (1992). Muscle function in locomotion. In R. M. Alexander (Ed.), *Mechanics of animal locomotion* (p. 191-250). Berlin: Springer.

Wager, J. C., & Challis, J. H. (2016). Elastic energy within the human plantar aponeurosis contributes to arch shortening during the push-off phase of running. *Journal of Biomechanics*, *49*(5), 704-709. doi: 10.1016/j.jbiomech.2016.02.023

Wakeling, J. M. (2004). Motor units are recruited in a task-dependent fashion during locomotion. *Journal of Experimental Biology*, *207*(22), 3883-3890.

Wakeling, J. M. (2008). The recruitment of different compartments within a muscle depends on the mechanics of the movement. *Biology Letters*, *5*(1), 30-34. doi: 10.1098/rsbl.2008.0459

Wakeling, J. M., Blake, O. M., Wong, I., & Rana, S. S., M. Lee. (2011). Movement mechanics as a determinate of muscle structure, recruitment and coordination. *Philosophical Transactions of the Royal Society B: Biological Sciences*, *366*(1570), 1554-1564.

Wakeling, J. M., Jackman, M., & Namburete, A. I. (2013). The effect of external compression on the mechanics of muscle contraction. *Journal of Applied Biomechanics*, *29*(3), 360-364. doi: 10.1123/jab.29.3.360

Wakeling, J. M., & Johnston, I. A. (1999). Predicting muscle force generation during fast-starts for the common carp cyprinus carpio. *Journal of Comparative Physiology B*, *169*(6), 391-401.

Wakeling, J. M., & Lee, S. S. (2011). Modelling muscle forces: From scaled fibres to physiological task-groups. *Procedia IUTAM*, *2*, 317-326.

Wakeling, J. M., Lee, S. S., Arnold, A. S., de Boef Miara, M., & Biewener, A. A. (2012). A muscle's force depends on the recruitment patterns of its fibers. *Annals of Biomedical Engineering*, *40*(8), 1708-1720. doi: 10.1007/s10439-012-0531-6

Wakeling, J. M., Ross, S. A., Ryan, D. S., Bolsterlee, B., Konno, R., Dominguez, S., & Nigam, N. (2020). The energy of muscle contraction. i. tissue force and deformation during fixed-end contractions. *Frontiers in Physiology*, *11*, 813. doi: 10.3389/fphys.2020.00813

Wakeling, J. M., Tijs, C., Konow, N., & Biewener, A. A. (2021). Modeling muscle function using experimentally determined subject-specific muscle properties. *Journal of Biomechanics*, *117*, 110242.

Wakeling, J. M., Uehli, K., & Rozitis, A. I. (2006). Muscle fibre recruitment can respond to the mechanics of the muscle contraction. *Journal of the Royal Society Interface*, *3*(9), 533-544.

Walmsley, B., Hodgson, J. A., & Burke, R. E. (1978). Forces produced by medial gastrocnemius and soleus muscles during locomotion in freely moving cats. *Journal of Neurophysiology*, *41*(5), 1203-1216.

Weis-Fogh, T., & Alexander, R. M. (1977). The sustained power output from striated muscle. In T. J. Pedley (Ed.), *Scale effects in animal locomotion* (p. 511-525). London, UK: Academic Press.

Wickiewicz, T. L., Roy, R. R., Powell, P. L., & Edgerton, V. R. (1983). Muscle architecture of the human lower limb. *Clinical Orthopaedics and Related Research*(179), 275-283.

Williams, T. L. (2010). A new model for force generation by skeletal muscle, incorporating work-dependent deactivation. *Journal of Experimental Biology*, *213*(4), 643-650.

Williamson, M. R., Dial, K. P., & Biewener, A. A. (2001). Pectoralis muscle performance during ascending and slow level flight in mallards (anas platyrhynchos). *Journal of Experimental Biology*, *204*(3), 495-507.

Wilson, R. S., & James, R. S. (2004). Constraints on muscular performance: Trade–offs between power output and fatigue resistance. *Proceedings of the Royal Society B: Biological Sciences*, *271*(S4), S222-S225.

Winters, T. M., Takahashi, M., Lieber, R. L., & Ward, S. R. (2011). Whole muscle length-tension relationships are accurately modeled as scaled sarcomeres in rabbit hindlimb muscles. *Journal of Biomechanics*, *44*(1), 109-115. doi: 10.1016/j.jbiomech.2010.08.033

Woittiez, R. D., & Huijing, P. A. (1983). The effect of architecture on skeletal muscle performance: A simple planimetric model. *Netherlands Journal of Zoology*, *34*(1), 21-32.

Woittiez, R. D., Huijing, P. A., Boom, H. B., & Rozendal, R. H. (1984). A three-dimensional muscle model: A quantified relation between form and function of skeletal muscles. *Journal of Morphology*, *182*(1), 95-113. doi: 10.1002/jmor.1051820107

Woledge, R. C., Curtin, N. A., & Homsher, E. (1985). *Energetic aspects of muscle contraction*. London: Academic Press.

Wu, J. Z., & Herzog, W. (1999). Modelling concentric contraction of muscle using an improved cross-bridge model. *Journal of Biomechanics*, *32*(8), 837-848.

Yeoh, O. H. (1993). Some forms of the strain energy function for rubber. *Rubber Chemistry and Technology*, *66*(5), 754-771.

Zajac, F. E. (1989). Muscle and tendon: Properties, models, scaling, and application to biomechanics and motor control. *Critical Reviews in Biomedical Engineering*, *17*(4), 359-411.

Zuurbier, C. J., & Huijing, P. A. (1993). Changes in geometry of activity shortening unipennate rat gastrocnemius muscle. *Journal of Morphology*, *218*(2), 167-180. doi: 10.1002/jmor.1052180206